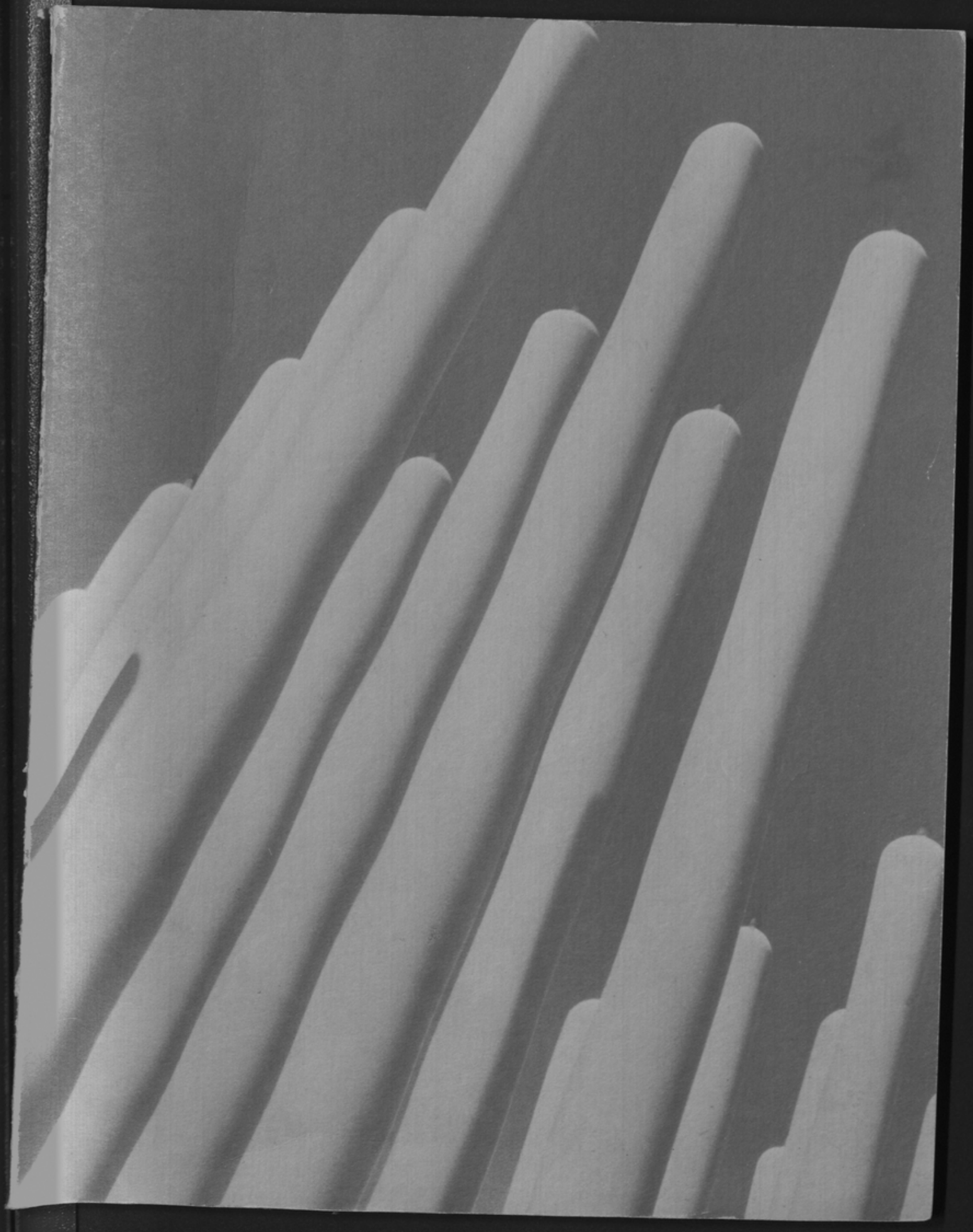

ANNUAL REPORT

Nuclear Physics Laboratory
University of Washington
June, 1970

Program "A" --
Experimental Nuclear Physics
Program (Cyclotron)
under
U.S. Atomic Energy Commission
Contract A.T.(45-1)-1388

THE COVER DESIGN

Each year we endeavor to find a cover picture which has interest for both the physicist and non-physicist, and which might be classed as somewhat unique to our laboratory.

This year we settled on our high pressure gas cylinders which store the nitrogen and carbon dioxide mixture used for insulating the high potential terminals of the two Van de Graaff machines.

The architect of our building managed to turn the knotty problem of where to put the cylinders into an architectual conversation piece. They form a group of towers which front on the Van de Graaff building and have aroused considerable local interest and curiousity.

The reader can best appreciate the design by opening both front and back covers. The visitor can best observe the towers by lying on the grass and gazing at the yellow colored tanks against a blue sky background.

INTRODUCTION

The research and technical work described in this report was performed at the Nuclear Physics Laboratory of the University of Washington during the year ending April 15, 1970. It was directed and executed by faculty and graduate students from the Departments of Physics and Chemistry, by the staff of the Laboratory, and by visitor groups from both within and outside the University community.

The principal facilities of the Laboratory are a three-stage Model-FN tandem Van de Graaff accelerator, constructed by the High Voltage Engineering Company and completed in 1967, and a conventional cyclotron -- the "Sixty-Inch"-- constructed by laboratory personnel, and completed in 1952. The three-stage Van de Graaff accelerator produces a direct current beam of protons with energies variable up to 24.6 MeV. It is also used for deuteron, alpha particle, and heavy ion acceleration. The cyclotron accelerates protons, deuterons, and alpha particles to essentially fixed energies of 11, 22, and 44 MeV, respectively.

Financial support for the laboratory and for operations conducted with the Van de Graaff accelerator is provided by the Atomic Energy Commission under Contract A.T.(45-1)-1388, Program "A", and the State of Washington. Cyclotron operations are supported by State funds and by financial assistance from outside user groups. A National Science Foundation grant provided funds for the purchase of the Van de Graaff accelerator, a portion of the associated equipment, and approximately one half the construction costs of the laboratory building. The remainder of the building funds came from State sources.

The research in the Laboratory involves a wide range of current problems in the study of nuclear structure and nuclear reactions. Within the limitations imposed by facilities and time, we encourage individuals and groups to pursue any avenue of research appropriate to nuclear physics.

Each individual report is intended to describe the status of experiments or developments which in some cases are incomplete. Although many are continuations of work described in earlier Annual Reports, an effort has been made to insure that enough background material is included so that the *raison d'etre* of the work is clear to the reader. The appearance of specific numerical results and conclusions here does not constitute publication, and should not be quoted without permission of the investigators. All names are listed in alphabetical order.

Most of the reports have been written by graduate students and are chiefly their responsibility. We regard this chore as important in their training. The act of writing encourages one to focus upon objectives, and the completed sum

of reports provides excellent intra-laboratory communication. We therefore believe our annual report has an intrinsic value beyond letting the agencies know we've tried hard. It even allows those who write introductions momentarily to be captivated by their own rhetoric.

This year, in recognition of the logic that all good experimental work must begin with good equipment, we have inverted our usual subject order by placing the instrumentation sections at the beginning. However, it should not be construed that order denotes importance or even always logic. For example, the high regard we hold for our staff is not reflected in the fact that our group picture, also an innovation this year, appears at the end of the report.

Section 12 of this report contains brief descriptions of a wide variety of research projects conducted at The Sixty-Inch Cyclotron by groups from outside the Laboratory. These visitor groups, which come from other organizations within the University, from other universities and colleges, and from industrial organizations, have provided the material contained in this section, and we appreciate their contributions. Because of the obvious benefits of this work both to the Laboratory, and to the scientific community in general, such groups will continue to be welcomed here to the fullest extent possible within the limitations of time, maintenance, and safety.

TABLE OF CONTENTS

1. ACCELERATOR RESEARCH AND DEVELOPMENT

1.1 Van de Graaff Accelerator Improvements and Operation

Major emphasis in Van de Graaff accelerator development this year has been on production of new ion beams. During the summer of 1969 both ^{6}Li and ^{18}O ions were accelerated for the first time and subsequently used in experiments. The techniques used to obtain these beams are described in Sections 1.4 and 1.5 of this report. In addition, the direct extraction ion source described in Sec. 1.2 has been installed and is being used routinely for the production of proton, deuteron and ^{16}O beams. This source has a large enough output of oxygen ions that it is now possible to obtain intense beams of $^{16}O^{7+}$, which can be accelerated to an energy of 72 MeV. The direct extraction source has also freed the charge exchange source for use entirely as a helium or lithium ion source. This has greatly simplified accelerator operations because the conversion of the charge exchange source from hydrogen to helium ions takes an entire working day.

The statistics of accelerator operation are given in Table 1.1-1 and the list of tank opening for both the tandem and injector are given in Tables 1.1-2 and 1.1-3. The most significant maintenance problem involved the injector accident described in detail in Sec. 1.9. The repair of the injector took 39 days to complete. In addition the tandem tank was opened eight times during the year to repair leaks in the sylphon that is part of a rotary motion feedthrough for the terminal foil changing mechanism. After nearly two years of continuous service, porosity developed in the solder joints at the ends of this sylphon. A number of repairs were attempted but the porosity reappeared within a few weeks in each case. A feedthrough involving no solder joints has been installed and appears to have solved the problem.

In addition to the improvements and maintenance mentioned above, or described in Secs. 1.3,1.6,1.7, and 1.8, the following were also accomplished during the year.

a. Magnet power supply cooling water was changed from the chilled to the condensate water system to eliminate sweating in the transister bank.

b. Blower type mechanical pumps in the injector vacuum modules were replaced by vane type pumps to improve reliability.

c. A network of multiple conductor cables was installed to provide additional wiring capacity between the control room and the caves and accelerator tunnel.

d. Safety interlocks were improved.

e. Electrical wiring drawings were brought up to date.

(C.E. Linder, J.W. Orth, G.J. Rohrbaugh, G.E. Saling, and W.G. Weitkamp)

Table 1.1-1. Statistics of Van de Graaff operation during the period from April 16, 1969 to April 15, 1970.

1. Division of time among activities:

	Time (Hrs)	Per Cent
Normal operation[a]	6618	76
Accelerator testing[b]	105	1
Scheduled maintenance[b]	907	10
Unscheduled maintenance[b]	792	9
Unrequested time[c]	338	4
Total[d]	8760	100

2. Division of beam-on time among particles

a. Two-stage operation

Protons	1175	24
Deuterons	260	5
^{3}He	409	8
^{4}He	522	11
^{16}O	251	5
^{18}O	86	2
^{6}Li	138	3
Total	2841	58

b. Three-stage operation

Protons	1327	27
Deuterons	753	15
Total	2080	42
TOTAL BEAM TIME	4921	100

a Includes all time accelerator was under control of an experimentor.

b Includes time machine is idle on account of these activities.

c. Includes legal holidays if the machine was not run.

d. This equals the number of hours in one year.

Table 1.1-2. The tandem tank has been 14 times during the past year for the following reasons:

1.	4-21-69	- Installed new terminal ripple remover.
2.	4-25-69	- Replaced leaking foil sylphon.
3.	5-26-69	- Fixed terminal ripple remover, re-installed down charge screen, replaced foils, replaced corona needles.
4.	6-30-69	- Frozen alternator bearing. Replaced alternator, greased drive motor.
5.	7-23-69	- Adjusted screens, re-tensioned belt, repaired terminal ripple remover.
6.	8-5-69	- Removed leaking foil sylphon.
7.	8-11-69	- Installed new foil sylphon.
8.	9-2-69	- Repaired terminal ripple remover.
9.	10-14-69	- Repaired foil sylphon leak. Calibrated upper drive motor thermistor.
10.	12-30-69	- Installed new foil sylphon. Greased alternator drive motor. Installed new foils.
11.	1-28-70	- Repaired vacuum leak in foil wheel port. Installed new foils.
12.	2-11-70	- Repaired vacuum leak in foil sylphon. Replaced foil wheel mechanism.
13.	2-14-70	- Replaced foil wheel sylphon. Repaired leak in L.E. gate valve.
14.	2-27-70	- Replaced an open resistor. Repaired broken wire to corona head.

Table 1.1-3. The injector tank has been opened 5 times during the past year for the following reasons:

1.	5-15-69	- Filled adder gas bottle.
2.	9-1-69	- Replaced drivemotor, greased alternator.
3.	9-20-69	- Repaired broken Septier lens, realigned injector.
4.	11-19-69	- Replaced a loose spring on column. Removed extra saddle which was shorting out column insulator.
5.	11-24-69	- Repaired loose spring on back-biasing at midsection.

1.2 Direct Extraction Ion Source

The direct extraction ion source[1] has been completed and is now in use. The source was installed between the negative ion source and the injector after having been set up and tested outside of the accelerator area.

The source was installed primarily to provide a beam suitable for use with the beam buncher.[2] Momentum variation of the protons from the charge exchange type source limits its usefulness for bunched beam experiments. The momentum variation places a lower limit on the pulse width of 5 nsec.

The secondary purpose was to decrease down time when switching from one type of ion to another. There is only one location for the charge exchange negative ion source, the alpha source, and the lithium source, so considerable time was spent removing and installing ion sources. The DEIS, a completely independent system, cuts down on the number of source exchanges since it replaces the charge exchange negative ion source.

The buncher used with the DEIS has delivered 200 nA of protons on target with a pulse width at half maximum of 1.8 nsec. This is 1/3 the minimum width attainable using the charge exchange negative ion source.

With 45 kV extraction voltage, proton beams from the source have exceeded 40 μA. With an input into the tandem of 40 μA, 12 μA have been measured at the output. The transmission is improved with lower intensities and an output of 5 ua has been observed for an input of 7 μA. So far there has been no attempt to put beams of this size on target.

The oxygen emitted from the barium oxide coating on the filament is sufficient to provide 16 μA of oxygen beam. This beam has made it possible to get 300 nA of charge state 7^+ on target at an energy of 70 MeV.

The source uses an ORTEC 358 duoplasmatron. The portion of the focus electrode that faces the duoplasmatron was also purchased from ORTEC. The geometry of the source is shown in Fig. 1.2-1.

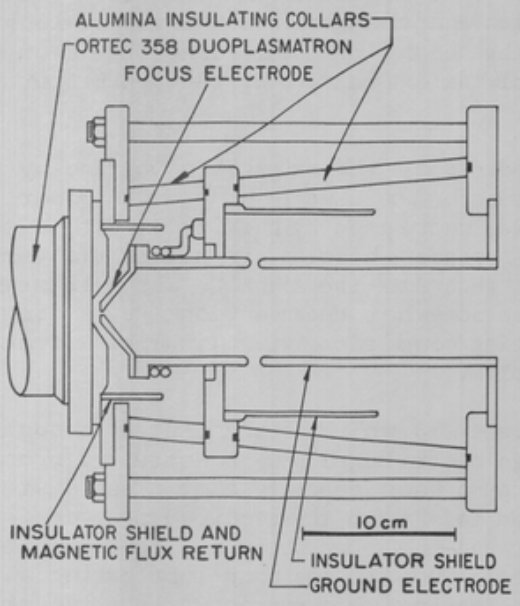

Fig. 1.2-1. Side view of direct extraction ion source.

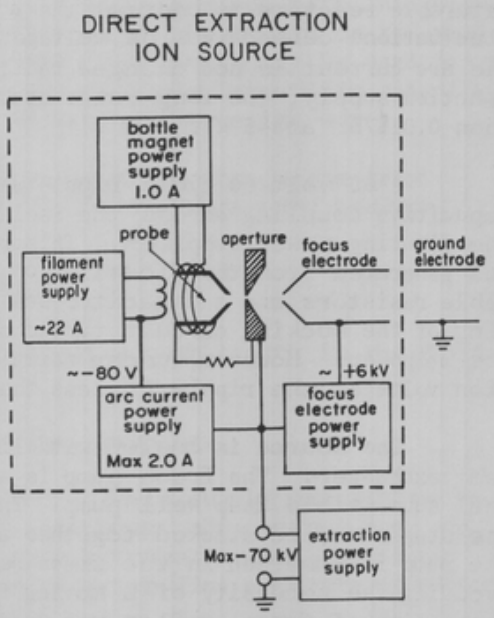

Fig. 1.2-2. Block diagram of direct extraction ion source.

As is shown in Fig. 1.2-2 the focus supply, arc supply, filament supply, and bottle magnet supply must float at the extraction potential. Control of these supplies and the source gas needle valve which must also be elevated in potential is accomplished by using lucite rods. These rods are turned with 0.67 rpm motors that can be operated from either the control room or the ion source area.

The focus voltage power supply is wired parallel with a 12 kV spark gap to protect it from excess voltage in the event that the focus electrode sparks to laboratory ground. The other power supplies do not have as great an over voltage problem since they are negative supplies. Any currents resulting from sparks between the outputs and laboratory ground will forward bias the power supply diodes. However, voltage regulator tubes have been installed parallel to the supplies to prevent possible damage to the meters due to transients.

The arc voltage supply has two parallel 150 watt light bulbs in series with the load to protect against runaway arcs. The light bulbs were chosen in preference to standard resistors because their resistance increases rapidly with current. The light bulbs provide an added benefit; they make adjustment of the arc current much easier since the arc current of the ORTEC duoplasmatron increases very rapidly with arc voltage.

A Voltronics Bam-70-5.5 UM high voltage supply is used to provide the extraction potential. It has a capacitive resistance filter that limits 60 cycle ripple to less than 0.1%. A regulator was built for this supply which uses

saturable reactors to control the ac input. This regulator prevents slow voltage fluctuations caused by line voltage variation and changes in loading. As long as the arc current is not changed radically, thus changing the loading on the extraction supply, the long range stability of the extraction voltage is better than 0.01%/hr at 45 kV.

A 60 volt 60 cycle ripple was introduced on the extraction voltage by capacitive coupling across the isolation transformer used to provide ac power to the floating power supplies. This ripple was decreased by bucking it with a signal generated from the floating ac power. A phase shifting circuit of two variable resistors and a capacitor was used to generate the signal. The null setting of the bucking circuit turned out to be somewhat dependent on the loading of the ac power. However, under normal operating conditions with 45 kV of extraction voltage, the ripple is less than 30 volts.

The source is cooled with liquid freon 113 which is circulated through a heat exchanger. The freon pump is a 5-stage centrifugal pump constructed from a Teal submersible deep well pump. The Teal pump uses separate cast plastic stages. The stages may be stacked together as needed to obtain the required pressure. The pump is immersed in the freon reservoir and the pump motor is above, thereby avoiding the necessity of a moving freon seal. Due to the poor lubricating properties of freon, teflon was used in the bearing that supports the drive shaft.

Substantial interlock protection has been built into the source system. If the pressure monitored with an ion gauge becomes excessive all source power supplies are turned off. Work is currently being done to integrate this ion gauge monitor into the accelerator interlock system so that when the ion gauge trips the automatic beam line, valves will isolate the ion source from the rest of the vacuum system.

None of the source power supplies can be on without the freon circulation pump on. A thermostat on the duoplasmatron provides further protection against overheating. If the temperature of the duoplasmatron exceeds 150°F, it turns off.

There are flow switches in the freon and water lines of the heat exchanger so that once the heat exchanger is on, a loss of either water or freon flow turns off the water and freon pump. This prevents overheating due to water failure and protects against freon loss and pump damage in the event of a freon leak.

The doors on the high voltage protection cages are interlocked so that all power supplies are turned off if the doors are opened.

The extraction power supply is interlocked so that the voltage control knob must be turned to zero in order to turn the supply on.

A vacuum system has been adapted to make possible the baking out of replacement filaments. Filaments can be baked out in containers mounted on the vacuum system. These containers can then be sealed off, filled with argon, and stored until needed.

A switching magnet was installed to provide an entrance path into the beam line for the DEIS. The magnet also provides an entrance path on the opposite side of the straight-through beam line which will eventually be used for the polarized ion source. The magnet was constructed by Alpha Scientific according to our pole face design. The primary needs motivating the design were:

a. An entrance angle sufficiently large to allow the source to be located near the switching magnet. This was necessary because available space was limited.

b. Equal vertical and horizontal focusing.

c. A large focal length, that is, as large a path length in the field as was economically feasible.

d. An air gap large enough to permit good pumping.

The magnet power supply is an Alpha 45-30. This supply was altered so that it could be remotely controlled from two locations, the control room and the ion source area. An interlock prevents control transfer when the magnet power is on. A flow switch in the magnet cooling water line prevents operation without cooling. (H. Wieman)

---

1. Nuclear Physics Laboratory Annual Report, University of Washington (1969), p. 153.
2. Nuclear Physics Laboratory Annual Report, University of Washington
2. (1966), p. 103.

1.3 Testing and Optimizing the Operation of the Lamb-Shift Polarized Ion Source

The construction and bench testing of the Lamb-shift polarized ion source has now been virtually completed.

The ion source which is to provide polarized negative hydrogen and deuterium ions utilizes the Lamb shift,[1] i.e., the energy splitting between the metastable $2S_{\frac{1}{2}}$ state and the $2P_{\frac{1}{2}}$ state. To produce a polarized ion beam one of the hyperfine components of the metastable level is induced to decay via the short lived $2P_{\frac{1}{2}}$ state. The method used is the same as that described by Meiner *et al.*[2,3] and is shown schematically in Fig. 1.3-1.

A beam of metastable deuterium (hydrogen) atoms, produced by charge exchange in cesium vapor, travels through a longitudinal magnetic field of 575 gauss, where the $m_s = -\frac{1}{2}$ Zeeman split hyperfine component of the metastable state is Stark quenched to decay via the $2P_{\frac{1}{2}}$ state. With a second quenching arrangement and a magnetic field of same magnitude but opposite polarity and a certain field distribution along the beam axis one can obtain different degrees of polarization[4] or for the case of deuterium a different degree of mixing between tensor and vector polarization. The remaining metastables are selectively ionized in an argon gas cell[5] to produce a negative beam for injection into the

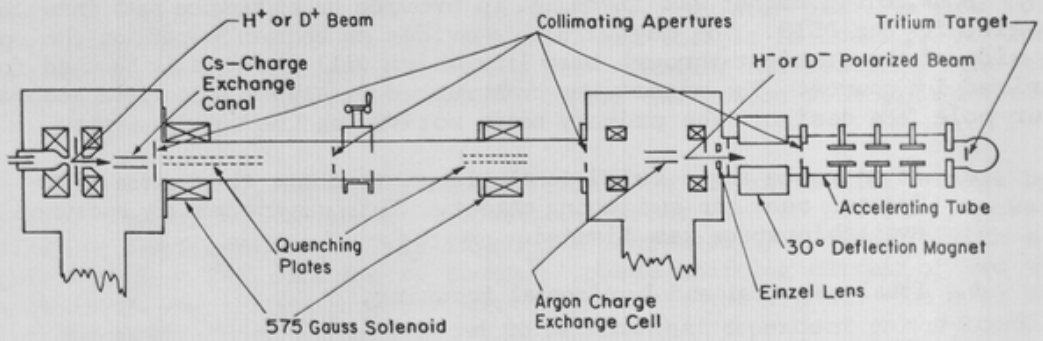

Fig. 1.3-1. Diagram of Lamb-shift source as used during bench testing.

tandem Van de Graaff accelerator.

The ion source had to satisfy several requirements: (a) high polarization and large beam output, (b) good reliability and serviceability, (3) variability of polarization and spin orientation.

To achieve a large beam output it was necessary to replace the RF ion source[6] with a duoplasmatron of the type used in the Los Alamos ion source.[7] The source current output was found to be relatively high so that various apertures had to be installed to eliminate the unwanted beam and reduce the contamination of the quenching plates and the argon gas cell.

Even so, a significant buildup of contamination occurred, making the operation of the source very unreliable. Replacing the solid brass surface of the quenching plates by a baffled wire grid surface solved this problem to a great extent. The construction of the argon gas cell was altered so that it could be heated while in position as well as readily removed to be cleaned. Oil deposition from the diffusion pumps, which were specified to run without additional bafflinf, continued to be a problem but was reduced by using higher quality oil for both the diffusion pumps and the backing pump.

The source output and beam profile were studied using a neutral beam detector and phosphorous screens at various points along the beam line. In this way the size of the collimating apertures as well as the geometry of the accelerating beam tube and the Einzel lens behind the argon cell were optimized. Furthermore to optimize the operation of the source it became necessary to rebuild the source box itself with the duoplasmatron and the extraction assembly separately mounted on a detachable optical bench. The arc and beam-plasma profile could be monitored through viewing ports.

The tensor polarization of a double quenched deuterium beam served as a guide to the performance of the source. Typically we obtained a polarization of $-.622 \pm .009$ with $-.740 \pm .018$ the most favorable result compared to the theoretically expected value of -1.0. The beam output after acceleration to 125 KV was typically between 60 nA and 100 nA, with 130 nA the highest output obtained.

We suspect that the lower than expected value of polarization is due to the fact that the cesium and argon are not localized in the respective gas-vapor cells but do cause an appreciable amount of charge exchange outside of that region. It is hoped that with a clean system and an improved geometry of the cesium canal a higher polarization can be obtained.

Over the past few months the operation of the source has proved to be quite reliable so that the operation of the Wien filter and the associated beam optics can now be tested before final installation of the polarized ion source. (H. Fauska, T. Lewellen, G. Michel, L. Page, E. Preikschat, and G. Roth)

---

1. W.E. Lamb, Jr., and R.C. Retherford, Phys. Rev. *79*, 549 (1950).
2. H. Meiner, G. Michel, and K. Corrigan, Nucl. Instr. and Meth. *62*, 203 (1968).
3. T.B. Clegg, G.R. Plattner, and W. Haeberli, Nucl. Instr. and Meth. *63*, 343 (1968).
4. P.G. Sona, Energia Nucleare *14*, 295 (1967).
5. B.L. Donnally and W. Sawyer, Phys. Rev. Letters *15*, 439 (1965).
6. Nuclear Physics Laboratory Annual Report, University of Washington (1969), p. 156.
7. G.P. Lawrence, G.G. Ohlsen, and J.L. McKibben, Phys. Letters *28B*, 594 (1969). We are indebted to Los Alamos Scientific Research Laboratory for supplying us with plans for the construction of the duoplasmatron and extraction assembly.

1.4 The Lithium Source

The lithium source[1] for the tandem Van de Graaff was successfully tested for the first time in June 1969 briefly delivering 70 na of analyzed $^{6}Li^{+++}$ beam. Since then, effort has been directed toward increasing the stability and dependability of the source. During the most recent use of the source in January 1970, we were able to deliver approximately 300 na of $^{6}Li^{+++}$ on target continuously for two days. The output of the source was 1 μA of $^{6}Li^{-}$ measured on the low energy cup of the Van de Graaff. Having achieved stability of the source, we are now making modifications to increase its output. Following is a list of steps we have taken and are taking.

The major stability problems with the source have been directly connected with the lithium cell, the exchange canal, and their heating systems. Lithium melts at 186°C and boils at 1336°C. The cell and canal must be heated to 500-600°C to provide reasonable lithium vapor densities in the canal. Lithium is reactive especially when hot and therefore it was necessary for the cell and canal to be made of stainless steel to reduce corrosion. The cell is a cylinder 5 in. long with an outer diameter of 7/8 in. The canal is 6 in. long with a 1/2 in. diameter opening at the ends which steps down to a 3/16 in. diameter opening in the center. The cell and canal heaters have separate power supplies and controls. The original heaters were composed of nichrome heater wound between two boron nitride sleeves around the cell and the canal. The heaters readily amalgamated with stray lithium and proved unreliable. We have replaced these old heaters with coaxial heater cable[2] which does away with the need for

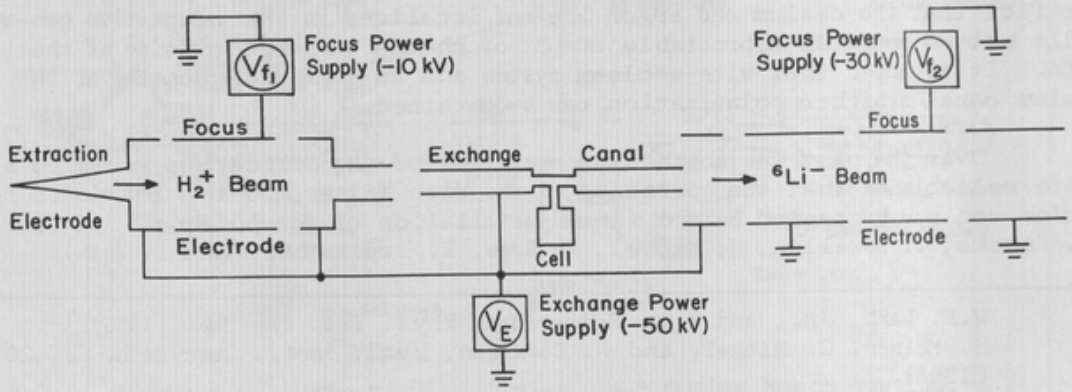

Fig. 1.4-1. Schematic of the lithium source. The H_2^+ beam is extracted from the duoplasmatron.

the boron nitride insulation. The coaxial cable has increased the heating efficiency for the cell and the canal and has reduced the cooling requirements for the rest of the source. A heat reflector was also installed on the support for the exchange canal.

Originally we used small 2.9 ohms/ft coaxial heater cable with a 0.062 in. outer diameter. The cell and canal float at the voltage of the exchange canal (- 40 kV) and when excessive sparking to ground occurred the delicate heater cable exploded. We covered the heater cable with tantalum shielding but this did not completely solve the problem. We believe the sparking caused current surges in the coaxial cable which caused it to explode. We changed to larger coaxial cable 0.73 ohms/ft with 0.125 in. outer diameter and the problem vanished.

Recent revisions have been made to the optics of the source to improve its output. The $^6Li^-$ ions coming out of the exchange canal have an energy distribution which is unknown. Previously the optics of the source have been such that only $^6Li^-$ ions emerging from the exchange canal with an energy of about 12 keV were correctly focused into the beam transport system. We would like to be able to focus $^6Li^-$ of any energy. To accomplish this we have moved the ground electrode closer to the exchange canal and have placed an Einzel lens at the end of the source (see Fig. 1.4-1).

A photograph of the source is shown in Fig. 1.4-2. This new configuration will allow us to focus $^6Li^-$ ions with any energy larger than 7.5 keV (with - 40 kV exchange voltage).

(W.R. Wharton, J.G. Cramer, W.W. Eidson,* and K.G. Nair).

1. Nuclear Physics Laboratory Annual Report, University of Washington (1969), p. 156.
2. Purchased from American Standard, Aero Research Div., 9000 King Street, Franklin Park, Illinois 60137.
3. Permanent address: University of Missouri at St. Louis, Missouri.

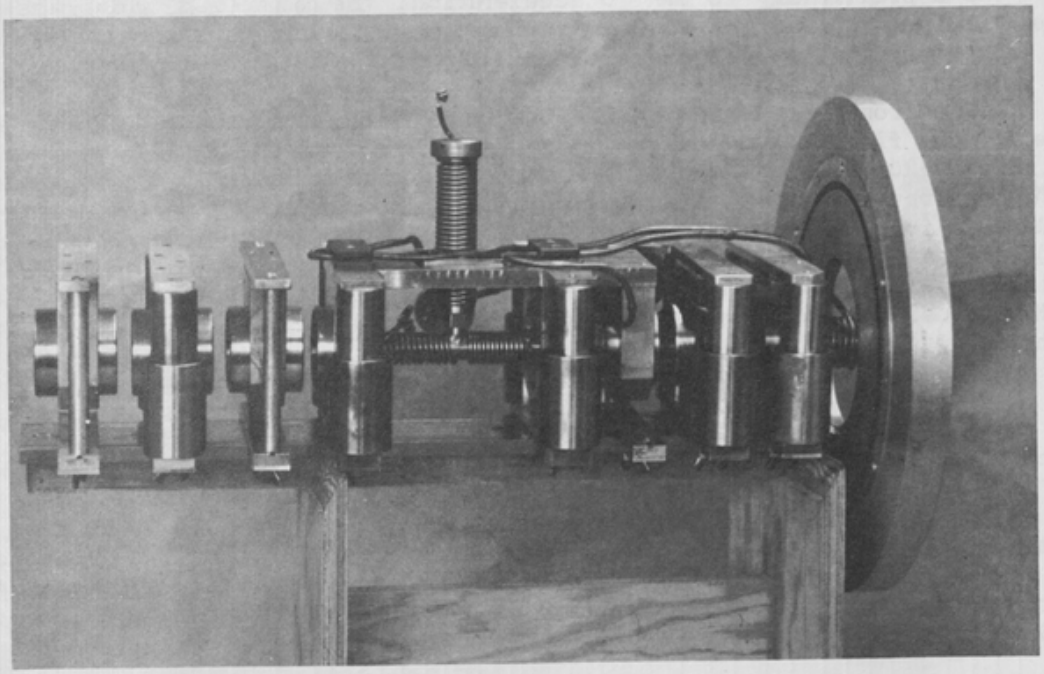

Fig. 1.4-2. Photograph of the lithium source in the upside-down position.

1.5 Acceleration of ^{18}O

Previous acceleration of ^{16}O in this laboratory was carried out on the tandem Van de Graaff accelerator, following the directions of the manufacturer,[1] by bleeding a source gas mixture of H_2 and O_2 into the duoplasmatron ion source. A barium oxide coated platinum wire mesh filament was used in the duoplasmatron. The operation of the ion source under these conditions was often unstable and unsatisfactory. In particular, the aperture through which the ions are extracted from the plasma was often damaged -- eroded or welded shut. Because of this instability and because the oxide filament coating contributed to the ^{16}O ions in the plasma, we sought a different method for ^{18}O acceleration.

Following a suggestion by Tombrello,[2] we simply used enriched ^{18}O water vapor as the source gas and a single wire tungsten filament. Ten grams of 50% enriched ^{18}O water was purchased;[3] about half this amount was used for the fabrication of ^{18}O targets. The remaining 5 grams was placed in a stainless steel cylinder closed with a needle valve. This cylinder was immersed in a dry ice-acetone mixture and the air pumped out. The cylinder was then connected to the ion source through small-diameter copper tubing. The needle valve was adjusted to achieve the empirically correct gas flow, corresponding to about 300 microns Hg in the connecting tubing, which was monitored with an attached thermocouple gauge.

As a preliminary to the ^{18}O acceleration, the connecting tubing was purged with pure H_2 and the duoplasmatron run on a hydrogen arc for an hour or so. This procedure cleaned the system of adsorbed atmospheric oxygen.

Ions from the tandem negative ion source are momentum selected by two magnets: the first is located immediately after the ion source and bends the ions through 20° into the main accelerator tube; the second, 90° magnet, is on the high energy end of the accelerator, and momentum and charge selects the fully accelerated ions. In practice we set up the accelerator on ^{16}O (always the larger beam) and then turned up the magnets an appropriate amount, at which point the ^{18}O beam appeared beyond the 90° magnet. Running at terminal voltages between 7-8 MV and using carbon foil stripping at the terminal to the 5^+ charge state, ^{18}O beams of several hundred nA were attained.

When running on ^{18}O, especially during an excitation function, one must keep very close watch on magnet currents, the terminal voltage, and the ion source extraction voltage to prevent slipping onto an ^{16}O beam.

The cost of 50% ^{18}O water is approximately $100/gram. Although this appears extremely expensive, it must be remembered that 1 gram of water evaporates to a volume of more than 1 liter (S.T.P.). The rated consumption of the tandem negative ion source is about 2 cm^3/hour; in practice it runs somewhat higher. (R. Shaw)

---

1. High Voltage Engineering, Burlington, Mass.
2. T.A. Tombrello (private communication)
3. Biorad, Richmond, California.

1.6 N.M.R. Frequency Calibration

An energy calibration of the 90° magnet N.M.R. was carried out with the two-stage Van de Graaff. A gas stripper was used with hydrogen beams from the duoplasmatron negative ion source.

A window set on the elastic protons from the reaction $^{12}C(p,p)$ measured the resonance near 15 MeV. The proton counter was at 165° in the laboratory. The target was 30 $\mu g/cm^2$ carbon.

One excitation function was measured with an object slit width of 0.060 in. and image slit width of 0.030 in., and a second with object and image slit widths of 0.020 and 0.010 in., respectively. The N.M.R. was field locked.

The first measurement located the resonance at an N.M.R. frequency of 22,905 G with a full width at half maximum of 1.1 keV. The second measurement located a 1.3 keV wide resonance at 22,907 G. (The frequency to energy ratio is 0.81 keV/G in this region.) Deviation from the previous calibration (3/11/68) was smaller than the energy uncertainty at the resonance frequency due to the uncertainty in the previously derived magnet calibration constant. (P.A. Russo and J.R. Tesmer)

1.7 Neutral Beam Monitor

The original device for measuring the neutral beam entering the injector measured an increase in the temperature of water which cooled a small copper disc bombarded by the beam.[1] The time required for this system to reach thermal equilibrium was more than 10 seconds. This made adjustment of the neutral source a tedious and time-consuming operation. In addition this device was only sensitive to currents near the maximum output of the source.

To overcome these problems, a neutral beam monitor has been designed and installed which measures the secondary electron current produced by the neutral atoms striking a copper plate. Figure 1.7-1 shows a cross section of this monitor. The secondary electrons are collected by a ring maintained at +22 volts. This electrode is shielded from electrons from other sources in the beam tube by an outer shield ring. The entire unit is water-cooled and mounted on an air cylinder so it may be removed from the beam remotely.

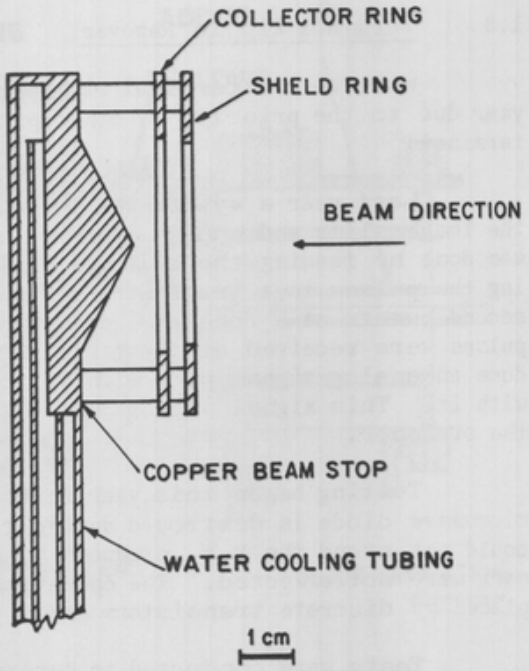

Fig. 1.7-1. Cross section through neutral beam monitor.

The secondary electron current i_e is given by

$$i_e = e\gamma N_i$$

where e is the electronic charge, γ is a constant and N_i is the number of incident neutral atoms per unit time. We have attempted to measure γ by observing the temperature rise in the cooling water, when the monitor is absorbing 27 keV neutrals from the source. Unfortunately there is no convenient way to separate effects of atomic and molecular hydrogen in the beam. Wittkower *et al.*[1] in a description of a prototype of our accelerator, points out that the atomic beam has been maximized, and constitutes more than 70% of the beam. Assuming that the beam is all atomic hydrogen, we get a value of $\gamma = 3.4$, in fair agreement with previous measurements.[2] (W.G. Weitkamp)

---

1. A.B. Wittkower, P.H. Rose, R.P. Bastide and N.B. Brooks, Rev. Sci. Instr. *35*,1 (1964).
2. N. Molhs and F.P.G. Valckx, EUR-CEA-FC-197.

1.8 Terminal Ripple Remover

Work on the terminal ripple remover has continued at a reduced pace this year due to the priority of other projects and limited access to the Van de Graaff terminal.

Last year a system was designed and built to sense an analog signal from the image slits and apply a correction voltage to the terminal stripper.[1] This was done by feeding the slit signal into a voltage to frequency converter, applying the pulses to a transistor switch, and turning a klystron on for four microsecond bursts at a frequency corresponding to the slit signal. The microwave pulses were received at the terminal by a diode, amplified and integrated to produce an analog signal proportional to the terminal ripple but 180° out of phase with it. This signal voltage was then amplified to about 10 kV and applied to the stripper.

Testing began this year in the terminal and it was discovered that the microwave diode is destroyed during tank sparks. Also integrated circuit chips could not stand the R.F. produced by a spark. Discrete transistors for the most part were not affected. The operational amplifier integrated circuits were replaced by discrete transistors and a passive integrator.

Tests were conducted to determine how to preserve the diode. Filters were installed in the waveguide preceding the diode but to no avail. Measurements showed that the noise spectrum above 6000 Mhz in a tank spark was too small to destroy a diode at the tank walls. Pickup in the wiring was suspected, but extensive shielding and bypassing had no effect. Then a diode with no external wiring was mounted and successfully preserved.

Thus, at this writing, an entirely new electronics package for the terminal is being designed which is battery-powered and can be mounted directly on the diode holder. This should greatly reduce the amount of pickup and improve isolation. Also, concurrently, a gallium arsenide diode-phototransistor system is being studied which may replace the klystron-diode pair. (G. Roth)

---

1. Nuclear Physics Laboratory Annual Report, University of Washington (1969), p. 152.

1.9 Injector Accident

On September 20, 1969, a glass-to-metal seal in the beam tube of the injector rank parted, venting high pressure insulating gas into the accelerator vacuum system. The resulting damage, which was substantially less than might be expected for this kind of accident, caused the injector to be out of commission for a total of 39 days, and has been repaired at a cost of about $10,000. This report will describe the injector beam tube, the events leading up to the accident, and the damage, and will discuss possible causes and repair and preventative action taken.

1. *Description of the injector beam tube.* The injector beam tube is of

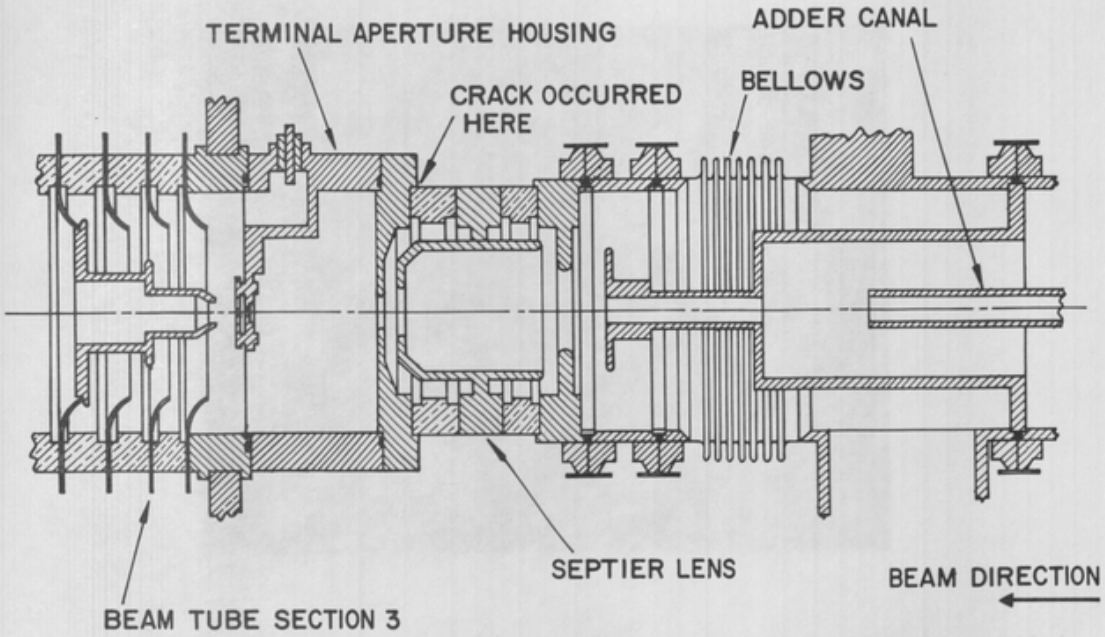

Fig. 1.9-1. Sectional view of beam tube components in the terminal of the injector.

conventional design with four sections numbered in the order the beam passes through them. Sections 1 and 2 comprise the neutral tube and sections 3 and 4 the high energy tube. Inside the terminal the neutral tube is separated from the high energy tube by the adder canal, the Septier lens,and the terminal aperture housing (see Fig. 1.9-1). The neutral tube is connected by a bellows to the adder canal, which is in turn connected by a bellows to the Septier lens. The Septier lens, the component which failed, is bolted to the terminal aperture housing which is in turn bolted to the upstream end of tube section 3. The Septier lens consists of three stainless steel electrodes separated by ring-shaped glass insulators.

The ends of the adder canal are pumped by a barium getter pump located behind and below the exchange canal. This pump can be isolated from the exchange canal by a remotely operable butterfly valve. The adder canal is also pumped through the differential pumping tube which runs along the column parallel to the neutral tube. The outside end of the differential pumping tube and each end of the beam tube are pumped by large mercury diffusion pumps.

The pressure in the injector tank is maintained from 190 to 225 psi of a mixture of 80% N_2 and 20% CO_2.

2. *Events leading up to the accident.* On the evening of September 18, 1969, two days before the accident, the injector tank was depressurized to investigate a problem with the charging belt drive motor. The next day, a short circuit in the drive motor protection system was repaired. Nothing was done in

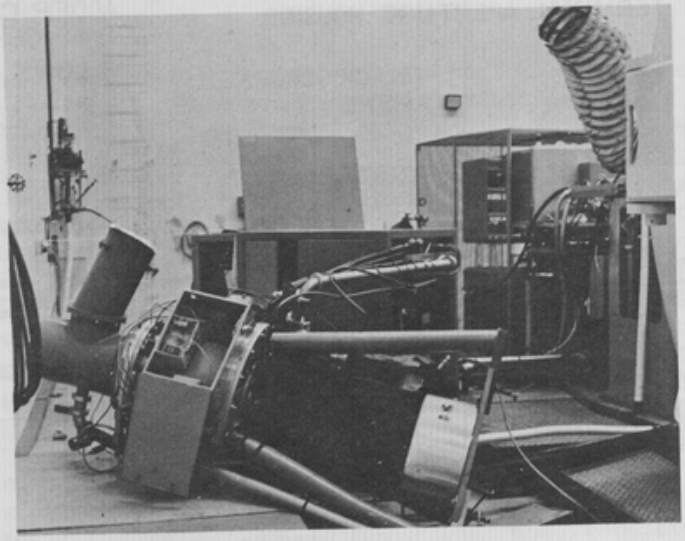

Fig. 1.9-2. View of damage to differential pumping tube diffusion pump.

the tank which would in any way affect the area where the accident was to occur. The air was evacuated from the tank during the night of September 19 and the tank was repressurized on the morning of September 20, 1969.

The pressurization was routine, going from vacuum to 190 psi in a little over three hours. The accelerator was started in the normal manner and by early afternoon was running with 4 MV on the terminal. Beginning at 1:00 pm the barium pump was opened for about an hour and a half to aid in conditioning the machine to higher voltage. The machine ran well at about 5 MV throughout the rest of the afternoon and evening. At 8:58 pm the barium pump was opened again. The pressure in the differential pumping tube reacted normally to the opening valve.

Two minutes later, at 9:00 pm, the vacuum systems of the injector and the injector drive motor shut off automatically, indicating that something was wrong with the beam tube vacuum. About 30 seconds later the tandem drive motor and vacuum systems automatically shut off. The crew attempted to restart the vacuum systems without success. Then at about 9:03 pm the crew heard a muffled explosion followed by a lour roaring sound coming from the accelerator. The crew investigated immediately and found that insulating gas from the injector tank was being vented into the room through two pressure relief valves in the beam tube outside the tank, and through an opening created in the bellows which usually connects the differential pumping tube to its diffusion pump. This diffusion pump was lying on its side on the floor, and water from a severed cooling line was spraying over the wreckage of the pump.

Aware of the personnel hazard caused by tank gas displacing the normal air in the accelerator vault, the crew immediately opened a large shielding door which permitted the tank gas to escape to the outside.

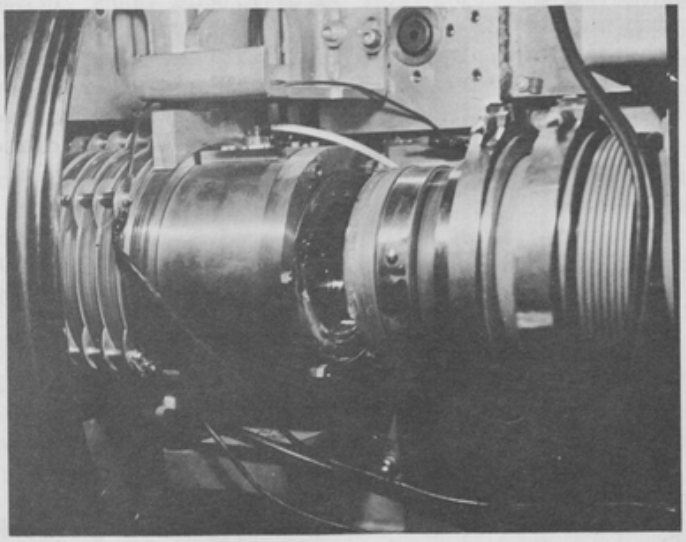

Fig. 1.9-3. View of damage to the Septier lens.

3. Description of the damage. The most spectacular damage was in the vicinity of the differential pumping tube diffusion pump. The bellows which connects the pump to the tank had stretched to the limit of its flexibility and had torn loose from the pump. The pump assembly, which stands about seven feet tall, was lying on its side on the floor (see Fig. 1.9-2). The forevacuum line, roughing line and water cooling lines to the pump were twisted and broken.

Inside the injector tank the most obvious damage was the crack in the Septier lens (see Fig. 1.9-3). The crack occurred along the glass-to-metal seal on the downstream end of the lens (see Fig. 1.9-1). This seal is made by bonding both the glass and metal to a thin kovar washer. About 80% of the circumference of the seal between the glass and the kovar washer had separated cleanly along the interface with only a few small slivers of glass still adhering to the kovar. On the remaining circumference a large chip of glass about 1/4 in. thick was still bonded to the kovar. The kovar washer had pulled loose from the stainless flange over about 70% of its circumference.

A gap of about 1-1/2 in. opened up between the two parts of the Septier lens. This gap was caused by displacement of beam tube sections 2 and 3 of about 3/4 in. each. The aluminum electrodes of the beam tubes have small tabs protruding beyond the glass insulators on the top and bottom of the tube. The downstream end of tube 3 was found jammed against its support bracket, and the top and bottom tabs were bent back at about a 45 degree angle. The most upstream tabs on tube section 2 were also bent in this manner, but the tube section was not jammed up tight against the support structure, indicating that tube section 2 bounced after it hit the support structure.

Damage to the glass insulators of the differential pumping tube was also

observed. This consisted of transverse chips in the upper inside surface of the glass of tube section number 2. The chips were about 1/4 in. wide and from 1/2 to 2 in. long. Each chip had a thin dark line at the center of the chip in the direction of the axis of the beam tube. Originally these chips were thought to have been caused by the accident, since they had not been observed previously. It appears more likely, however, that this chipping was associated with sparking in the tube, and probably represents a degenerative effect which appears in normal operation of the machine.

4. Discussion of the accident. From the evidence at hand, the events that took place during the accident are fairly clear. The accident began with the appearance of a crack in the glass-to-metal seal in the Septier lens. What caused this crack is, however, not clear, and will be discussed in detail below. The crack was immediately enlarged by tension exerted on the Septier lens by the adjoining bellows. Once large amounts of gas began rushing down the two parts of the beam tube, aerodynamic drag on the beam tube walls tended to widen the crack even further.

As soon as the pressure in the neutral tube diffusion pump and the high energy tube diffusion pump began to rise, the pumps and the injector drive motor shut off automatically. In addition, valves automatically closed which isolated the beam tube from the rest of the accelerator vacuum system. The pressure in the beam tube continued to rise until it exceeded atmospheric pressure. At this point pressure relief valves at each end of the beam tube opened, venting the tank gas into the accelerator room, and preventing further pressure rise. Each end of the beam tube outside the tank is connected to an expensive accelerator component; the neutral source at the neutral tube end, and the negative ion source at the high energy end. It was therefore particularly fortunate that the pressure was vented at these locations since extensive damage to these components might otherwise have resulted.

The pressure also rose in the differential pumping tube as soon as the Septier lens cracked. Here, however, there was no pressure relief valve, and the pressure simply increased until it pushed over the diffusion pump, rupturing the bellows connecting the pump to the tube. The rupturing bellows caused the explosive sound heard by the crew.

The question to be answered in this accident, then, is what caused the crack in the Septier lens which initiated these events? There are several possibilities, none of which is entirely reasonable. One possibility is that the crack was caused by thermal or mechanical stress produced by the tank pressurization on the morning of the accident. This is unlikely because the tank has been pressurized in an identical manner many times before. Furthermore, the lens held together for about 10 hours after the pressurization was completed that morning. Another possibility is that the crack was caused by thermal or mechanical shock accompanying the opening of the barium pump valve. This is a likely hypothesis since it appears more than coincidental that the barium pump was opened only two minutes before the first symptoms of the accident were observed. But, there are also difficulties with this hypothesis. First, the barium pump was opened about 8 hours earlier without incident. Second, the accelerator crew specifically observed the vacuum in the differential pumping tube as the pump valve was opened.

The normal change seen in this vacuum as the valve opened implies strongly that the barium pump was operating properly. In addition, the barium pump is located far enough from the Septier lens that it is difficult to imagine how a thermal or mechanical shock sufficient to crack the lens could have been transmitted to the lens.

Aside from the possibilities mentioned above, investigation has not revealed any other clue as to what caused the lens to crack. Perhaps a flaw had been present in the lens for a long time and at this particular time a small vibration, possibly associated with the actuation of the barium pump valve, had converted the flaw into a crack.

Although it is not clear what caused the lens to crack, it is clear that a design error in the bellows located just upstream from the lens played a significant role in converting this crack into the large opening seen in Fig. 9.1-3. As mentioned above, this bellows exerts a tensile force on the lens, and this force opened up the crack. As may be seen from Fig. 9.1-1, the colvolutions of the bellows have a larger diameter than the tube to which the bellows is attached. This means that when the outside of the bellows is pressurized, the convolutions tend to contract, setting up a tension in structures to which the bellows is connected. This tension is about 1,000 lbs. when the tank is fully pressurized. Because of the uncertain nature of the ultimate tensile strength of glass, especially glass-to-metal seals, it is good engineering practice to put glass under compression rather than tension. This practice was followed in the design of other glass components of the accelerator, such as the columns, but was not followed in the design of the terminal components shown in Fig. 1.9-1.

5. *Repair and preventative action taken.* The repair of the injector was carried out as expeditiously as possible because of the large demand for experimental use of the accelerator. The two most time-consuming repair activities were realigning and leak chasing the beam tube. Tube sections 2 and 3, which had been jammed against support structures, were inspected and tested carefully for soundness. Neither tube section had to be replaced, a fact which reduced the cost of repair by a factor of 2 or 3. Repair of the injector was completed by October 29, 1969, a loss of 39 days of operation.

Preventative action centered around two considerations: how to reduce the probability of such an accident occurring again, and how to minimize the damage if it did. Since the cause of the crack in the lens is not known, it is not possible to completely prevent reoccurrence. However, the probability of reoccurrence can be significantly reduced by eliminating all tensile forces on glass components. The preferred way to do this would be to replace all the bellows with bellows having convolutions of smaller diameter than the connecting tubes. Such bellows would exert compressive rather than tensile forces on adjacent tubes when pressurized. However, bellows of this type were not available when the repair was carried out. Instead, the flanges at each end of the bellows were braced by compressed springs; the compression was adjusted to slightly exceed the tension exerted by the bellows when the tank is pressurized. This arrangement insures that components connected to the bellows are in compression rather than tension.

From a safety standpoint, the ideal way to minimize the damage in the event of a reoccurrence of this accident would be to install large high-pressure gate valves just outside the tank in the beam tubes and the differential tube. These valves, closed automatically in the event of a vacuum accident, would contain the tank gas and would prevent the displacement of the beam tubes caused by gas rushing through the tubes. However, such valves are difficult to install because of a lack of space between the tank and other components in the beam line. Much simpler, and nearly as effective, are the pressure relief valves mentioned above. These valves consist of a plate covering a 6 in. diameter or larger hole in the tube. Instead of being bolted to the tube, the plate is held by light springs against an O-ring. If the pressure in the tube exceeds atmospheric pressure, the plate is forced away from the O-ring, and the gas in the tube is vented. Such valves are now installed at all locations in the accelerator where a pressure rise might conceivably occur in the event of an accident.

By way of conclusion, it should be pointed out that although this machine is the only Model FN injector in existence, and although the manufacturer has pointed out that such accidents are exceedingly rare, nevertheless the possibility of such an accident exists in a number of accelerators of this general type now in use. Furthermore, had this accident produced damage to ion sources or beam tubes, the cost of repair might have been a factor of five larger. It is conceivable also that personal injury might have resulted. The experience at this laboratory should point up the advisability of checking other machines of this type and installing such equipment as is necessary to minimize the probability of the occurrence of such an accident, and minimizing the damage should it occur. (C.E. Linder, J.W. Orth, G.J. Rohrbaugh, G.E. Saling, F.H. Schmidt, and W.G. Weitkamp)

1.10 The ^{3}He Gas Recovery System

A mechanical system has been built to collect the exhaust gas from the large pump that backs the tandem ion source diffusion pump. The exhaust side of the mechanical pump has been sealed and connected to a small hand pump which is used to force gas from the pump reservoir into a gas bottle. Hand pumping is required once every 12 to 24 hours and the ultimate bottle pressure easily reached is about 10 atmospheres. The gas thus collected is later processed through a LN_2 cooled Zeolite trap to rid it of gases other than ^{3}He.

This recovery system separates the collection and the processing of recovered source gas. This can conceivably be an advantage when recovering rare gases, but for a source gas as frequently used as ^{3}He it is a nuisance. This method will be used temporarily until our copy of the Stanford ^{3}He recovery system is completed. This system will directly recirculate the gas from the pump exhaust, through a LN_2 cooled Zeolite trap, back into the ion source as source gas. It uses a much smaller specially sealed fore pump which can be connected at the end of the run to a ballast storage tank whose volume greatly exceeds that of the pump reservoir thereby eliminating the need for a compressor hand pump. The completion of this system is held up pending the delivery of our special-order pump. (W.J. Braithwaite and D.R. Brown)

1.11 Cyclotron Improvements and Operations

Improvements to the cyclotron included installation of an automatic plate voltage rundown. This consists of two fixed resistors and two thermistors in a bridge, one thermistor in the water inlet and one in the water outlet of the oscillator tube. The unbalance of this bridge is a measure of temperature difference, a direct indication of plate power dissipation. This signal, via an amplifier and relay, now runs the power down whenever maximum rating is exceeded.

Statistics of cyclotron operation are given in Table 1.11-1. Major maintenance activities involved repair of a leaking duct seal in the water room and fireproofing of the wooden decking on the balcony after a small fire destroyed part of the decking. (B. Lewellen, C.E. Linder, J.W. Orth, G.E. Saling, and W.G. Weitkamp)

Table 1.11-1. Statistics of Cyclotron Operation During the Period from April 16, 1969 to April 15, 1970

1. Division of Time Among Activities[a]

	Time (Hrs)	Per Cent
Normal Operation	3212	73
Scheduled Maintenance	265	6
Unscheduled Maintenance	695	16
Unrequested Time	248	5
Total[b]	4420	100

2. Division of Beam-on Time Among Particles

Alpha Particles	1998	83
Deuterons	351	14
Protons	68	3
Total	2417	100

3. Division of Normal Operation Time Among Users

University of Washington Nuclear Physics Laboratory	2022	63
University of Washington Department of Nuclear Medicine	660	21
Atomics International	227	7
University of California at Berkeley	153	5
General Electric	47	1
Oregon State University	35	1
Simon Fraser University	33	1
University of Washington Physics Department	15	1
Battelle Northwest	13	-
Western Washington State College	4	-
University of Oregon	3	-
Total	3212	100

a. These categories we defined in the same way as those in Table 1.1-1

b. This number equals 52 5-day weeks at 17 hours per day.

2.1 Installation of the 90 cm Broad Range Spectrograph

The installation of the 90 cm Browne-Buechner type magnetic spectrograph described previously[1] is now complete except for final testing and calibration. The most recently completed components include the magnet current regulator[1] and the beam line to the tandem.

To produce a sufficiently small beam spot to match the resolution of the spectrograph, it has been necessary to place the beam line quadrupole lens 3 meters from the center of the scattering chamber, resulting in a distance of 10 meters from the tandem image slits to the lens. This means that in order to use an available 2 inch aperture quadrupole in this beam line it is necessary to reduce the emittance of the accelerator so as to avoid problems associated with beam hitting the inside of the beam tube in the quadrupole lens. Reducing the emittance of course means that beam must be thrown away, but calculations indicated that the remaining beam will be adequate for nearly all anticipated experiments. An aperture of variable size has been constructed and will be located just upstream from the entrance to the tandem analyzing magnet. This aperture will enable the emittance to be reduced as desired without introducing a significant low energy, slit-scattered component to the beam. (J.G. Cramer, H. Fauska, D. Gough, C. Linder, J. Orth, and W.G. Weitkamp)

---

1. Nuclear Physics Laboratory Annual Report, University of Washington (1969), p. 124.

2.2 Spectrometer Magnet Nuclear Magnetic Resonance Regulator

Magnet regulators used for controlling magnetic fields usually employ a stable reference voltage which is compared to the voltage across a fixed resistor in series with the power supply. This type of regulator does not correct for hysteresis effects, changes due to temperature shifts, or external fields. Such effects can decrease the resolution of a magnetic spectrometer. We therefore designed and constructed a nuclear magnetic resonance regulator which would supplement the current regulator to correct such errors.

Fig. 2.2-1 is a block diagram of the system. Integrated circuits were employed where possible. The regulation signal is digital until the last stage; thus one does not need the amplitude stability required of many stages in the usual phase lock system.

The marginal oscillator is a low noise field effect circuit. Tuning is accomplished through a remote motor control and the use of a solid state diode for fine tuning. The oscillation frequency is read by a digital frequency meter, driven by a decoupled oscillator output signal. The circuit does not require a marginality adjustment over the range from 4 to 32 MHz.

The oscillator coil and sample are swept by a 60 Hz modulation signal (which is also used to provide timing reference).

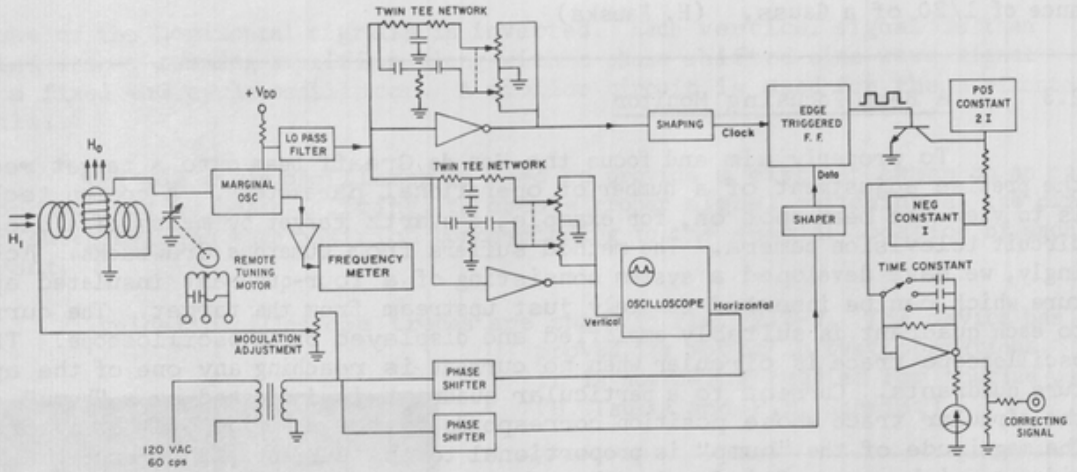

Fig. 2.2-1. Block Diagram of NMR Regulator

Audio absorption signals are derived across a resistor in series with the fet drain in the marginal oscillator. These audio signals from the resonance crossing are filtered and selectively amplified by operational amplifiers with tunable twin tee filters in the negative feedback paths. One such signal is used as the vertical signal for oscilloscope display. The other signal is further shaped and used to provide a timing signal for the digital correction system.

Timing detection is accomplished by an edge triggered flip-flop. The modulation sine wave is phase shifted and shaped to provide a timing reference signal for the data input of the flip-flop, while the shaped audio signal is supplied to the flip-flop clock input. When the system is correctly adjusted successive absorption signals are equally spaced (1/120 sec. apart) and the flip-flop output is a square wave with equal positive and negative excursion times.

Error signals are developed by an integrating operational amplifier with selectable time constants. The input consists of two constant current networks, one positive at twice the current of the other which is negative. The square wave from the flip-flop alternatly by-passes the positive current to ground. If the square wave has equal positive and negative excursions, the integrator output is zero. If the absorption line shifts in time with respect to the modulation reference a positive or negative error signal is developed.

A meter is provided to indicate balance of the system. The full scale range is ± 0.5 Gauss which provides aid in adjusting the regulator.

The system has been bench tested with a small permanent magnet of about 2 Kilogauss. The stability is excellent over a six hour period even in the inhomogenous field provided by the permanent magnet. The sensitivity is such that the system will develope an error signal due to the influence of a small ferromagnetic object 30 inches from the magnet which produces a total field disturb-

ance of 1/20 of a Gauss. (H. Fauska)

2.3 A Beam Focusing Monitor

To properly aim and focus the Van de Graaff beam onto a target requires the precise adjustment of a number of operational parameters. A common technique is to view the beam spot on, for example, a quartz target by means of a closed circuit television camera. The method suffers from numerous drawbacks. Accordingly, we have developed a system consisting of a four-quadrant insulated aperture which can be inserted remotely just upstream from the target. The current to each quadrant is suitably amplified and displayed on an oscilloscope. The oscilloscope trace is circular when no current is reaching any one of the aperture quadrants. Current to a particular quadrant is indicated by a "bump" on the circular trace whose position corresponds to the position of that quadrant. The magnitude of the "bump" is proportional to the current. The trace thus provides a quick means of informing the operator what beam alignment adjustment must be made.

Fig. 2.3-1 shows a block diagram of the system. The four-quadrant pickup aperture is located on the beam centerline in the 60 inch scattering chamber. Each quadrant is connected to an electrometer with remotely selectable ranges of 3, 10, or 100 nA. Each quadrant is automatically shorted to ground if power fails on the electrometers in order to prevent charge build-up on the quadrant sensors.

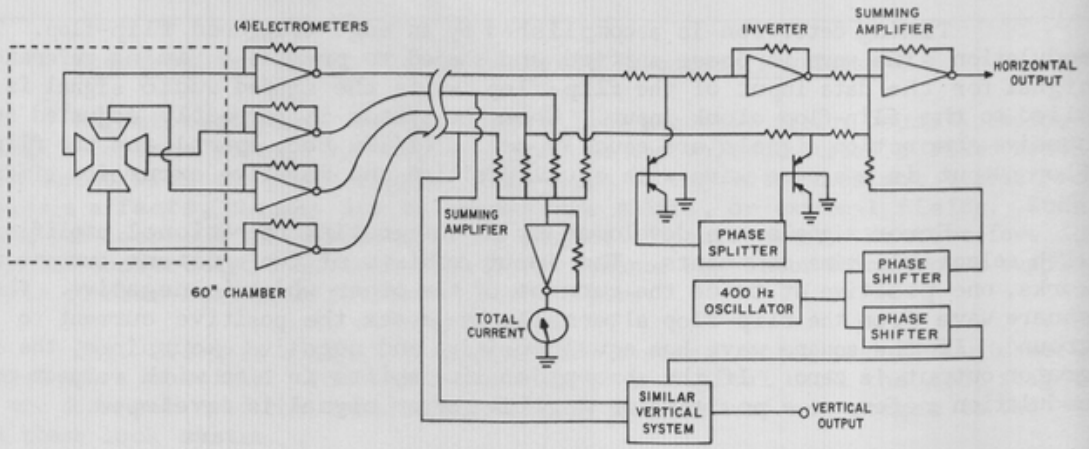

Fig. 2.3-1. Block Diagram of the Beam Focusing Monitor

The output signals of the electrometers are transmitted via coaxial cables to the control room. Summing amplifiers provide a reading of total current and feed signals to a decoupled "chopping" network. One of the vertical

and one of the horizontal signals is inverted. Each vertical signal is then coupled into a summing smplifier along with a phase shifted sine wave signal from a fixed 400 cycle oscillator. A similar circuit is used for the horizontal signals.

The 400 cycle oscillator is used to provide a circular sweep on an oscilloscope, and by phase shifting, to create proper signal switching as the circular sweep reaches each position corresponding to the spacial location of each quadrant.

Typical oscilloscope traces are shown in Fig. 2.3-2. The device has proved its worth in test operations. It is now being readied for routine use. (H. Fauska and F.H. Schmidt)

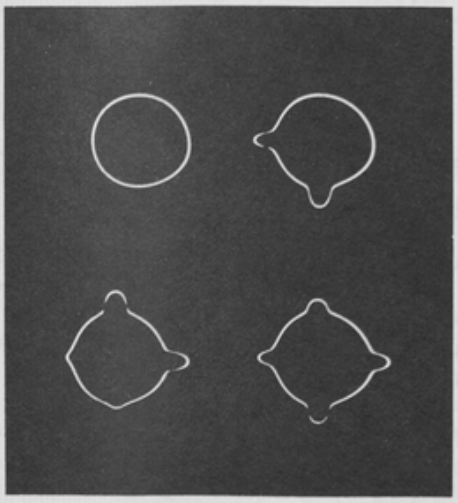

Fig. 2.3-2. Typical beam centering patterns.
Upper left: No beam striking the quadrant aperture. Upper right: Beam off center low and left. Lower left: Beam off center high and right. Lower right: Beam centered but focus bad.

2.4 A System to Facilitate Ion Source Metering Across an Elevated Voltage

The need for a closed circuit television to read out metering at the elevated voltage of an ion source is both costly and involves setup time. The system described will replace the closed circuit television and provide panel metering at the remote operating console.

Fig. 2.4-1 is a block diagram of the system constructed and tested. The initiating information for both voltage and current circuits is a shunt resistor developing 0-100 millivolts for the full scale range of the device metered. The signal across the shunt is sensed by a voltage-to-frequency converter with a linearity of 1% or better, and provides shaped signals with a repetition rate of 0-50,000 pulses per second. The shaped pulses then fire a photo emitting diode which is optically coupled to a 8 or 16 in. lucite light pipe. The other end of the light pipe is sensed by a phototransistor and drives a count rate metering circuit. The use of the lucite for insulating the signals from high voltage allows the output metering to be at a ground reference.

The parts involved cost little more than two meters.

The system was tested with more than two feet of lucite with no signal to noise problems. The system is basically digital at any possible noise pickup areas which is of considerable importance in noise reduction. The 8 inch lucite

provides sufficient insulation for our purposes. (H. Fauska and K.H. Lee)

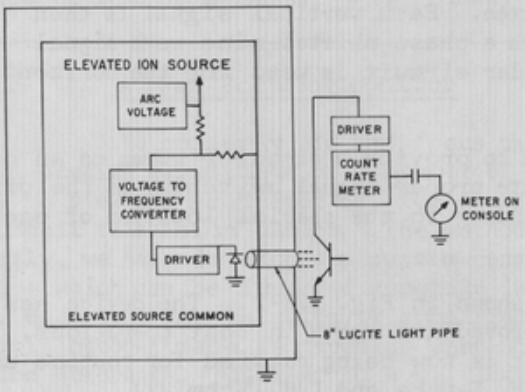

Fig. 2.4-1. Block Diagram of High Voltage Isolation Metering System.

2.5 Design and Construction of Electronic Equipment

Major electronic projects are discussed in sections 2.2, 2.3, and 2.4 of this report. Additional projects carried out during the last year include:

a. A saturable reactor control system for regulating the 70 kilovolt supply for the direct extraction ion source was designed and installed.

b. Provision was made to control remotely from the operation console the extraction voltage and the 30° bending magnet of the direct extraction ion source.

c. The two bending magnets in the ion source area must at times be returned to a residual magnetic flux of less than one Gauss to prevent interference with the beam optics for other sources. To sense the residual field two hall probe units with remote readout at the console were designed and constructed.

d. To provide metering in the control room of the vacuum systems for newly constructed ion sources, three remote range selection and readout solid state ion gauge controllers were designed and constructed.

e. To allow the possibility of using the cyclotron beam chopper for pulsing at every fifth period of the cyclotron frequency, a one to two and one half frequency divider was constructed.

f. The original charge exchange negative ion source used a voltage mode regulator for the exchange voltage. Such a system had poor line frequency correction when remoted due to the long time constants in the reference pickoff divider resistor string. A current mode solid state regulator was designed and constructed to replace the original regulator and eliminate the correction problem.

g. The Wien filter of the polarized ion source requires tracking between an electrostatic field and a magnetic field. (See Sec.1.3.) A power supply to provide regulation and a selectable tracking ratio was designed and constructed.

h. The polarized ion source requires an electrometer elevated to ≈160 kilovolts to test the polarization. (See Sec. 1.3.) A small solid state battery operated unit was designed and constructed.

i. One audio alert system for a laboratory radiation monitor was constructed. The system is designed so that the clicking sound of the monitor is barely audible when the monitor is only counting background, but increases to an irritating volume when the monitor detects radiation above background level. The system is capable of up to thirty watts of output at high counting rates.

j. One dual three-channel mixer system for the mixing of linear signals was constructed.

k. One gamma neutron discriminator circuit was constructed.

l. One dual channel linear pulse adder for particle identification was constructed.

Items purchased during the past year include:

1 - Hewlett Packard Calculator Printer
1 - CANBERRA No. 1411 Double Delay Line Timing Amplifier
1 - Used Packard-Bell Closed Circuit Television Camera
1 - Used 21 inch Television Monitor
1 - E.G.&G. T105/N Dual Discriminator
1 pr. - Heath Kit GW21-2 Transceivers
1 - ORTEC 437A Time-to-Pulse Height Converter
1 - Used exact Model 505 Function Generator
1 - E.G.&G. TR204 Updating Descriminator
1 - E.G.&G. C-102 Dual Two-fold Coincidence Unit

(L.H. Dunning, H. Fauska, K.H. Lee, R.E. Stowell, and N.G. Ward)

2.6 Preparation of ^{18}O Targets

It is possible to prepare very thin, strong and uniform self-supporting targets of Al_2O_3 by anodizing Al foil in a dilute aqueous electrolyte[1,2]. One may vary the target thickness by varying the voltage across the electrolytic cell. Briefly, one anodizes the foil and produces an Al_2O_3-Al-Al_2O_3 sandwich. The Al_2O_3 layer on one side and the Al are etched away by NaOH and a solution of $CuCl_3$ in HCl respectively. A self-supporting layer of Al_2O_3 remains.

Accordingly, a simple small volume glass cell with a platinum cathode and replaceable aluminum foil anodes was assembled. Approximately 5 cm^3 of 50% enriched ^{18}O water were mixed with citric acid to a 3% solution and placed in the

cell. The voltage across the cell was raised slowly both to insure uniform oxidation of the foil and to prevent significant evaporation of electrolyte caused by power dissipated in the cell. The cell was also cooled in an ice-water bath.

The targets thus prepared were quite strong and uniform. Target 1 was used for the bulk of the scattering study and checked repeatedly for changes in thickness. There were no discernible changes.

We noticed that there is a practical limit to the thickness of targets prepared in this way. Above 200 volts, sparking occurs between the liquid surface and the unsubmerged part of the anode, and pieces of blackish material appear in the electrolyte. Perhaps if thicker targets were desired, this problem could be avoided with a larger volume of material and different cell geometry.

Final cell voltages and resulting target thicknesses are given in Table 2.6-1. Target thicknesses were determined by elastic oxygen scattering below the oxygen-oxygen Coulomb barrier. Targets 1 and 5, those used for data collection, were measured in steps of 1 MeV from 15 to 20 MeV and in steps of 0.5 MeV from 17 to 20 MeV. These excitation functions were then fit to the appropriate Mott and Rutherford scattering functional dependence on energy, and the target thickness determined by comparison to calculated Mott and Rutherford scattering cross sections. Alpha particle range measurements were consistent with these results. (R. Shaw)

Table 2.6-1. Cell Voltages and Target Thicknesses

Target	Voltage	^{18}O ($\mu g/cm^2$)
1	200	41.2 ± 0.5
2	100	27
4	100	30
5	50	20.9

1. R. Vandenbosch (private communication).
2. W.A. Sherwood and R.E. Hester, UCRL 6722, 1961 (unpublished)

2.7 Target Preparation

During the past year approximately 110 targets were prepared. The majority of these targets were self-supporting films of isotopically enriched metals ranging in thickness from 3-5000 $\mu g/cm^2$, but generally between 300 and 1000 $\mu g/cm^2$. However, when self-supporting films are not feasible, i.e. when films of amorphous compounds or thin deposits of reactive metals are desired, a suitable backing is necessary. This backing must be thin, strong and cause minimal interference with the nuclear reaction being studied. In general the most suitable and therefore the most widely used backing is carbon. Carbon has additional advantages such as temperature resistance, good vacuum properties, easy availability and films as thin as 3-5 $\mu g/cm^2$ are used as backings. Since it is not unusual for 3-5 $\mu g/cm^2$/hr of carbon to build up on a target (cracked pump oil) during

bombardment, these thin carbon backings contribute negligible background.

The tandem Van de Graaff 40 position foil wheel assembly has been replaced 10 times in the past year. These replacements were generally prompted by convenience due to mechanical failure of terminal components and not to lack of useable foils. In general, the foils used are 5-10 $\mu g/cm^2$ carbon. (J. Heagney)

---

3. DETECTOR SYSTEMS

3.1 Silicon Detectors

All lithium-drifted silicon detectors used in the laboratory continue to be made here. A method used at Lawrence Radiation Laboratory in Berkeley[1] for drifting thick (3 mm and up) detectors in a helium-oxygen mixture after heating in ethanol is being tried.

Surface barrier fission fragment detectors are being made without encapsulation or edge protection. They are mounted in the same way as our lithium-drifted detectors. A stainless steel pin held in place by a spring provides a positive contact and a washer made of an electrically conductive elastomer (Choseal 1212, Chomerics, Inc., Arlington, Mass.) between the face and the brass detector case grounds the p side of the detector. Usually these detectors are cooled with a thermoelectric cooler during use to reduce the leakage current. Virtues of these detectors are ease of manufacture, the use of mountings already available, and satisfactory lifetime. We also are making some narrow rectangular fission fragment detectors for use in small angle multiple detector arrays. (S. Kellenbarger)

---

1. Robert P. Lothrop, UCRL-19413 (1969).

3.2 Direct-Coupled Low Noise Time Pick-Off Amplifier for Si(Li) Detectors

New fast rising, low noise time pick-off amplifiers to provide fast timing signals from Si(Li) detectors being used with charge sensitive preamplifiers have been developed. Such time pick-offs were developed by slightly modifying and combining a preamplifier and insertion amplifier designed by I.S. Sherman, R.G. Roddick, and A.J. Metz.[1]

The circuit diagram is shown in Fig. 3.2-1. The output to the slow preamplifier (such as an ORTEC 109A) is in parallel with the input of the fast preamplifier stage of the time pick-off through a 150 μH inductor. This inductor delays the charge transfer to the slow system and is large enough to essentially allow full voltage amplitude at the input to the fast preamplifier before the pulse decays as the charge transfers to the slow preamplifier.

The resistor R1 in Fig. 3.2-1 is used to set the current through the FET at about 10 mA or less. The 2N4393 is selected to have a transconductance of 15 mA/volt or more at this current.[1]

The basic operation and theory of the time pick-off are discussed by Sherman *et al.* The differences between the time pick-offs developed here and by Sherman *et al.* are the elimination of two trim capacitors, changing the transistors to less expensive types, and putting the fast preamplifier and insertion amplifier into a single aluminum box 4" × 1 3/4" × 7/8".

A total of eight time pick-offs were built. These were tested by connecting a 3 mm Si(Li) detector to the detector input, a fast pulse generator to

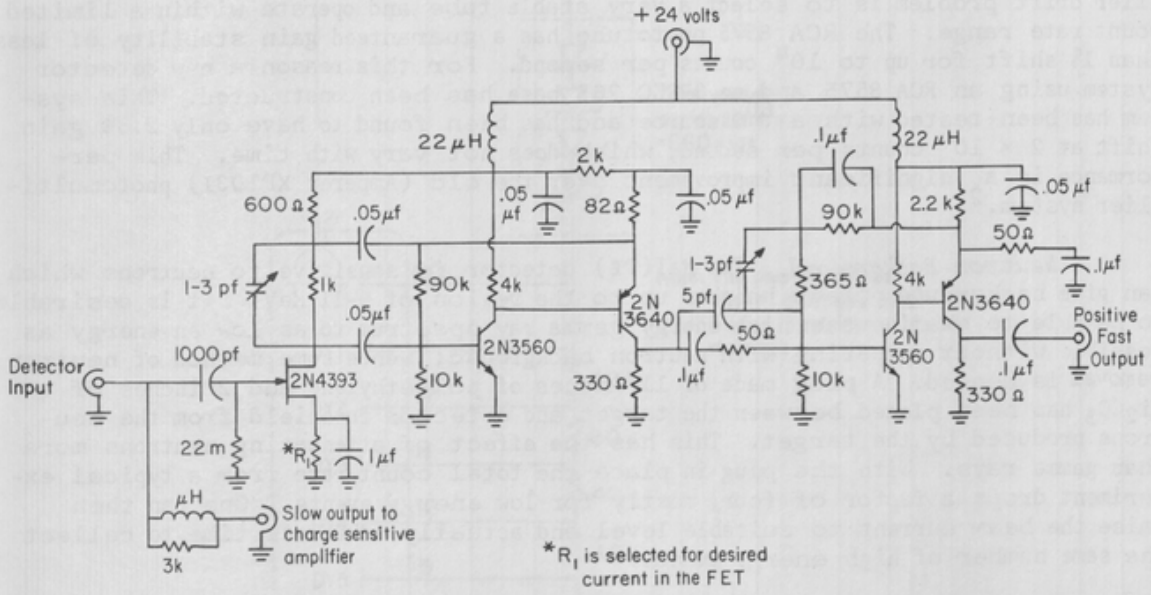

Fig. 3.2-1. Direct coupled low noise time pick-off amplifier.

the slow output, and monitoring the fast output of the time pick-off with a Tektronic type 454 oscilloscope. The typical gain was measured to be 100. The noise was typically 10 millivolts while the rise time was 6 nanoseconds (about the same as the input pulse).

The time pick-offs have been used in several experiments and performed well. In all cases the detector was connected directly to the time pick-off inside the scattering chamber. The $(p,p'\gamma)$ and $(\alpha,\alpha'\gamma)$ experiments discussed in Sec. 6 all used the new time pick-off amplifiers. (T. Lewellen, D. Patterson, and J. Tesmer)

---

1. I.S. Sherman, R.G. Roddick, and A.J. Metz, IEEE Transactions on Nuclear Science *3*, 500 (1968).

3.3 Improvements in the (NaI) High Energy Gamma Ray Detector

Gain stability of photomultiplier. Gain drifts have been a serious problem[1,2] in high energy gamma ray experiments due to the high counting rates that are necessary. One solution is to monitor the gain with a stable light pulser and make corrections to the spectra. The light pulser described last year[1] has been tested for long term stability. The pulser uses light emitting diodes which when driven hard at a rate of about 100 pulses per second tend to drift. It was found that when the light output was lowered to the equivalent of 30 MeV gamma rays or less the drifts become negligible. A second solution to the photomulti-

plier drift problem is to select a very stable tube and operate within a limited count rate range. The RCA 8575 phototube has a guaranteed gain stability of less than 1% shift for up to 10^4 counts per second. For this reason a new detector system using an RCA 8575 and an ORTEC 265 base has been constructed. This system has been tested with a ^{60}C source and has been found to have only 2.5% gain shift at 2×10^4 counts per second, which does not vary with time. This performance is a significant improvement over the old (Amperex XP1031) photomultiplier system.[2]

Neutron Background. The NaI(Tℓ) detector is sensitive to neutrons which can give background pulses heights up to the region of 9-11 MeV. It is desirable to be able to examine the high energy gamma ray spectrum to as low an energy as possible without competing with neutron background; hence some method of neutron removal is needed. A plug made of 11 inches of polyethylene and 2 inches of Li_2CO_3 has been placed between the target and detector to shield from the neutrons produced by the target. This has the effect of attenuating neutrons more than gamma rays. With the plug in place the total count rate from a typical experiment drops a factor of four, mostly for low energy events. One can then raise the beam current to suitable level and actually take less time to collect the same number of high energy events.

A test of detailed effects of the neutron plug indicates that while it is effective in reducing the low pulse height background there still remains a significant amount in the region up to 9-11 MeV. With 10 MeV protons on ^{27}Al about 10% of the events in this region were due to neutron. Of these neutron events, about 1/4 to 1/3 could not be filtered out by putting more material directly between the target and detector.

If accurate spectra below 9-11 MeV are desired then background subtraction by the time-of-flight technique must be employed.
(I. Halpern and D.L. Johnson)

---

1. Nuclear Physics Laboratory Annual Report, University of Washington (1969), p. 132.
2. Nuclear Physics Laboratory Annual Report, University of Washington (1968), p. 154.

3.4 5" Diameter by 4" Long Gamma Detector Assembly Efficiency Measurements

A new gamma-ray detector assembly employing a 5" × 4" NaI(Tℓ) crystal coupled to an RCA 4522 photomultiplier tube has been completed and is currently being used in particle-gamma angular correlation studies.[1] Figure 3.4-1 shows the voltage divider network used for the dynodes. Zener diodes are used between the photocathode and focusing electrode to maintain a constant voltage difference of 660 volts despite possible current variations in the voltage divider network. Since the tube is used in vacuum, the zeners are encased in epoxy to provide a vacuum seal, and high wattage, wirewound resistors are used to provide sufficient heat dissipation in the absence of convective cooling.

The tube has good gain-shift stability for rapid changes in the counting

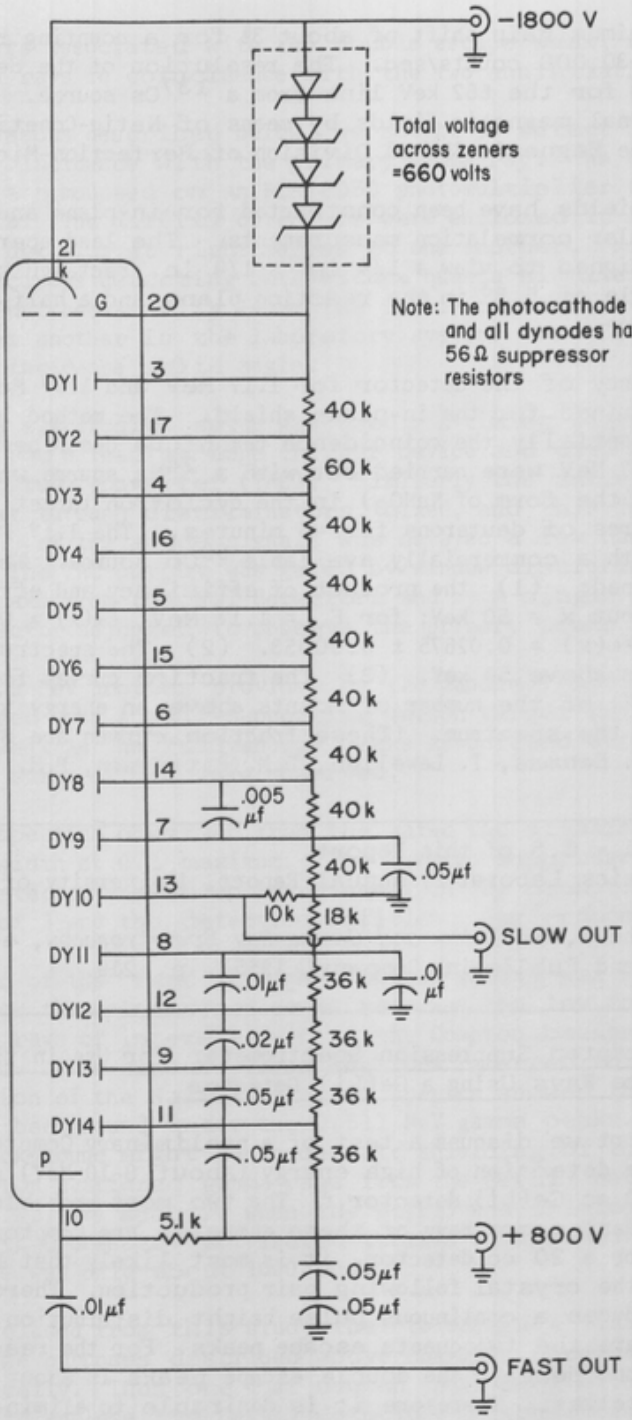

Fig. 3.4-1. Voltage divider network for the RCA 4522 photomultiplier tube.

rate, showing a maximum gain shift of about 3% for a counting rate change from 2500 counts/sec to 30,000 counts/sec. The resolution of the detector has been measured to be 8.3% for the 662 keV line from a ^{137}Cs source. The tube is shielded from external magnetic fields by means of Netic-Conetic magnetic shielding, supplied by the Magnetic Shield Division of Perfection-Mica.

New lead shields have been constructed for in-plane and out-of-plane particle-gamma angular correlation measurements. The lead aperture of the in-plane shield is designed to view a 1/4 in. × 1/4 in. rectangular beam spot, and subtends a half-angle of 5.5° in the reaction plane and a half-angle of 4.5° out of the reaction plane.

The efficiency of the detector for 1.17 MeV and 1.37 MeV gamma-ray energies has been determined for the in-plane shield. The method has been described earlier[2] and is essentially the coincidence technique described in Ref. 3. The measurements at 1.37 MeV were carried out with a ^{24}Na source which was made by bombarding ^{23}Na (in the form of $NaNO_3$) in the cyclotron target box with approximately 25 microamperes of deuterons for 45 minutes. The 1.17 MeV measurements were carried out with a commercially available ^{60}Co source. The following quantities were determined: (1) the product of efficiency and effective solid angle for counts above about x = 50 keV; for E_γ = 1.17 MeV, $\varepsilon\omega(x) = 0.02787 \pm 0.00052$; for E_γ = 1.37 MeV, $\varepsilon\omega(x) = 0.02675 \pm 0.00053$. (2) The spectrum shapes for the above two gamma rays above 50 keV. (3) The fraction curves for the above gamma rays, i.e., the ratio of the number of counts above an energy x to the total number of counts in the spectrum. (These fraction curves are normalized to 1.00 at x = 50 keV.) (J. Eenmaa, T. Lewellen, D.M. Patterson, F.H. Schmidt, and J.R. Tesmer)

---

1. Sections 6.1 - 6.5 of this Report.
2. Nuclear Physics Laboratory Annual Report, University of Washington (1964), p. 54.
3. A.C.G. Mitchell, in *Beta- and Gamma-Ray Spectroscopy*, ed. by K. Siegbahn (North Holland Publishing Company, 1955), p. 219.

3.5 Test of a Compton Suppression Spectrometer for Use in the Study of Proton Capture Gamma Rays Using a Ge(Li) Detector

In this report we discuss a test of a preliminary Compton suppression spectrometer for the detection of high energy (about 8-10 MeV) proton capture gamma rays with a 20 cc Ge(Li) detector.[1] The two most probable energy-loss mechanisms for incident gamma rays of these energies are Compton scattering and pair production. For a 20 cc detector, it is most likely that both annihilation gammas will escape the crystal following pair production. Therefore, since the Compton process produces a continuous pulse height distribution, the dominant strengths observed are the two quanta escape peaks. For the reaction of interest[1] the Compton background beneath the double escape peaks is about twice as large as the peak areas themselves. Therefore it is desirable to eliminate as much of this background as possible.

One technique to achieve this Compton suppression is to measure only

those primary events associated with the double escape peak; that is, to detect the incident gamma rays in coincidence with the two annihilation quanta.

For the reasons described below, we sought to detect only one of these escape quanta in coincidence with the primary gamma ray. We used two 3" × 3" NaI(Tℓ) crystals each mounted on an RCA 8050 photomultiplier tube to detect the 0.511 escape quanta. The NaI(Tℓ) detectors were enclosed in lead shielding and viewed the Ge(Li) detector at right angles to one another. Note that this right angle geometry precludes detecting both escape quanta simultaneously, since these gamma rays must necessarily leave the Ge(Li) crystal in almost opposite directions from one another in the laboratory system. We chose this geometry to increase the coincidence solid angle.

A standard electronics setup was used. A timing signal from the Ge(Li) preamp was taken from a leading edge trigger device and used as a start signal for a time to amplitude converter (TAC). Similarly the anode signals from the phototubes were put through discriminators, mixed, and this "or" signal used to stop the TAC. (One of the anode signals was delayed a few nsec to be in time with the other.) The TAC output was gated by window discriminators set on the 0.511 MeV photo peaks from the NaI detectors and by a single level discriminator on the Ge(Li) detector adjusted to observe the primary peaks of interest.

We used 5.5 MeV protons provided by the tandem Van de Graaff accelerator. The protons impinged upon a self-supporting carbon target and the double and single escape as well as the full energy peaks associated with the gammas from the first excited state of ^{12}C were observed.

The time spectrum observed from the gated TAC signals was 5.5 nsec FWHM and 13 nsec full width at 0.1 maximum. The Compton-suppressed energy spectrum from the Ge(Li) detector showed an improvement in the peak to background ratio by only a factor of 3 and the detection efficiency was reduced by a factor of 15.

The source of the "feed through" Compton gammas was investigated, but not exhaustively, since the coincidence count rate was too low for the detection of the capture gamma rays of interest even if the Compton background had been completely eliminated. (The capture cross sections referred to here are about 10-20 μb/sr.) Examination of the NaI(Tℓ) singles spectra showed the scintillators were accepting a large background under the 0.511 MeV gamma peaks. Two obvious causes of this background might be inadequate shielding of the NaI(Tℓ) from the beam tube or Compton scattered gamma rays from the Ge(Li) detector itself. Observations of the NaI(Tℓ) spectra when the Ge(Li) was shielded from the target indicated that both processes contributed to this background. The maximum total NaI(Tℓ) count rate was only about 1000 cps.

It is concluded from this study that to obtain a viable Compton suppression device for the purposes described above one must increase the coincidence efficiency drastically. Thus one must use an annulus of either plastic or NaI(Tℓ) which would enclose the Ge(Li) detector. Furthermore the annulus should be split into halves or quarters so that one could independently detect both annihilation gammas simultaneously, thus significantly reducing the "feed-through" background described above. The problem of adequately shielding such a

large suppression detector from the beam tube may be non-trivial in the present context, however, since this could entail moving the Ge(Li) detector too far back from the target -- to make room for the shielding -- thus further reducing the already small count rate. We have no plans at this time for building such a device. (D.R. Brown, J.R. Calarco, R. Heffner, and Derek W. Storm)

---

1. For a description of the particular experiment referred to here see Nuclear Physics Laboratory Annual Report, University of Washington (1969), p. 70.

3.6 Neutron Detector Characteristics

A neutron detector system has been developed and used in several experiments in the laboratory. It consists of an NE 213 scintillator (5" × 1") optically coupled to an RCA 4522 photomultiplier tube via a 1" lucite light pipe. The photomultiplier is connected to an ORTEC 271 constant fraction discrimination tube base. The efficiency as a function of neutron energy and other characteristics of this system have been measured and are reported below.

The efficiency of the neutron scintillator system was measured by the T(p,n)He associated particle method, using incident protons ranging from 3.375 MeV to 6.5 MeV. The target, provided by ORNL, consisted of tritium absorbed in a layer of titanium ($\sim$100 $\mu g/cm^2$) on a copper backing ($\sim$1 mg/cm^2). A 25-μ surface barrier detector was used to detect the ^{3}He; since protons of more than 1.3 MeV pass through the counter the ^{3}He peak in most cases was free from serious background problems. A tight aperture system was used to limit kinematic broadening. The angles of the ^{3}He and neutron counters were dictated by the desired neutron energy. The neutron counter was placed at a distance from the target such that the kinematically allowed neutron cone did not exceed 3/4" in dimension. The ^{3}He signals provided start pulses for a TAC and the stops were furnished by the neutrons. The efficiency of the scintillator is then the ratio of neutron counts in the time spectrum, after subtraction of accidentals, to ^{3}He counts in the particle spectrum. The efficiency profile across the scintillator surface was also measured; the profile is flat over about 60% of the diameter. Profiles measured at neutron energies of 1.4 MeV and 1.8 MeV exhibit the same shape within counting statistics. An average efficiency was extracted by integrating over the efficiency profile and dividing by the total area. The average efficiency was found to be about 10% less than that at the center. Figure 3.6-1 shows the average efficiency plotted against neutron energy.

The ORTEC constant fraction discrimination base enabled the detector to be used for accurate time-of-flight experiments. In particular the constant fraction timing technique is designed to reduce time walk due to variations in pulse heights. During an (α,n) experiment on the cyclotron, de-excitation gammas from induced reactions in the target were observed in the time of flight spectrum with a time dispersion of the order of 1 nsec FWHM. This includes the intrinsic time width of the cyclotron beam pulse.

An additional feature of the neutron detector system is its ability to distinguish between neutrons and gamma rays when used with the appropriate

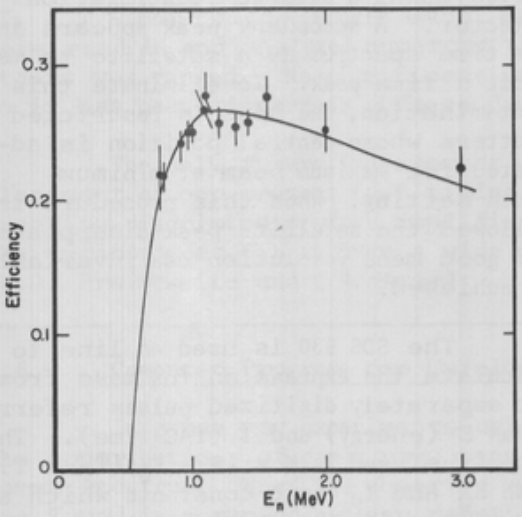

Fig. 3.6-1. Neutron detector efficiency as a function of neutron energy. Detector threshold equals 0.5 MeV.

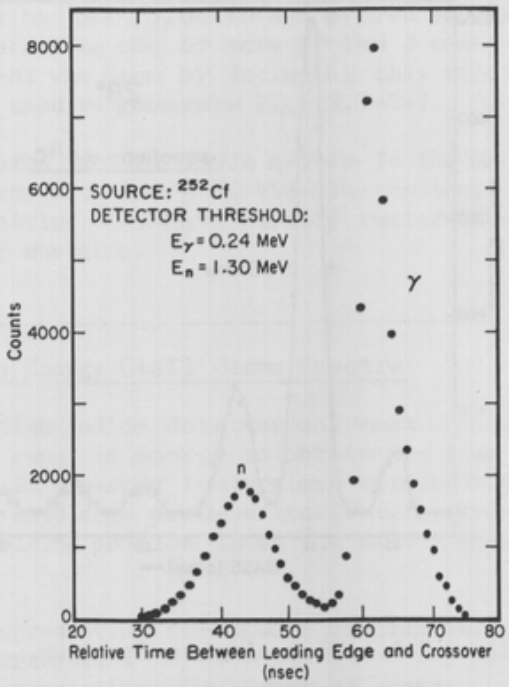

Fig. 3.6-2. Spectrum of relative time differences between the leading edge and crossover of the shaped detector signal.

modular electronics. The technique, that of pulse shape discrimination, makes use of the fact that decay time of the light output from NE 213 depends on the identity of the detected particle. (See, for example, Kuchnir and Lynch[1].) Integration of the output results in signals having different risetimes for different types of particles. These risetimes are determined by observing the time between the leading edge of the initial current pulse and the zero-crossover point of the linear integrated signal, after bipolar shaping in a double delay line clipped amplifier. A typical spectrum of crossover times is shown in Fig. 3.6-2. (J.R. Calarco, J.M. Cameron, D. Chamberlin, and C. Ling)

---

1. F.T. Kuchnir and F.J. Lynch, IEEE Trans. Nucl. Sci. *NS-15*, No. 3, 107 (1968).

3.7 Mass Identification by Time of Flight Analysis

Last year we reported our initial successes at charged particle time of flight mass identification using the 42 MeV alpha beam from our fixed frequency 60 in. cyclotron. The mass resolution thus far achieved has been between .25 and .5 amu (FWHM) in the region of mass 12 when the particle counter is placed at approximately 60 cm from the target (see Fig. 3.7-1).

Mass is calculated from the non-relativistic expression $M \propto Et^2$, where E is the particle's energy and t is the particle's time of flight from the target

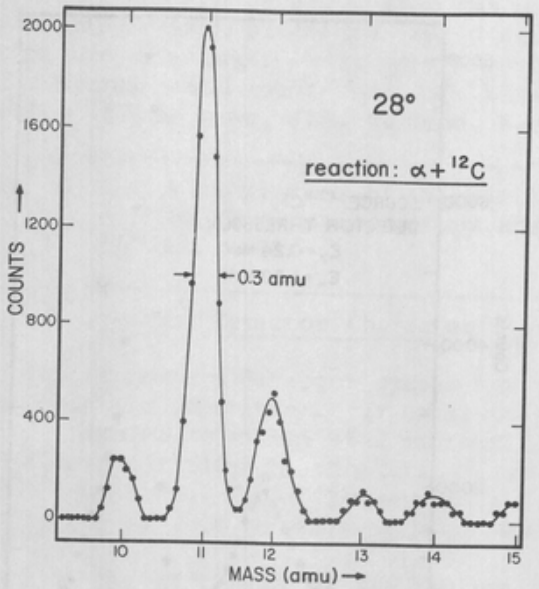

Fig. 3.7-1. Mass singles spectrum.

to the detector. Differentiating this expression gives: $dM/M = dE/E + 2dt/t$ which can be used to estimate the contributions of energy and time uncertainties to the variance in calculated mass. Counter energy resolution is invariably better than 50 keV so for energies greater than 5 MeV this contribution to mass spread may be completely ignored. The time width of the cyclotron alpha beam is estimated to be between .8 and 1.0 ns from recent measurements with a plastic scintillation counter which looked at the beam generated gamma flash. This value for time resolution of the beam is just the right size to singlehandedly account for the observed mass spread.

It should be noted at this point that good mass resolution requires that the cyclotron beam be single-turn extracted. The alpha particle orbits near extraction radius differ by approximately 300 keV giving a difference in transit time through the beam transport system of about 2 ns. This effect has been observed using a plastic scintillation detector. A secondary peak appears in the time spectrum as a satellite to main orbit's time peak. To eliminate this contamination, the beam is restricted by shutters whose central position is adjusted for maximum beam at minimum width setting. When this procedure is followed the satellite peak disappears and good mass resolution can invariably be achieved.

The SDS 930 is used on line to calculate the expression for mass from two separately digitized pulses referred to as E (energy) and T (TAC time). The algorithm used is $M \propto (E - E_0)(T_0 - T)^2$ with E_0 and T_0 input constants which are varied to give the straightest mass lines in a M × E plot. Figure 3.7-2 shows a typical plot of this. The mass lines are straight to well within the resolution although a slight distortion can be seen at the lowest energies. This was initially attributed to the slight time walk resulting from leading edge discrimination in the time pickoff system. A computer generated correction for this time walk was included in the

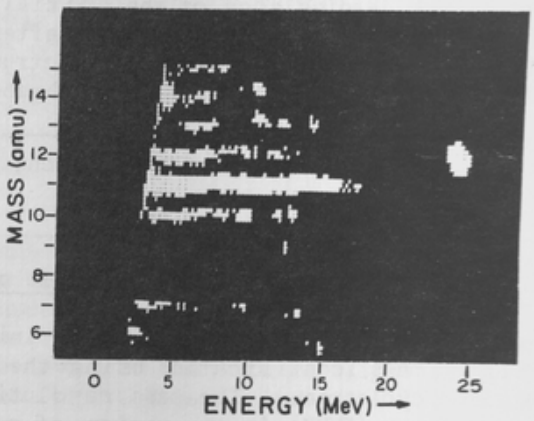

Fig. 3.7-2. Count level contour plot using the same data as Fig. 3.7-1.

expression used to calculate mass. The algorithm then becomes: $M \propto (E - E_0) \times (T_0 - T - \text{const}/E)^2$. Single event data that had been blocked and stored on tape were read in and analyzed numerous times. Each time one or more of the 3 constants was varied. No significant improvement was seen by including this term so it has been discarded. (These data were used to generate Fig. 3.7-2.)

The only future improvement anticipated in this basic system is the replacement of our present fast timing equipment with an ORTEC 453-454 constant fraction discriminator-fast amplifier combination. We have already tested it on the cyclotron at 0.8 ns over a wide range of energies.
(W.J. Braithwaite and C.R. Rudy)

3.8 Computer Programs for Unfolding High Energy (NaI) Gamma Spectra

In gamma ray experiments using a sodium iodide detector one must unfold the contributions of gamma rays over a wide range in energy to obtain the true gamma spectrum. When the observed spectrum is a nearly featureless continuum as are found in compound nuclear reactions the unfolding process itself can introduce large errors. One way to view the unfolding problem is as the matrix equation $\|R\|G = E$, where

- G is a column vector representing the number of incident gammas per energy increment,
- E is a column vector representing the number of counts observed in the experimental data per energy interval,
- and $\|R\|$ (the response matrix) represents the response of the detector to the various energy gamma rays.

The straightforward solution is then $G = \|R^{-1}\|E$, where $\|R^{-1}\|$ is the inverse of the response matrix.

Unfolding Program. A program to perform the unfolding by direct inversion has been written and tested. One can unfold groups of data until the whole spectrum is done or unfold the whole spectrum at once. A sample spectrum was generated with a Gaussian response whose width was about 10 channels FWHM. It was found that no more than about 30 channels from the top end of the spectrum could be unfolded accurately before large errors resulted. This is due to the limitation in the number of significant digits (12 digits) available in SDS FORTRAN language. It will be necessary to program in double precision for the unfolding technique to accurately cover more channels.

Data Fitting Program. When the direct inversion method is used it usually produces large unrealistic oscillations in the resulting spectrum. This is due to statistical errors in both the experimental spectra and the measured response matrix which are amplified by the inversion process. To eliminate these oscillations an attempt has been made to minimize the statistical errors present. The most probable function representing a spectrum can only have fluctuations which are consistent with the resolution of the detector; that is, there is an upper limit to the allowed frequencies in a Fourier analysis of the spectrum. Other experimenters have attempted to remove the fluctuations by smoothing with a

predetermined function. It is felt that this does not use all of the information that a measured spectrum can provide. If one could take a very long data run the spectrum could be represented by a continuous function whose statistical errors were negligible. If one fits this function to the data from a shorter run, the statistical fluctuation of the data about the function should be consistent with a chi square distribution. Since the function is not known beforehand, an approximation can be made by fitting groups of data points to a polynomial and requiring that the fit be consistent with a chi square distribution. A program has been written which does this by varying the order of the fit until the chi-square is within certain limits. To assure that the resulting fit is continuous the groups of data points are overlapped and required to be equal in magnitude and first derivative somewhere in the overlap region. The program has been preliminarily tested on several gamma ray spectra and works well as long as the region of the fit does not contain gamma rays of widely differing resolution. Figure 3.8-1 shows the results of the fitting program in smoothing out statistical fluctuations in the pulse height spectrum of a 15.1 MeV gamma ray. Note that the differences between data and fit compare well with the expected standard deviations.
(I. Halpern and D.L. Johnson)

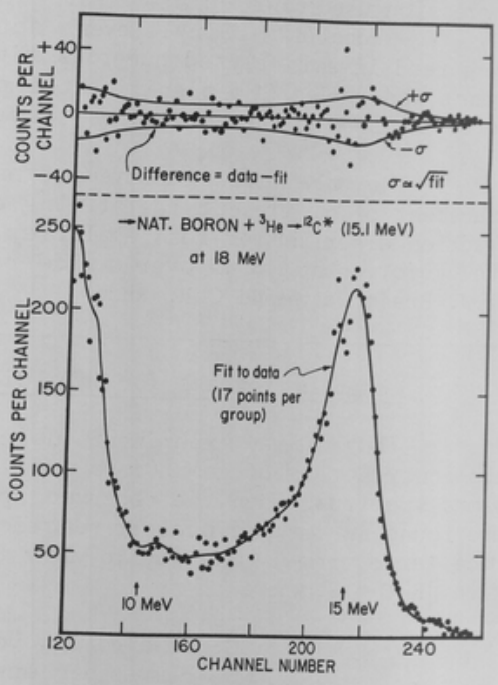

Fig. 3.8-1. Plot of the best fit to the spectrum of a 15.1 MeV gamma ray of ^{12}C produced by 18 MeV ^{3}He bombardment of natural boron. The differences between data and fit are compared to the expected value of the standard deviation.

4. COMPUTER SYSTEM IMPROVEMENTS AND PROGRAMMING

4.1 Computer Expansion

In late 1969 the Laboratory received an AEC grant to expand the existing computer system to the configuration shown in Fig. 4.1-1. The purpose of this expanded system is to allow foreground/background, background/background, and potentially foreground/foreground computation. Of particular importance to the Laboratory is the fact that the system will allow off-line computation, i.e., data reduction, scientific calculations, program development, and debugging, to be performed by one arithmetic/control unit while on-line data collection is taking place in the other.

As can be seen in Fig. 4.1-1, the system is quite symmetrical in structure and will make full use of the existing peripherals. A drum storage unit is included in the expansion to perform several functions. It will provide storage for the software system, serve as general purpose memory, and buffer the communications between the two arithmetic/control units and the card punch and printer peripherals. This last function is necessary in order to eliminate competition between the 2 A/Cs for the use of these 2 peripherals, and insure that hard copy and punched cards are generated in a job-by-job sequence.

To date mechanical design and fabrication of the logic chassis in which the additional memory and arithmetic/control unit are mechanized have been completed. The wire list for the memory is finished and the unit is now being wired. Work is still being done on the arithmetic/control wire list.

Layout of the printed circuitry for the 56 types of circuit board modules used in the memory, arithmetic/control unit, and peripheral interfaces has been completed. Approximately 90% of the 450 modules required by these three areas of the computer expansion project have been etched, cut, and drilled.

A list of the transistors, diodes, resistors, capacitors, etc., required to build the 450 circuit board modules has been compiled and is being readied for bids. (N.R. Cheney, J. George, P. Rabinovitch, E. Schnellman, and F. Weiss)

4.2 Interrupt System Modification

The logical design of the computer's Interrupt System has been modified to overcome some undesirable handling characteristics of the Basic and Priority Interrupts. The original system configuration gave the Basic Interrupts (primarily I/O) precedence of execution over the Priority Interrupts (data collection, outside world). The modification allows this order of execution to be reversed or operate as originally designed. The option is controlled manually by a switch located on the computer control console. (N.R. Cheney)

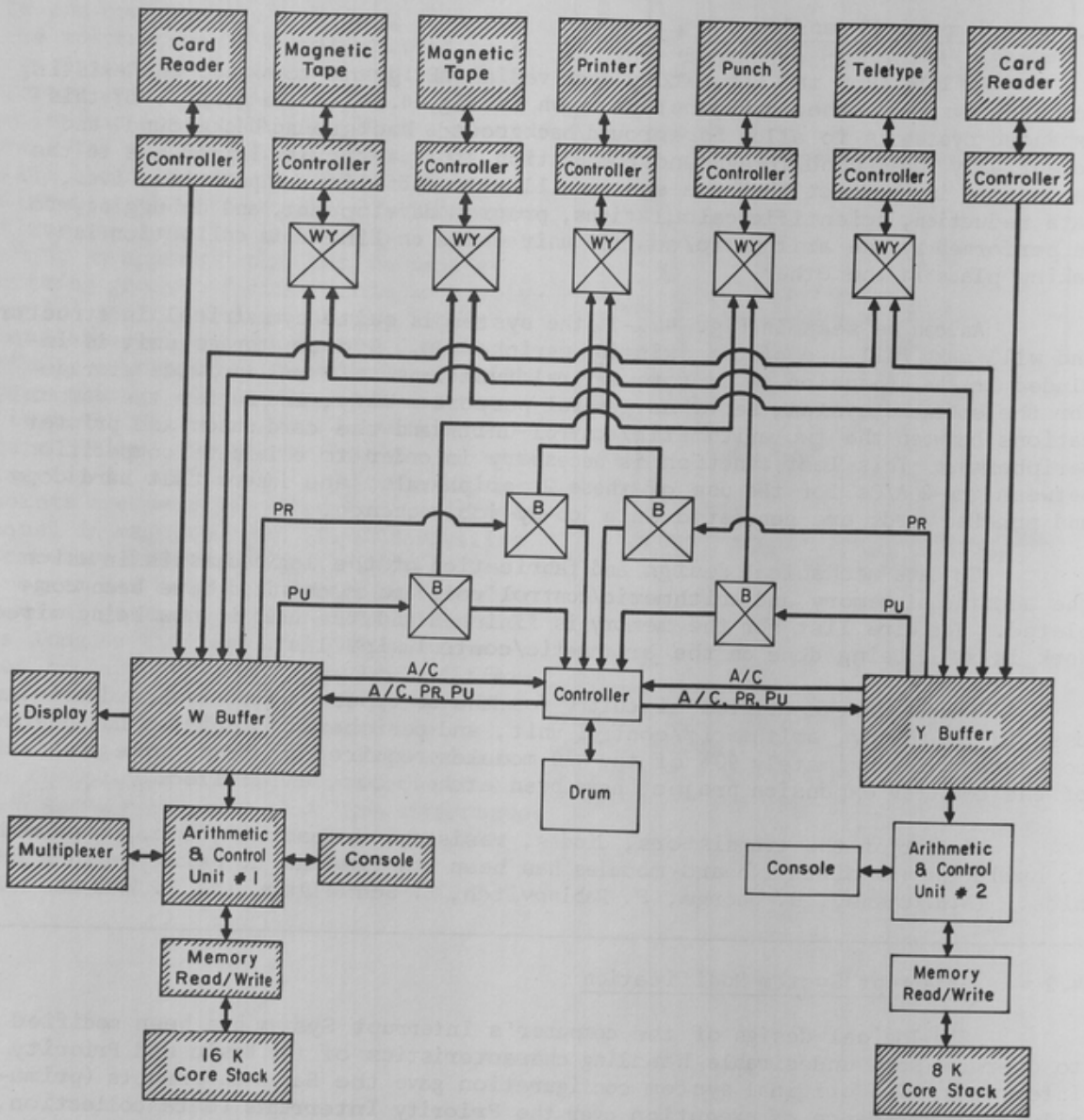

Fig. 4.1-1. Expanded Computer System. (Shaded items are already on hand.)

4.3 System Class EOM Expansion

A device has been designed and built to improve the computer's external communication capability. The hardware consists of a matrix to decode 132 of the 4096 possible System Class EOM's, a 24 bit holding register, and 8 flip-flops for general purpose communication. Data is transferred to the 24 bit holding register by executing the appropriate EOM/POT instructions. The 8 general purpose flip-flops each have a pair of set/reset EOMs assigned for their control. The outputs of the 24 bit holding register and the 8 general purpose flip-flops are buffered through line drivers for use outside the computer.

The decode matrix is readily expandable to make available as many of the remaining System Class EOMs as might be needed.
(N.R. Cheney, J.G. Cramer, and E. Schnellman)

4.4 Card Reader Improvements

Due to the requirements of our computer expansion project, the Laboratory is building an additional card reader. Some changes are being incorporated in the design of this reader to improve its performance over that of the reader the Laboratory built previously.[1] In particular, 2 areas are being modified: the reading scheme, and the pickerknife clutch/brake mechanism.

In the original reader, filament lamps and photodiodes were used as the light source and reading elements; they are being replaced by infrared emitting gallium arsenide diodes and phototransistors, respectively. These new elements have an improved life expectancy over that of the old (although there have been no failures in the filament lamps and photodiodes), and will simplify the reading electronics.

The clutch/brake mechanism that controls pickerknife action in the present reader uses a magnetic particle clutch to drive the pickerknife, and a mechanical brake to stop it. This brake wears out quite rapidly, and is the weakest part of the present reader. It will be replaced by a unit identical to the clutch and will be made to function as a brake by holding its input pulley stationary. This change is expected to improve the reliability of the new reader, and increase its reading rate.

The machine shop has started fabrication of the new reader.
(N.R. Cheney, N. Ward)

4.5 Reduction of Computer Dead Time for On Line Data Collection[1]

Work on a hardware device to reduce computer dead time while collecting data via the multiplexer and ADCs has been discontinued temporarily due to the workload of the higher priority computer expansion project (see Sec. 4.1). Before work was stopped several logic modifications were installed in the arithmetic/control section of the computer, and a test fixture was designed and built to proof our approach to the dead time problem. Included in the test fixture are provisions to add a manually set computer memory base address to a 12 bit

operand from the ADCs, plus timing and control logic for transferring the resulting sum to the computer. The test fixture will be tied into the computer system and the proofing exercise will be done as the workload permits. (N.R. Cheney)

---

1. Nuclear Physics Laboratory Annual Report, University of Washington (1969), p. 139.

4.6 Multiparameter Data Acquisition Using a De-Randomizing Buffer

Several multiparameter data collection programs have been written which include as a common feature the storage of raw data in a block of core memory before processing. Such a temporary buffer region allows some separation of the collection part of the program from the processing part.

This region in core memory is allocated by a Real Time Fortran Program to accept the simultaneous conversions from up to 6 ADCs. This buffer array is logically separated into blocks of 7 words: one word for each of the 6 possible ADC conversions and one word to act as a "table of contents" (the format register) indicating which of the ADCs successfully converted. The filling of this buffer array is the only task of the interrupt portion of the program.

All processing of this raw information is done in the main part of the program while waiting for the next interrupt to occur heralding the arrival of a new data group. The computer will immediately leave this processing part of the program, collect the new data into the buffer array, and then return to processing where it left off. The data processing does not tie up the computer as would be the case if the interrupt routine which reads it in were also to process it. There is no dead time so long as the time for processing data is less than the average time between arriving groups of data.

Buffering the ADC input has obvious advantages for high counting rate multiparameter applications such as the single counter Et^2 and/or E-Δ particle identification. Nevertheless, it is a convenient and flexible method of data taking that it is preferable even for low counting rates. Since the method allows processing outside of the interrupt routine, Fortran statements can be incorporated into the data reduction without the nuisance of "SAVE-RELEASE" precautions. Even more important, the novice can write his own multiparameter code by just taking his information directly from the core memory and without requiring any knowledge of how to read data in from the hardware.

Since the processing portion of the program operates completely independently of whether the buffer is filled directly from the ADC's or from raw event-by-event data stored on magnetic tape, the method lends itself particularly well to re-analysis of stored data using the same processing program. Moreover, processing programs can be easily debugged and checked after modification, using previously collected data stored on magnetic tape to fill the buffer.
(M.P. Baker and W.J. Braithwaite)

4.7 An On-Line Program for Collecting Particle-Gamma Correlation Data Using 5 Particle Detectors

An on-line data collection program has been written for use with multi-detector experiments. The program is written for the Laboratory's SDS 930 computer in a combination of FORTRAN and SYMBOL. This program differs from other data collection programs in use at this Laboratory in that incoming data may be analyzed on-line using the light pen data analysis package.[1] The program requires 50 μsec to process each event and this time is not affected by the data analysis.

Data may be collected on-line from up to 6 independent ADC's, any or all of which may be routed. The program in its present form will accept up to ten 256 channel spectra. The values of parameters which are required for the on-line analysis and which remain fixed for a series of data runs are read into the computer when the program is initialized. Other parameters, such as peak areas and integrated incident charge, are obtained by the computer when they are needed as data is being collected. The light pen is used in conjunction with the live CRT data display to specify the start and end channels of peaks, to request that information about specific peaks be displayed on the CRT screen, to indicate which peaks are to be used in special calculations, and to specify selected regions of the data for expanded display. The basic analysis program calculates peak areas corrected for background, peak cross sections corrected for ADC dead time, and the statistical errors of the above. The results of the various calculations may be displayed live on the nixie display units of the computer and are included in the hard copy output produced at the end of a data run. The on-line peak analyses usually agree with post-run hand analyses to better than several per cent with differences being due mainly to overestimating the background in the computer analyses. Thus the statistical errors calculated on-line are usually slightly larger and the peak areas slightly smaller than those obtained by hand analyses.

This program has been used for the past year to obtain particle-gamma correlation data.[2] 5 ADC's were used to collect the particle singles spectra and 1 ADC with routing was used to collect the 5 gated time (or particle) spectra. Routines were included in the analysis program to calculate the number of true particle-gamma coincidences and the experimental correlation values. It was found most useful to be able to monitor the quantities of specific interest, i.e., the correlation and its statistical error, rather than just the number of counts in a peak or in a spectra, and to have a reasonably accurate preliminary data analysis available as soon as a data run was finished. (D.M. Patterson)

---

1. Nuclear Physics Laboratory Annual Report, University of Washington (1969), p. 142.
2. Sections 6.1 through 6.5 of this report.

4.8 Magnetic Tape Input/Output Program Package

A subroutine package has been written to allow binary magnetic tape

input/output operations to be performed while the computer is being used for on-line data collection. The subroutines in the package are written in assembly language (Symbol) and may be used in either a Fortran or a Real Time Fortran operating environment by making slight modifications to some of the subroutines. Information is written on tape in the same format used by the SDS binary tape I/O routines supplied with the computer.

The primary design criterion was for the tape writing process to have the smallest possible effect on the rate at which data could be collected on-line. This made it desirable to allow the System interrupts, which are used for data collection, to have priority over the I/O interrupts. Since this is not the normal interrupt priority configuration, a modification was made to the interrupt hardware that allows the selection of the relative priority of the System and I/O interrupts by a toggle switch on the computer control console.[1] One of the two Time-Multiplexed Communication Channels with interlace, which is part of the I/O system of the Nuclear Physics Laboratory's SDS 930 computer, is used to control the actual I/O process. Once the I/O operation is initialized the channel operates essentially independently of the central processor, thus allowing the computer to perform other operations while the I/O is in process. The channel requires at most 3.5 μsec of every 67 μsec of central processor time to transfer data to or from memory. At the end of the I/O operation the channel sets an interrupt so that the validity of the transmission can be checked and, if desired, a new transmission started.

Subroutines that are entered by Fortran CALL statements have been written for the following tape operations: read tape binary, write tape binary, write tape end-of-file mark, scan forward/reverse for a specified number of tape end-of-file marks, scan for a specified binary record which follows a tape end-of-file mark, and rewind tape. The binary read/write routines are slightly restrictive in that they must be called for each block of data. However, the only restriction on the allowed size of a data block is that it cannot exceed the size of the computer memory. (D.M. Patterson)

---

1. Section 4.2 of this report.

4.9 A 3-Body Relativistic Kinematics Program for Reaction Studies Using Energy-Energy or Energy-TOF Measurements

A fully relativistic three-dimensional three-body kinematics program has been written which calculates permitted kinematic loci and related kinematic parameters for two-counter 3-body reaction studies where either energy vs energy or energy vs time-of-flight (TOF) is studied. In the latter case provision is made for either TOF measured with respect to a timing pulse from a cyclotron oscillator or beam buncher, or with respect to the arrival time of the other coincident particle.

The program allows both counters and the beam direction to be positioned at any pair of polar and azimuthal angles (θ,ϕ) in the three-dimensional coordinate system. The arbitrary specification of the beam direction permits calcula-

tions of the kinematics of 4-body reactions in the special case where the reaction may be sequentially described by a two-body reaction followed by three-body breakup of a recoiling nucleus, e.g., the reaction $^{124}Sn(^{3}He,n\ 2p)^{124}Sn$ as discussed in Sec. 11.6. In this case the recoil angles of the recoiling nucleus in the 2-body reaction become the "beam" direction for the 3-body calculation.

Basically, the program uses energy and momentum conservation,

$$\vec{P}_1 = \vec{P}_2 + \vec{P}_3 + \vec{P}_4 \tag{1}$$

and

$$W_1 = W_2 + W_3 + W_4 \tag{2}$$

with the side conditions

$$W_i = T_i + A_i, \tag{3}$$

$$W_i^2 = p_i^2 + A_i^2 \tag{4}$$

$$T_1 = T_{beam} \tag{5}$$

$$A_1 = Q + A_2 + A_3 + A_4 \tag{6}$$

and

$$P_1 = (T_1(2A_{beam} + T_1))^{\frac{1}{2}}. \tag{7}$$

Here the subscript 1 refers to the compound beam + target system, 2 and 3 refer to the detected breakup particles, and 4 refers to the undetected breakup particle; p is momentum in MeV/c; A is mass, W is total energy, and T is kinetic energy, all in units of MeV.

If we solve Eq. (1) for $\vec{P}_4$ and square, we obtain

$$P_4^2 = P_1^2 + P_2^2 + P_3^2 - 2P_1P_2\,G_{12} + 2P_2P_3\,G_{23} - 2P_3P_1\,G_{31} \tag{8}$$

where

$$G_{ij} \equiv \hat{P}_i \cdot \hat{P}_j = \cos\phi_i \cos\phi_j(\sin\theta_i \sin\theta_j + \cos\theta_i \cos\theta_j) + \sin\phi_i \sin\phi_j. \tag{9}$$

Here ϕ_i is the standard azimuthal angle, measured with respect to the normal beam direction, and θ_i is a non-standard polar angle defined as $\theta_i = 90° - \theta_{polar}$ so that $\theta_i = 0$ in the median plane, and is positive above and negative below the median plane. Thus $\theta_i = 0°$, $\phi_i = 0°$ is the standard beam direction and particles which lie in the median plane have $\theta = 0°$. This non-standard angular convention was established to simplify the punching of data cards for the program.

From Eq. (2) and (4) we can obtain

$$2W_3(W_2 - W_1) = (p_4^2 - p_3^2) + [A_4^2 - A_3^2 - (W_2 - W_1)^2]. \quad (10)$$

Substituting for $p_4^2 - p_3^2$ from Eq. (4) leads to

$$2W_3(W_2 - W_1) = B_1 + B_2 p_3 \quad (11)$$

where

$$B_1 = p_1^2 - 2p_1p_2\, G_{12} + p_2^2 + A_4^2 - A_3^2 - (W_3 - W_1)^2$$
$$B_2 = 2(p_2\, G_{23} - p_1\, G_{31}). \quad (12)$$

Squaring Eq. (11) and again using Eq. (4) leads to

$$S_1 p_3^2 + S_2 p_3 + S_3 = 0 \quad (13)$$

where

$$S_1 = B_2^2 - 4(W_2 - W_1)^2 \quad (14)$$

$$S_2 = 2B_1B_2 \quad (15)$$

$$S_3 = B_1^2 - 4A_3^2(W_2 - W_1)^2. \quad (16)$$

Since $B_{1,2}$ and $S_{1,2,3}$ all involve only $p_{1,2}$, $\theta_{1,2,3}$, $\phi_{1,2,3}$, $W_{1,2}$, $p_{1,2}$, and $A_{3,4}$ we may solve Eq. (13), a quadratic equation, for $p_{3\pm}$ where the $\pm$ indicates the two roots of the equation. The remaining unknown momentum $p_{4\pm}$ can be calculated from Eqs. (2) and (4). The angles of particle 4 are

$$\theta_{4\pm} = \mathrm{Tan}^{-1}(Y_\pm / X_\pm), \quad (17)$$

$$\phi_{4\pm} = \mathrm{Tan}^{-1}\left[Z_\pm / \sqrt{X_\pm^2 + Y_\pm^2}\right] \quad (18)$$

where

$$X_\pm = p_1 \cos\phi_1 \cos\theta_1 - p_2 \cos\phi_2 \cos\theta_2 - P_{3\pm} \cos\phi_3 \cos\theta_3 \quad (19)$$

$$Y_\pm = p_1 \cos\phi_1 \sin\theta_1 - p_2 \cos\phi_2 \sin\theta_2 - p_{3\pm} \cos\phi_3 \sin\theta_3 \quad (20)$$

$$Z_\pm = p_1 \sin\phi_1 - p_2 \sin\phi_2 - p_{3\pm} \sin\phi_3. \quad (21)$$

The relative energy between particles j and k, for a 3-body final state involving particles i, j, and k is:

$$E_{jk} = A_{jk} - (A_j + A_k) \quad (22)$$

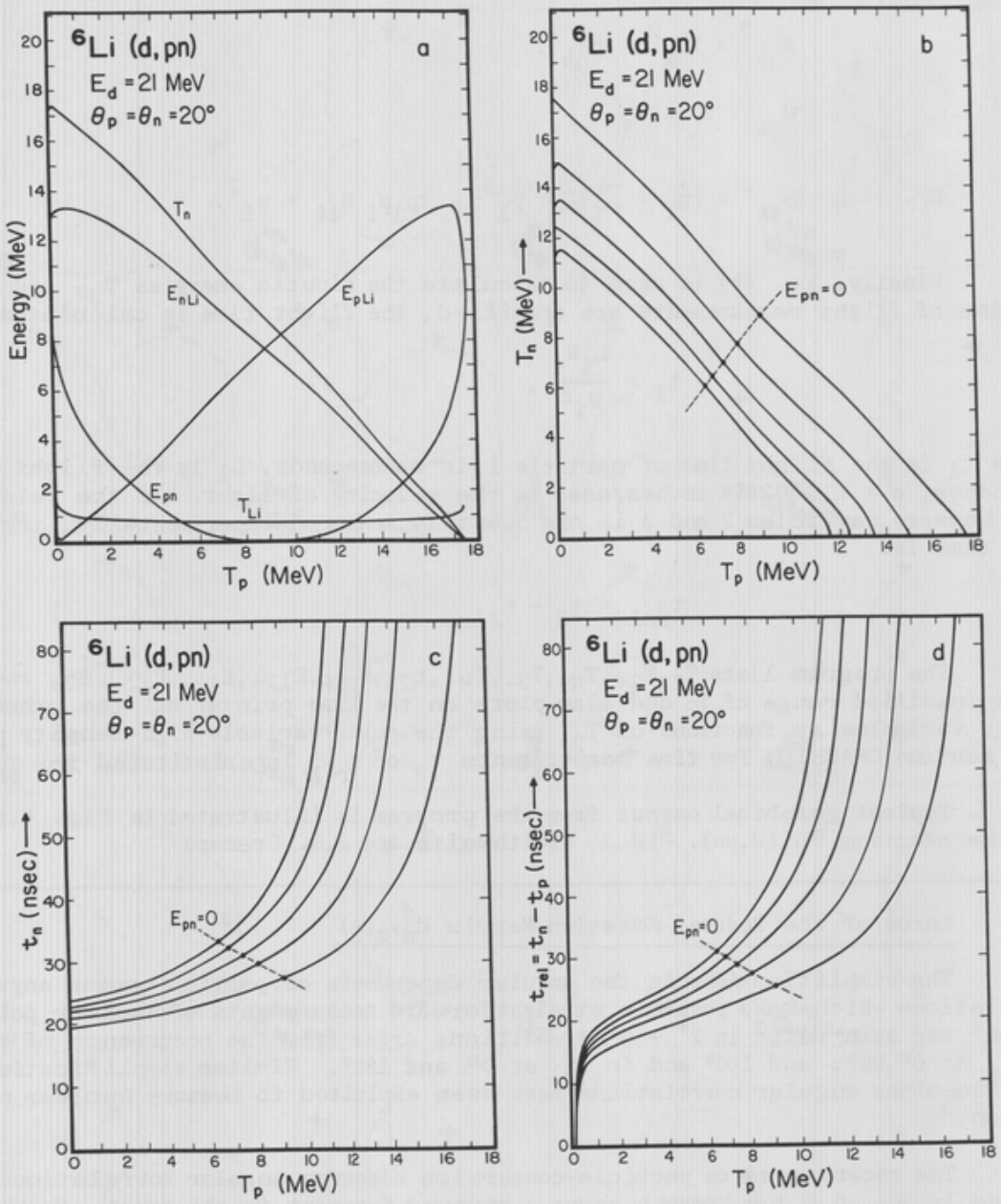

Fig. 4.9-1. a) Typical output plot of T_3, T_4, E_{23}, E_{13}, and E_{12} vs T_2 for the reaction ^{6}Li(d,pn); b) T_3 vs T_2 for a range of final nuclear states; c) t_3 vs T_2 for the same states; d) relative flight time $t_{rel} = t_3 - t_2$ vs T_2 for the same states.

where

$$A_{jk}^2 = W_{jk}^2 - p_{jk}^2, \tag{23}$$

$$W_{jk} = W_1 - W_i, \tag{24}$$

and

$$p_{jk}^2 = |\vec{p}_1 - \vec{p}_i|^2 = p_1^2 - 2p_1p_i\, G_{1i} + p_i^2. \tag{25}$$

Finally, Eq. (4) is used to calculate the kinetic energies $T_{3\pm}$ and $T_{4\pm}$. If time of flight measurements are specified, the flight time is calculated from:

$$t_i = \frac{L_i W_i}{p_i c}, \tag{26}$$

where t_i is the flight time of particle i in nanoseconds, L_i is the flight path in inches, c = 11.802854 inches/nsec is the velocity of light. If the relative time between particles 2 and 3 is the quantity measured experimentally, the relative time is:

$$t_{rel} = t_3 - t_2. \tag{27}$$

The program lists $T_2, T_{3+}, T_{4+}, T_{3-}, T_{4-}, E_{23}, E_{13+}, E_{12+}, E_{13-}, E_{12-}, \theta_{3+}$ and ϕ_{3+} for a specified range of T_2 and also plots on the line printer all the other energy variables as functions of T_2, using the multi-variable high-density plotting routine GRAPHIC. For time measurements t_3 or t_{rel} is substituted for T_3.

Typical graphical output from the program is illustrated in Fig. 4.9-1 for the reaction ^{6}Li(d,pn). (W.J. Braithwaite and J.G. Cramer)

4.10 Zeros of the Reduced Rotation Matrix $d^j_{m',m}(\theta)$

The simplifications in the angular dependence of particle-gamma angular correlations which make possible straightforward measurements of nuclear polarization[1] and spin flip[2] in $2^+ \rightarrow 0^+$ transitions arise from the occurrence of zeros in d^2_{01} at 0°,90°, and 180° and in d^2_{21} at 0° and 180°. Similar simplifications in particle-alpha angular correlations have been exploited to measure nuclear polarization.[3]

The recent work on particle-conversion electron angular correlations described in Sec. 6.6 has brought about a renewed interest in the zeros of the rotation matrix, particularly for half-integer spins. We have generated polar plots of the rotation matrix elements of order 2 and smaller. These are shown in Fig. 4.10-1. We have also combined the previously written function subprogram DS for calculating rotation matrix elements by an extension of the method of Wills[4] with ROOT, a program for finding the real roots of an equation numerically, and have generated a table of the zeros of integer and half integer reduced rotation matrices. The results of this calculation, up to j = 8, are given in

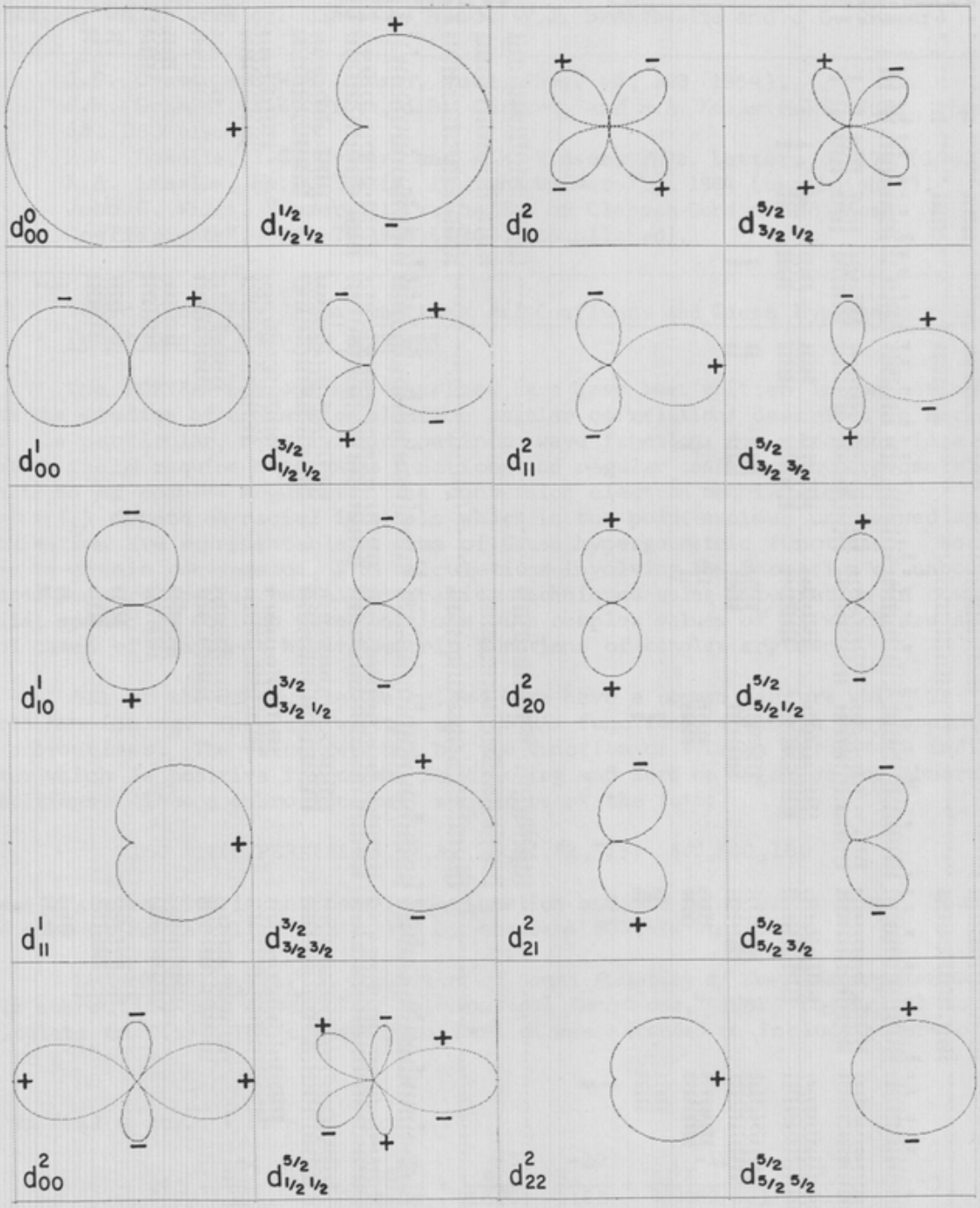

Fig. 4.10-1. Polar plots for the reduced rotation matrix elements $d^j_{m',m}$ of order $j = 2$ or less.

Table 4.10-1. Zeros of the Reduced Rotation Matrix $d^{j}_{m\sigma}(\theta)$

ZEROS OF THE REDUCED ROTATION MATRIX

J	MF	MI	ANGLES OF ZEROS					
0	0	0						
1/2	1/2	1/2	180.000					
1	0	0	90.000					
1	1	0	.000	180.000				
1	1	1	180.000					
3/2	1/2	1/2	70.529	180.000				
3/2	3/2	1/2	.000	180.000				
3/2	3/2	3/2	180.000					
2	0	0	54.736	125.264				
2	1	0	.000	90.000	180.000			
2	1	1	60.000	180.000				
2	2	0	.000	180.000				
2	2	1	.000	180.000				
2	2	2	180.000					
5/2	1/2	1/2	46.378	106.852	180.000			
5/2	3/2	1/2	.000	74.463	180.000			
5/2	3/2	3/2	53.130	180.000				
5/2	5/2	1/2	.000	180.000				
5/2	5/2	3/2	.000	180.000				
5/2	5/2	5/2	180.000					
3	0	0	39.231	90.000	140.768			
3	1	0	.000	63.435	116.565	180.000		
3	1	1	40.977	99.066	180.000			
3	2	0	.000	90.000	180.000			
3	2	1	.000	75.529	180.000			
3	2	2	48.190	180.000				
3	3	0	.000	180.000				
3	3	1	.000	180.000				
3	3	2	.000	180.000				
3	3	3	180.000					
7/2	1/2	1/2	34.631	79.568	125.122	180.000		
7/2	3/2	1/2	.000	56.844	105.141	180.000		
7/2	3/2	3/2	37.115	86.576	180.000			
7/2	5/2	1/2	.000	81.787	180.000			
7/2	5/2	3/2	.000	64.623	180.000			
7/2	5/2	5/2	44.415	180.000				
7/2	7/2	1/2	.000	180.000				
7/2	7/2	3/2	.000	180.000				
7/2	7/2	5/2	.000	180.000				
7/2	7/2	7/2	180.000					
4	0	0	30.556	70.124	109.876	149.444		
4	1	0	.000	49.107	90.000	130.893	180.000	
4	1	1	31.349	73.142	114.205	180.000		
4	2	0	.000	67.792	112.208	180.000		
4	2	1	.000	51.976	95.658	180.000		
4	2	2	34.175	80.057	180.000			
4	3	0	.000	90.000	180.000			
4	3	1	.000	75.523	180.000			
4	3	2	.000	60.000	180.000			
4	3	3	41.410	180.000				
4	4	0	.000	180.000				
4	4	1	.000	180.000				
4	4	2	.000	180.000				
4	4	3	.000	180.000				
4	4	4	180.000					
9/2	1/2	1/2	27.651	63.493	99.824	136.094	180.000	
9/2	3/2	1/2	.000	44.861	82.347	120.517	180.000	
9/2	3/2	3/2	28.654	66.570	105.871	180.000		
9/2	5/2	1/2	.000	62.453	103.901	180.000		
9/2	5/2	3/2	.000	48.190	90.000	180.000		
9/2	5/2	5/2	31.640	74.836	180.000			
9/2	7/2	1/2	.000	83.621	180.000			
9/2	7/2	3/2	.000	70.529	180.000			
9/2	7/2	5/2	.000	56.251	180.000			
9/2	7/2	7/2	38.942	180.000				
9/2	9/2	1/2	.000	180.000				
9/2	9/2	3/2	.000	180.000				
9/2	9/2	5/2	.000	180.000				
9/2	9/2	7/2	.000	180.000				
9/2	9/2	9/2	180.000					
5	0	0	25.017	57.420	90.000	122.579	154.983	
5	1	0	.000	40.088	73.427	106.573	139.912	180.000
5	1	1	25.445	58.480	91.954	126.278	180.000	
5	2	0	.000	54.736	90.000	125.264	180.000	
5	2	1	.000	41.564	76.500	113.437	180.000	
5	2	2	26.875	62.110	99.194	180.000		
5	3	0	.000	70.529	109.471	180.000		
5	3	1	.000	58.224	97.273	180.000		
5	3	2	.000	45.130	84.378	180.000		
5	3	3	29.926	70.529	180.000			
5	4	0	.000	90.000	180.000			
5	4	1	.000	78.463	180.000			
5	4	2	.000	66.422	180.000			
5	4	3	.000	53.130	180.000			
5	4	4	36.870	180.000				
5	5	0	.000	180.000				
5	5	1	.000	180.000				
5	5	2	.000	180.000				
5	5	3	.000	180.000				
5	5	4	.000	180.000				
5	5	5	180.000					
11/2	1/2	1/2	23.018	52.645	82.874	113.012	143.411	180.000
11/2	3/2	1/2	.000	37.127	68.069	98.996	130.600	180.000
11/2	3/2	3/2	23.495	54.510	85.889	118.493	180.000	
11/2	5/2	1/2	.000	50.987	84.004	117.462	180.000	
11/2	5/2	3/2	.000	38.985	71.737	105.865	180.000	
11/2	5/2	5/2	25.255	58.450	93.671	180.000		
11/2	7/2	1/2	.000	68.057	102.945	180.000		
11/2	7/2	3/2	.000	54.763	91.406	180.000		
11/2	7/2	5/2	.000	42.590	80.045	180.000		
11/2	7/2	7/2	28.322	64.864	180.000			
11/2	9/2	1/2	.000	84.784	180.000			
11/2	9/2	3/2	.000	74.173	180.000			
11/2	9/2	5/2	.000	62.964	180.000			
11/2	9/2	7/2	.000	50.479	180.000			
11/2	9/2	9/2	35.047	180.000				
11/2	11/2	1/2	.000	180.000				
11/2	11/2	3/2	.000	180.000				
11/2	11/2	5/2	.000	180.000				
11/2	11/2	7/2	.000	180.000				
11/2	11/2	9/2	.000	180.000				
11/2	11/2	11/2	180.000					
6	0	0	21.177	48.604	76.195	103.805	131.392	158.823
6	1	0	.000	33.878	62.040	90.000	117.960	146.122	180.000
6	1	1	21.433	49.229	77.276	105.565	134.596	180.000
6	2	0	.000	45.943	75.488	104.511	134.057	180.000
6	2	1	.000	34.743	63.760	92.917	123.113	180.000
6	2	2	22.264	51.260	80.919	112.069	180.000	
6	3	0	.000	58.518	90.000	121.482	180.000	
6	3	1	.000	47.925	79.110	111.041	180.000	
6	3	2	.000	36.702	67.781	100.364	180.000	
6	3	3	23.896	55.374	88.997	180.000		
6	4	0	.000	72.452	107.548	180.000		
6	4	1	.000	62.357	97.806	180.000		
6	4	2	.000	51.659	87.188	180.000		
6	4	3	.000	40.437	76.179	180.000		
6	4	4	26.950	63.773	180.000			
6	5	0	.000	90.000	180.000			
6	5	1	.000	80.456	180.000			
6	5	2	.000	70.529	180.000			
6	5	3	.000	60.000	180.000			
6	5	4	.000	48.190	180.000			
6	5	5	33.557	180.000				
6	6	0	.000	180.000				
6	6	1	.000	180.000				
6	6	2	.000	180.000				
6	6	3	.000	180.000				
6	6	4	.000	180.000				
6	6	5	.000	180.000				
6	6	6	180.000					

ZEROS OF THE REDUCED ROTATION MATRIX

J	MF	MI	ANGLES OF ZEROS					
13/2	1/2	1/2	19.718	45.264	70.972	96.739	122.579	148.637	180.000
13/2	3/2	1/2	.000	31.696	58.073	84.324	110.723	137.742	180.000
13/2	3/2	3/2	20.137	46.274	72.714	99.544	127.414	180.000
13/2	5/2	1/2	.000	43.215	71.001	98.488	126.801	180.000
13/2	5/2	3/2	.000	32.767	60.192	87.878	116.866	180.000
13/2	5/2	5/2	21.064	48.535	76.742	106.631	180.000
13/2	7/2	1/2	.000	55.200	85.052	115.226	180.000
13/2	7/2	3/2	.000	45.361	74.999	105.614	180.000
13/2	7/2	5/2	.000	34.836	64.423	95.663	180.000
13/2	7/2	7/2	22.736	52.741	84.971	180.000
13/2	9/2	1/2	.000	68.608	102.175	180.000
13/2	9/2	3/2	.000	59.226	92.872	180.000
13/2	9/2	5/2	.000	49.277	83.215	180.000
13/2	9/2	7/2	.000	38.582	72.930	180.000
13/2	9/2	9/2	25.761	61.053	180.000
13/2	11/2	1/2	.000	85.588	180.000
13/2	11/2	3/2	.000	76.658	180.000
13/2	11/2	5/2	.000	67.380	180.000
13/2	11/2	7/2	.000	57.421	180.000
13/2	11/2	9/2	.000	46.187	180.000
13/2	11/2	11/2	32.204	180.000
13/2	13/2	1/2	.000	180.000
13/2	13/2	3/2	.000	180.000
13/2	13/2	5/2	.000	180.000
13/2	13/2	7/2	.000	180.000
13/2	13/2	9/2	.000	180.000
13/2	13/2	11/2	.000	180.000
13/2	13/2	13/2	180.000
7	0	0	18.358	42.138	66.056	90.000	113.944	137.862	161.642
7	1	0	.000	29.336	53.722	77.919	102.081	126.278	150.664	180.000
7	1	1	18.524	42.534	66.726	91.036	115.554	140.674	180.000
7	2	0	.000	39.895	65.106	90.000	114.892	140.305	180.000
7	2	1	.000	29.890	54.793	79.644	104.773	130.844	180.000
7	2	2	19.051	43.799	68.893	94.481	121.360	180.000
7	3	0	.000	50.160	79.933	103.067	129.840	180.000
7	3	1	.000	40.890	67.249	93.450	120.736	180.000
7	3	2	.000	31.096	57.171	83.603	111.930	180.000
7	3	3	20.040	46.206	73.163	101.940	180.000
7	4	0	.000	61.289	90.000	118.710	180.000
7	4	1	.000	52.398	80.866	109.898	180.000
7	4	2	.000	42.173	71.441	100.939	180.000
7	4	3	.000	33.230	61.524	91.579	180.000
7	4	4	21.730	50.463	81.452	180.000
7	5	0	.000	73.898	106.102	180.000
7	5	1	.000	65.332	97.565	180.000
7	5	2	.000	56.530	88.858	180.000
7	5	3	.000	47.222	79.748	180.000
7	5	4	.000	36.962	69.890	180.090
7	5	5	24.716	58.656	180.000
7	6	0	.000	90.000	180.000
7	6	1	.000	81.787	180.000
7	6	2	.000	73.398	180.000
7	6	3	.000	64.623	180.000
7	6	4	.000	55.150	180.000
7	6	5	.000	44.415	180.000
7	6	6	31.003	180.000
7	7	0	.000	180.000
7	7	1	.000	180.000
7	7	2	.000	180.000
7	7	3	.000	180.000
7	7	4	.000	180.000
7	7	5	.000	180.000
7	7	6	.000	180.000
7	7	7	180.000
15/2	1/2	1/2	17.246	39.588	62.068	84.589	107.143	129.756	152.558	180.000
15/2	3/2	1/2	.000	27.664	50.669	73.528	96.415	119.466	143.071	180.000
15/2	3/2	3/2	17.524	40.250	63.179	86.263	109.719	134.063	180.000
15/2	5/2	1/2	.000	37.553	61.829	85.277	109.054	133.644	180.000
15/2	5/2	3/2	.000	28.362	52.021	75.669	99.744	124.640	180.000
15/2	5/2	5/2	18.124	41.686	65.827	90.148	116.143	180.000
15/2	7/2	1/2	.000	47.957	73.074	98.066	123.953	180.000
15/2	7/2	3/2	.000	38.908	64.046	89.142	115.517	180.000
15/2	7/2	5/2	.000	29.658	54.569	79.912	106.892	180.000
15/2	7/2	7/2	19.152	44.185	70.049	97.833	180.000
15/2	9/2	1/2	.000	58.324	85.765	113.490	180.000
15/2	9/2	3/2	.000	49.989	77.258	105.277	180.000
15/2	9/2	5/2	.000	41.275	68.424	96.851	180.000
15/2	9/2	7/2	.000	31.827	58.988	87.986	180.000
15/2	9/2	9/2	20.846	48.441	76.342	180.000
15/2	11/2	1/2	.000	70.529	101.537	180.000
15/2	11/2	3/2	.000	62.493	93.547	180.000
15/2	11/2	5/2	.000	54.175	85.333	180.000
15/2	11/2	7/2	.000	45.328	76.686	180.000
15/2	11/2	9/2	.000	35.530	67.282	180.000
15/2	11/2	11/2	23.789	56.521	180.000
15/2	13/2	1/2	.000	86.177	180.000
15/2	13/2	3/2	.000	78.463	180.000
15/2	13/2	5/2	.000	70.529	180.000
15/2	13/2	7/2	.000	62.182	180.000
15/2	13/2	9/2	.000	53.130	180.000
15/2	13/2	11/2	.000	42.833	180.000
15/2	13/2	13/2	29.926	180.000
15/2	15/2	1/2	.000	180.000
15/2	15/2	3/2	.000	180.000
15/2	15/2	5/2	.000	180.000
15/2	15/2	7/2	.000	180.000
15/2	15/2	9/2	.000	180.000
15/2	15/2	11/2	.000	180.000
15/2	15/2	13/2	.000	180.000
15/2	15/2	15/2	180.000
8	0	0	16.801	37.187	58.296	79.430	100.570	121.704	142.813	163.799
8	1	0	.000	25.874	47.378	68.708	90.000	111.292	132.624	154.126	180.000
8	1	1	16.915	37.456	58.742	80.095	101.539	123.164	145.322	180.000
8	2	0	.000	34.931	57.275	79.124	100.876	122.725	145.069	180.000
8	2	1	.000	26.247	48.091	69.828	91.653	113.781	136.711	180.000
8	2	2	16.970	38.301	60.154	82.233	104.744	128.394	180.000
8	3	0	.000	43.995	67.339	90.000	112.661	136.005	180.000
8	3	1	.000	35.776	58.865	81.256	104.089	127.984	180.000
8	3	2	.000	27.048	49.635	72.284	95.407	119.491	180.000
8	3	3	17.320	39.853	62.794	86.378	111.575	180.000
8	4	0	.000	53.316	78.017	101.983	126.684	180.000
8	4	1	.000	45.396	69.758	93.762	118.855	180.000
8	4	2	.000	37.191	61.268	85.397	110.952	180.000
8	4	3	.000	28.403	52.295	76.679	102.805	180.000
8	4	4	18.373	42.409	67.307	94.196	180.000
8	5	0	.000	63.435	90.000	116.565	180.000
8	5	1	.000	55.762	82.131	108.938	180.000
8	5	2	.000	47.688	74.105	101.213	180.000
8	5	3	.000	39.609	65.733	93.233	180.000
8	5	4	.000	30.589	56.744	84.791	180.000
8	5	5	20.063	46.852	75.346	180.000
8	6	0	.000	75.037	104.963	180.000
8	6	1	.000	67.594	97.537	180.000
8	6	2	.000	60.000	90.000	180.000
8	6	3	.000	52.095	82.204	180.000
8	6	4	.000	43.647	73.955	180.000
8	6	5	.000	34.283	64.944	180.000
8	6	6	22.959	54.604	180.000
8	7	0	.000	90.000	180.000
8	7	1	.000	82.819	180.000
8	7	2	.000	75.522	180.000
8	7	3	.000	67.976	180.000
8	7	4	.000	60.000	180.000
8	7	5	.000	51.318	180.000
8	7	6	.000	41.410	180.000
8	7	7	28.955	180.000
8	8	0	.000	180.000
8	8	1	.000	180.000
8	8	2	.000	180.000
8	8	3	.000	180.000
8	8	4	.000	180.000
8	8	5	.000	180.000
8	8	6	.000	180.000
8	8	7	.000	180.000
8	8	8	180.000

Table 4.10-1. These values are in good agreement with those seen in Table A.5 of Ref. 1, which were calculated by hand. (W.J. Braithwaite and J.G. Cramer)

1. J.G. Cramer and W.W. Eidson, Nucl. Phys. *55*, 593 (1964).
2. F.H. Schmidt, R.E. Brown, J.B. Gerhart, and W.A. Kolasinski, Nucl. Phys. *52*, 353 (1964).
3. R.A. Lasalle, J.G. Cramer, and W.W. Eidson, Phys. Letters *5*, 170 (1963); R.A. Lasalle, Ph.D. Thesis, Indiana University, 1964 (unpublished).
4. John G. Wills, "Numerical Evaluation of Clebsch-Gordon and Racah Coefficients", ORNL-TM-1949 (1967)(unpublished).

4.11 Subroutines for Gamma Functions and Confluent and Gauss Hypergeometric Functions of Complex Argument

The FORTRAN subroutines described here have been written in connection with the studies of conversion electron angular correlations described in Sec. 6.6. In particular, relativistic continuum wave functions for electrons in a Coulomb field require both gamma functions and regular confluent hypergeometric functions of complex argument.[1] The conversion electron matrix elements $\langle j_f|L\pi|j_i\rangle$ depend on radial integrals which in the point-nucleus unscreened approximation are representable as sums of Gauss hypergeometric functions.[2] Moreover to obtain convergence, DWBA calculations involving the formation of unbound states require special radial integration techniques using integration in complex radial space[3] of Coulomb wave functions with complex values of ρ, which are special cases of confluent hypergeometric functions of complex argument.

All of the subroutines described here have a common feature which is worth mentioning. They are written as FORTRAN functions, although they operate as subroutines. The value returned by the function call is an error test indicator which is positive for normal functioning and zero or negative for abnormal conditions. Thus a subroutine call should be of the form:

```
150  IF(HYPERM(AR,AI,BR,BI,ZR,ZI,FR,FI))  500,500,160
```

where statement 160 is the normal continuation and 500 is an error trap. Thus the subroutine is called and tested by the same FORTRAN statement.

LGAMMA(ZR,ZI,FR,FI): *Logarithm of Gamma Function of Complex Argument.* This subroutine uses *Handbook of Mathematical Functions*,[4] (HMF) Eq. 6.1.41 to calculate $\ln \Gamma(z)$. The series approximation was extended to include powers of z up to z^{-14}:

$$\ln \Gamma(z) = \ln\sqrt{2\pi} + (z - \tfrac{1}{2}) \ln z - z\left(1 - \frac{z^{-2}}{12} + \frac{z^{-4}}{360} - \frac{z^{-6}}{1260} + \frac{z^{-8}}{1680} - \frac{z^{-10}}{1188} + \frac{z^{-12}}{360360/691} - \frac{z^{-14}}{156} + \cdots\right). \quad (1)$$

A test is made to determine if $|z|^2 > 100$. If so, the series is used directly. If not, the recursion relation

$$\Gamma(z) = \frac{1}{z}\,\Gamma(z+1) \tag{2}$$

is used to recur z upward until the condition on $|z|^2$ is satisfied. The subroutine does complex arithmetic explicitly rather than using the complex arithmetic features of FORTRAN IV so that the code may be used on machines for which FORTRAN IV complex arithmetic is not available.

The logarithm of $\Gamma(z)$ is evaluated rather than $\Gamma(z)$ itself because the logarithm series goes in powers of z^{-2} rather than z^{-1}, and because $\Gamma(z)$ becomes large very rapidly with increasing z. Usually the quantity of interest is a ratio of gamma functions, and computer word overflows can be avoided by taking the difference of $\ell n\,\Gamma$ before exponentiation, i.e.,

$$\frac{\Gamma(z_1)}{\Gamma(z_2)} = \mathrm{EXP}(\ell n\,\Gamma(z_1) - \ell n\,\Gamma(z_2)). \tag{3}$$

HYPER M(AR,AI,BR,BI,ZR,ZI,FR,FI): *Regular Confluent Hypergeometric Function of Complex Arguments.* This subroutine uses HMF Eq. 13.1.2 as the basic power series in z for calculating the function:

$$M(a,b,z) = 1 + \frac{a}{b}\frac{z}{1!} + \frac{a(a+1)}{b(b+1)}\frac{z^2}{2!} + \frac{a(a+1)(a+2)}{b(b+1)(b+2)}\frac{z^3}{3!} + \cdots. \tag{4}$$

However, for *Re*(2a) > *Re*(b) or for $|z| > 30$ convergence of this series is poor, and transformations must be employed. For *Re*(2a) > *Re*(b) we use HMF Eq. 13.1.27:

$$M(a,b,z) = e^{z}M(b-a,b,-z), \tag{5}$$

which makes $2Re(a') = 2Re(b-a) < Re(b')$ and so puts the parameters in a more favorable region for convergence.

For $|z| > 30$ the transformation to U(a,b,z), the irregular confluent hypergeometric functions (see (6) below) which converge better for large $|z|$. From HMF Eqns. 13.1.3,13.1.9, and 6.1.17 we obtain:

$$M(a,b,z) = \frac{\Gamma(b)\,U(a,b,z)}{e^{i\pi a}\,\Gamma(b-a)} + \frac{\Gamma(b)\,U(b-a,b,ze^{i\pi})}{e^{i\pi(a-b)-z}\,\Gamma(a)}\,. \tag{6}$$

For special cases of poles or simplifications, e.g., n = integer, M(a,-n,z) = pole, M(a,b,0) = 1, M(0,b,z) = 1, $M(a,a,z) = e^{z}$, etc., special evaluation procedures are used.

HYPER U(AR,AI,BR,BI,ZR,ZI,FR,FI): *Irregular Confluent Hypergeometric Function of Complex Argument.* This subroutine uses HMF, Eq. 13.5.2 as the basic power series in (- 1/z) for calculating the function:

$$U(a,b,z) = z^{-a}\left[1 + \frac{(a)(a+1-b)}{1!\,(-z)} + \frac{a(a+1)(a+1-b)(a+2-b)}{2!\,(-z)^2}\right.$$

$$\left. + \frac{a(a+1)(a+2)(a+1-b)(a+2-b)(a+3-b)}{3!\,(-z)^3} + \cdots\right]. \quad (7)$$

However, for *Re*(b) > 1 or for |z| < 30 convergence of this series is poor and transformations must be employed. For *Re*(b) > 1 we use HMF Eq. 13.1.29:

$$U(a,b,z) = z^{1-b}\, U(a+1-b,2-b,z) \quad (8)$$

which makes *Re*(b') = *Re*(2 - b) < 1 and so improves the convergence of the series.

For |z| < 30 we use the transformation to the regular confluent hypergeometric function M(a,b,z) discussed above, which converges well for small |z|. From HMF Eqs. 13.1.3 and 6.1.17 we obtain:

$$U(a,b,z) = \frac{\Gamma(1-b)\, M(a,b,z)}{\Gamma(a+1-b)} - \frac{\Gamma(b-1)\, M(a+1-b,2-b,z)}{z^{1-b}\,\Gamma(a)}. \quad (9)$$

For special cases of poles and special values, e.g., U(a,b,0) = pole, U(0,b,z) = 1, U(a,a + 1,z) = 1, etc., special evaluation procedures are used.

HYPER F(AR,AI,BR,BI,CR,CI,ZR,ZI,FR,FI): *Gauss Hypergeometric Function of Complex Arguments.* This subroutine uses HMF Eq. 15.1.1 as the basic power series in z for calculating the function:

$$F(a,b;c;z) = 1 + \frac{ab}{c}\frac{z}{1!} + \frac{a(a+1)b(b+1)}{c(c+1)}\frac{z^2}{2!} + \frac{a(a+1)(a+2)b(b+1)(b+2)}{c(c+1)(c+2)}\frac{z^3}{3!} + \cdots. \quad (10)$$

However, the series diverges for *Re*(a + b) ≥ *Re*(c + 1) and for |z| > 1, and is only conditionally convergent for *Re*(c) ≤ *Re*(a + b) < *Re*(c + 1) and transformations must be employed.

For *Re*(a + b) ≥ *Re*(c + 1) we use HMF Eq. 15.3.3:

$$F(a,b;c;z) = (1-z)^{c-b-a}\, F(c-a,c-b;c;z) \quad (11)$$

which makes *Re*(c) > *Re*(a' + b') if *Re*(c) < *Re*(a + b) and so puts the arguments

in the convergent region.

For $Re(c) \leq Re(a + b) < Re(c + 1)$ we must recur upward in c using HMF Eq. 15.2.12:

$$F(a,b;c;z) = \frac{c - z(2c + 1 - a - b)}{(1 - z)c} F(a,b;c + 1;z) + \frac{z(c + 1 - a)(c + 1 - b)}{(1 - z)c(c + 1)} F(a,b;c + 2;z) \tag{12}$$

which insures that $Re(c') > Re(a + b)$.

For $|z| > 1$ we must use the reciprocal transformation, HMF Eq. 15.3.7:

$$F(a,b;c;z) = \frac{\Gamma(c)\,\Gamma(b - a)}{\Gamma(b)\,\Gamma(c - a)} (-z)^{a} F(a,a + 1 - c;a + 1 - b;\tfrac{1}{z}) + \frac{\Gamma(c)\,\Gamma(a - b)}{\Gamma(a)\,\Gamma(c - b)} F(b + 1 - c,b;b + 1 - a,\tfrac{1}{z}) \tag{13}$$

which puts z in a convergent region. Note that this transformation does not alter the quantity (a + b - c).

Special cases are handled by special evaluation procedures, e.g.,

$$F(a,b,c,1) = \frac{\Gamma(c)\,\Gamma(c - a - b)}{\Gamma(c - a)\,\Gamma(c - b)}, \quad F(a,b;b;z) = 1 - z)^{-a}, \text{ etc.} \tag{14}$$

Testing. The testing of these subroutines have thus far been confined to reproducing tabulations, and to consistency checks. In particular, HMF Table 13.1 has been reproduced, using HYPER M. However more stringent testing procedures are necessary. A program now being prepared will accomplish this by generating random complex arguments in specified regions and testing to make sure that selected recurrence relations and sum rules are satisfied. This, it is hoped, will solve the problem of testing mathematical function subroutines in many-dimensional parameter spaces. (J.G. Cramer)

---

1. M.E. Rose, Phys. Rev. *51*, 484 (1937).
2. M.E. Rose, G.H. Goertzel, B.I. Spinrad, J. Harr, and P. Strong, Phys. Rev. *83*, 79 (1951).
3. R. Huby and J.R. Mines, Rev. Mod. Phys. *37*, 406 (1965); T. Fortune (private communication).
4. *Handbook of Mathematical Functions,* National Bureau of Standards Applied Mathematics Series, *55*(M. Abrahamowitz and I.A. Stegun, Editors) U.S. Government Printing Office, Washington, D.C. (1964).

---

5. LIGHT NUCLEUS STUDIES

5.1 Proton-Proton Bremsstrahlung at 20 MeV

The proton-proton bremsstrahlung (PPB) experiment described in last year's Annual Report[1] has been finished. We used the experimental techniques described in that report to take additional data with outgoing proton angles near 25° on either side of the beam. We also measured the cross section for outgoing proton angles near 30°. The resulting values for $d\sigma/d\Omega_1 d\Omega_2$, averaged over the angular acceptances of the counters, are .60 ± .06 μb/sr^2 for both protons at 25° and .61 ± .07 μb/sr^2 for both protons at 30°. After folding in an estimate for the azimuthal angular dependence of the cross section (based on the calculations of Drechsel and Maximon[2]), we determined coplanar cross sections of .68 ± .07 μb/sr^2 and .69 ± .07 μb/sr^2 for those two cases, respectively. These values are consistent with published theoretical calculations[2] which use various proton-proton potentials to calculate the PPB cross section.

We will describe the experimental techniques only briefly, as they have been reported elsewhere.[1,3] The gas target was designed to prevent particles multiply scattered in the entrance foil from hitting the front slits of the counter system; such particles can scatter into the counters, creating a background of the same energy as PPB protons. Each of the two counters consisted of three detectors. The PPB protons stopped in the second, while the third stopped the elastically scattered protons. A fast anticoincidence was formed between the signals from the second and third detector, so an output would result only from particles not entering the third counter. This anticoincidence output started or stopped a TAC. The high count rate (2.5×10^4 counts/sec) of elastically scattered protons would cause distortion in the linear amplifiers; consequently we canceled the analog signals from the first two detectors with the signal from the third, thereby maintaining good energy resolution ($\sim$ 75 keV) in spite of the high count rate.

The TAC signal and the signals from the first two detectors (with the elastic proton signals canceled) in each counter were fed into the SDS 930 computer for each coincidence. Using the computer we were able to identify the product of the mass and the square of the charge for each particle, from the energies in the two detectors of each counter. About half the events were eliminated because at least one particle was not a proton leaving all its energy in the first two counters. With the computer we also were able to correct the TAC output for energy dependent time walk and were able to obtain about 5 nsec coincidence resolving times, instead of the 20 nsec obtained before time walk correction.

We had three successful runs this year, with most of the emphasis on obtaining data at equal proton angles of 25 deg. Due to a malfunction of the automatic counter angle readout on the 60 in. scattering chamber, one of the runs had one counter at 27.50° while the other was at 25°. Since theoretical predictions[2] indicate that the cross section should not change rapidly with proton angle, we have included the data from this run with the other data taken with both counters at 25°. The combined data gives us 183 counts (after subtraction of accidental coincidences) for the 25° case and 97 counts for 30°. In the first

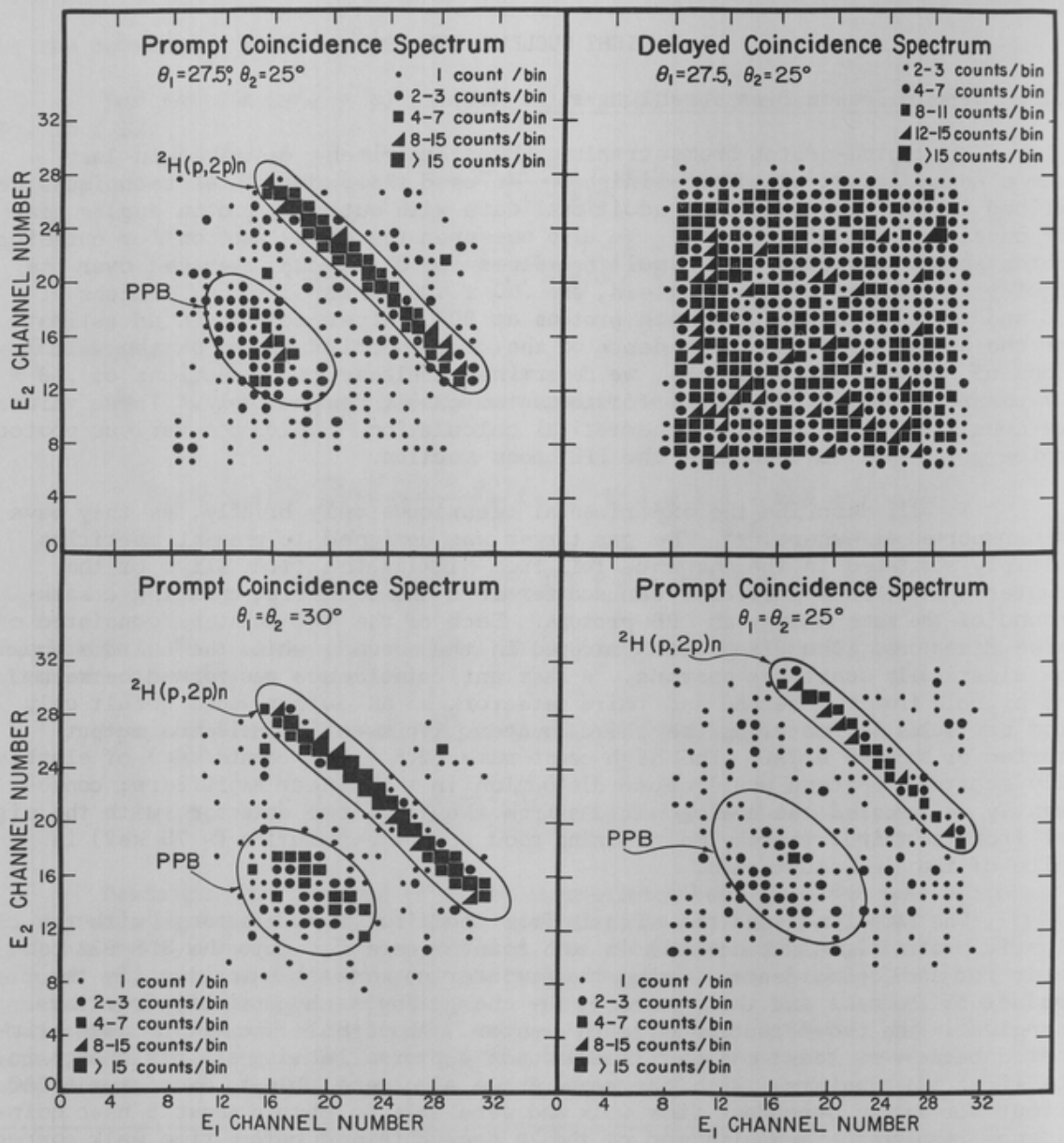

Fig. 5.1-1. Some raw spectra. Each spectrum shown is the result of an entire run. The top two panels show spectra of corresponding prompt and delayed coincidence spectra. The bottom panels show prompt coincidence spectra. In all the prompt spectra the events from PPB as well as from $^2H(p,2p)n$ show clearly above the background, which is almost entirely due to accidental coincidences. The delayed coincidence spectrum is typical, and it shows that the accidental background varies slowly with the energy of the detected protons.

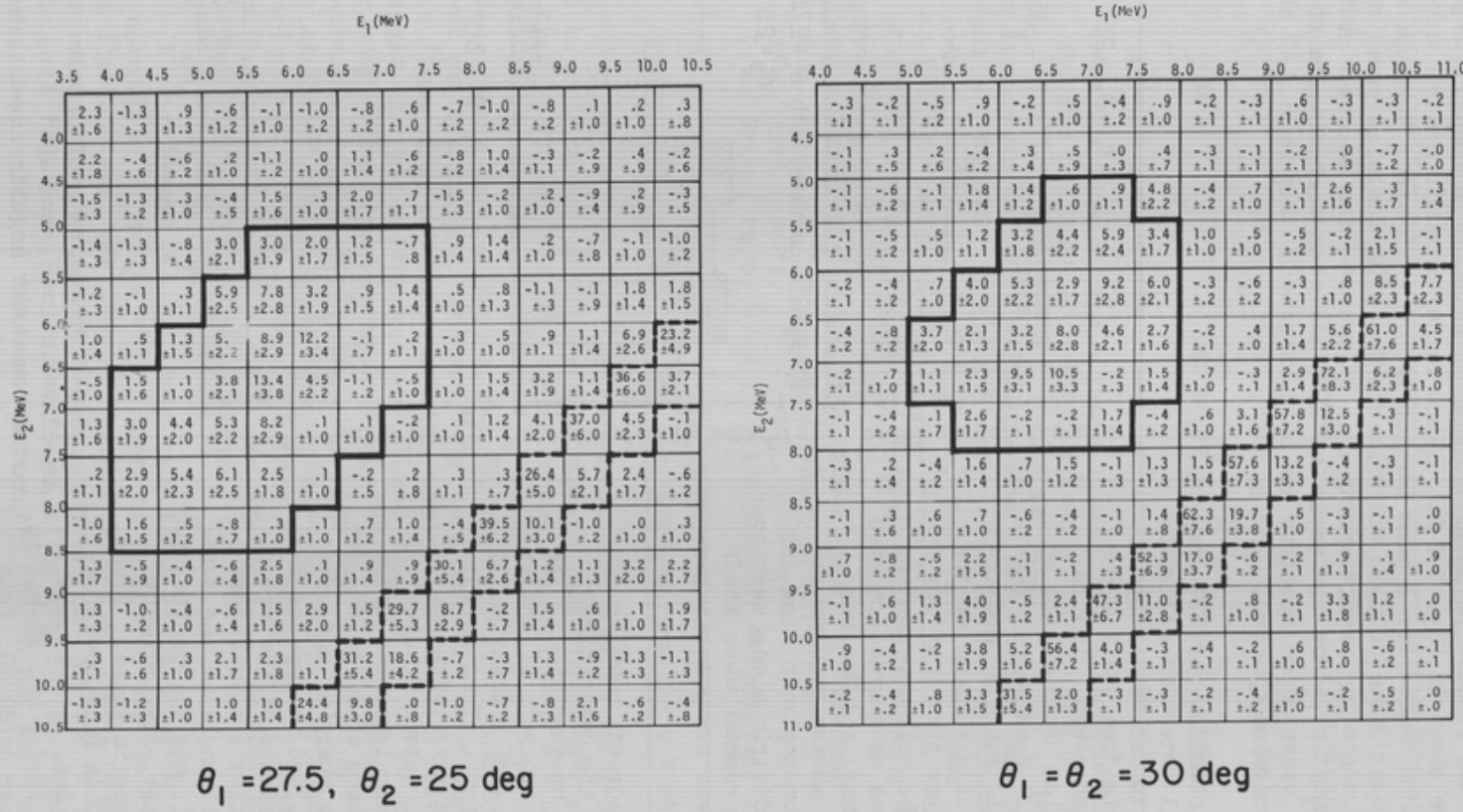

Fig. 5.1-2. Rehistogrammed spectra with accidental coincidence background subtracted and with statistical uncertainties. The spectra are from the runs at $\theta_1 = \theta_2 = 30$ deg and at $\theta_1 = 27.5$ and $\theta_2 = 25.0$ deg. The PPB regions are outlined by heavy, solid lines. The regions for events from the ^{2}He(p,2p)n reaction are outlined by heavy dashed lines. The number of counts per bin is given.

case the overall true-to-accidental ratio was about 1, while in the second case it was about 11 (primarily because of lower singles background in the PPB region). Some raw spectra are shown in Fig. 5.1-1. Since the electronic system accepted accidental coincidence events for a much longer period (∿75 nsec) than prompt coincidence events (∿5 nsec), the delayed coincidence spectrum contains many more counts than the corresponding prompt spectrum. Of course, the delayed coincidence spectrum had to be multiplied by the ratio of time acceptance intervals to determine the accidental coincidence spectrum to be subtracted. Figure 5.1-2 shows resulting true coincidence spectra.

From the kinematics for PPB and from the geometrical detection efficiencies, we were able to determine the probable photon angle from the two proton energies for each event. The resulting photon angular distribution appears in Fig. 5.1-3. Because our counters accepted the full range of non-coplanarity kinematically allowed to the protons, these angular distributions do not correspond to the coplanar photon angular distributions usually calculated by theorists. Drechsel and Maximon[2] have calculated the photon angular distribution for the non-coplanar case, and our photon angular distributions seem to be in qualitative agreement with their results, averaged over our counter geometry.[3]

The most important results of this experiment are the quantities $d\sigma/d\Omega_1 d\Omega_2$, obtained by summing all the counts obtained at each pair of angles within the energy region kinematically allowed for PPB protons. This result also represents an average over the counters' angular acceptances. Drechsel and Maximon[2] have calculated the azimuthal angular dependence of $d\sigma/d\Omega_1 d\Omega_2$ for a number of incident energies and outgoing proton angles, and it appears that the functional dependence of the cross section on the quantity ϕ/ϕ_{max} (where ϕ_{max} is the azimuthal angle of the maximum kinematically allowed non-coplanarity) varies very little with incident energy or outgoing proton angle. Since they had not given this functional dependence for the 25-deg, 20-MeV case, we used their form for 30-deg and 30-MeV to determine the coplanar $d\sigma/d\Omega_1 d\Omega_2$ from

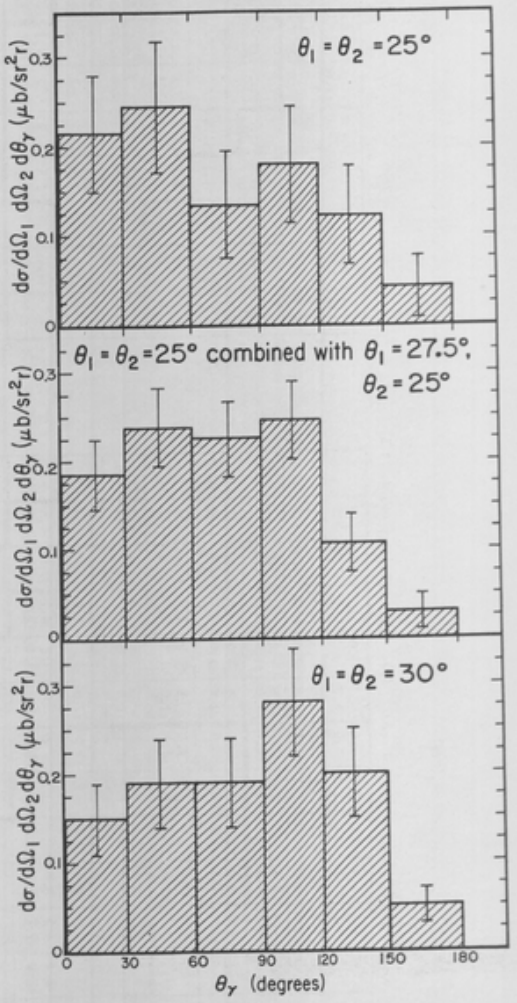

Fig. 5.1-3. Histograms of photon angular distributions, averaged over the proton counters' angular acceptance, for the pairs of angles indicated.

our measured average value. There is about a 10% correction necessary and the average and coplanar values appear in Table 5.1-1.

Table 5.1-1. Values of $d\sigma/d\Omega_1 d\Omega_2$

Proton Angles	$d\sigma/d\Omega_1 d\Omega_2$	$(d\sigma/d\Omega_1 d\Omega_2)_{coplanar}$
25°	.60 ± .06 μb/sr^2	.68 ± .07 μb/sr^2
30°	.61 ± .07 μb/sr^2	.69 ± .07 μb/sr^2

The 30° value agrees with .75 μb/sr, the value determined from graphs of Ref. 2. On the basis of an extrapolation of the results of Ref. 2 we expect $d\sigma/d\Omega_1 d\Omega_2$, for both protons at 25°, to be between .5 and .6 μb/sr^2 (although Maximon is presently calculating the cross section for that case). We thus find both results consistent with available potential model calculations.
(D.R. Brown, I. Halpern, R.H. Heffner, K.G. Nair, P.A. Russo, and D.W. Storm)

1. Nuclear Physics Laboratory Annual Report, University of Washington (1969), p. 1.
2. V.R. Brown, Phys. Rev. *177*, 1498 (1969); D. Drechsel and L.C. Maximon, Ann. Phys. (N.Y.) *49*, 403 (1968); D. Marker and P. Signell, Phys. Rev. *185*, 1286 (1969).
3. D.W. Storm, Ph.D. Thesis, University of Washington, 1970 (unpublished).

5.2 Search for a State in ^{3}He via the Reaction d + p → d* + p

There has been considerable work done looking for evidence of excited states in the three-nucleon system; however, no states have yet been definitely identified. Niiler *et al.*[1] have reported a measurement of the excitation function for the reaction d + p → d* + p (where d* is a p-n system of small relative energy). Their results show a bump in the excitation function at about 10.5 MeV incident proton energy, correspondkng to a possible resonance at 12.5 MeV excitation in ^{3}He. They have measured the excitation function only for one angle, and that angle did not correspond to a fixed c.m. angle for the outgoing d*, but rather was a fixed d* laboratory angle of 30 deg. Consequently, we have measured the excitation function for this reaction from 7 to 14.5 MeV incident proton energy at two angles. In this experiment the laboratory angle of each detector was varied with incident energy so that the outgoing p-n system, with zero relative energy, would be at 30 or 90 deg in the c.m. We find no structure in the excitation functions for either angle.

Since the d* + p system in the final state consists of three particles, it is necessary to detect two of them to determine all the kinematical variables of the final state. We detected both protons, at angles chosen to include the case of zero relative energy between the neutron and one of the protons. The kinematical relationships in the final state can be understood readily by considering the center of mass system for the proton and neutron that comprise the

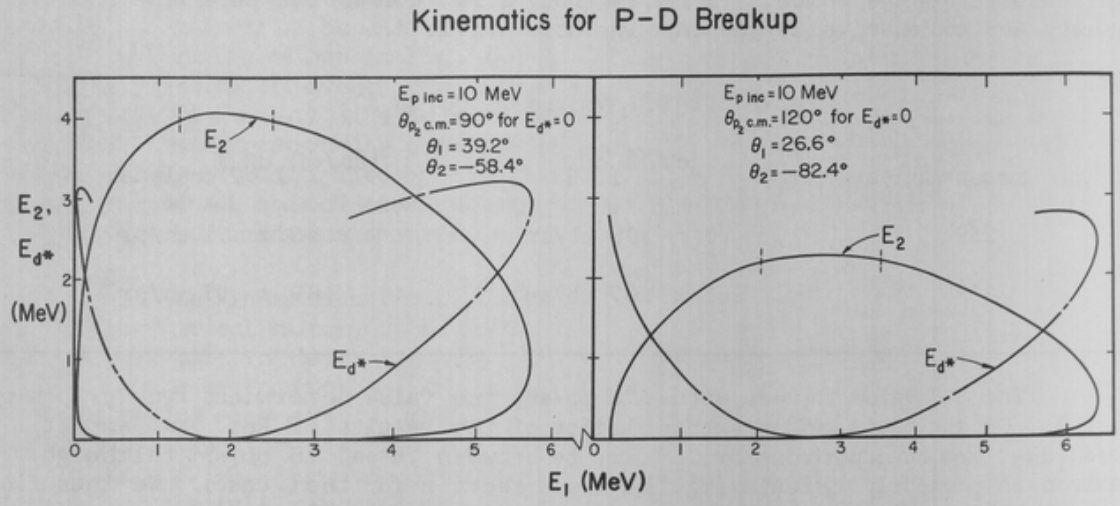

Fig. 5.2-1. Kinematics for p-d breakup at proton angles chosen to include d*'s in the final state. The subscripts 1 and 2 refer to the proton coming from the d* and the other proton in the final state, respectively. The vertical marks on the E_1-E_2 curve indicate the points corresponding to d* excitations for 100 keV.

d*. If we consider the d*'s with zero to a few hundred keV excitation energy to be leaving the reaction at an angle θ_{d*}, then the recoil proton angle θ_2 is fairly well defined. (For any particular excitation of the d*, θ_2 is defined exactly, and it changes slowly over a few hundred keV range of d* excitation when the incident proton energy is several MeV.) If we detect the scattered proton at θ_2 and then place a second counter at θ_{d*}, we can simultaneously detect in it the proton which comes from the decay of the zero excitation d*. However, for non-zero d* excitation, the proton from the d* need not be at θ_{d*}, but is constrained to lie within a cone centered along the direction of motion of the d*'s c.m. system. The tangent of the angle at the apex of the cone is equal to the velocity of the proton in the d*'s c.m. system, divided by the velocity of the d* in the lab system. Thus, as the incident energy is increased, the d* lab energy is increased and for given d* excitation the cone in which the d*'s proton must lie becomes narrower. The kinematic loci for the proton energies E_1 and E_2 are shown in Fig. 5.2-1, along with the d* excitation energy. E_1 is the energy of the proton from the d*, E_2 is the energy of the other proton.

The data show a strong enhancement for pairs of proton energies corresponding to d*'s of low (less than 200 keV) excitation energy. To determine the excitation function for the production of d*'s, one must subtract the background due to other three body breakup processes, one must set a limit on the relative excitation energy of the p-n system that is to be considered a d*, and one must correct for the losses of d* protons if the d*'s proton detector is smaller than the cone allowed to these protons. Niiler *et al.* have carried out these procedures, and report an apparent resonance in the excitation function. Since the three-body breakup background in the energy region corresponding to the d* is

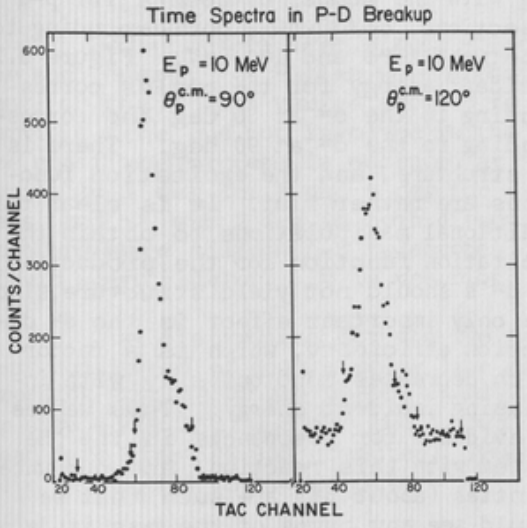

Fig. 5.2-2. Time spectra from the two sets of proton angles corresponding to c.m. d* angles of 90 and 30 deg, or, equivalently, proton number 2 c.m. angles of 90 or 120 deg. The small arrows indicate the acceptance intervals used to determine prompt and accidental coincidences.

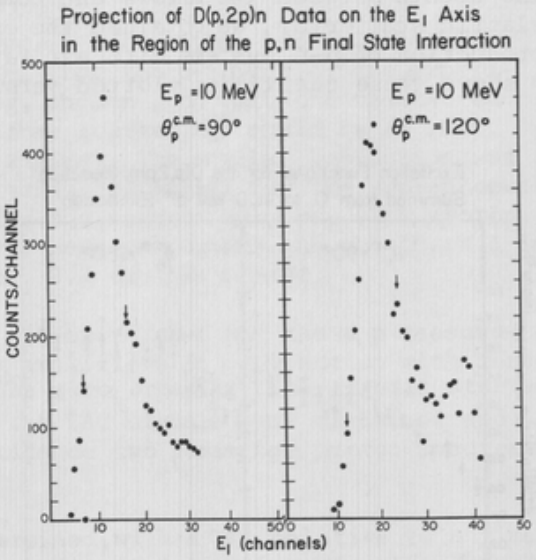

Fig. 5.2-3. E_1 spectra for the two sets of proton angles. The small arrows indicate excitation of 100 keV in the d* system.

small, and since the geometrical efficiency correction factor is monotonically decreasing with increasing incident energy, any resonances should appear as bumps in the data before these corrections are made.

In the present experiment a deuterated polyethylene target was bombarded with protons from the Van de Graaff accelerator. The outgoing protons were detected in two Si(Li) detectors. These were set at angles corresponding to outgoing d* c.m. angles of 30 and 90 deg. Time signals corresponding to the zero crossing of doubly differentiated pulses started or stopped a time-to-amplitude converter (TAC). The two energy signals and the TAC signal were digitized and read into the SDS 930 computer. Using the computer, we were able to vary the acceptable TAC values corresponding to prompt coincidences to suit the appropriate energy region and thus were able to obtain time resolutions of about 20 nsec for the events of interest. This resolving time was adequate to eliminate most accidental coincidence background. Figure 5.2-2 shows typical time spectra taken from the E_1-E_2 region corresponding to the d*.

Typical energy spectra appear in Fig. 5.2-3. We have projected the appropriate region of the two dimensional energy spectra onto the E_1 axis. The effect of the p-n dinal state interaction enhancement is apparent in the peak. The peak center corresponds very nearly to zero d* excitation energy, and the

arrows indicate the E_1 corresponding to d* excitations of 100 keV. By summing the counts between the arrows and comparing with the number of counts for p-d elastic scattering, we obtained the cross sections, $d\sigma/d\Omega_1 d\Omega_2$, corresponding to production of p-n systems with excitation between zero and 100 keV. Figure 5.2-4 shows these quantities plotted versus incident energy for the angles corresponding to the d* at 30 deg and corresponding to the d* at 90 deg. There is no structure, and the excitation functions are rather flat. It is clear that additional manipulations to obtain the excitation function for the production of d*'s should not yield structure, since the only important effect is the d* detection efficiency, which is a factor which decreases monotonically with increasing incident energy. Thus we see no evidence for resonances in the ^{3}He system with this reaction, and our uncertainties (about 5%) are such that we should see any bumps of the magnitude of those reported[1] from the experiment at a d* lab angle of 30 deg.

(W.J. Braithwaite, J.M. Cameron, D.W. Storm, and T. Tombrello)

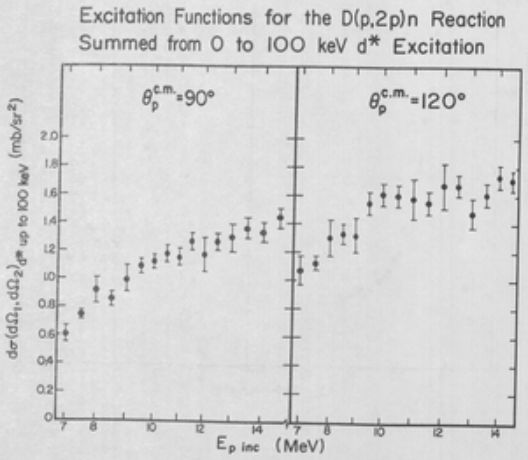

Fig. 5.2-4. Excitation functions for c.m. cross sections, $d\sigma/d\Omega_1 d\Omega_2$, corresponding to d*'s of excitation up to 100 keV. There is no evidence of structure in these excitation functions.

1. A. Niiler, W. von Witsch, and G.C. Phillips, Bull. Am. Phys. Soc. *13*, 1652 (1968).

5.3 Quasifree Scattering in the p + d → p + p + n Reaction

We have undertaken a study of the energy dependence of the quasifree scattering of an incident proton by one of the nucleons in the deuteron in conjunction with a group from UCLA.[1] Our work includes p-p and p-n quasifree scattering at incident proton energies of 11,14,17,20, and 23 MeV. The UCLA group has studied p-p quasifree scattering at 36, 41, and 46 MeV. The experimental techniques are similar; we will only report on the details of the experiment at this laboratory. We have attempted to fit the data with an expression for quasifree scattering:

$$\frac{d\sigma}{d\Omega_1 d\Omega_2 dE_1} = |\phi(q_n)|^2 \, (d\sigma/d\Omega)_{free} \times (\text{phase space factor}). \qquad (1)$$

In this formula $\phi(q_n)$ is the momentum wave function for the neutron in the deuteron, as determined from the parameterization of the Hulthén wave function, and $(d\sigma/d\Omega)_{free}$ is the free nucleon-nucleon scattering cross section at the same momentum transfer and c.m. energy as those of the two nucleons in the final

state.

Two counters were placed at equal angles θ on either side of the beam. For each energy the angles were either 43 deg (for the p-p part of the experiment) or the angles varied from 38 to 43 deg, chosen such that the undetected particle (the one not involved in the quasifree scattering) could be at rest. The quasifree process is enhanced at these angles. The angular resolution was typically 1 deg for θ and 4 deg for φ (the azimuthal angle) for the proton counters, and it was 2 deg in both directions for the neutron counter. The proton counters were silicon Δ-E telescopes, and the neutron counter was a 5 in. × 1 in. liquid scintillator. It is described in Sec. 3.6 of this report.

The electronics for the two proton detectors used for the p-p measurement consisted of double delay line shaping amplifiers in conjunction with zero crossing timing single channel analyzers. The zero crossing time signals started or stopped a TAC, and the two Δ, two E and the TAC signals were digitized and read into the SDS 930 computer. True coincidence two parameter proton spectra were extracted in the computer.

The neutron time-of-flight was determined, with a TAC, relative to a time signal derived from the leading edge of the proton's Δ detector signal. This TAC signal, the proton's Δ and E signals, the neutron scintillator pulse height signal, and a signal derived from a pulse shape discrimination neutron-gamma separation system (see Sec. 3.6) were digitized and read into the computer. Two-parameter spectra for neutron time-of-flight versus proton energy were extracted in the computer.

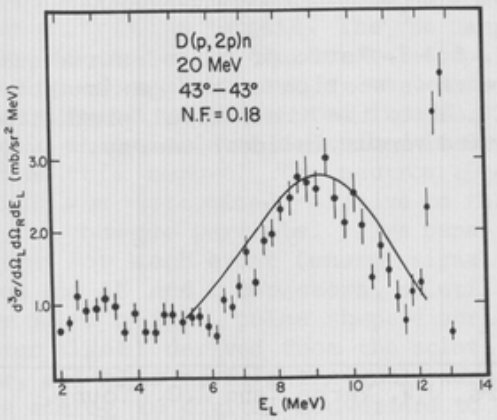

Fig. 5.3-1. Projected spectra for d+p→p+p+n for quasifree p-p scattering at 20 MeV incident energy, along with theoretical peak shape.

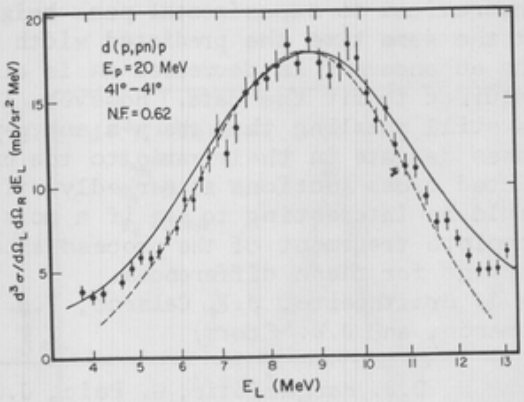

Fig. 5.3-2. Projected spectra for d+p→p+p+n fpr quasifree p-n scattering at 20 MeV incident energy, along with theoretical peak shapes. The solid curve results from the calculation with no cutoff radius. The dashed curve corresponds to a cutoff of 4.5 Fm.

By projecting the appropriate (corresponding to p-d breakup) region of the two parameter spectra on a proton energy axis, we obtained spectra such as shown in Figs. 5.3-1 and 5.3-2. Also shown in Figs. 5.3-1 and 2 are theoretical shapes for the quasifree scattering process, as determined from Eq. (1). The theory has been normalized to the experimental data at the top of the quasifree peak. Note that for the p-p quasifree scattering, the data form a peak narrower than predicted by the theory, while for the p-n case, the shapes are similar. In Fig. 5.3-3 we have plotted this normalization factor (the ratio of the maximum of the experimental quasifree scattering peak to the maximum of the theoretical peak) versus incident energy. Note that the normalization factors are significantly different for p-p and p-n quasifree scattering, although in both cases the factor increases with energy. Other p-n experiments have shown similar results.[2]

The results of these measurements confirm that at these low energies the impulse approximation must be modified to take account of the increasing DeBroglie wavelength of the incoming proton. Attempts have been made to do this by including a cutoff radius. It is found that a cutoff radius of about 3 Fm greatly improves the ratio of the theoretical to experimental peak height. At the same time the predicted width of the enhancement is decreased as is also required to fit the data. However, it is still puzzling that the p-n and p-p cases deviate in their ratio to the predicted cross sections so markedly. It would be interesting to see if a more complete treatment of the processes can account for these differences.
(W.J. Braithwaite, J.R. Calarco, J.M. Cameron, and D.W. Storm)

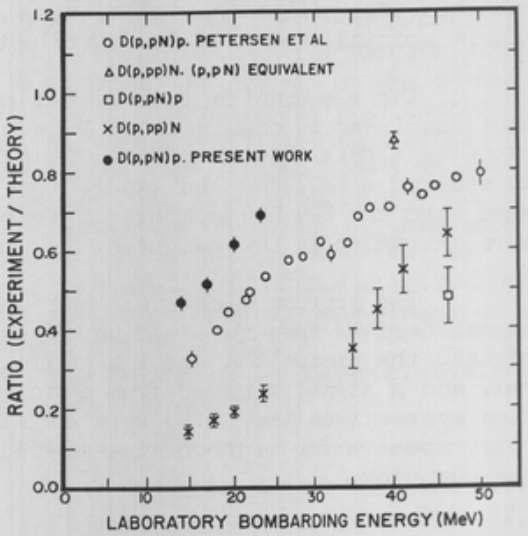

Fig. 5.3-3. Ratio of the measured quasifree cross section at the maximum of the peak to the theoretical prediction, plotted versus incident energy.

1. D.J. Margaziotis, G. Paic, J.G. Rogers, J.W. Verba, and J.C. Young, private communication.
2. E.L. Petersen, R.G. Allas, R.O. Bondelid, A.G. Pieper, and R.B. Theus, Phys. Letters *31B*, 209 (1970).

5.4 Determination of Nucleon-Nucleon Scattering Lengths Using the Reactions $^3He(d,tp)^1H$ and $^3H(d,^3He\ n)n$

Measurements of the p-p, n-p and n-n low energy elastic scattering are important for studying charge independence. Direct measurements of n-n scattering are not yet possible, and indirect means must be used to determine the low energy elastic scattering parameters. To obtain information about the n-n scattering length, three body final states, two of which are neutrons, must be studied. To extract accurate n-n parameters one must choose experimental conditions so that there are no other final state interactions, or one must be able to take account of these interactions in some manner. The most accurate measurements of the n-n scattering length, a_{nn}, have been made using the $\pi^- + d \rightarrow \gamma + 2n$ reaction,[1] in which there is little interaction between the two neutrons and the photon. This experiment yields a result for a_{nn} of -18.42 ± 1.53 Fm. Processes in which there are more than two strongly interacting particles in the final state may be useful in determining a_{nn} if one makes use of a comparison procedure.[2] In this procedure, processes leading to pp, pn, and nn final state interactions should be measured and analyzed under equivalent conditions. Agreement of predictions of some model with well established values of pp and np parameters allows one to have confidence in the value of the nn parameters extracted.

We have initiated a study of the reactions

$$d + {}^3He \rightarrow t + p + p,$$

$$d + t \rightarrow {}^3He + n + n.$$

Some preliminary measurements have been made on tritium targets. The ^3He targets were detected in a counter telescope consisting of a 35μ ΔE and a 2mm E detector. The neutrons were detected in a NE 213 liquid scintiallator described in Sec. 3.6 of this report. The neutron time of flight was determined relative to that of the charged particle. Five parameters for each event (energy signals from the ΔE and E detectors, scintillator pulse height, pulse shape discriminator signal derived from the scintillator, and time of flight signal) were fed via analog to digital converters to the SDS 930 computer. A program was used which performed particle identification and allowed windows to be set around the required identification signal for each event and then displayed the ^3He energy versus neutron flight time for each event.

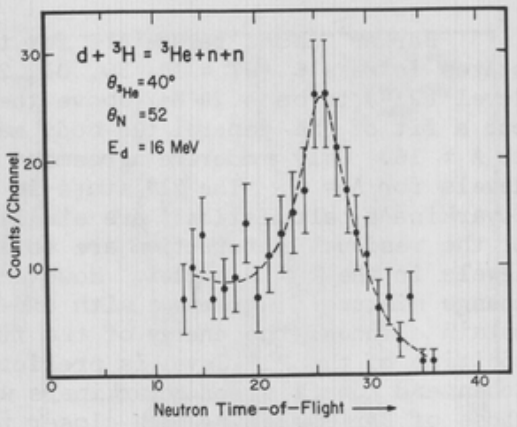

Fig. 5.4-1. Spectrum for $d+{}^3H \rightarrow {}^3He+n+n$ projected on the neutron time of flight axis. The peak is due to the n-n final state interaction.

Preliminary measurements were

made on a number of targets. The best results were obtained with one containing tritium absorbed in 500 μgm/cm^2 Ti on a 2 mg/cm^2 Pt backing; this target was obtained from ORNL. It was found that a very low neutron background could be obtained by positioning paraffin and lead shielding around the neutron detector. The data obtained for the d + t → ^{3}He + n + n reaction is shown in Fig. 5.4-1., projected onto the neutron time of flight axis. The enhancement due to the final state interaction was clearly distinguishable as shown in Fig. 5.4-1. Further measurements on both reactions are planned for the near future.
(W.J. Braithwaite, J.R. Calarco, J.M. Cameron, W.W. Jacobs, and D.W. Storm)

---

1. David Nygren, Ph.D. Thesis, University of Washington, (unpublished).
2. W.T.H. Van Oers and I. Slaus, Phys. Rev. *160*, 853 (1967).

5.5 A Search for the Second 2^+ T = 1 State in A = 6 Nuclei

Predictions of the energies and wave functions of T = 1 levels in the mass 6 nuclei have been made by Barker,[1] Boyarkina,[2] and Cohen and Kurath.[3] These calculations use a basis set of either LS coupled or jj coupled states for the two 1p shell nucleons perturbed by a two-body interaction with exchange as well as a one body spin orbit term.

In the LS scheme, two 1p nucleons in a T = 1 state can have spins coupled to S = 0 or 1. To maintain overall antisymmetry, S = 0 requires the orbital angular momenta (ℓ = 1) to couple to L = 0 or 2 ($J^\pi = 0^+, 2^+$); these space symmetric states are expected to lie lowest in energy due to the short range nature of the nuclear force. At higher excitation, there are three states with T = 1, S = 1, L = 1 ($J^\pi = 0^+, 1^+, 2^+$). Introduction of the residual interaction causes the multiplets to be split and those members of the two multiplets with the same total angular momentum to be mixed.

Barker[1] chose parameters for the residual interaction by fitting the lowest states in mass 6 (JT = 10, 30, 01, 20 and 21); he predicts the second 2^+ T = 1 level (21*) to be 4.24 MeV above the JT = 01 state. Cohen and Kurath[3] carried out a fit of the general two-body matrix elements to the 1p shell data from A = 6 to A = 16. Only moderate agreement is obtained with the spacings of the known levels for A = 6. The 21* state is predicted to lie 7.94 MeV above the 01 state. Boyarkina's calculations[2] are similar to those of Barker in that the parameters of the residual interaction are obtained by optimizing agreement with known levels in the A = 6 nuclei. However Boyarkina chooses a fixed (Rosenfeld) exchange mixture. Agreement with experiment is much better than Cohen and Kurath obtain although the energy of the first 21 level is somewhat overestimated. The position of the 21* level is predicted to be 7.0 MeV above the 01 level. Both Cohen and Kurath's and Boyarkina's wave functions show much less mixing than those of Barker, being much closer to pure LS coupled states.

The experimental work up to 1966 pertaining to the A = 6 nuclei has been summarized by Lauritsen and Ajzenberg-Selove.[4] They found no direct evidence confirming the existence of excited T = 1 states above the first 21 level. Since then Batty *et al.*[5] and Wakefield and Macefield[6] have reported evidence for an excited state in ^{6}Be at 3.0 - 3.5 MeV excitation in the reaction ^{6}Li(p,n)^{6}Be.

Somewhat conflicting data has been obtained from various other reactions.[7-9]

Using the various shell-model predictions we have made estimates for the relative cross sections of the two 21 states for nucleon pickup reactions such as $^{7}Li(p,d)^{6}Li^{*}$ and two nucleon stripping reactions such as $^{4}He(^{3}He,p)^{6}Li^{*}$. The predicted ratio of cross sections, $\sigma(21^{*})/\sigma(21)$, is approximately 0.25 for neutron pickup and 0.50 for two-nucleon stripping using Barker's wave functions. Using Boyarkina's and Cohen and Kurath's wave functions, the calculations indicate $\sigma(21^{*})/\sigma(21) \sim 0.05$ for two-nucleon stripping and ~ 0.01 for neutron pickup.

Thus the best reaction to use in a search for the 21* state appears to be two nucleon stripping. Since Barker was able to fit available mass 6 data well and since his wave functions predict strong two nucleon transfer it is of interest to see if the 21* state can be observed at the energy and with roughly the strength predicted by his results. A search was therefore made for this state using the reactions $^{3}He(\alpha,n)^{6}Be$, $^{3}He(\alpha,p)^{6}Li$ and $^{3}H(\alpha,p)^{6}He$ with the hope that the reactions would proceed via the transfer of two nucleons from the target to the incident projectile.

The three reactions were carried out using the 42 MeV alpha particle beam from the 60" cyclotron. In the $^{3}He(\alpha,n)^{6}Be$ reaction the beam impinged on a ^{3}He gas cell. Neutrons were detected in a 5 in. × 1 in. NE 213 liquid scintillator coupled to an RCA 4522 photomultiplier. Neutron energies were determined by time-of-flight using a flight path of 4m. at 45° in the laboratory. The inherent system time resolution including the duration of the beam pulse was observed to be of the order of 1 nsec. Gamma rays were rejected using pulse shape discrimination (see Sec. 3.6 of this report). The results are shown in Fig. 5.5-1. At 4m. the available time between beam bursts (87 nsec) limits the region of observable excitation energy to below about 5 MeV. No structure was observed in the region corresponding to 3.5 MeV excitation energy in ^{6}Be where a state has been previously reported.[5,6] Additional runs at 45° using a 3m flight path and at 60° using 2m are planned in order to be able to search at higher excitation energies.

The $^{3}He(\alpha,p)^{6}Li$ reaction was carried out using the same gas cell. Protons were detected and identified using a conventional E-ΔE two detector telescope. Data were obtained at 25°, 35° and 45°. Typical results are shown in Fig. 5.5-2. Identification of levels above the first 21 states was found to be impossible due to the background produced by the opening of channels with 3- and 4-body final states.

The most promising reaction with which to locate the 21* level appears

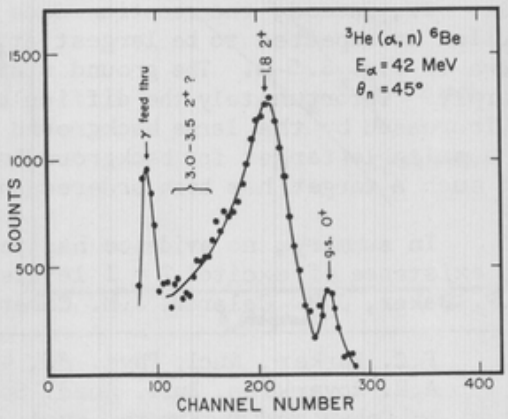

Fig. 5.5-1. Neutron time of flight spectrum from the reaction $^{3}He(\alpha,n)^{6}Be$ at 45°.

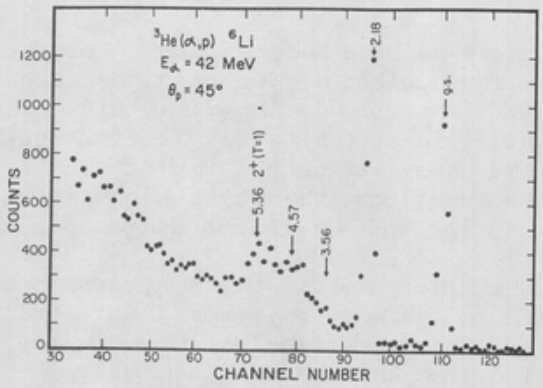

Fig. 5.5-2. Proton energy spectrum from the reaction ^{3}He(α,p)^{6}Li at 45°.

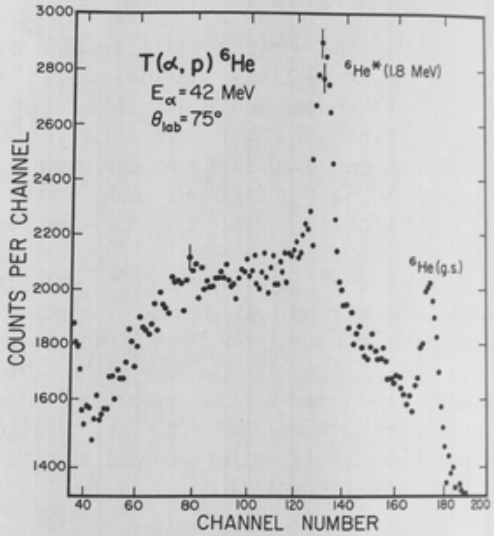

Fig. 5.5-3. Proton spectrum from the reaction ^{3}H(α,p)^{6}He at 75°.

to be ^{3}H(α,p)^{6}He. The decay width of the first 2⁺ state in ^{6}He is ten times smaller than in ^{6}Be. The excited states should also be somewhat narrower although by smaller factors as the decay energy increases. Furthermore the proton background due to multi-particle final states is expected to be less than in ^{3}He(α,p). The alphas bombarded a target of tritiated titanium (∿ 500 μg/cm^2) evaporated onto a platinum backing (∿ 2 mg/cm^2). A ΔE-E-Anti 3-counter telescope was used to detect the reaction products. Energetic particles were rejected by the third (Anti) counter before particle identification was made. Data were taken at large angles in the laboratory (70°-90°) which correspond to forward angles in the c.m. system in which the triton is considered as the projectile. If, indeed, the reaction does proceed by two-nucleon stripping, the cross section is expected to be largest at forward angles. The data taken at 75° are shown in Fig. 5.5-3. The ground state and first excited state of ^{6}He stand out sharply. Unfortunately the difficulty in extracting evidence for higher states is increased by the large background due to the target backing material. Lack of a suitable target for background measurements has prevented further analysis, but such a target has been ordered and additional runs are planned.

In summary, no evidence has yet been found in the reactions studied for the existence of excited T = 1 levels in mass 6 above the first 2⁺, T = 1 state. (M.P. Baker, J.R. Calarco, J.M. Cameron, and N.S. Chant)

1. F.C. Barker, Nucl. Phys. *83*, 418 (1966).
2. A.N. Boyarkina, Bull. Acad. Sci. USSR Phys. Ser. *28*, 255 (1964).
3. S. Cohen and D. Kurath, Nucl. Phys. *73*, 1 (1965).
4. T. Lauritsen & F. Ajzenberg-Selove, Nucl. Phys. *78*, 1 (1966).
5. C.J. Batty *et al.*, Nucl. Phys. *A120*, 297 (1968).
6. B. Wakefield and B.E.F. Macefield, Nucl. Phys. *A114*, 561 (1968).
7. K.W. Allen *et al.*, Proc. Phys. Soc. *75*, 913 (1960).

8. J. Linck *et al.*, J. Phys. Rad. *24*, 983 (1963).
9. C.L. Cocke, Nucl. Phys. *A110*, 321 (1968).

5.6 The Structure of High Lying Levels in the A = 5 Nuclei

The investigation of high lying levels in the A = 5 nuclei reported previously[1,2] has been extended by use of the $^{6}Li(^{3}He,\alpha)^{5}Li$ reaction. The experiment was performed using 25.5 MeV ^{3}He ions from the Van de Graaff to bombard a 500 $\mu g/cm^2$ ^{6}Li foil of 99.9% purity. The emitted particles were identified using a ΔE-E counter telescope and an ORTEC identifier unit, as described in detail elsewhere.[3]

An energy spectrum for the $^{6}Li(^{3}He,\alpha)^{5}Li$ reaction at a laboratory angle of 35° is shown in Fig. 5.6-1. In addition to the ground state and the $3/2^{+}$ level at 16.7 MeV there are two broad peaks centered at 19.8 and 22.8 MeV excitation. In Fig. 5.6-2 the alpha particle energies corresponding to the centers of the two broad peaks are plotted against angle; the kinematical variation for a level in the $^{16}O(^{3}He,\alpha)^{15}O$ reaction is included for comparison.

The data for the $^{7}Li(d,\alpha)^{5}He$ reaction at an incident deuteron energy of 24 MeV has been further analyzed; an energy spectrum for this reaction taken at

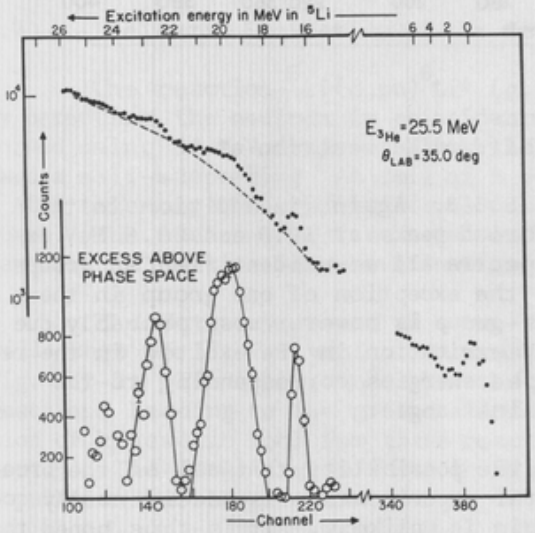

Fig. 5.6-1. The energy spectrum for the $^{6}Li(^{3}He,\alpha)^{5}Li$ reaction at 35°.

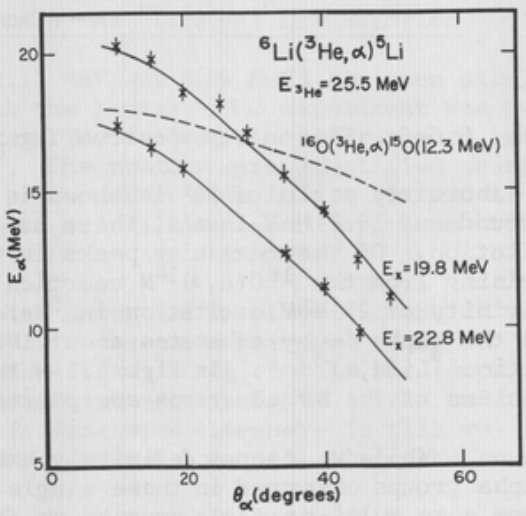

Fig. 5.6-2. The angular variation of the energy of the broad peaks observed in the $^{6}Li(^{3}He,\alpha)^{5}Li$ reaction. The solid lines are the results of kinematic calculations for excitations of 19.8 and 22.8 MeV.

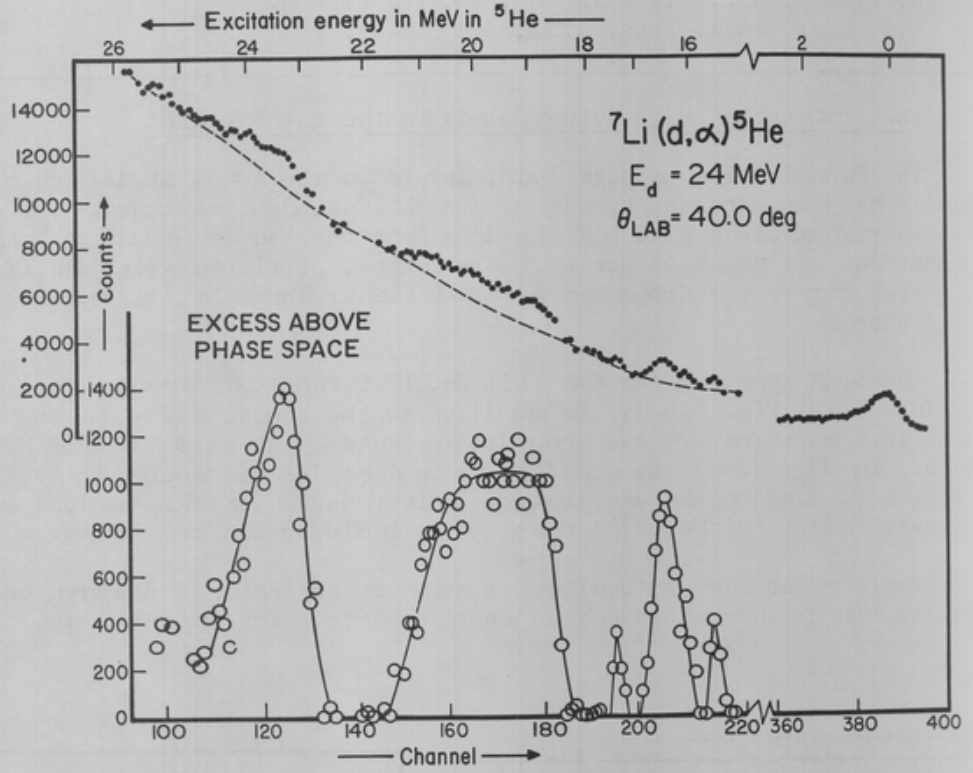

Fig. 5.6-3. The energy spectrum for the ^{7}Li(d,α)^{5}He reaction at 40°.

a laboratory angle of 40° is shown in Fig. 5.6-3. Again, in addition to the ground and 16.7 MeV levels, there are two broad peaks at 19.8 and 23.8 MeV excitation. Of the remaining peaks in the spectra all were identified as groups arising from the ^{16}O(d,α)^{14}N reaction with the exception of one group in the vicinity of 25 MeV excitation in ^{5}He. This group is however most probably due to the alpha decay of states about 16.7 MeV excitation in ^{8}Be excited in the reaction ^{7}Li(d,n)^{8}Be*. In Fig. 5.6-4 the alpha energies corresponding to the centers of the broad groups are plotted against angle.

While we cannot definitely exclude the possibility that all of the broad alpha groups observed in these single counter experiments arise accidentally from some multi-particle process we feel this is unlikely. It is thus hoped that the comparison of the results obtained for these two reactions, taking into consideration the different selection rules involved, will allow some conclusions to be made about the various levels at excitations above 20 MeV in the A = 5 system.

(M.P. Baker, J.M. Cameron, N.S. Chant, N.F. Mangelson, and D.W. Storm)

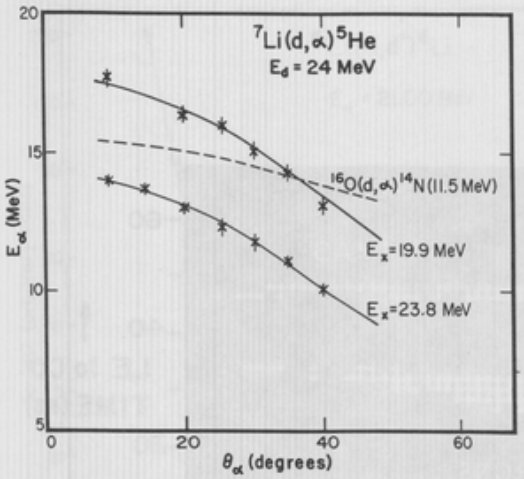

Fig. 5.6-4. The angular variation of the energy of the broad peaks observed in the ^{7}Li(d,α)^{5}He reaction. The solid lines are the result of kinematic calculations for excitations of 19.9 and 23.8 MeV.

1. Nuclear Physics Laboratory Annual Report, University of Washington (1969), p. 7.
2. M.P. Baker, J.M. Cameron, N.S. Chant, N.F. Mangelson, and D.W. Storm, *Proceedings of the International Conference on Properties of Nuclear States, Montreal*, 1969.
3. Nuclear Physics Laboratory Annual Report, University of Washington (1969), p. 9.

5.7 Inelastic Excitation of the Deuteron in the ^{6}Li(d,pn)^{6}Li* Reaction

The reaction ^{6}Li(d,pn)^{6}Li* (g.s., 2.18 MeV and 3.56 MeV) has been studied by detecting the neutron in coincidence with the proton. The experiment was performed using 21 MeV deuterons from the 3-stage Van de Graaff accelerator to bombard a self-supporting ^{6}Li foil of 1 mg/cm^2. The protons were identified using a ΔE-E telescope, the identification being performed on-line in the SDS 930 computer. The neutrons were detected in a liquid scintillator counter system which gave the n-γ separation shown in Fig. 5.7-1.

The data was stored in a two-parameter array and displayed in the CRT oscilloscope as (T_n-T_p) vs E_p. An example of this two-parameter data is shown in Fig. 5.7-2. The solid lines show the allowed kinematic regions for the (d,pn) reactions leading to the ground and first 4 excited states of ^{6}Li. (The calculation of kinematic loci for these reactions is discussed elsewhere in this report.[1]) The data is also shown in Fig. 5.7-2 for those channels where the count population was larger than 15.

The ^{6}Li(d,d') angular distributions to the ground and 2.18 MeV states for incident deuterons of 21 MeV is shown in Fig. 5.7-3. An angular distribution for ^{7}Li(d,d') is available[2] for incident deuterons of 23 MeV. The elastic shapes for ^{6}Li and ^{7}Li are quite similar and what small differences show up between them also show up between the ^{6}Li and ^{7}Li elastic at 11.8 MeV.[3] In addition the first excited state data at our higher energies (21 and 23 MeV) are quite similar in

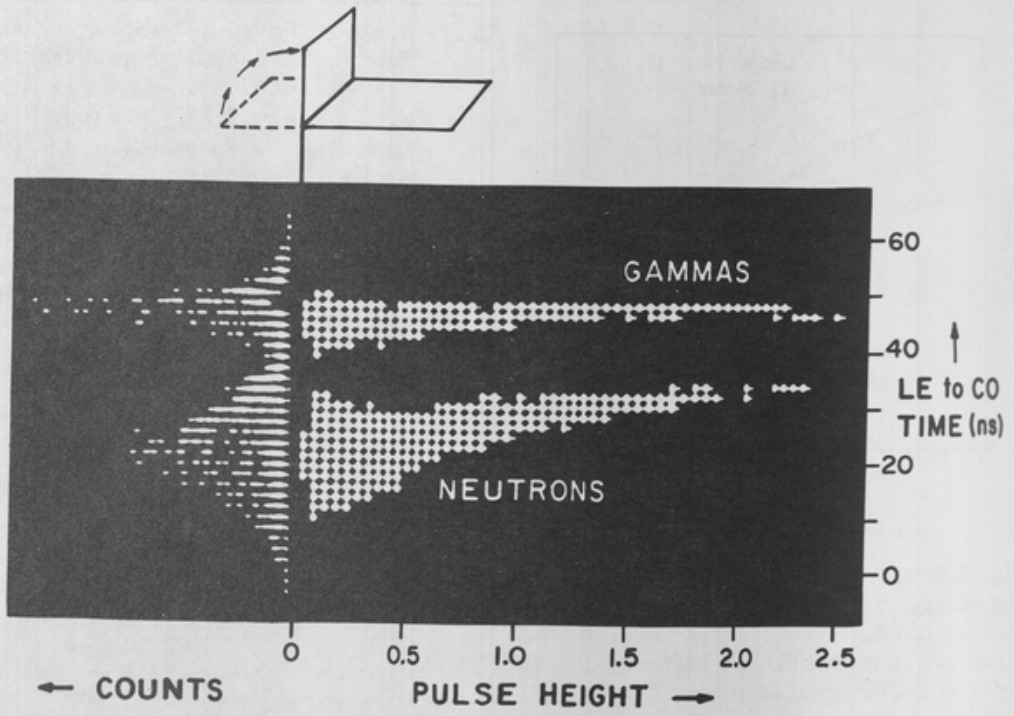

Fig. 5.7-1. Neutron-gamma separation using pulse shape discrimination.

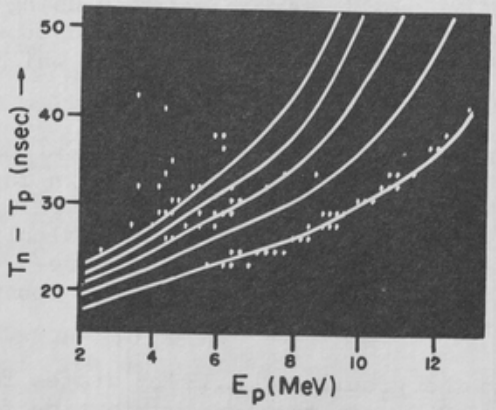

Fig. 5.7-2. Two parameter data and kinematics for the reaction ^{6}Li(d,pn) where $\theta_p = \theta_n = 30°$.

shape to the 11.8 MeV data for both ^{6}Li and ^{7}Li.

These observations strongly suggest that the reaction mechanism for ^{6}Li(d,d') is direct and if (d,d') is direct it would not be surprising if (d,pn) is also direct near the region $E_{pn} = 0$. If the (d,pn) mechanism were compound nuclear the p and n would most likely be emitted sequentially. There would be substantial time between emissions and they would likely leave the nucleus from markedly different surface locations. Thus the proton and neutron would not have an opportunity for a final state interaction (FSI). If an enhancement is seen that can only come about due to a FSI this would be strong evidence for the direct mechanism.

The yields from the ground, 2.18 and 3.56 MeV states have each been pro-

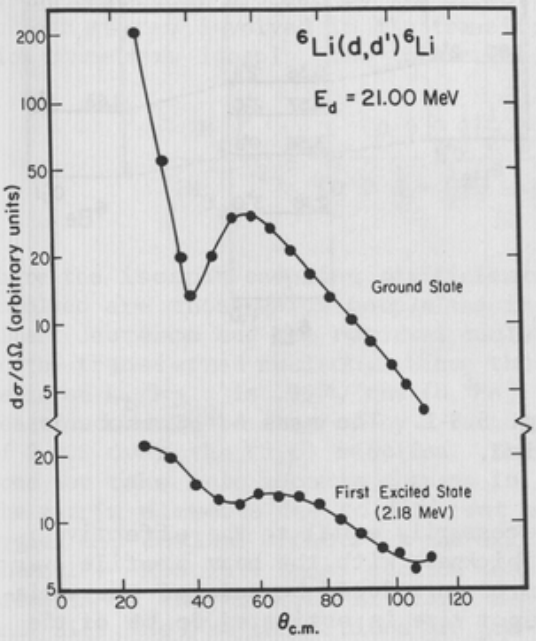

Fig. 5.7-3. Elastic and inelastic deuteron scattering from ^{6}Li.

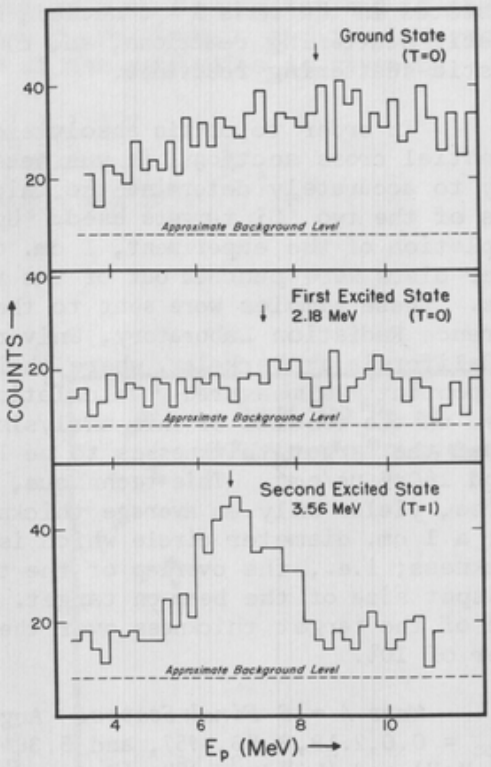

Fig. 5.7-4. Yield projections to the proton axis for the data of Fig. 5.7-2. Note the strong enhancement for the second excited state near E_{pn} = 0 (arrow).

jected onto the proton axis. These results are shown in Fig. 5.7-4. A strong enhancement can be seen on the plot corresponding to the 3.56 MeV state (T = 1) in the region E_{pn} = 0. (An arrow marks each case where E_{pn} = 0.) This enhancement is attributed to the pn final state interaction which, near E_{pn} = 0, strongly favors the $^1S_0$ (T = 1). The $^1S_0$ final state can populate the 3.56 MeV (T = 1) state but is isospin forbidden to populate either the ground (T = 0) or the 2.18 MeV (T = 0) states. (W.J. Braithwaite, J.M. Cameron, J.G. Cramer, and C.R. Rudy)

---

1. Section 4.9 of this report.
2. Section 5.8 of this report.
3. H. Lüdecke *et al*, Nucl. Phys. *A109*, 676 (1968).

5.8 Analysis of Some Proton and Deuteron Induced Reactions on ^{7}Li

Angular distribution for several reactions induced by bombarding isotopically enriched targets of ^{7}Li with 23 MeV protons and deuterons have been measured as previously reported.[1,2] The reaction products were detected with a ΔE-E telescope so that data for several reactions could be obtained simultaneously. These reactions fall naturally into three categories: a) Reactions which lead

to states in the mass A = 6 nuclei, b) Elastic scattering reactions, and c) Inelastic scattering reactions.

In order to obtain absolute differential cross sections, it was necessary to accurately determine the thickness of the two ^{7}Li targets used. Upon completion of the experiment, 1 cm. diameter discs were punched out of the targets. These samples were sent to the Lawrence Radiation Laboratory, University of California at Berkeley, where their ^{7}Li content was measured. Calculations based on the results of this analysis showed the target thicknesses to be 172± 7 and 160±6 ug/cm^{2}. This technique, of course, yields only an average thickness over a 1 cm. diameter circle which is not necessarily equal to the effective thickness; i.e., the overlap of the target thickness with the beam profile over the spot size of the beam on target. The error introduced because of the variation of the target thickness over the beam spot size is estimated to be of the order of 10%.

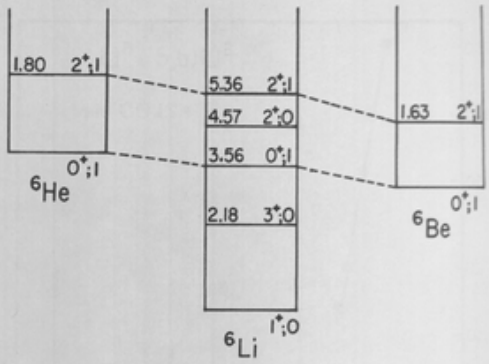

Fig. 5.8-1. The mass A = 6 isobaric triad.

Mass A = 6 Final States. Angular distributions for the $^{7}Li(d,t)^{6}Li$ (E_{exc} = 0.0,2.18,3.56,4.57, and 5.36 MeV), $^{7}Li(p,d)^{6}Li$ (E_{exc} = 0.0,2.18,3.56, and 5.36 MeV) and $^{7}Li(d,^{3}He)^{6}He$ (E_{exc} = 0.0 and 1.80 MeV) reactions have been measured and displayed previously.[1] The data have been more carefully analyzed with contributions from the ^{12}C and ^{16}O contaminants subtracted from the spectra where necessary. This was possible because spectra were recorded at the appropriate angles using ^{12}C and mylar targets. Absolute differential cross sections were extracted from the data after the target thicknesses were obtained.

The mass A = 6 nuclei form a T = 1 isobaric triad as shown in Fig. 5.8-1. The ^{6}He and ^{6}Be ground states and the 3.56 MeV second excited state of ^{6}Li are isobaric analogs. This is also true of the ^{6}He and ^{6}Be first excited states and the 5.36 MeV level of ^{6}Li. There are higher-lying levels in ^{6}Li whose isospin is unknown, but their analogs have yet to be found in ^{6}He and ^{6}Be so these levels probably have T = 0.[3]

Direct reactions which proceed from a given initial state to analog final states serve as an experimental test of the charge independence of nuclear forces. In our data, examples of this are the $^{7}Li(d,^{3}He)^{6}He$ - $^{7}Li(d,t)^{6}Li^{*}$(3.56 MeV) reactions and the $^{7}Li(d,^{3}He)^{6}He^{*}$(1.80 MeV) - $^{7}Li(d,t)^{6}Li^{*}$(5.36 MeV) reactions.

For these reactions the differential cross sections are related in the following way:

$$\frac{d\sigma/d\Omega(d,t)}{d\sigma/d\Omega(d,^{3}He)} = \frac{k_t}{k_{^{3}He}} \frac{|M_t|^2}{|M_{^{3}He}|^2} .$$

If the reactions proceed by the direct transfer of a single nucleon and if the nuclear states involved in the transitions have "pure" isospin and the interaction conserves isospin, the theoretical ratio of the amplitudes is given by

$$\frac{|M_t|^2}{|M_{^3He}|^2} = \frac{(0\ 0\ \frac{1}{2}\ \frac{1}{2}|\frac{1}{2}\ \frac{1}{2})^2(1\ 0\ \frac{1}{2}\ \frac{1}{2}|\frac{1}{2}\ \frac{1}{2})^2}{(0\ 0\ \frac{1}{2}\ -\frac{1}{2}|\frac{1}{2}\ -\frac{1}{2})^2(1\ 1\ \frac{1}{2}\ -\frac{1}{2}|\frac{1}{2}\ \frac{1}{2})^2} = \frac{1}{2}\ ,$$

where the isospin coupling coefficients involved are those which couple the incident deuteron and the residual nucleus to the transferred nucleon. Since the ratio of $k_t/k_{^3He}$ is .997, the $(d,^3He)$ reaction should be favored by a factor of 2.006 over the (d,t) reaction. This does not take into account changes in the matrix elements due to different energies and Coulomb effects in the exit channels. Absolute cross section measurements of the $^7Li(d,t)^6Li^*$ (3.56 MeV) and $^7Li(d,^3He)^6He$ transitions are presented in Fig. 5.8-2. The $(d,^3He)$ differential cross sections have been multiplied by a factor of .997/2 as discussed above. The comparison is very good through the first oscillation in the differential cross sections and acceptable over the remainder of the angular range if one considers that different experimental arrangements were used for the two measurements.[1]

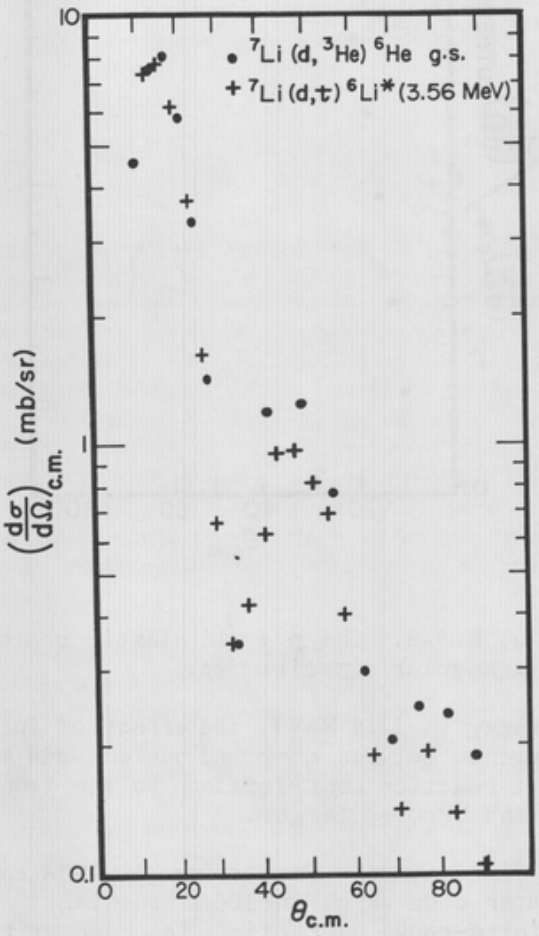

Fig. 5.8-2. Angular distributions for the $^7Li(d,t)^6Li^*$[3.56 MeV,0^+,T = 1] and $^7Li(d,^3He)^6He$ [g.s.,0^+,T = 1] transitions; the latter have been multiplied by .499.

A similar comparison has been made of the $^7Li(d,t)^6Li^*$(5.36 MeV) and $^7Li(d,^3He)^6He^*$ (1.80 MeV) transitions. The angular distributions do not compare as favorably and the data are being reanalyzed. However, there is no compelling reason to believe the data are in error. Thus, it may be that the 5.36 MeV level in ^6Li is not a pure T = 1 state, but has some admixture of other T = 0 states. Cerny and Pehl[4] have shown that only small admixtures of $T \neq 1$ states need by assumed to cause relatively large deviations from unity in the predicted ratio of the integrated cross sections for (p,t)-$(p,^3He)$ analog transitions. It is also possible that at this somewhat lower center-of-mass excitation

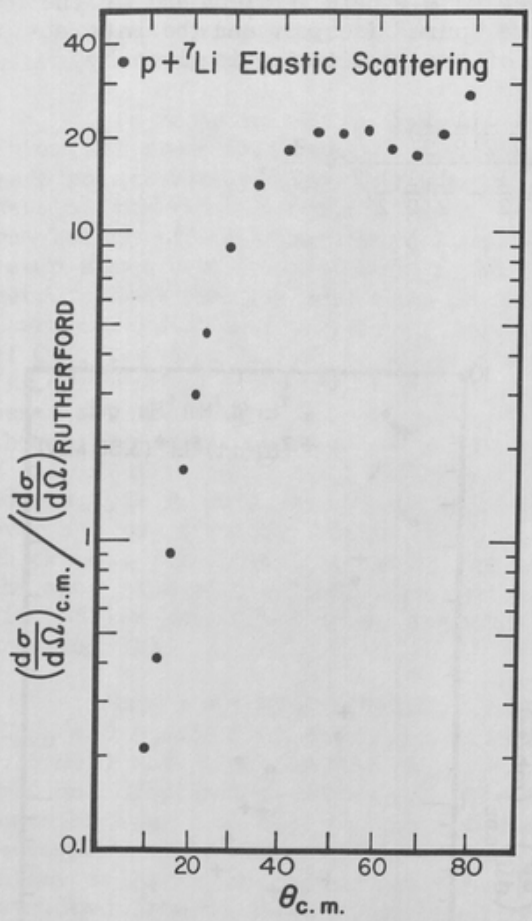

Fig. 5.8-3. The p + ^{7}Li elastic scattering angular distribution.

energy ($\sim$ 11.5 MeV), the effect of interference between compound nucleus and direct reaction contributions to the transitions becomes larger.

Elastic Scattering. A DWBA computer code which includes Gaussian finite-range corrections has been written in order to extract spectroscopic factors for the single nucleon transfer reactions leading to mass A = 6 discussed above.[5] Entrance and exit channel optical model parameters are needed in order to carry out such an analysis. Absolute differential cross sections have been measured for the elastic scattering of protons and deuterons on ^{7}Li so that entrance channel optical model parameters could be obtained. The ratios of these cross sections to the Rutherford scattering cross sections are presented in Figs. 5.8-3 and 5.8-4 respectively. An especially careful analysis was required at the laboratory angles forward of 25° because of large contributions to the elastic peak from the ^{12}C and ^{16}O contaminants.

Theoretical fits to the elastic scattering data are currently being calculated using an optical model search computer program written by W.R. Smith[6] which has been adapted for use on the University of Washington CDC-6400 computer.

The optical model parameters for the exit channel in the (d,t) and (d,^{3}He) reactions are available from the ^{3}He + ^{6}Li elastic scattering data of Lüdecke *et al.*[7] The d + ^{6}Li optical

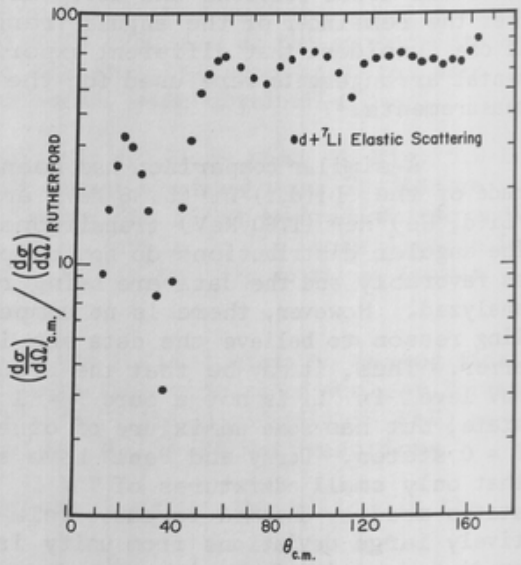

Fig. 5.8-4. The d + ^{7}Li elastic scattering angular distribution.

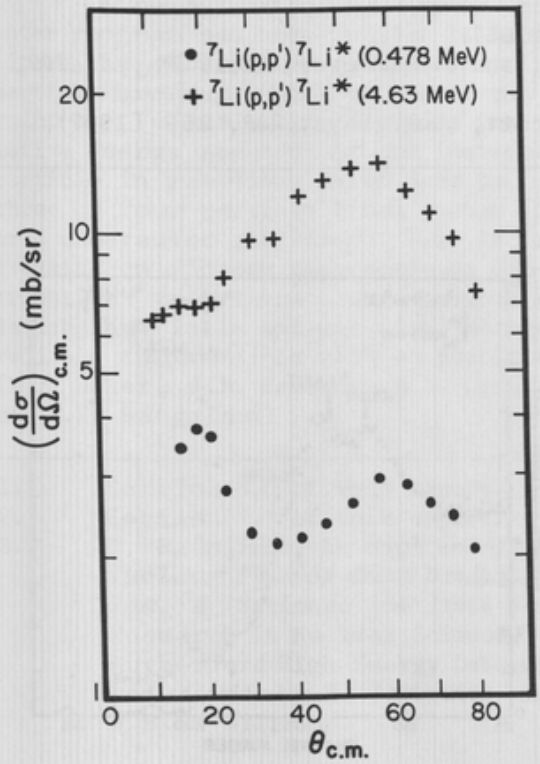

Fig. 5.8-5. Angular distributions for the ^{7}Li(p,p')^{7}Li*(E_{exc} = .478 and 4.63 MeV) reactions.

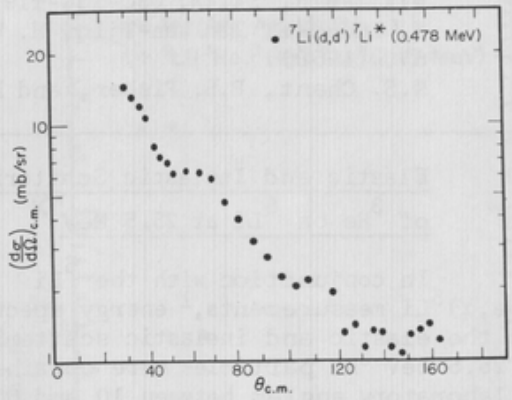

Fig. 5.8-6. Angular distribution for the ^{7}Li(d,d')^{7}Li* (.478 MeV) reaction.

model parameters necessary for the DWBA calculations of the (p,d) transitions are not readily available. Valid parameters for incident deuteron energies of 13 to 20 MeV are required. The best approximation to this seems to be the d + ^{6}Li elastic scattering data of the Heidelberg group at an incident deuteron energy of 11.8 MeV.[7] Some authors have found it necessary to vary the deuteron optical model parameters in order to obtain reasonalbe DWBA fits to (p,d) reaction data obtained with light target nuclei.[8]

Inelastic Scattering. Absolute differential cross sections have been determined for the ^{7}Li(p,p')^{7}Li* (E_{exc} = .478 and 4.63 MeV) and ^{7}Li(d,d')^{7}Li* (.478 MeV) reactions. The inelastic proton and deuteron cross sections are illustrated in Fig. 5.8-5 and 5.8-6 respectively. The ^{7}Li(d,d')^{7}Li* (.478 MeV) cross section data are not in final form in that a more careful subtraction of contributions from ^{12}C and ^{16}O contaminants must be made. Analysis of the ^{7}Li(d,d')^{7}Li* (4.63 MeV) reaction data is still in progress but has not as yet been completed. Either a microscopic or collective model may be used in the DWBA code mentioned above to obtain theoretical fits to these inelastic scattering angular distributions. (M.P. Baker, J.M. Cameron, and N.S. Chant)

---

1. Nuclear Physics Laboratory Annual Report, University of Washington (1969), p. 9.
2. *Ibid.*, p. 14.
3. Section 5.5 of this report.
4. J. Cerny and R.H. Pehl, Phys. Rev. Letters *12*, 619 (1964).

5. Section 8.9 of this report.
6. William R. Smith, USC-136-119, Feb. 1967.
7. H. Lüdecke, Tan Wan-Tjin, H. Werner, and J. Zimmerer, Nucl. Phys. *A109*, 676 (1968).
8. N.S. Chant, P.S. Fisher, and D.K. Scott, Nucl. Phys. *A99*, 669 (1967).

5.9 Elastic and Inelastic Scattering of ^{3}He on ^{6}Li at 25.5 MeV

In conjunction with the ^{6}Li ($^{3}He,\alpha$)^{5}Li measurements,[1] energy spectra for the elastic and inelastic scattering of 25.5 MeV ^{3}He particles were obtained at laboratory angles between 10 and 60 degrees in 5 degree steps. The target used was an isotopically enriched self-supporting foil 584 ± 24 μg/cm^2 thick. The thickness was determined by weighing the ^{6}Li in a 1 cm diameter sample of the target.[2] Peaks resulting from the elastic and inelastic scattering of ^{3}He on contaminants of ^{16}O, ^{12}C and ^{1}H were observed in the spectra. An energy spectrum of ^{3}He particles detected at a laboratory angle of 45° is shown in Fig. 5.9-1.

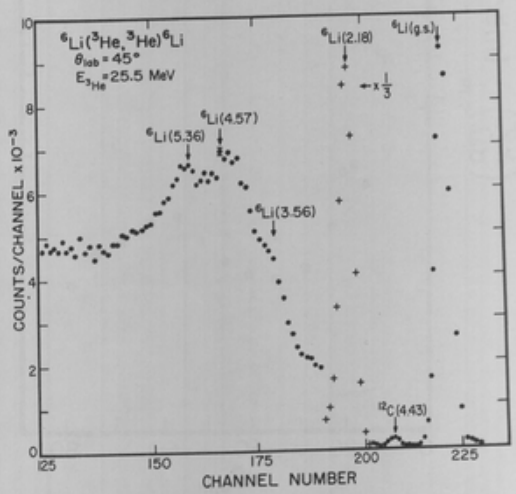

Fig. 5.9-1. ^{3}He energy spectrum for the reaction $^{6}Li(^{3}He,^{3}He)^{6}Li$ at a laboratory angle of 45°. The incident ^{3}He energy was 25.5 MeV. There are small contributions to the spectra due to ^{12}C and ^{16}O contaminants in the region of 4 to 6 MeV excitation energy in the residual ^{6}Li.

In all the ^{3}He energy spectra obtained, the reactions which leave the residual ^{6}Li in its ground and 2.18 MeV first excited state have the highest yields. Angular distributions have been extracted for these reactions and are presented in Fig. 5.9-2.

Peaks due to ^{3}He inelastic scattering reactions which leave the residual ^{6}Li in its 3.56, 4.57, and 5.36 MeV excited states are also present in all the spectra. The yields for these transitions are more difficult to determine because of large continuum contributions to the energy spectra from multiple particle breakup of the residual ^{6}Li nucleus. ^{6}Li is unstable to particle decay at excitation energies above 1.43 MeV. Excited states significantly above this excitation will have larger widths than the ground state because of their particle decay instability (except, of course, the 3.56 MeV, T = 1 second excited state whose only energetically allowable decay to α + d is isospin forbidden). Thus any strength a transition to one of these excited states may have is spread out over more channels in an energy spectrum. To obtain enough events to determine reliable differential cross sections therefore becomes time consuming. Using a relatively thick target approximately one hour was required to obtain the spectrum in Fig. 5.9-1.

A relativistic phase space[3] computer program has been written to facilitate the subtraction of these multiple particle breakup contributions to the spectra. The calculation yields the relative energy spectrum of one (detected) particle in reactions which lead to three or four particle final states (2 or 3 undetected particles). Work is progressing on fitting the continuum contributions with these phase space calculations but it is not yet clear whether reliable subtractions will be possible. (M.P. Baker, J.M. Cameron, N.S. Chant, and N.F. Mangelson)

---

1. Section 5.6 of this report.
2. Section 5.8 of this report.
3. D. Radojicic, in *High Energy and Nuclear Physics Data Handbook, Sec. X* (National Institute for Research in Nuclear Science, Rutherford High Energy Laboratory), ed. by W. Galbraith and W.S.C. Williams.

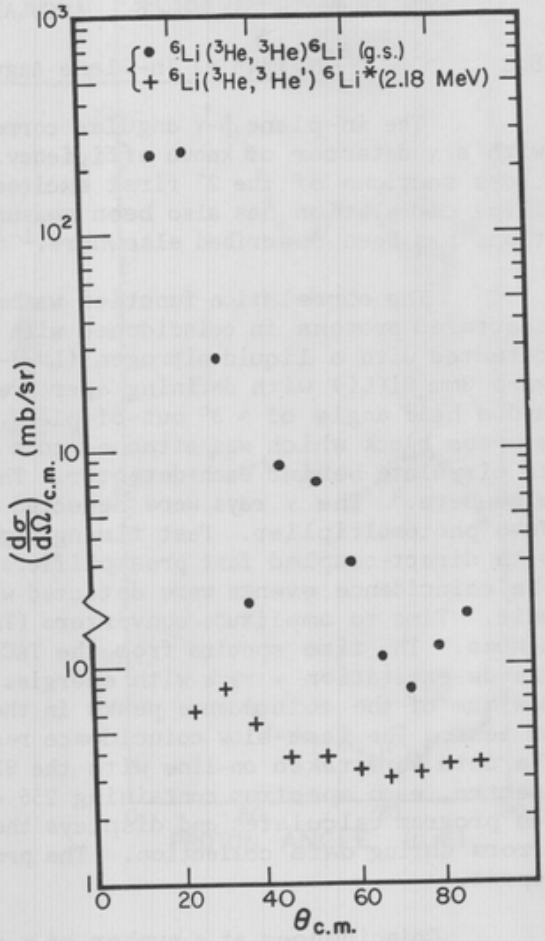

Fig. 5.9-2. Angular distributions for the ^{6}Li(^{3}He,^{3}He)^{6}Li and ^{6}Li(^{3}He,^{3}He')^{6}Li* (2.18 MeV) reactions.

6. ANGULAR CORRELATIONS

6.1 ^{12}C, $^{58}Ni(p,p'\gamma)$ In-Plane Angular Correlations at 20 MeV

The in-plane p-γ angular correlations on ^{12}C and ^{58}Ni have been measured with a γ detector of known efficiency. This permits one to separate the substate cross sections of the 2^+ first excited state of these nuclei if the z-axis (spin-flip) correlation has also been measured. The results of the spin-flip correlations has been described elsewhere.[1-3]

The correlation function was measured by detecting the inelastically scattered protons in coincidence with the de-excitation γ rays. The protons were detected with a liquid-nitrogen (LN_2)-cooled 5-detector array. The detectors were 3mm Si(Li) with defining apertures subtending a full angle of 2° in-plane and a half angle of $\sim$ 3° out-of-plane. The detectors were mounted 10° apart on a brass block which was attached to a LN_2 dewar. The brass block allows the LN_2 to circulate behind each detector. The dewar and LN_2 supply system is described elsewhere.[4] The γ rays were detected with a 4" × 4" NaI(Tℓ) coupled to an RCA 7046 photomultiplier. Fast timing signals were derived from the proton detectors with direct-coupled fast preamplifiers as described in Sec. 3.2 of this report. The coincidence events were detected with a standard fast-slow coincidence circuit. Time to amplitude converters (TACs) were used to detect the fast coincidences. The time spectra from the TACs were gated by the inelastic protons and the de-excitation γ rays with energies over 0.511 MeV. The full-width at half-maximum of the coincidence peaks in the gated time spectra was typically 2 nsec or less. The fast-slow coincidence resolving time (peak base width) was $\sim$10 nsec. The data were taken on-line with the SDS 930 computer. Five time and five proton spectra, each spectrum containing 256 channels, were collected in the computer. The program calculates and displays the correlation values and their statistical errors during data collection. The program is described in Sec. 4.7 of this report.

Coincidences at a number of γ angles were measured for each proton angle. The correlation function at a given proton angle has the form

$$W(\theta_\gamma = \pi/2, \phi_\gamma) = \frac{5}{16\pi}\left[D - E_1 \cos(2\phi_\gamma - \delta_1) - E_2 \cos(4\phi_\gamma - \delta_2)\right].$$

Only the second term in W is associated with protons which spin flip during the interaction. This form is fitted to the data by the least-squares method, and the parameters D, E_1, E_2, δ_1 and δ_2 extracted. The only parameter directly associated with the substate cross sections is D. D can be determined if the γ detector efficiency is known. The other parameters contain complicated, but independent, combinations of substate amplitudes and their relative phases. A complete description of these parameters is given by Schmidt *et al.*[5] D is related to the probability of exciting the 0^{th} substate by

$$D = 1 - S_0$$

where S_i is the probability for exciting the $|i|^{th}$ substates with an unpolarized

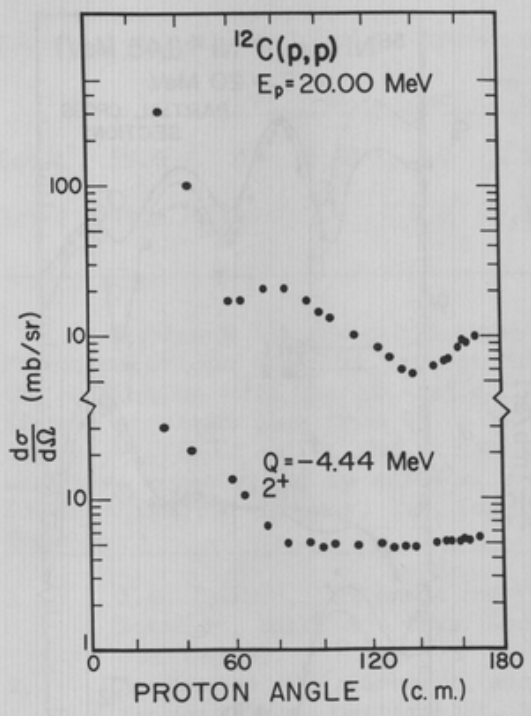

Fig. 6.1-1. ^{12}C elastic and inelastic cross sections.

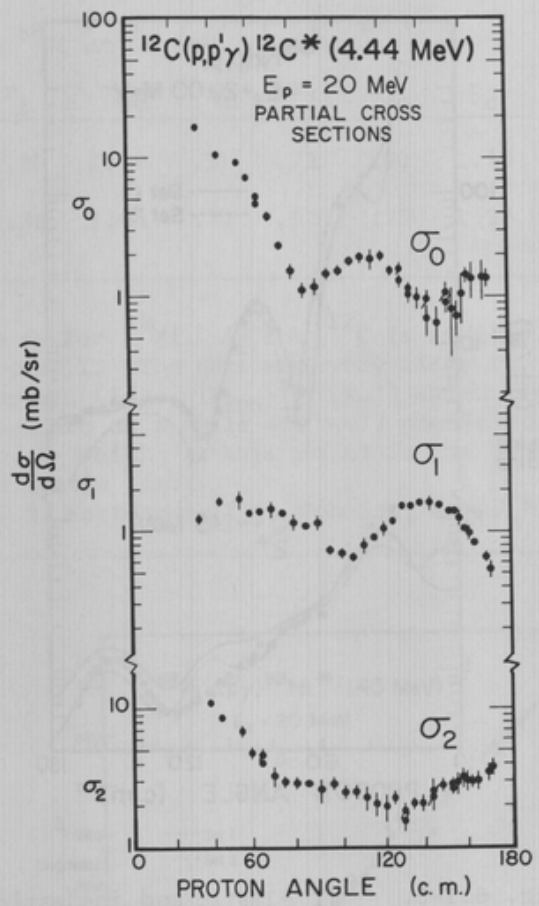

Fig. 6.1-2. ^{12}C substate cross sections

incident beam and the z-axis in the direction $\vec{k}_{inc} \times \vec{k}_f$, i = 0,1,2. S_1 and S_2 can also be determined if the z-axis correlation has been measured. It is related to S_1 by

$$W(\theta_\gamma = 0) = \frac{5}{8\pi} S_1.$$

This, together with the normalization condition

$$S_0 + S_1 + S_2 = 1,$$

permits the determination of S_1, S_2 and S_0 as well as σ_0, σ_1, and σ_2 where

$$\sigma_i = S_i \left(\frac{d\sigma}{d\Omega}\right)_{2^+}.$$

Figure 6.1-1 shows the elastic and inelastic cross sections for ^{12}C. Figure 6.1-2 shows the substate cross sections. Note that the inelastic cross section is quite featureless while its substate cross sections show considerable structure. σ_0 is especially interesting since it is out of phase with the

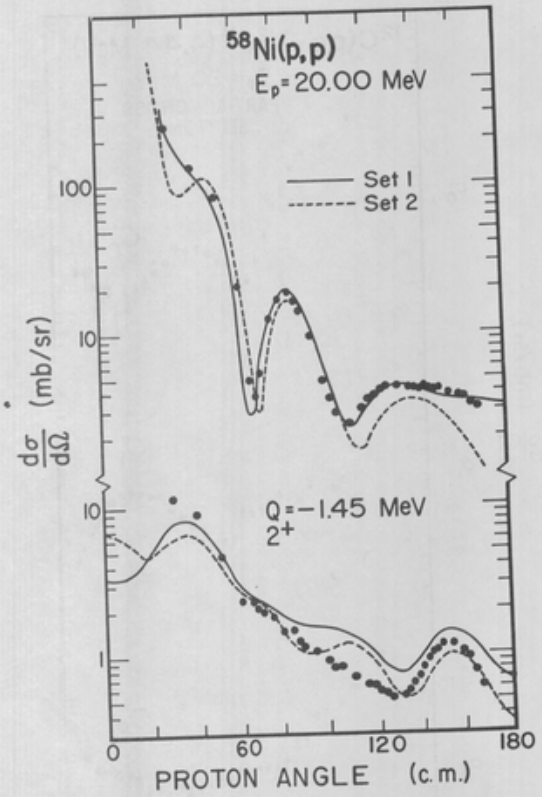

Fig. 6.1-3. ^{58}Ni elastic and inelastic cross sections.

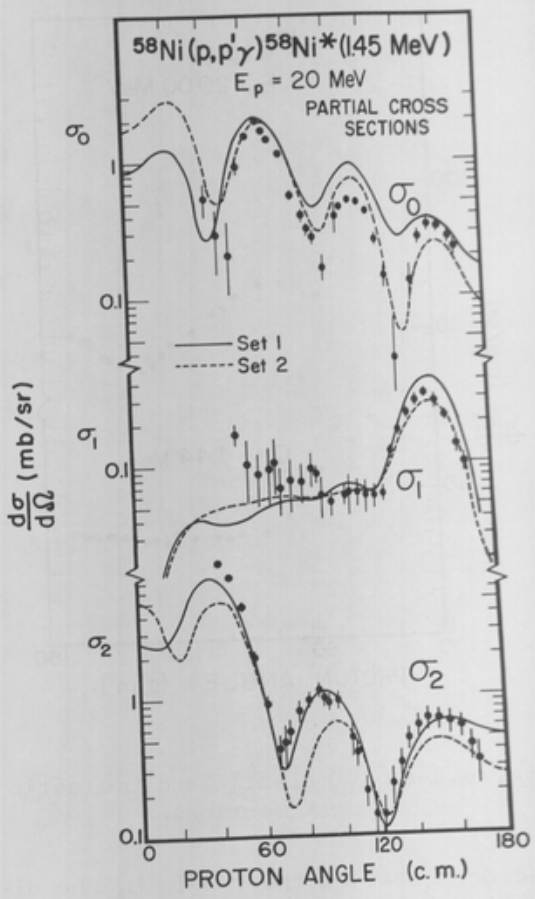

Fig. 6.1-4. ^{58}Ni substate cross sections.

elastic cross section -- this is similar to the effect described by the Blair phase rule for α-particle scattering.

Figures 6.1-3 and 6.1-4 show the cross sections for ^{58}Ni. The inelastic cross section is again quite featureless while the substate cross sections show strong oscillations. The Blair phase rule is again observed for σ_0. σ_2 is in phase with the elastic cross section. Two theoretical predictions are shown. The DWBA collective model calculations were made with the code of H. Sherif and include the full Thomas form of the spin-orbit potential.[6] Usually the form of the spin-orbit potential makes little difference at this energy but improves fits at higher energies. The Set 1 parameters were derived by fitting the spin-flip probabilities of the Ni isotopes.[3] The Set 2 parameters are taken from Becchetti and Greenlees' optimum standard parameters.[7] The parameters are shown in Table 6.1-1. There are large differences between the parameters of these sets. It is difficult, however, to decide which set gives the best fit to the data.

Table 6.1-1. Optical Model Parameters for ^{58}Ni at 20 MeV.

	V	W_V	W_s	V_{so}	r_R	r_I	r_{so}	a_R	a_I	a_{so}	r_c
Set 1	59.9	0	6.91	5.3	1.10	1.25	1.00	.71	.71	.70	1.10
Set 2	48.6	1.7	7.2	6.2	1.17	1.32	1.01	.75	.53	.75	1.25

Figure 6.1-5 shows the phase angle δ_2 for ^{58}Ni. δ_2 for ^{12}C is similar. The calculations for ^{58}Ni predict this very well. The data are very close to the prediction with the adiabatic limit imposed (i.e., $|k_{inc}| = |k_f|$) which predicts a straight line from 0° to 360°. The data as a whole are well predicted in the adiabatic limit; the exception being δ_1 which, at this point in the data analysis, appears not to agree with the adiabatic limit.
(J. Eenmaa, J.B. Gerhart, T.K. Lewellen, D.M. Patterson, F.H. Schmidt, and J.R. Tesmer)

1. J.R. Tesmer, J. Eenmaa and F.H. Schmidt, Bull. Am. Phys. Soc. *13*, 884 (1968).
2. J. Eenmaa, F.H. Schmidt, and J.R Tesmer, Phys. Letters *28B*, 321 (1968).
3. W.A. Kolasinski, J. Eenmaa, F.H. Schmidt, H. Sherif, and J.R. Tesmer, Phys. Rev. *180*, 1006 (1969).
4. Nuclear Physics Laboratory Annual Report, University of Washington (1966), p. 83.
5. F.H. Schmidt, R.E. Brown, J.B. Gerhart, and W.A. Kolasinski, Nucl. Phys. *52*, 353 (1964).
6. H. Sherif, Ph.D. Thesis, University of Washington, 1968 (unpublished).
7. F.D. Becchetti, Jr. and G.W. Greenlees, Phys. Rev. *182*, 1190 (1969).

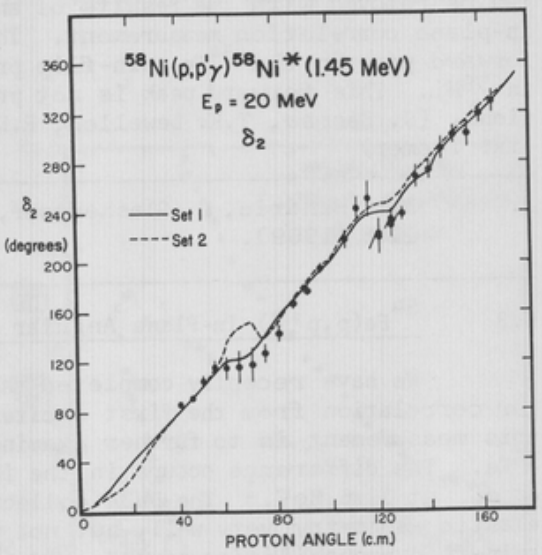

Fig. 6.1-5. ^{58}Ni phase angle, δ_2.

6.2 ^{54}Fe(p,p'γ) Proton Spin Flip at 19.6 MeV

The spin-flip probability for ^{54}Fe has previously been measured at 19.6 MeV, over a limited angular range, by Hendrie *et al.*[1] Our purpose was to extend the angular range of the measurements so that they could be used with the in-plane angular correlation data to determine substate cross sections of the 2^+ (1.409 MeV) first excited state of ^{54}Fe. See Sec. 6.3 of this report.

The experimental arrangement for the spin-flip measurement was the same as that described in Sec. 6.1 except that the γ detector was located perpendicular to the reaction plane. The γ detector was 5" × 4" NaI(Tℓ) coupled to an RCA 4522 photomultiplier. It is described in Sec. 3.4.

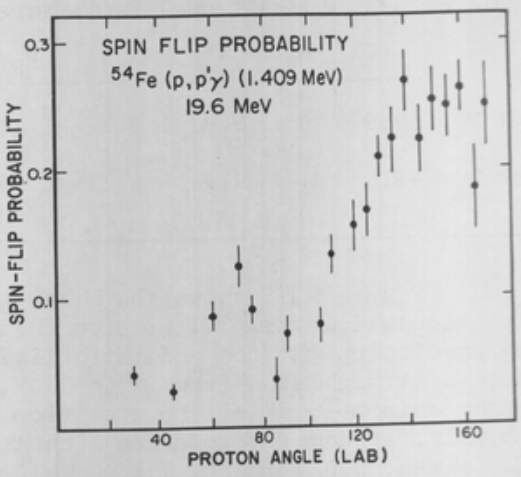

Fig. 6.2-1. ^{54}Fe proton spin-flip probability at 19.6 MeV.

The measured spin-flip probability is shown in Fig. 6.2-1. These data agree very well with the data taken by Hendrie. Only the statistical uncertainties are shown. Additional uncertainties of approximately the same magnitude as the statistical errors arise from the γ detector accepting γ-rays from substates other than the +1 or -1 (because of finite solid angle). The uncertainties due to the other substates can be removed with the results of an in-plane correlation measurement. The forward peak in the ^{54}Fe spin-flip probability is a feature which does not appear in ^{58}Ni. This forward peak is not predicted by DWBA collective model calculations. (J. Eenmaa, T.K. Lewellen, R.E. Marrs, D.M. Patterson, F.H. Schmidt, and J.R. Tesmer)

1. D.L. Hendrie, C. Glashausser, J.M. Moss, and J. Thirion, Phys. Rev. *186*, 1188 (1969).

6.3 ^{54}Fe(p,p'γ) In-Plane Angular Correlations at 19.6 MeV

We have recently completed the measurement of the (p,p'γ) in-plane angular correlation from the first excited state (1.409 MeV) of ^{54}Fe. The purpose of this measurement is to further examine the observed difference between ^{54}Fe and ^{56}Fe. The difference occurs in the inelastic asymmetries measured by Glashausser *et al.* at 19.6 MeV.[1] The DWBA collective model calculations predict the ^{56}Fe inelastic asymmetry very well, but not that of ^{54}Fe. Recent measurements of the spin-flip probabilities of ^{54}Fe and ^{56}Fe are very similar.[2] We hope that the in-plane correlation measurement, which determines the substate cross sections as well as other parameters (see Sec. 6.1) will help clarify the situation.

The experimental arrangement is identical to that described in Sec. 6.1 except that the γ detector is a 5" × 4" NaI(Tℓ) crystal coupled to an RCA 4522 photomultiplier (see Sec. 3.4).

Detailed analysis of the data is now in progress. Preliminary analysis gives results similar to those of ^{58}Ni (see Sec. 6.1).
(J. Eenmaa, T.K. Lewellen, R.E. Marrs, D.M. Patterson, P.A. Russo, F.H. Schmidt, and J.R. Tesmer)

1. C. Glashausser, R. de Swiniarski and J. Thirion, Phys. Rev. *164*, 1437 (1967).
2. D.L. Hendrie, C. Glashausser, J. Moss, and J. Thirion, Phys. Rev. *186*, 1188 (1969).

6.4 Status of the ^{3}He Spin-Flip Experiment

The ^{3}He spin-flip reaction is being studied to try to obtain a more accurate value of the ^{3}He spin-orbit potential depth of the optical potential.[1,2] Spin-flip measurements utilize the fact that only $0^+ \rightarrow 2^+$ inelastic scattering events involving spin-flip along the axis perpendicular to the reaction plane can give rise to ground state deexcitation gamma-rays along this axis.[3] This type of experiment is in many ways similar to an inelastic polarization measurement and provides a way of estimating the ^{3}He spin-orbit potential that does not require either a polarized ^{3}He beam or a double scattering experiment.

During the past year preliminary measurements have been made of 22.5 MeV ^{3}He scattering from ^{58}Ni. Cross section data were taken with an on-line particle identification program that can collect data from two independent ΔE,E detector arrays simultaneously.[4] Figure 6.4-1 shows the experimental results. There is an estimated 5% systematic error in the absolute normalization of the cross sections due primarily to uncertainty in target thickness.

After obtaining the cross section data, it was decided to attempt to measure the spin-flip probability in the reaction ^{58}Ni(^{3}He,^{3}He')^{58}Ni (1.45) at 22.5 MeV without particle identification. This allowed the use of a 5 particle detector array and a faster on-line data collecting program[5] which was expected to reduce the data collecting time required by about a factor of 10. The background due to the (^{3}He,^{4}He) reaction in the region around the peak corresponding to the first excited state of ^{58}Ni was found to be comparable to or greater than the peak area, but there was no problem extracting the differential scattering cross sections with reasonably small errors since the alpha particle spectrum in this region was featureless. However, the ^{4}He background was found to be associated with gamma-rays of sufficient energy to qualify a relatively large number of these events as true particle-gamma coincidences in the fast-slow coincidence

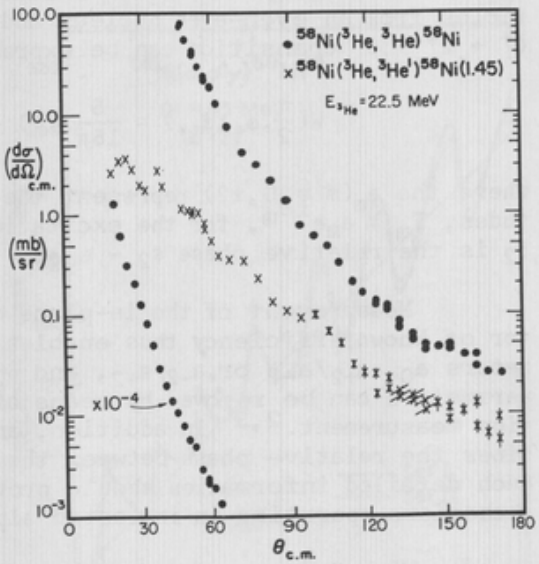

Fig. 6.4-1. Differential cross sections for the reactions ^{58}Ni(^{3}He,^{3}He)^{58}Ni and ^{58}Ni(^{3}He,^{3}He')^{58}Ni (1.45) as a function of center of mass.

electronics. This resulted in a large alpha-particle background in the fast-slow gated particle spectrum which made it impossible to extract the spin-flip probability from the data. Thus, it was found that one must do particle identification, or its equivalent, to obtain reasonable data. Work is almost complete on such a system. (J.G. Cramer, J. Eenmaa, T.D. Hayward, D.M. Patterson, and J.R. Tesmer)

1. D.M. Patterson and J.G. Cramer, Phys. Letters *27B*, 373 (1968).
2. Nuclear Physics Laboratory Annual Report, University of Washington (1968), p. 87.
3. F.H. Schmidt, R.E. Brown, J.B. Gerhart, and W.A. Kolasinski, Nucl. Phys. *52*, 353 (1964).
4. Nuclear Physics Laboratory Annual Report, University of Washington (1969), p. 142.
5. Section 4.7 of this report.

6.5 $^{58}Ni(\alpha,\alpha'\gamma)^{58}Ni^*$ (1.45 MeV) In-Plane Angular Correlation Measurements

Measurements of the in-plane angular correlations between inelastically scattered alpha particles and de-excitation gamma rays in the reaction $^{58}Ni(\alpha,\alpha'\gamma)^{58}Ni^*$ (1.45 MeV, 2^+) have been performed at an incident alpha particle energy of 23.25 MeV.

The angular correlation function for inelastically scattered alpha particles from an even-even nucleus and the coplaner de-excitation gamma rays in a $0^+ \rightarrow 2^+ \rightarrow 0^+$ transition can be expressed as:[1]

$$W(\tfrac{\pi}{2},\phi_\gamma;\phi_{\alpha'}) = \frac{5}{16\pi}\left[(1 - a_0^2) - 2a_{+2}a_{-2}\cos(4\phi_\gamma - \delta_2)\right]$$

where the $a_m(m \neq 0,\pm 2)$ represent the magnitudes of the complex transition amplitudes, $T_m = a_m e^{i\varepsilon_m}$, for the excitation of the m'th substates of the 2^+ state, and δ_2 is the relative phase $\varepsilon_2 - \varepsilon_{-2}$.

Measurement of the in-plane correlation function with a gamma-ray detector of known efficiency thus enables one to determine, absolutely, the parameters a_0, a_{+2}/a_{-2} or a_{-2}/a_{+2}, and δ_2. The ambiguity between the a_{+2} and a_{-2} parameters can be removed by means of a polarization-sensitive angular correlation measurement.[2,3] In addition, an out-of-plane correlation measurement determines the relative phase between the m = 0 and m = +2 or m = -2 substates, δ_0.[1] Such detailed information should provide a test of theories of the interaction mechanisms operating in inelastic alpha-particle scattering.

Measurements of the in-plane correlation function and of the circular polarization have been performed by Hayward[2,3] for the reaction $^{12}C(\alpha,\alpha'\gamma)^{12}C^*$ (4.44) at 22.75 MeV. The parameters a_0, a_{+2}, a_{-2}, and δ_2 were unambiguously determined but δ_0 was not determined. Although ^{12}C is an attractive nucleus from an experimental point of view because of its large inelastic cross section, it is quite unyielding to theoretical interpretation, and attempts to fit the above data with the standard nuclear theories (optical model, DWBA, etc.) were unsuc-

cessful. Experiments carried out on medium mass nuclei could therefore be extremely interesting.[4]

The experiment reported on herein is the start of a program to completely determine all of the nuclear polarization parameters $a_0, a_{+2}, a_{-2}, \delta_2, \delta_0$ for $^{58}Ni(\alpha,\alpha'\gamma)^{58}Ni^*$ (1.45,2^+) at an incident alpha-particle energy of 23.25 MeV.

The in-plane correlation was measured at 7 gamma-ray angles between 25° and 150° for each of 20 alpha-particle scattering angles between 35° and 82.5°. Inelastically scattered alpha particles were detected by an array of five 700 μ-thick Si(Li) solid state detectors. The solid-angle defining apertures for these detectors were 0.208 × 0.602 in. and defined an angular acceptance of 2° in the reaction plane. Gamma rays were detected by means of a 5 × 4 in. NaI(Tℓ) crystal coupled to an RCA 4522 photomultiplier tube. The absolute efficiency of the gamma-ray detector has been measured and is reported in Sec. 3.4 of this report. The experimental arrangement is similar to that used in the $(p,p'\gamma)$ angular correlation experiments as described in Sec. 6.1. In previous measurements,[2] it had been found efficacious to cool the particle detectors to LN_2 temperatures to improve the coincidence time resolution. This was found to be unnecessary in the present case because of the use of new direct-coupled low-noise fast preamplifiers (described in Sec. 3.2). The coincidence time resolution obtained was better than 2 nsec FWHM.

The analysis of the data is currently in progress. Figure 6.5-1 shows the results of preliminary analyses for the parameter δ_2. Also shown in the figure are the DWBA predictions for δ_2 with the optical model parameters of Sec. 7.4. The diagonal line in the figure is the prediction of the adiabatic limit.[5] The DWBA predictions are quite good for the range of data thus far obtained.

It is intended in subsequent runs to extend the range of the data to more forward and more backward angles. A gamma-ray detector carriage is being fabricated to position the gamma-ray detector out of the scattering plane and thus allow the measurement of the out-of-plane correlation function and the determination of the parameter δ_0.
(J. Eenmaa, T.K. Lewellen, R. Marrs, D.M. Patterson, F.H. Schmidt, and J.R. Tesmer)

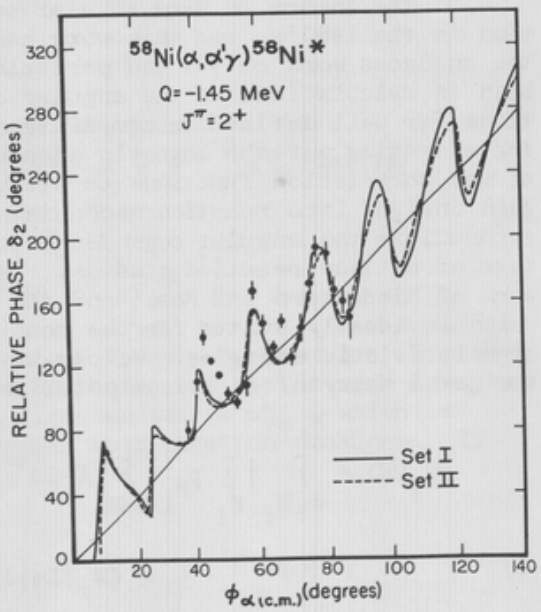

Fig. 6.5-1. Relative phase, δ_2 and DWBA predictions for the optical model parameters (Set I and II) of Sec. 7.4

1. J.G. Cramer and W.W. Eidson, Nucl. Phys. *55*, 593 (1964).
2. T.D. Hayward, Ph.D. Thesis, University of Washington 1969 (unpublished).

3. Nuclear Physics Laboratory Annual Report, University of Washington (1969), p. 16.
4. W.W. Eidson, J.G. Cramer, and G.P. Eckley, Phys. Letters *18*, 34 (1965).
5. J.S. Blair and L. Wilets, Phys. Rev. *121*, 1493 (1961).

6.6 Nuclear Reaction Studies Using Particle-Conversion Electron Angular Correlations

The success of particle-gamma angular correlation measurements of nuclear polarization[1] and proton,[2] deuteron,[3] and ^{3}He spin flip,[4] and generally as probes for nuclear reaction studies has prompted the extension of the angular momentum formalism for particle-gamma and particle-α triple correlations[5] to include particle-conversion electron correlations.

This type of angular correlation is of particular interest because of the recent availability of Si(Li) detectors which permit the detection with good resolution of conversion electrons at energies down to about 20 keV and because nuclear reactions in the very interesting region of large deformation A = 150 to 180 are essentially inaccessible to study with conventional particle-gamma techniques because the gamma-ray energies (> 100 keV) would be low enough to be masked by neutrons, annihilation radiation, and the tails of higher energy gamma rays. Therefore, we have attempted to determine whether nuclear polarization and spin-flip measurements can in practice be accomplished with conversion-electrons (ce) rather than gamma rays.

The theory of γ-ce angular correlations received much theoretical attention in the 1950's, and this work has continued to the present.[6,7] However, like the analgous work on γ-γ and particle-γ angular correlations, the emphasis has been on calculations of the angular dependence of individual correlation functions for well defined intermediate states by using elegant formal procedures for averaging out the magnetic quantum numbers, rather than on using the trends of the correlation functions to study spin-flip and nuclear polarization and to gain insight into reaction mechanisms. For this reason it has been necessary to reformulate the angular dependence of conversion electron processes in the context of nuclear reaction studies. In this we will, up to a point, follow the work of Biedenharn and Rose[7] and the helicity formalism of Jacob and Wick,[8] which is ideally suited for the consideration of conversion electron processes at relativistic energies. We can write the gamma ray correlation function, for the gamma decay of a nucleus polarized by a nuclear reaction, as:

$$W_\gamma(\mathcal{R}) \propto \sum_{\sigma,M_f} \Big| \sum_{M_i} P^{J_i}_{M_i} \sum_{LM\pi} (-1)^{\pi(\sigma+1)/2} (2L+1)^{\frac{1}{2}} D^{L}_{\sigma,M}(\mathcal{R}^{-1}) \times \langle J_f | L\pi | J_i \rangle C(J_i L J_f; M_i M M_f) \Big|^2 \quad (1)$$

where the gamma transition is of multipolarity L and type π = 0 for electric and 1 for magnetic transitions from a state of total angular momentum J_i to a state of total angular momentum J_f, and where M_i, M, and M_f are the magnetic quantum numbers of J_i, M_i, and M_f. Also σ = ±1 is the gamma ray helicity, or circular

polarization, $p_{M_i}^{J_i}$ is the nuclear polarization tensor,[5] and $D_{O,M}^{L}(\mathcal{R}^{-1})$ is the rotation operator, $\mathcal{R}$ is the set of Eulerion angles describing the rotation from the quantization axis to the direction of gamma ray emission, and $\langle J_f | L\pi | J_i \rangle$ is the reduced matrix element describing the gamma ray transition. If we concern ourselves only with E2 transitions from a 2^+ excited state to a 0^+ ground state in an even nucleus, then this relation becomes:

$$W_\gamma(\phi,\theta,0) \propto \sum_\sigma \left| \sum_M p_M^{\,2} D_{\sigma,M}^{2}(0,-\theta,-\phi)\, C(220,-MM0) \right|^2 \propto \sum_\sigma \left| \sum_M (-1)^M p_{M}^{\,2} e^{-im\phi} d_{M,\sigma}^{2}(\theta) \right|^2 \tag{2}$$

which is just the relation given in Ref. 5.

The analogous expression to Eq. (1) for a conversion electron transition from a nucleus polarized by a nuclear reaction is:

$$W_{ce}(\mathcal{R}) \propto \sum_{\substack{\sigma \\ \mu_i M_f}} \left| \sum_{M_i} p_{M_i}^{J_i} \sum_{LM\pi} (-1)^{\sigma+\frac{1}{2}} (2L+1)^{\frac{1}{2}} E^{j_i L}_{-\sigma\mu_i;2\sigma,M}(\mathcal{R}^{-1}) \times \langle J_f | L\pi | J_i \rangle\, C(J_i L J_f; M_i M M_f) \right|^2 \tag{3}$$

where

$$E^{j_i L}_{-\sigma\mu_i;2\sigma,M}(\mathcal{R}^{-1}) = \sum_{j_f} \left\{ (-1)^{j_f+\frac{1}{2}-L} \left[\frac{2j_f+1}{2L+1} \right]^{\frac{1}{2}} e^{i\Delta j_f} \langle j_f | L\pi | j_i \rangle \times C(j_i L j_f; \mu_i M \mu_f) \right] D^{j_f}_{\sigma\mu_f}(\mathcal{R}^{-1}) \right\}. \tag{4}$$

Thus the angular correlation differs from W_γ only in that $\sigma = \pm\frac{1}{2}$ rather than ± 1, the π is not involved in the sign alternation and the integer spin rotation matrix $D^{L}_{\sigma M}$ is replaced by an effective rotation matrix $E^{L}_{2\sigma,M}$ which is formed from a linear combination of half integer spin rotation matrices. It should also be noted that:

$$D^{j_i}_{-\sigma\mu_i} D^{L}_{2\sigma,M} = \sum_{j_f} C(j_i L j_f; -\sigma, 2\sigma, \sigma)\, C(j_i L j_f; \mu_i M \mu_f)\, D^{j_f}_{\sigma\mu_f}(\mathcal{R}^{-1}) \tag{5}$$

and that in the limit $k \to \infty$

$$(-1)^{j_f+\frac{1}{2}-L}\left(\frac{2j_f+1}{2L+1}\right)^{\frac{1}{2}} e^{i\Delta j_f}\langle j_f|L\pi|j_i\rangle \rightarrow N\, C(j_i L j_f;-\sigma,2\sigma,\sigma) \qquad (6)$$

where N is an arbitrary normalization factor and k is the transition energy. Thus in the high energy limit $k \rightarrow \infty$,

$$E^{j_i;L}_{-\sigma\mu_i;2\sigma,M} \rightarrow D^{j_i}_{-\sigma\mu_i}\, D^{L}_{2\sigma,M} \text{ and } W_{ce} \rightarrow W_\gamma,$$

since the incoherent sum over μ_i in (3) averages $D^{j_i}_{-\sigma\mu_i}$ to 1.

In the more realistic case where $k < m_0c^2$, i.e., $k < .511$ MeV, $E^{j_i;L}_{-\sigma\mu_i;2\sigma,M}$ will be a function of z, k, and the other characteristics of the conversion electron transition. In particular, the fortuitous zeros in $d^2_{\pm1,0}(\theta)$ at 0°, 90°, and 180° and in $d^0_{\pm1\pm2}$ at 0° and 180° which greatly simplify nuclear polarization[5] and spin flip measurements[8] may be moved to less convenient angles in the effective rotation matrix.

Calculations using tabulated values[9] of $\langle j_f|L\pi|j_i\rangle$ to determine the positions of the zeros in E are now in progress. These will determine, to a significant degree, the feasibility of conversion electron correlations.

In conclusion, it is appropriate to enumerate the problems and advantages of particle-ce correlations.

Problems:
1. Must use LN_2 cooled detectors.
2. Transition is split between γ, K, L_I, L_{II}, and L_{III}, etc., reducing the intensity of any one decay made.
3. Interpretation and analysis are complicated, as discussed above.
4. Since $\tau_{\frac{1}{2}} \sim$ 2-5 nsec, the nucleus might be depolarized by external fields before ce decay takes place.
5. Lab to CM angular corrections may be necessary, particularly for low energy electrons.

Advantages:
1. Good energy resolution.
2. 100% detection efficiency.
3. Background from higher energy decays and from neutrons is greatly reduced.
4. Shielding and collimation are simplified.
5. Helicity measurements are easier.

The author would like to acknowledge valuable discussions with W.W. Eidson and C. Fred Moore which prompted the undertaking of these calculations. (J.G. Cramer)

---

1. W.W. Eidson, J.G. Cramer, D.E. Blatchley, and R.D. Bent, Nucl. Phys. *55*, 613 (1964).

2. F.H. Schmidt, R.E. Brown, J.B. Gerhart, and W.A. Kolasinski, Nucl. Phys. *52*, 353 (1964); W.A. Kolasinski, J. Eenmaa, F.H. Schmidt, H. Sherif, and J.R. Tesmer, Phys. Rev. *180*, 1006 (1969).
3. J.A.H. Pfleger, H.M. Vieth, and R. Jahr, *Contributions to International Conference on Nuclear Structure*, p. 285, Tokyo, Japan (1967); Nuclear Physics Laboratory Annual Report, University of Washington (1969), p. 19.
4. D.M. Patterson and J.G. Cramer, Physics Letters *23B*, 373 (1968).
5. J.G. Cramer and W.W. Eidson, Nucl. Phys. *55*, 593 (1964).
6. M.E. Rose, L.C. Biedenharn, and G.B. Arfken, Phys. Rev. *85*, 5 (1952); L.C. Biedenharn and M.E. Rose, Rev. Mod. Phys. *25*, 729 (1953); Robert C. Young, Phys. Rev. *115*, 577 (1959); E.L. Church, A. Schwartzschild, and J. Weneser, Phys. Rev. *133*, 885 (1964); P. Hornshøj, B.I. Deutch, and A. Miranda, Nucl. Phys. *A95*, 65 (1967).
7. L.C. Biedenharn and M.E. Rose, Phys. Rev. *134*, 88 (1964).
8. M. Jacob and G.C. Wick, Annals of Physics *7*, 404 (1959).
9. I.M. Band, M.A. Listengarten, and L.A. Sliv, Appendix 6 "Tables of the Conversion Matrix Elements" in *Alpha, Beta, and Gamma-Ray Spectroscopy*, (K. Siegbahn, Editor) North Holland Publ. Co., Amsterdam (1965); I.M. Band, M.A. Listengarten, and L.A. Sliv, Appendix 1 "Conversion Matrix Elements and Phases" in *Internal Conversion Processes*, (J.H. Hamilton, Editor) Academic Press, New York (1966).

6.7 A DWBA Code for $0^+ \rightarrow 3^- \rightarrow 0^+$ (p,p'γ) Angular Correlations

The DWBA computer code written by Helmy Sherif[1] has been modified to include calculation of the (p,p'γ) angular correlation function for $0^+ \rightarrow 3^- \rightarrow 0^+$ transitions. The original code used a distorted optical potential to calculate cross sections, spin flip probabilities, and several other parameters for even-even nuclei. In the special case that the excited state is a 2^+ state, the original code also calculated the in-plane (p,p'γ) angular correlation function. The modifications were quite straightforward, consisting essentially of combining the transition amplitudes that the code already calculated in the appropriate equations to yield the in-plane and out-of-plane correlation functions for a 3^- state.

For convenience, the modified code also offers the option of having the transition amplitudes, elastic and inelastic cross sections, spin flip probability and cross section, and the correlation function parameters (if the excited state is a 2^+ or a 3^- state) punched out on cards for input to data analysis and plotting programs. (T.K. Lewellen)

1. H.S. Sherif, Ph.D. Thesis, University of Washington, 1968 (unpublished).

7. ELASTIC AND INELASTIC SCATTERING

7.1 Studies of the Mutual Excitation Reaction $^6Li + {}^6Li \rightarrow {}^6Li^* + {}^6Li^*$

The investigations of the elastic, inelastic, and double inelastic scattering of ^6Li by ^6Li has continued.[1] The principal problem, that of obtaining $^6Li^{+++}$ beams of reasonable intensity, reliably and continuously during an experimental run has been solved by extensive revisions of the basic He ion source design.[2] In the most recent run, 1 μamp of analyzed lithium beam was obtained and a beam of about 300 na of 30 MeV $^6Li^{+++}$ was obtained continuously on target for 2½ days, and further modifications of the source show promise of even more beam and improved reliability over long runs.

The principal goal of the experiment has been to observe the double excitation in which both ^6Li particles are excited to their $0^+(T = 1)$ second excited states. This excitation is of particular interest because in a direct reaction it must arise from the $(\vec{\sigma}_1 \cdot \vec{\sigma}_2)(\vec{\tau}_1 \cdot \vec{\tau}_2)$ part of the nuclear potential.

The experiment used a self-supporting ^6Li target and a pair of thin 56 and 69 micron transmission mounted surface barrier detector backed by thick 1.0 mm Si(Li) anti-coincidence detectors. The thickness of the transmission detectors was selected to stop ^6Li while passing α's with energies above 7.5 MeV, and all lighter particles into the anti-coincidence counter. Both ^6Li particles were detected in coincidence which kinematically constrains the Q of the reaction thus detected. Runs were made with $\theta_1 = \theta_2 = 45°$, i.e., elastic scattering at 90° (c.m.) and with $\theta_1 = \theta_2 = 35.9°$, i.e., inelastic scattering at 90° (c.m.) with Q = - 7.12 MeV. The coincident events thus detected were accumulated in using a dual 64 × 64 two parameter analyzer program for the SDS 930 on-line computer. The program stores true coincidences in one array and chance events outside the true-coincidence time window in a second array. A small but detectable peak in the 35.9° spectrum indicated the presence of the double-excitation process with

$$\frac{d\sigma_{El}}{d\Omega}(90°) / \frac{d\sigma_{DEx}}{d\Omega}(90°) \approx 4 \times 10^3.$$

At the completion of the most recent run, we received a preprint of a paper by Nagatani *et al.*[3] in which the same experiment was performed at Rutgers at 32 MeV with about 15 na of beam on target, and complete angular distributions and excitation functions were reported. We therefore plan no further work on this reaction.

An interesting side-effect of the above work is perhaps worth mentioning. In studying the elastic reaction at $\theta_1 = \theta_2 = 45°$, two small peaks were observed in the two-parameter spectrum in addition to the elastic peak. The intensity of this pair of peaks is 1/100 of the elastic scattering. These peaks had energies in the two counters of $E_1 = 7.8$ MeV and $E_2 = 12.5$ MeV and conversely, corresponding to a reaction with Q = - 9.7 ± .6 MeV. Since the kinematics of the system is overdetermined, by assuming the mass of one of the detected particles, the other mass can be calculated. Table 7.1-1 gives the results of this calculation. As indicated, the only reasonably likely reaction is $^6Li + {}^{12}C \rightarrow {}^{11}B + {}^7Be$, with Q = - 10.35 MeV. However, a run with a natural carbon target failed to show the unidentified peaks. Thus their presence is still unexplained.

Table 7.1-1. Particle 2 Mass as a Function of Particle 1 Mass

M_1 (AMU)	M_2 (AMU)
6	9.4 ± .4
7	11.2 ± .5
8	12.8 ± .6
9	14.3 ± .7
10	15.9 ± .7

(W.J. Braithwaite, J.G. Cramer, W.W. Eidson*, K.G. Nair, and W.R. Wharton)

1. Nuclear Physics Laboratory Annual Report, University of Washington (1969), p. 14.
2. Section 1.4 of this report.
3. K. Nagatani, D.P. Boyd, P.F. Donovan, E. Beardsworth, and P.A. Assimakopoulos, Phys. Rev. Letters *24*, 675 (1970).

* Permanent address: Physics Department, University of Missouri at St. Louis, St. Louis, Missouri.

7.2 Elastic Scattering of ^{18}O - ^{18}O

Broad structure in the elastic excitation functions of light nuclei has been observed in several instances;[1-7] the most dramatic being the scattering of ^{16}O on ^{16}O.[7] To study further the source of this structure we carried out an excitation function for ^{18}O - ^{18}O and ^{18}O - ^{16}O scattering.

Targets were prepared by anodizing Al foils in 50 atom % ^{18}O water. ^{18}O ions for acceleration through the tandem Van de Graaff were prepared by bleeding enriched ^{18}O water vapor into the duoplasmatron ion source. Particle identification was accomplished by selecting the proper kinematic angles for the desired scattered particle and its recoil partner. A coincidence technique was employed using a heavy ion surface barrier angle defining detector and a position sensitive coincidence detector. The detector pulses were analyzed on line by the SDS 930 computer using a data acquisition program written by R. Aley.[8]

Excitation functions for ^{18}O - ^{18}O and ^{18}O - ^{16}O scattering were carried out in 1 MeV steps between 15 and 55 MeV ^{18}O bombarding energy at 90° c.m. scattering angle. The results, along with the corresponding ^{16}O - ^{16}O scattering excitation function are shown in Fig. 7.2-1.

Efforts are currently being made to identify the interactions responsible for the very different behavior of these identical particle systems.

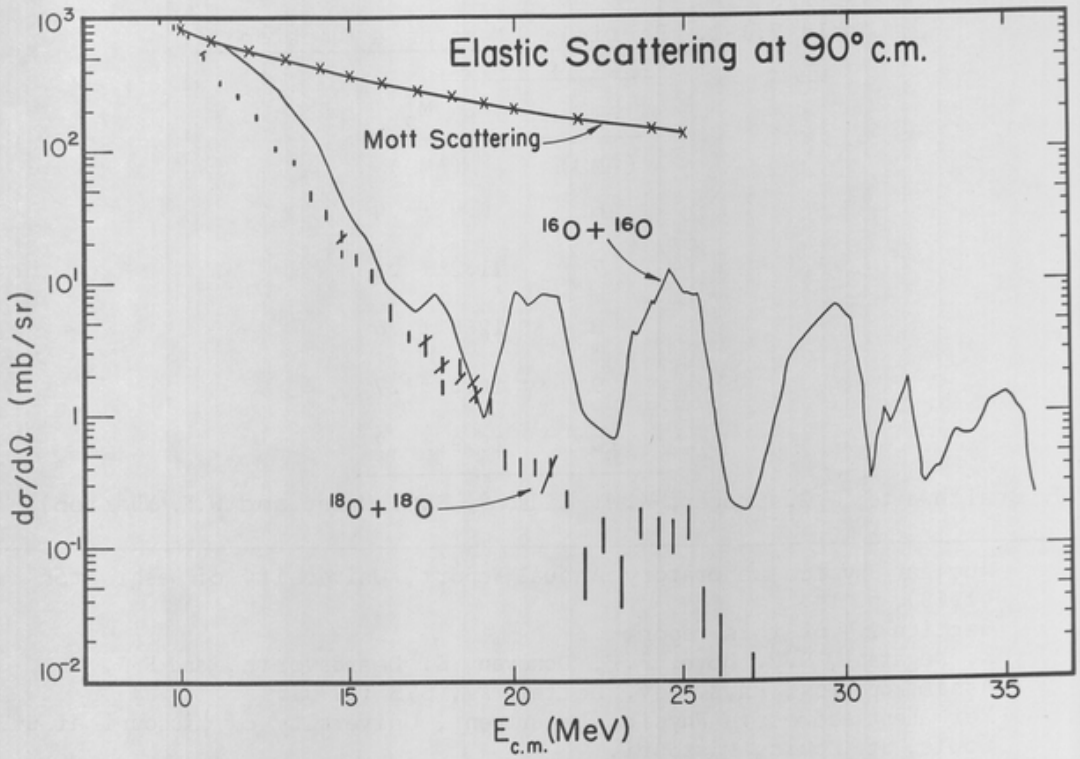

Fig. 7.2-1. Elastic scattering at 90° c.m. The smooth line is the ^{16}O - ^{16}O excitation function (gross structure only) measured by Maher *et al.*[7]

Calculations within the general framework of the optical model have reproduced the general behavior of the ^{16}O - ^{16}O scattering using a shallow real potential and a shallow energy dependent imaginary potential.[7] The general form of the ^{18}O - ^{18}O scattering excitation function requires a potential with somewhat greater diffuseness and an imaginary potential roughly three times deeper than that describing ^{16}O - ^{16}O scattering. More detailed fits to the ^{16}O - ^{16}O elastic cross section have been achieved with an ℓ-dependent imaginary potential;[9] we are currently exploring the justification for such a potential.
(M. Mehta, R. Shaw, and R. Vandenbosch)

---

1. ^{6}Li + ^{6}Li: G.C. Morrison *et al.*, Argonne National Laboratory (private communication).
2. ^{12}C + ^{12}C: A. Gobbi *et al.*, Yale University (private communication).
3. ^{14}N + ^{14}N: W. Reilly *et al.*, Yale University (private communication).
4. ^{14}N + ^{16}O, ^{15}N + ^{16}O: R.H. Siemssen *et al.*, Argonne National Laboratory (private communication).
5. ^{14}N - ^{14}N, ^{14}N - ^{16}O: L.A. Jacobson, Phys. Rev. *188*, 1509 (1969).
6. ^{16}O - ^{18}O: H.T. Fortune *et al.*, Argonne National Laboratory (private communication.

7. ^{16}O - ^{16}O: J.V. Maher, Ph.D. Thesis, Yale University, 1969 (unpublished); J.V. Maher *et al.*, Phys. Rev. *188*, 1665 (1969).
8. R. Aley, University of Washington (1969).
9. R.A. Chatwin *et al.*, Florida State University (private communication).

7.3 Excitation Functions for ^{54}Fe and ^{92}Mo (p,p) and (p,p') Around 20 MeV

The ^{54}Fe and ^{92}Mo (p,p) and (p,p') excitation functions were measured in preparation for in-plane (p,p'γ) angular correlation measurements planned for these nuclei.

The detectors used for these measurements had an in-plane full-angle of 0.75°. The incident proton beam was produced by the three-stage tandem Van de Graaff and had a resolution of ∿ 5 keV. The target thicknesses were ∿ 1 mg/cm^2.

Figures 7.3-1 and 7.3-2 show the excitation functions for ^{54}Fe and ^{92}Mo respectively. The excitation functions show very little structure for the energy step-size taken. (J. Eenmaa, T.K. Lewellen, D.M. Patterson, F.H. Schmidt, and J.R. Tesmer)

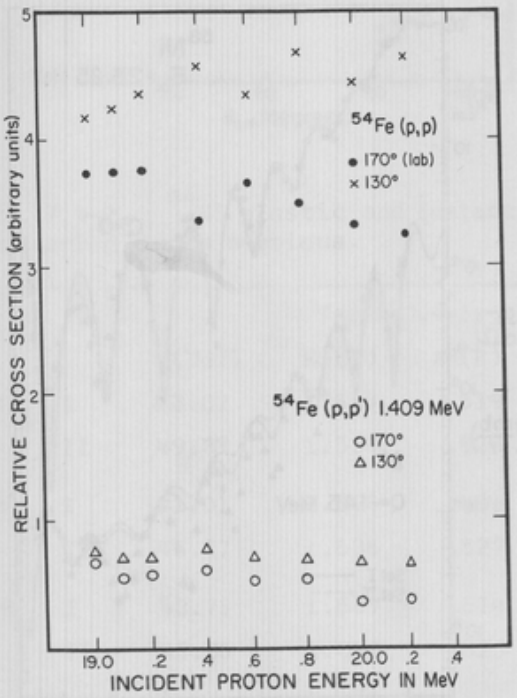

Fig. 7.3-1. ^{54}Fe(p,p) and (p,p') excitation functions at 130° and 170° (lab).

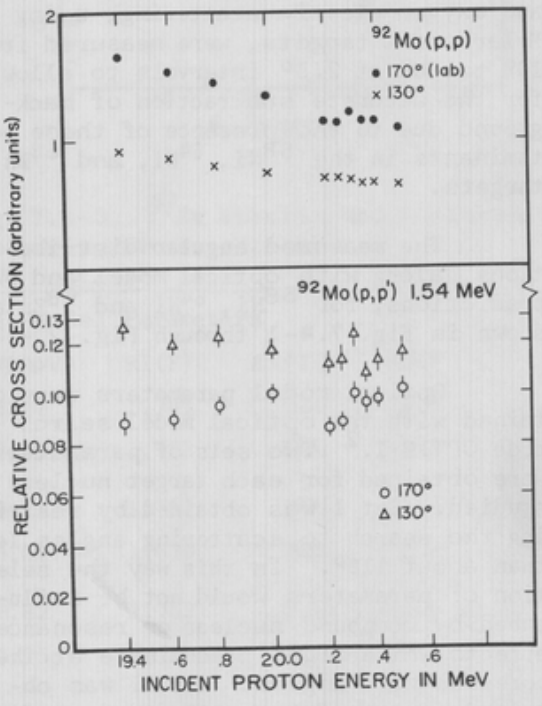

Fig. 7.3-2. ^{92}Mo(p,p) and (p,p') excitation functions at 130° and 170°(lab)

7.4 Elastic and Inelastic Scattering of 23.25 MeV Alpha Particles from ^{58}Ni, ^{64}Ni, and ^{68}Zn

We have measured the elastic and inelastic scattering angular distributions of 23.25 MeV alpha particles incident on the target nuclei ^{58}Ni, ^{64}Ni, and ^{68}Zn. These measurements were performed as a preliminary step to the intended measurements[1] of $(\alpha,\alpha'\gamma)$ correlations from nuclei in this mass region. Prior knowledge of the magnitudes of the inelastic cross sections of the first 2^+ excited states of these nuclei would be useful for estimating the counting rates available for the coincidence measurements. Second, it was desirable to obtain optical model parameters for subsequent collective-model distorted-wave Born-approximation analyses of the $(\alpha,\alpha'\gamma)$ correlation measurements.

The scattered particles were detected with six 700μ Si(Li) solid state detectors. The defining apertures for these detectors were 0.075 × 0.325 in. The angular acceptance of the 5 back-angle detectors which were placed 6 in. from the target and used to measure the cross sections at scattering angles greater than about 40° was about 0.7°, while that of the forward-angle counter (placed 24 in. from the target) was about 0.2°.

Angular distributions of carbon and oxygen elastic scattering, using Mylar and C targets, were measured from 10° to 80° at 2.5° intervals to allow for the accurate subtraction of background due to the presence of these contaminants in the ^{58}Ni, ^{64}Ni, and ^{68}Zn targets.

The measured angular distributions, along with optical model and DWBA predictions, for ^{58}Ni, ^{64}Ni and ^{68}Zn are shown in Fig. 7.4-1 through Fig. 7.4-3.

Optical model parameters were obtained with the optical model search code OPTIM-I.[2] Two sets of parameters were obtained for each target nucleus studied. Set I was obtained by restricting the search to scattering angles less than about 110°. In this way the selection of parameters would not be influenced by compound nuclear or resonance effects which might predominate at the more backward angles. Set II was obtained for the full angular range of the measurements. The parameters are listed in Table 7.4-1. Both parameter sets give quite good fits for ^{58}Ni over the full angular range of the data. The fits for ^{64}Ni and ^{68}Zn, however, deteri-

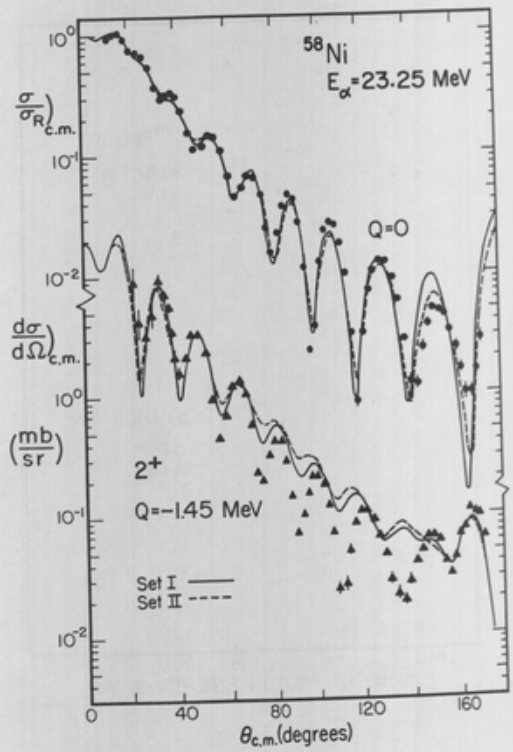

Fig. 7.4-1. ^{58}Ni elastic and inelastic scattering cross sections.

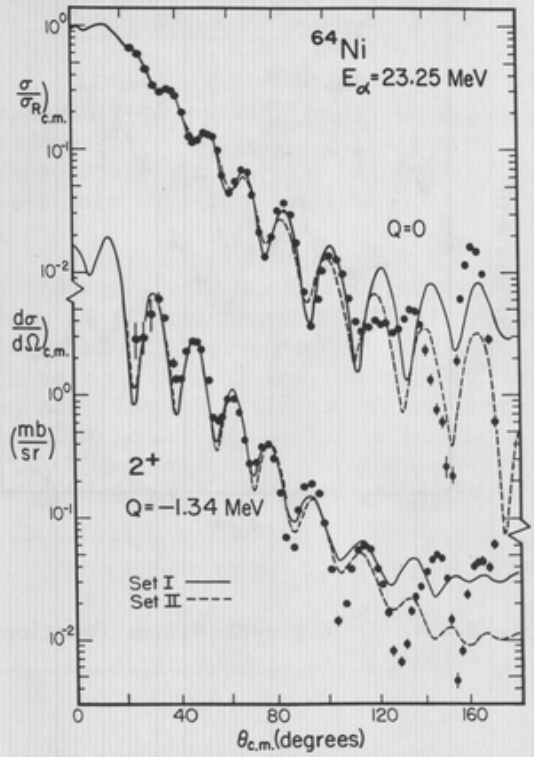

Fig. 7.4-2. ^{64}Ni elastic and inelastic scattering cross sections.

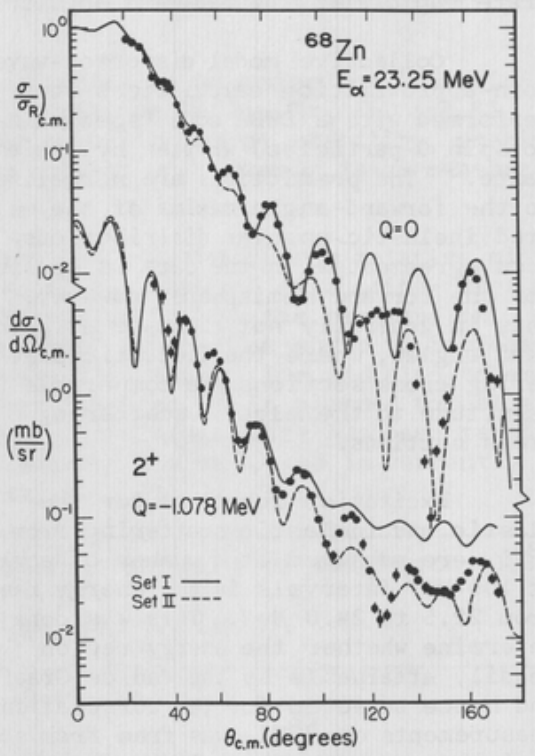

Fig. 7.4-3. ^{68}Zn elastic and inelastic scattering cross sections.

Table 7.4-1. Optical Model Parameters

		V(MeV)	RR(F)	AR(F)	WV(MeV)	RI(F)	AI(F)	RC(F)
^{58}Ni	I	43.62	1.657	.519	8.97	1.741	.309	1.4
	II	49.37	1.539	.629	7.53	1.783	.504	1.4
^{64}Ni	I	41.01	1.686	.499	10.29	1.752	.239	1.4
	II	46.27	1.636	.527	13.01	1.679	.335	1.4
^{68}Zn	I	43.75	1.657	.514	8.82	1.752	.230	1.4
	II	48.86	1.640	.525	10.25	1.710	.266	1.4

orate rapidly at the backward angles.

Collective model distorted-wave Born-approximation calculations were performed with a DWBA code (specialized to spin 0 particles) written by Braithwaite.[3] The predictions are normalized to the forward-angle maxima of the measured inelastic angular distributions. Good agreement with the data is obtained for the forward hemisphere; however, this is generally not the case at backward angles, where the inelastic scattering cross sections are comparable in magnitude to the elastic scattering cross sections.

Excitation functions for the elastic and inelastic scattering from ^{58}Ni were measured at a number of angles, at 100 keV intervals in the energy range from 22.5 to 24.0 MeV. This was done to determine whether the energy region readily attainable by the Van de Graaff, and hence selected for the correlation measurements on ^{58}Ni, was free from scattering resonances that might make the theoretical interpretation of the angular correlation measurements difficult.

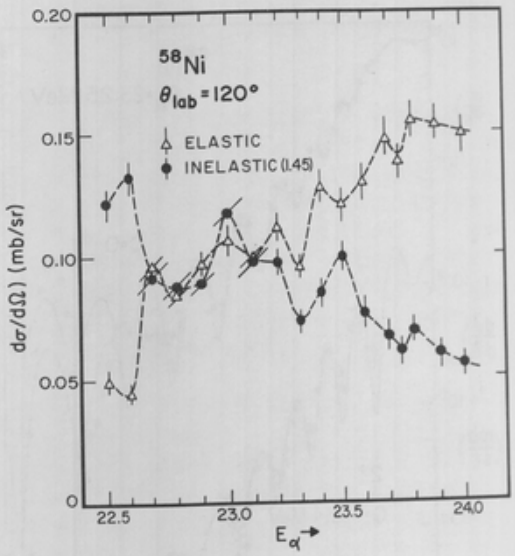

Fig. 7.4-4. ^{58}Ni; excitation function, θ_{lab} = 120°.

The data for θ_{lab} = 120° and θ_{lab} = 150° are shown in Figs. 7.4-4 and 7.4-5 respectively. Results at θ_{lab} = 130°, 140°, and 160° are similar to those shown. The cross sections do fluctuate somewhat but there appears to be no correlation between the different scattering angles, and little evidence for resonance structure for the energy step size taken. (J. Eenmaa, T.K. Lewellen, R. Marrs, D.M. Patterson, F.H. Schmidt, and J.R. Tesmer)

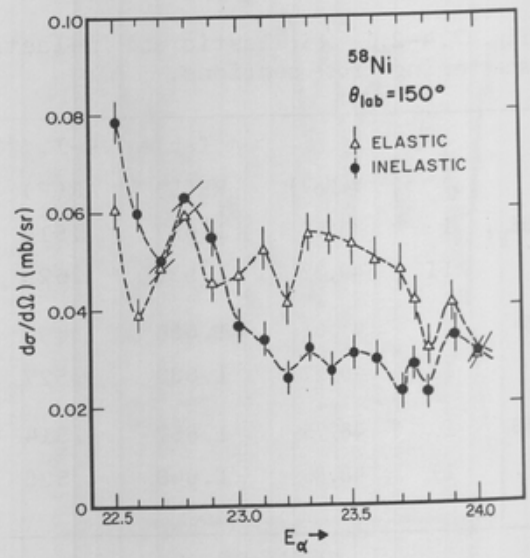

Fig. 7.4-5. ^{58}Ni; excitation function, θ_{lab} = 150°.

1. Section 6.5 of this report.
2. OPTIM-I, Optical Model Search Program, Report CYC-6835, University of Colorado Nuclear Physics Laboratory.
3. Nuclear Physics Laboratory Annual Report, University of Washington (1969), p. 20

7.5 Elastic Scattering of Alpha Particles from Zinc Isotopes and the Isotopic Dependence of Nuclear Radii

Elastic scattering of 42 MeV alpha particles to determine the isotopic dependence of nuclear radii has been done for various Ca, Ti, Cr, Fe, and Ni isotopes.[1,2] By using tight geometry and by requiring energy stability, precise comparisons can be made between radii. The present work extends these measurements into the zinc region.

Since the radii depend critically upon the location of the relative minima of the angular distribution of the scattered alphas, several data points must be taken where the cross section is relatively small. To ease the pressure on energy stability caused by long runs, some effort has been expended to increase the beam output of the cyclotron. To decrease data taking time and also to erase any question of angle reproducibility between isotopes, it is planned to use a position-sensitive detector in the regions of the minima. Data has been taken on ^{64}Zn, ^{66}Zn, and ^{68}Zn, in which earlier procedures[2] are used, and is currently being analyzed. (J.S. Blair and W.Q. Sumner)

---

1. Nuclear Physics Laboratory Annual Report, University of Washington (1968), p. 3.
2. B. Fernandez and J.S. Blair, Phys. Rev. *C1*, 523 (1970).

---

8. NUCLEON TRANSFER REACTIONS

8.1 The $^{12}C(\alpha,d)^{14}N$ Reaction at 42 MeV

Measurements have been made for the $^{12}C(\alpha,d)^{14}N$ reaction to the ^{14}N ground state and 3.95 MeV level. These data at E_α = 42 MeV, together with existing data at 47.5[1] and 53 MeV[2] allow us to study the energy dependence of this reaction over a considerable energy range and determine if this reaction is of a direct nature. This information is important to allow any conclusions to be drawn about the $^{12}C(\alpha,d^*)^{14}N$ reaction discussed in Sec. 8.2 of this report.

In this experiment a 200 $\mu g/cm^2$ natural carbon foil was bombarded with 42 MeV alphas from the cyclotron. The reaction products were identified using a detector telescope consisting of 200μ ΔE and a 3mm E counter. The amplified pulses were fed to an ORTEC particle identifier. A logic pulse from a single channel analyzer, set to include the output signals from the identifier corresponding to deuterons, was used to gate the energy signals. These gated signals were then stored in a 512 channel analyzer.

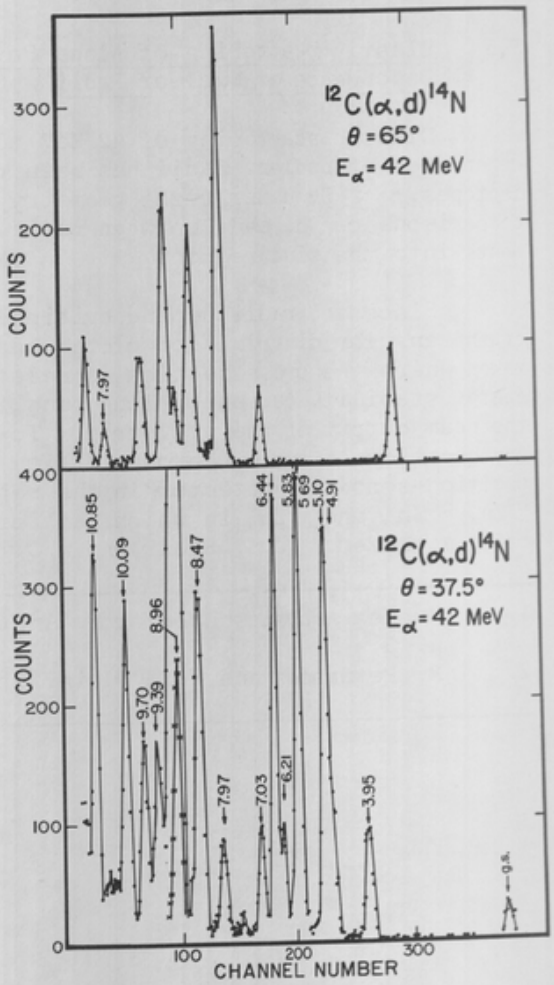

Fig. 8.1-1. Deuteron energy spectra from the reaction $^{12}C(\alpha,d)^{14}N$ at E_α = 42 MeV

The angular range covered by the measurements was 10° to 75° (lab). Spectra at scattering angles of 37.5° and 60° are shown in Fig. 8.1-1. The spectra at forward angles are dominated by the level at 9.0 MeV excitation as has been observed in the measurements made at higher energies. In the region of the 2.311 MeV ($J_\pi = 0^+$, T = 1) level no group was observed although a transition to this level having a strength of 5% of the 3.95 MeV level would easily be seen. This otherwise hindered, unnatural parity transition is completely forbidden by isospin conservation.

The angular distributions for the ground state and the 3.95 MeV level are shown in Fig. 8.1-2. These agree very well in shape and in absolute cross section with the data at the higher energies allowing one to conclude that the process is most probably proceeding via a direct reaction mechanism at these energies.

(W.J. Braithwaite, J.M. Cameron, J.G. Cramer, and C.R. Rudy)

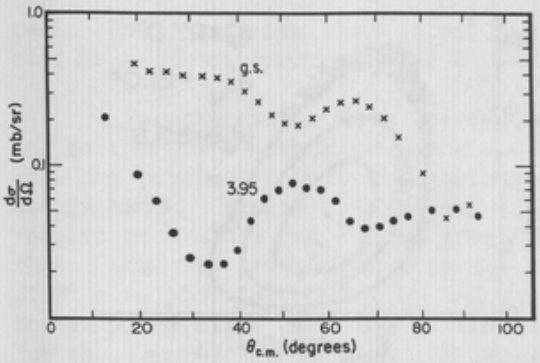

Fig. 8.1-2. Angular distribution for the reaction $^{12}C(\alpha,d)^{14}N$ for transitions to the ground state and 3.95 MeV level of ^{14}N.

1. B.G. Harvey and J. Cerny, Phys. R Rev. *120*, 2162 (1960).
2. R.H. Pehl, E. Rivet, J. Cerny, and B.G. Harvey, Phys. Rev.*137B*, 114 (1965).

8.2 Studies of p-n Final State Resonances Using the $^{12}C(\alpha,pn)^{14}N^*$ Reaction

The reactions $^{12}C(\alpha,p\ ^{14}N_{g.s.})n$, $^{12}C(\alpha,p\ ^{14}N_{2.31\ MeV})n$ and $^{12}C(\alpha,p\ ^{14}N_{3.95\ MeV})n$ have been studied by detecting recoiling ^{14}N nuclei in coincidence with protons in order to perform the isospin decomposition of the neutron-proton resonance (the $^1S_0$ portion referred to as the singlet deuteron) which occurs at low relative p-n energies. The experiment was performed using the 42 MeV alpha beam from the cyclotron to bombard a 40 μg/cm^2 carbon foil.

Protons were identified using a ΔE-E counter telescope, the identification being performed on-line using the SDS 930 computer. To accomplish this an integer array was generated to give $ID(I) = I^{\alpha}$ for $1 \leq I \leq 2048$ and $\alpha = 1.73$ (typically). Using this array as a look-up table, a particle identification number (PID) can be rapidly calculated using the algorithm $PID \propto ID(E+\Delta E)-ID(E)$. Figure 8.2-1 shows a typical PID spectrum generated in this fashion.

Recoiling mass-14 nuclei were identified on-line according to the criteria that mass $\propto Et^2$, the time of flight being determined relative to the cyclotron RF signal. A calibrated spectrum of mass values is shown in

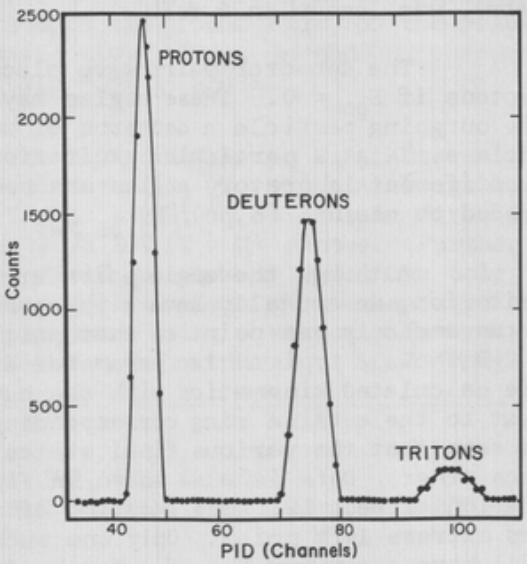

Fig. 8.2-1. A ΔE-E particle identification spectrum calculated on-line by the SDS 930 computer.

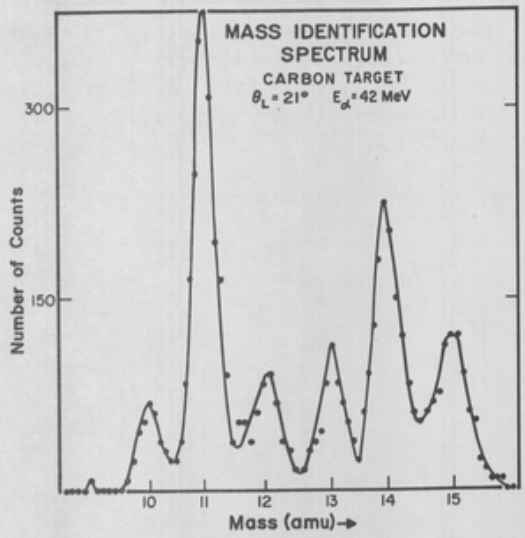

Fig. 8.2-2. Mass spectrum generated by the SDS 930 from the relation mass $\propto Et^2$.

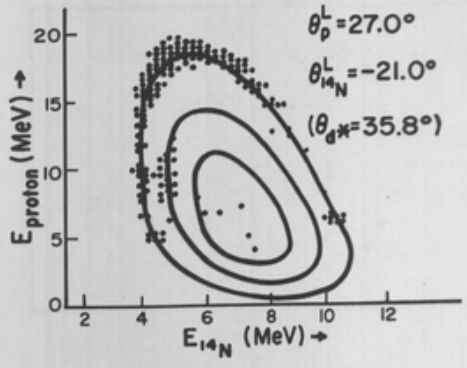

Fig. 8.2-3. Two-parameter data and kinematics for (α,pn) leading to the ground, 2.18 MeV and 3.95 MeV states in ^{14}N.

Fig. 8.2-2. The counter was placed at 45 cm from the target position since we needed to detect M = 14 nuclei at energies as low as 4 MeV. The beam repetition rate of our fixed frequency cyclotron is 87 nsec. This limits the length of transit time observable, thus imposing a low energy cutoff which, for our geometry, was less than 2 MeV.

The detector pairs were placed at angles which would allow detection of protons if $E_{pn} = 0$. These angles may be calculated from two-body kinematics with the outgoing particle a deuteron of zero binding energy (d*) and the recoil particle a ^{14}N at a particular excitation. Such angle pairs depend on Q-value and so different laboratory angles are needed to measure $(\alpha,pn)^{14}N_{g.s.}$ than are needed to measure $(\alpha,pn)^{14}N^*_{2.31\ MeV}$.

Although the angle pairs are chosen from the above mentioned two-body criterion, we actually have a three-body final state which defines a kinematic locus and only one point on that particular locus corresponds to $E_{pn} = 0$. Figure 8.2-3 shows a typical two parameter display of E_p vs E_{14_N}. The solid lines are the calculated kinematics with the outer ring corresponding to $(\alpha,pn)^{14}N_{g.s.}$, the next to the outside ring corresponding to $(\alpha,pn)^{14}N_{2.31\ MeV}$, etc. Thus it can be seen that the various final states of ^{14}N may be kinematically resolved from each other. Data is also shown in Fig. 8.2-3 for those channels whose count population exceeds 12. The location of minimum E_{pn} on a particular locus occurs at its extreme left point. Only one such locus may have minimum $E_{pn} = 0$, the others will have a minimum E_{pn} of a few hundred kilovolts.

Data was taken for the reaction $^{12}C(\alpha,d)^{14}N$(g.s. and 3.95 MeV) at incident alpha energies of 42 MeV.[1] This data is very similar to data[2] taken at 47.5 and 53 MeV which strongly suggests that $^{12}C(\alpha,d)$ is predominantly a direct pro-

cess. This suggests that (α,pn) may also be a direct process near $E_{pn} = 0$.

Two-parameter data corresponding to the left branch of the kinematic loci are projected onto the proton energy axis. Figure 8.2-4 shows the results of such a projection from two runs: the top projection when $\theta_{d^*} = 35.8°$ c.m. for $(\alpha,d^*)^{14}N_{g.s.}$ and the bottom projection when $\theta_{d^*} = 35.8°$ c.m. for the $(\alpha,d^*)^{14}N_{2.31\ MeV}$. An arrow in each frame shows the location of $E_{pn} = 0$.

The sharp peaks on the extreme right and left of the projected ground state plot correspond to strong sequential decays and are discussed elsewhere in the report.[3]

Similar data were taken for center of mass angles of about 20°, 30°, 40°, and 50°. In every case a strong enhancement was observed for (α,pn) leading to the 2.31 MeV (T = 1) state and no appreciable enhancement was seen for (α,pn) leading to the ground state (T = 0). Two further sets of angles were taken for (α,pn) leading to the 3.95 MeV (T = 0) state and no enhancement was seen there either. The enhancement seen in the 2.18 MeV (T = 1) yield is attributed to the pn final state interaction which, near $E_{pn} = 0$, strongly favors the $^1S_0$ (T = 1). Although the $^1S_0$ final state can populate the 2.18 MeV (T = 1) state, it is isospin forbidden to populate either the ground (T = 0) or the 3.95 MeV (T = 0) states. Further evidence from $^6Li(d,pn)^6Li^*$ work[4] shows a pn yield enhancement which can only correspond to a T = 1 pn final state. We therefore conclude that enhancement seen in the final state corresponds to the pn system being a strongly favored $^1S_0$. (W.J. Braithwaite, J.M. Cameron, J.G. Cramer, W.W. Eidson, and C.R. Rudy)

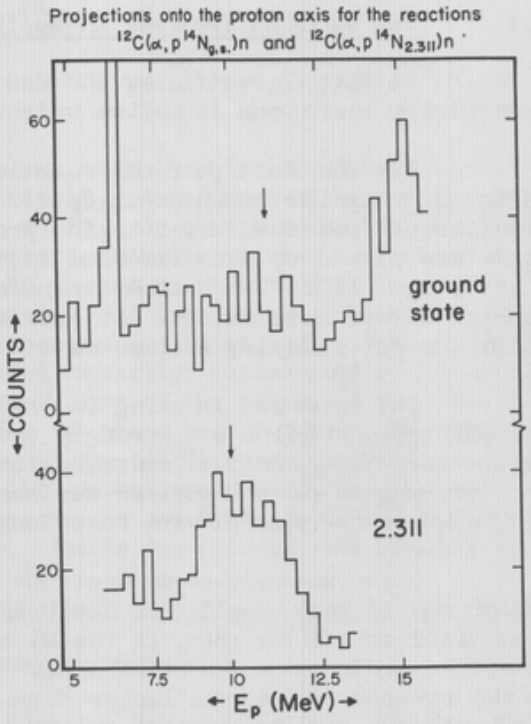

Fig. 8.2-4. Projections of two-parameter data onto the proton axis for the reactions $^{12}C(\alpha,p\ ^{14}N_{g.s.})n$ and $^{12}C(\alpha,p\ ^{14}N_{2.31\ MeV})n$.

---

1. Section 8.1 of this report.
2. B.G. Harvey and J. Cerny, Phys. Rev. *120*, 2162 (1960); R.H. Pehl, E. Rivet, J. Cerny, and B.G. Harvey, Phys. Rev. *137*, B114 (1965).
3. Section 11.1 of this report.
4. Section 5.7 of this report.

8.3 Two Nucleon Transfer in Medium Weight Nuclei Using the Reaction (α,^{6}He)

We have investigated the use of the (α,^{6}He) reaction to study two neutron pickup reactions in medium weight nuclei.

For the most part the reaction is subject to the same selection rules on parity and angular momentum as (p,t). Two neutrons in an s = 0 configuration are transferred from the target to the projectile. Thus, for example, if two neutrons are picked up from the same (ℓ,j) orbit the selection rules allow $0^+ \rightarrow 0^+$, $2^+, \cdots, (2j - 1)^+$. Two nucleon transfer reactions are discussed in more detail in Sec. 8.7 of this report. It suffices to say that they provide a sensitive technique for studying nuclear wave functions.

The interest in using (α,^{6}He) rather than (p,t) is that both incident and emitted particles are strongly absorbed in the nuclear potential. Thus it may be that the principal contributions to the transition matrix element arise from the region of the nuclear surface and exterior rather than the nuclear interior where the radial wave functions are less well known.

Unfortunately cross sections for the (α,^{6}He) reaction on medium weight nuclei may be very small. It has been observed[1] that (α,^{6}Li) reaction cross sections fall as 1/A so that, in the Ni region, the cross sections for (α,^{6}He) may be of the order of a few microbarns. Consequently the identification of ^{6}He ions in the presence of a much larger flux of α-particles is likely to be extremely difficult and the experiments are expected to be very time consuming.

In a preliminary attempt to observe the (α,^{6}He) reaction on ^{58}Ni and ^{60}Ni, a method of double particle identification was used. Targets of ^{58}Ni (350 $\mu g/cm^2$) and ^{60}Ni(920 $\mu g/cm^2$) were bombarded with 42 MeV alpha particles from the cyclotron. The outgoing particles were detected in a ΔE-E-anti 3 counter telescope using 35μ, 700μ and 1mm silicon detectors respectively. Determination of MZ^2 was made using the standard ΔE-E method of Goulding. An additional determination of particle mass was made by using the particle total energy in conjunction with a measurement of the particle time of flight with respect to the cyclotron beam pulse. This technique is discussed in Sec. 3.7 of this report. It was hoped that this double measurement would facilitate unambiguous identification of ^{6}He ions.

Using the ET^2 technique to determine mass, the uncertainty due to the time resolution ΔT is given by $\Delta M/M = 2\Delta T/T$ if the energy uncertainty is negligible. For 20 MeV ^{6}He particles and a flight path of 15 in. the observed time resolution of 2 nsec yields $\Delta M/M \sim 1/5$. With this resolution mass 4 and mass 6 particles were poorly separated so that little improvement in identification was obtained as a result of the additional mass determination.

In order to improve the mass resolution one must improve the time resolution, ΔT, and/or increase the flight path. At most the flight path can be 28 in. However the corresponding reduction in count rate would be unacceptable. Work is progressing on improving the resolution of the timing circuitry.
(M.P. Baker, D.R. Brown, J. Calarco, and N.S. Chant)

1. D.A. Bromley, BNL-948(C-46), Vol. 1, p. 121.

8.4 (p,t) Reactions on ^{46}Ti, ^{54}Fe, and ^{64}Zn

The study of two neutron pickup reactions on ^{46}Ti, ^{54}Fe, and ^{64}Zn, as reported last year,[1] has been continued.

Experimentally, one additional run was made in order to determine the energy levels of the final nuclei more accurately. A pulser was introduced into each spectrum to monitor any amplifier gain shift. An energy calibration curve was obtained from the kinematics of ground state transitions whose Q values were known; a separate curve was obtained for each target so target thickness uncertainties would only introduce errors of second order importance. Peaks in the spectra were fitted to a Gaussian to determine peak position. A number of data points were taken for each target at different detection angles and/or incident energies to give several independent determinations of the value of the excitation energies (E_x). To check the reliability of these measurements and the handling of the data, spectra were taken of the $^{48}Ti(p,t)^{46}Ti$ reaction, and the same method was followed to determine the E_x of the known levels of ^{46}Ti. For the first two levels, the measured and the known values are 0.884 ± 0.010, 2.008 ± 0.015 MeV and 0.889, 2.010 MeV respectively. Table 8.4-1 shows the summary of the levels observed.

Table 8.4-1. Summary of Levels

$^{64}Zn(p,t)^{62}Zn$	$^{54}Fe(p,t)^{52}Fe$	$^{46}Ti(p,t)^{44}Ti$
0.947 ± .008	.84 ± .01	1.085 ± .01
1.789 ± .015	2.382 ± .018	2.475 ± .015
2.786 ± .02		2.902 ± .015
3.204 ± .016		3.194 ± .03
		3.992 ± .021

Further attempts have been made to fit the angular distributions that have been obtained for these levels using the code JULIE. A complex form factor is calculated and read as input data to JULIE. Recently, however, JULIE has become unavailable and a new code has been written.[2] Attention has been given mainly to fitting the ground state, L = 0, transitions for the three target nuclei. So far, only pure wave function configurations have been used, both with and without the addition of finite range and non-locality. Although the fits in some cases are fair, it is hoped that consideration of the configuration mixing (which is expected particularly in the ^{54}Fe and ^{64}Zn region) will improve the results and make the fits more meaningful. (W. Jacobs, N. Mangelson and C. Ling)

1. Nuclear Physics Laboratory Annual Report, University of Washington (1969), p. 52.
2. Sections 8.7 and 8.9 of this report.

8.5 Sub-Coulomb Nucleon Transfer Reactions with Heavy Ions

An investigation was initiated to look for single nucleon transfer reactions induced by ^{16}O ions whose incident energies lie below the Coulomb barrier. Such reactions have long been heralded as tools for extracting spectroscopic factors in a relatively model-free fashion. Only recently, however, have successful experiments been reported[1] in which sub-Coulomb nucleon transfer has been induced by heavy ion bombardment of targets heavier than ^{40}Ca.

In the present preliminary study, ^{16}O ions with energies of 60 MeV (charge state 6^+) and 70 MeV (charge state 7^+) were directed onto 50 $\mu g/cm^2$ thick targets of ^{140}Ce and ^{208}Pb respectively and the reaction products were detected by silicon surface barrier detectors mounted in an array at angles of 90°, 110°, 160°, and 170° with respect to the incident beam direction. Beam collimators and defining slits in front of the detectors were chosen such that the solid

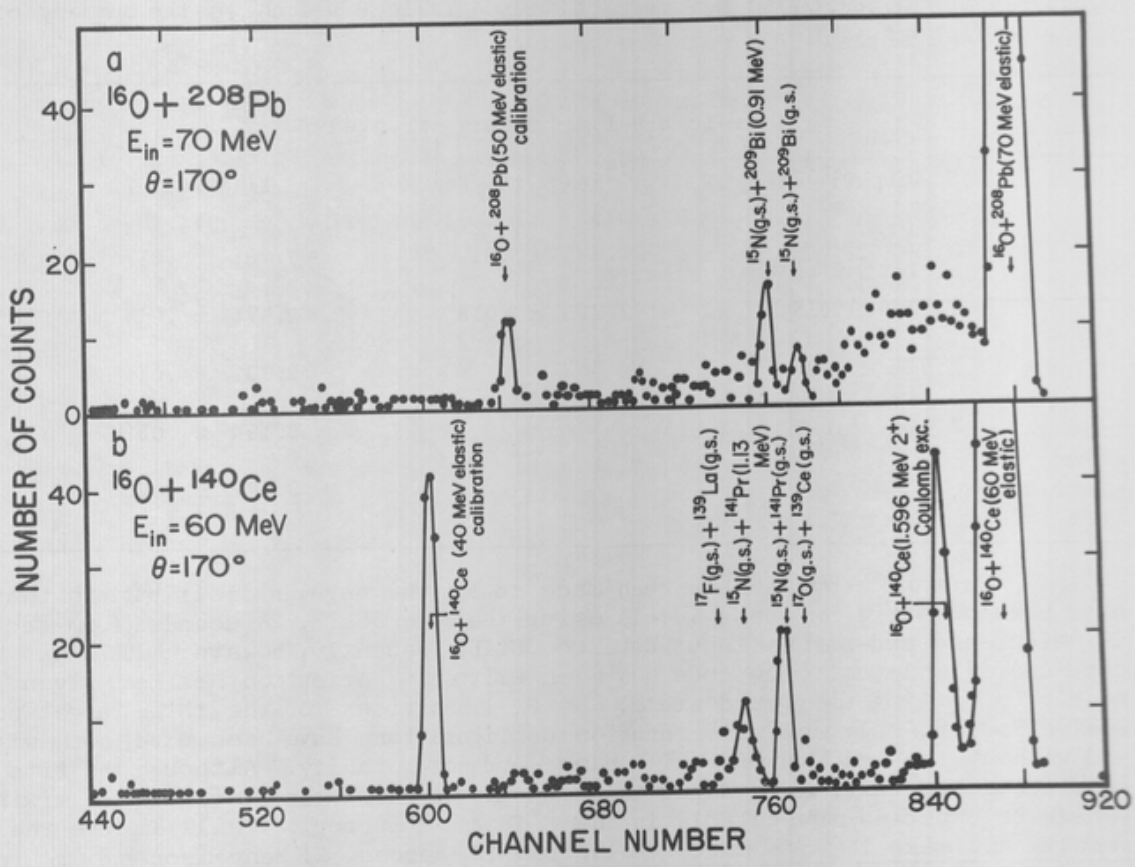

Fig. 8.5-1. The energy spectra of reaction products using 70 MeV and 60 MeV ^{16}O ions as projectiles and ^{208}Pb and ^{140}Ce as targets.

angle subtended at the detectors was 0.5×10^{-3} sr and the horizontal angular acceptance was 1°. With the aid of the recently installed direct extraction ion source,[2] an average beam intensity of 100 nanoamps at the target was obtained. With the ^{140}Ce target, the total integrated charge at the Faraday cup was 179 μC while with the ^{208}Pb target it was 213 μC.

Two typical energy spectra taken at 170° for the lead and cerium cases are shown in Figs. 8.5-1a and 1b respectively. No errors are indicated and the lines drawn through the points are intended only to guide the eye. The arrows indicate the kinematically allowed positions of peaks.

Because of our low beam intensity and the statistics of the run, the quality of the ^{208}Pb energy spectra is inferior to that reported by Barnett and Phillips. Only the reaction $^{208}Pb(^{16}O,^{15}N)^{209}Bi$(0.91 MeV) shows up clearly. However, in Fig. 8.5-1b, corresponding to the ^{140}Ce energy spectrum, there seems to be unambiguous evidence for the reactions $^{140}Ce(^{16}O,^{15}N)^{141}Pr$(g.s.) and $^{140}Ce(^{16}O,^{15}N)^{141}Pr$(1.13 MeV) as well as hints of other reactions.

Experiments are now in progress to increase the yield, improve the energy resolution and reduce the background for these heavy ion stripping and pickup reactions. Plans are also being made to accelerate ^{15}N ions so that highly favored positive Q-value reactions such as $(^{15}N,^{16}O)$ can be investigated. (J.S. Blair, W.J. Braithwaite, M. Mehta, and K.G. Nair)

1. A.R. Barnett and W.R. Phillips, *Reactions Induced by Heavy Ions*, ed. by R. Bock (North Holland Publishing Co., Amsterdam, 1970); Phys. Rev. *186*, 1205 (1969).
2. Section 1.2 of this report.

8.6 The $(^3He,\alpha)$ Reaction on ^{207}Pb and ^{90}Zr

The $(^3He,\alpha)$ reaction is unique among pickup reactions on heavier targets because of its large positive Q value. It is of interest to test if this feature makes possible the pickup of neutrons from deep lying single particle states where the ^3He and α particles have a good angular momentum overlap.[1] We report here on some preliminary work along this line.

In a previous study of the reaction $^{197}Au(^3He,\alpha)^{196}Au$ with $E_{^3He} = 22.5$ MeV, Chenevert and Halpern[2] observed a strong α yield at α energies corresponding to neutron pickup 15 MeV below the Fermi sea.

We did a DWBA calculation for $(^3He,\alpha)$ on ^{208}Pb which gave a similar strong α spectrum below the 3p-2f shell where the calculated α evaporation spectrum was negligible. The calculation was done on ^{208}Pb because it has good single particle configurations in the 3p-2f shell to which a bound state potential could be fit. Below the 3p-2f shell it is expected that the greatest difference between ^{208}Pb and ^{197}Au neutron states is in their spreading,not in their location; it was therefore thought the calculation on ^{208}Pb would be helpful in deciding if the α-particle strength could be attributed to neutron pickup from deep lying states. The observed binding energies of single-neutron states in the

3p-2f shell of ^{208}Pb can be fit with a Saxon-Woods potential V = 45.6 ± 0.8 MeV, with a spin orbit strength λ = 27.5 (where the spin orbit potential is λV/180.6 times the Thomas value) and a single set of geometric parameters.[3] This potential was used to compute the binding energies of single neutron states below the 3p-2f shell.[4] These binding energies were then used with the optical model parameters of Satchler *et al.*[5] in the DWBA code JULIE to calculate cross-sections for (^{3}He,α) pickup from these states. The splitting of the single particle strengths was approximated by spreading the cross section for each single particle pickup over a range of α particle energies with a Gaussian function. The spreading widths were varied for deep lying states until the best agreement with the α yield observed in the ^{197}Au(^{3}He,α) experiment was obtained. A graph of the observed and calculated α particle yield is shown in Fig. 8.6-1 where the agreement in shape and strength is seen to be quite good considering the simplicity of the calculation. The discrepancy above 31 MeV is attributed to the difference in the single particle configurations in the 3p-2f shell in ^{208}Pb and ^{197}Au.

The above calculation motivated us to do a (^{3}He,α) experiment on ^{208}Pb to see how well the calculated α spectrum fit the actual data. To see if the same simple pickup mechanism worked on other nuclei, ^{90}Zr was also investigated. ^{90}Zr was chosen because it has a closed neutron shell with good single particle states which would facilitate calculation. The ^{208}Pb and ^{90}Zr targets (1 mg/cm^2) were bombarded using, respectively, 24 MeV and 16 MeV ^{3}He beams from the tandem Van de Graaff. The particles were detected at 70° with respect to the beam direction in a ΔE-E counter telescope for particle identification. The ^{3}He and α particle spectra were each stored in 1024 channels on line in a SDS 930 computer.

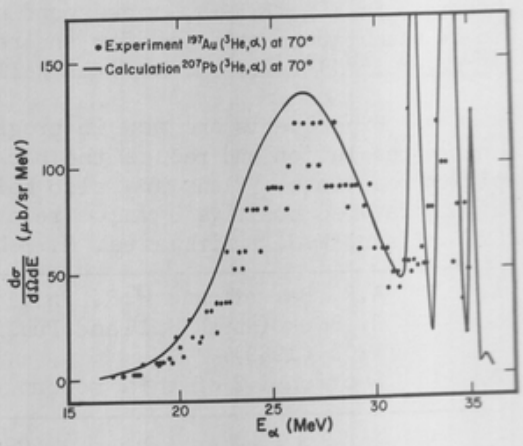

Fig. 8.6-1. Comparison of alpha particle energy spectrum for ^{197}Au(^{3}He,α) and calculated alpha particle spectrum from single neutron pickup from ^{208}Pb.

The data from this experiment are not completely analyzed but preliminary results are: 1) The appearance of strong α particle peaks at energies corresponding to neutron pickup from known single particle states in the 3p-2f and 2p shells in ^{208}Pb[5] and ^{90}Zr[7] respectively; (2) the appearance of α peaks in the ^{90}Zr data at energies corresponding to excitation of isobaric analog of the lowest proton hole states in ^{89}Y[8]; (3) a strong α spectrum in both Zr and Pb at energies below those corresponding to the single particle states mentioned in (1).

We are attempting to fit these latter spectra with a DWBA calculation of pickup from deeper lying neutron states assuming the Gaussian energy spreading described earlier.

(J.S. Blair, D.R. Brown, J.R. Calarco, I. Halpern, and R.H. Heffner)

1. R. Stack, R. Bock, P. David, H.H. Duhm, and T. Tamura, Nucl. Phys. *A104*, 136 (1967).
2. G. Chenevert and I. Halpern, Nuclear Physics Laboratory Annual Report, University of Washington (1967), p. 30.
3. W.C. Parkinson, D.L. Hendrie, H.H. Duhm, J. Mahoney, and J. Sandinos, Phys. Rev. *178*, 1976 (1969).
4. S.M. Perez, Oxford University Nuclear Physics Theoretical Group Report 35 (unpublished).
5. G.R. Satchler, W.C. Parkinson, and D.L. Hendrie, Phys. Rev. *187*, 1491 (1969).
6. R.H. Bassel, G.R. Satchler, and R.M. Dusko, Oak Ridge National Laboratory Report ORNL-3240 (1962) and Supplements (unpublished).
7. J.B. Ball and C.B. Fullmer, Phys. Rev. *172*, 1199 (1968).
8. C.M. Fou, R.W. Zurmühle and J.M. Joyce, Phys. Rev. *155*, 1248 (1967).

8.7 Studies in the Theory of Two-Nucleon Transfer Reactions

Our studies of the distorted wave Born approximation (DWBA) theory of two nucleon transfer reactions have been continued. As previously reported[1] we have been concerned largely with methods of taking into account effects due to the finite range of the nucleon-nucleon interaction and of the light particle wave functions. An approximate treatment of these effects has already been given by Bencze and Zimanyi[2] based upon the local W.K.B. approximation. We have shown that techniques for evaluating finite range effects in single nucleon transfer reactions[3-5] can be combined with current formulations of the DWBA theory for two-nucleon transfer in a simple manner and have obtained an expression for the DWBA radial integral which is expected to be more accurate than the local W.K.B. approximation result. In addition we have carried out calculations to indicate the magnitude of these effects.

Details of our derivation and sample calculations have been published.[6] In the formalism presented we considered pickup reactions A(a,b)B where a = 1 or 2 so that our results are applicable both to nucleon induced pickup and (d,α) reactions as well as the inverse processes.

For the emitted particle wave function and for the nucleon-nucleon residual interaction V_{ai} a Gaussian form was assumed

$$\Phi_b = N \exp(-\eta^2 \sum_{i<j} r_{ij}^2) \qquad (1)$$

$$V_{ij} = U_0 \exp(-\beta^2 r_{ij}^2) \qquad (2)$$

where $\underline{r}_{ij} = \underline{r}_i - \underline{r}_j$ and N is a normalization constant. The wave functions of the two picked up nucleons were assumed to be eigen-functions of a Woods-Saxon well. As pointed out by Glendenning,[7] the relative motion of two such nucleons can be dealt with exactly by expanding the wave functions as a series of eigenfunctions of an harmonic oscillator potential. By utilizing the transformation properties of the oscillator wave functions[8,9] the integration over the relative coordinate

of these nucleons was carried out and the remaining finite range effects were then taken into account using Taylor's series expansions. The following expression was obtained for the DWBA integral

$$I^{\ell_1 \ell_2 L}_{\Lambda} = \pi^{3/2} C_0 \varepsilon^{-3} \int \chi_b^{(-)*}(\underline{r}_b) \exp\left(\frac{[C_a \nabla_a^2 + C_b \nabla_b^2 + C_x \nabla_x^2]}{4\varepsilon^2}\right) \times F_x(\underline{r}_b)\, \chi_a^{(+)}(\gamma \underline{r}_b) d\underline{r}_b \tag{3}$$

where χ_a and χ_b are the distorted waves, F_x is the zero range form factor[6] and the exponential operator is defined by its series expansion. The quantities C_i are constants, $\gamma = B/A$ and $\varepsilon^2 = \beta^2 + 2a\eta^2$. The Laplacian operator ∇_a^2 operates on $\chi_a^{(+)}$ and is a function of $\gamma \underline{r}_b$, ∇_x^2 operates on F_x and ∇_b^2 operates upon both a and x. Equation 3 is exact. If we define a potential V_x such that

$$\frac{-\hbar^2}{2m_x} \nabla_x^2 F_x + V_x F_x = E_x F_x \tag{4}$$

where

$$m_x = \frac{xB}{A} m_0 \tag{5}$$

and where E_x is the total energy of the nucleon pair x and m_0 is one a.m.u. we can proceed as in Ref. 3 and obtain

$$I^{\ell_1 \ell_2 L}_{\Lambda} = \pi^{3/2} C_0 \varepsilon^{-3} \int \chi_b^{(-)*}(\underline{r}_b)\, F_x(\underline{r}_b)\, \chi_a^{(+)}(\gamma \underline{r}_b) \times \exp\left(\frac{2m_0}{\hbar^2} \cdot \frac{xa}{b} \cdot \frac{1}{4\varepsilon^2} [V_a + V_x - V_b + S_x]\right) d\underline{r}_b . \tag{6}$$

In the expression (6) V_a and V_b are the optical potentials for the particles a and b and the quantity $S_x = E_b - E_a - E_x$ is the energy required to break up b into a plus two nucleons. The expression (6) is obtained by evaluating the effects of the exponential operator in local W.K.B. approximation in which terms involving ∇^2 operating upon a potential are assumed to be negligible in comparison with terms in which ∇^2 operates upon a wave function. This procedure has been found to give useful results for single nucleon transfer and a second order correction term can be given.[5] However, in the present case, terms such as $\nabla_x^2 V_x$ may not be negligible and we prefer to evaluate the effects of the exponential operator acting upon the form factor F_x exactly. We write

$$G_x(\underline{r}_b) = \exp\left(\frac{C_x \nabla_x^2}{4\varepsilon^2}\right) F_x(\underline{r}_b) \tag{7}$$

where

$$\nabla_x^2 \equiv \frac{1}{r}\frac{d^2}{dr^2}\, r - \frac{L(L+1)}{r^2} \tag{8}$$

since F_x carries angular momentum L and Eq. (7) can be evaluated accurately by successive numerical differentiation.

Using (7) and proceeding in a similar manner to Ref. 5, we obtain

$$I^{\ell_1\ell_2 L}_{\Lambda} = \pi^{3/2} C_0 \varepsilon^{-3} \int \chi_b^{(-)*}(\underline{r}_b)\, G_x(\underline{r}_b)\, \chi_a^{(+)}(\gamma \underline{r}_b)$$

$$\times \exp\left(\frac{2m_0}{\hbar^2} \cdot \frac{xa}{b} \cdot \frac{1}{4\varepsilon^2}\,[V_a - V_b + Q]\right) d\underline{r}_b \tag{9}$$

$$+ \pi^{3/2} C_0 \varepsilon^{-3} \int [C_a^2\, \chi_b^{(-)*}(\underline{r}_b)\, G_x(\underline{r}_b)\, X_a + C_b\, X_b G_x(\underline{r}_b)\, \chi_a^{(+)}(\gamma \underline{r}_b)] \frac{1}{32\varepsilon^4}\, d\underline{r}_b .$$

The quantity $Q = E_b - E_a$ is the energy released in the reaction. The quantity X_a is given by

$$X_a = \frac{2m_a}{\hbar^2}\,[\chi_a \nabla^2 V_a + 2\nabla V_a \cdot \nabla \chi_a] \tag{10}$$

while X_b is defined similarly. The reduced masses are $m_a = aAm_0/(A + a)$ and $m_b = bBm_0/(B + b)$. The expression (9) is approximate. The first part results from including terms involving ∇^2 operating upon the distorted wave functions to all orders in the expansion of the exponential operator appearing in (3) in powers of $1/4\varepsilon^2$. The second part of (9) consists of terms involving ∇^2 operating upon the optical potentials and includes terms up to $(1/4\varepsilon^2)^2$.

In Eq. (9) we have given an approximate method for taking into account finite range effects in two-nucleon transfer calculations. The first integral of (9) can be regarded as the expression for the first order correction. Inclusion of the second order correction given in the second integral should give a valuable indication of the convergence and hence validity of our approach.

Even to first order our expression is expected to be more accurate than Bencze and Zimanyi's result.[2] These authors use Taylor's series expansions in order to carry out the integrations over both the relative coordinate of the transferred nucleon pair, $\underline{r}_{12}$, and the finite interaction coordinate, $\underline{p}$, which describes the separation of the center of mass of the nucleon pair from the projectile. The resultant Laplacian operators are evaluated in local W.K.B. approximation while an operator of the form $\exp(C\nabla_1 \cdot \nabla_2)$ is evaluated only after truncating the series expansion of the exponential. In contrast, in our expression in Eq. (9) the integration over the coordinate $\underline{r}_{12}$ has been carried out exactly.

In the integration over the coordinate $\underline{p}$, Taylor series expansions have been used. The resultant Laplacian operators acting upon the distorted waves are evaluated in local W.K.B. approximation. However, the remaining operator which acts upon the form factor is evaluated exactly using a numerical technique.

In order to investigate the importance of finite range corrections in two nucleon transfer we have carried out a series of distorted wave Born approximation calculations carried out using the first order finite range interaction theory (FRI) described above. These calculations were compared with calculations carried out using the more approximate finite range theory of Bencze and Zimanyi[2] (BZ) and with calculations in which the interaction was assumed to be of zero range in the separation of the centers of mass of the transferred nucleon pair and the incident projectile (ZRI).

In the derivation of the BZ theory in Ref. 2 the presentation was simplified by omitting recoil effects and by assuming that the range parameters were related by $\beta^2 \approx 2a\eta^2$. These approximations are somewhat unrealistic and have been eliminated in the BZ calculations presented here. An outline of the BZ theory used is given in Ref. 6. In the ZRI calculations the interaction was assumed to be zero range only in the coordinate $\underline{p}$. Calculations utilizing this approximation have been performed by Drisko and Rybicki.[10] The expression evaluated in our own calculations is actually given by Eq. (14a) with the exponential operator replaced by

$$\exp\left(\frac{2m_0}{\hbar^2} \cdot \frac{xa}{b} \cdot \frac{S_x}{4\varepsilon^2}\right). \tag{11}$$

This corresponds to choosing the normalization of the ZRI calculations so that the radial form factor has approximately the same amplitude at large radii as in the FRI calculations.

All three types of calculation depend upon the inverse ranges η and β. . Values of η, the size parameter of the emitted particle wave function, are reasonably well established by electron scattering experiments. We have used the values tabulated by Glendenning[7] $0.242F^{-1}$ for tritons and $0.202F^{-1}$ for ^{3}He particles. Unfortunately the parameter β, which is the reciprocal of the range of the nucleon-nucleon effective interaction, is less well determined. Bencze and Zimanyi[2] choose $\beta^2 \approx 2\eta^2 = 0.14F^{-2}$. However the range of the effective interaction is not expected to exceed the range of the free nucleon-nucleon interaction. For the free interaction the effective range and scattering length are reproduced by a Gaussian potential with $\beta^2 \approx 0.3F^{-2}$. Thus the choice made by Henley and Yu[11] of $\beta^2 = 0.4F^{-2}$ (and $U_0 = 70$ MeV) which is consistent with the deuteron binding energy is reasonable and is used in the calculations which follow.

In Fig. 8.7-1 calculations are shown for the ^{58}Ni(p,t)^{56}Ni reaction at 50 MeV leading to the ground state. This is an L = 0 transition. In Fig. 8.7-2 calculations are shown for an L = 2 transition leading to the 2.64 MeV excited state of ^{56}Ni. In both cases the transferred neutrons were assumed to originate from the 1f shell. The optical parameters used are taken from the literature and

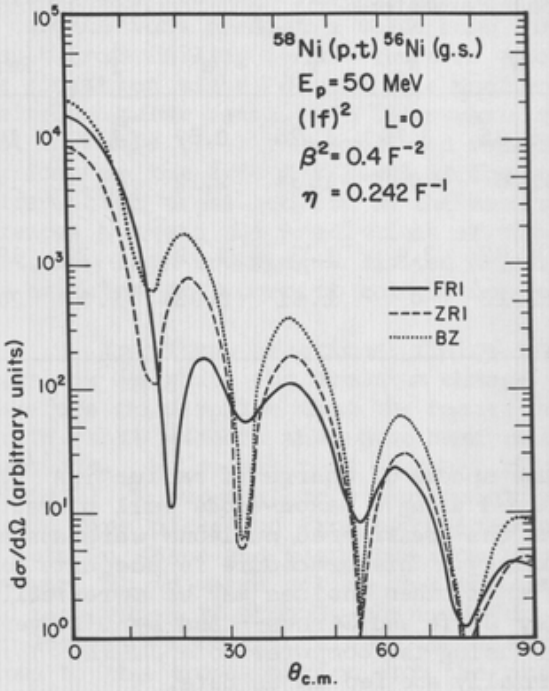

Fig. 8.7-1. Distorted wave calculations for the reaction ^{58}Ni(p,t)^{56}Ni(g.s.) at E_p = 50 MeV. The transferred nucleons were assumed to originate from a pure $(1f)^2$ configuration with total orbital angular momentum L = 0. The finite range interaction calculation is denoted by FRI, the zero range interaction calculation by ZRI and the calculations following the method of Bencze and Zimanyi by BZ.

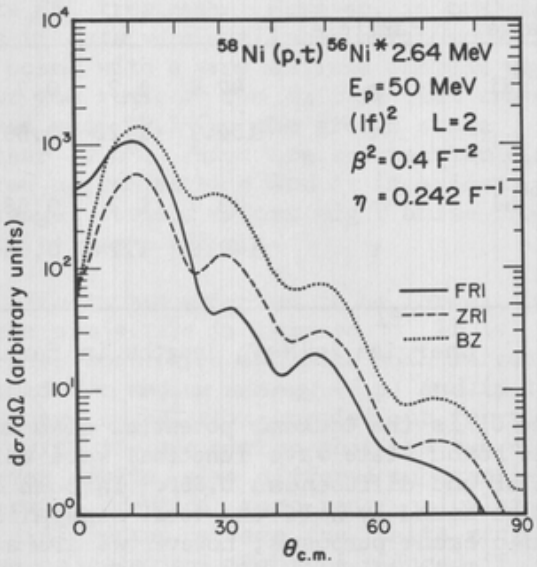

Fig. 8.7-2. Distorted wave calculations for the reaction ^{58}Ni(p,t)^{56}Ni(g.s.) at E_p = 50 MeV. The transferred nucleons were assumed to originate from a pure $(1f)^2$ configuration with total orbital angular momentum L = 2. The finite range interaction calculation is denoted by FRI, the zero range interaction calculation by ZRI and the calculations following the method of Bencze and Zimanyi by BZ.

are listed in Table 8.7-1. The optical potential used is defined by

$$U(r) = -\frac{V}{1+e^{x}} - \frac{iW}{1+e^{x'}} - \frac{4iW_D\, e^{x'}}{(1+e^{x'})^2} + U_c$$

where

$$x = \frac{r - r_0 A^{1/3}}{a} \qquad (12)$$

$$x' = \frac{r - r_0' A^{1/3}}{a'}$$

Table 8.7-1 Optical Parameters[a]

Target	Particle	V	r_0	a	W	W_0	r_0'	a'	r_c	Ref.
^{58}Ni	p	42.6	1.2	0.7	5.65	3.75	1.25	0.67	1.2	14
	t	152.9	1.26	0.69	31.6	0	1.34	1.12	1.26	14
^{60}Ni	p	43.0	1.2	0.68	4.42	3.4	1.3	0.62	1.3	19
	t	149.87	1.245	0.68	25.13	0	1.61	0.934	1.3	20

a Energies in MeV, lengths in fermis.

and U_c is the Coulomb potential of a uniform sphere of charge of radius $r_c A^{1/3}$. The bound state wave functions were calculated using a Saxon-Woods well of radius 1.25F and diffuseness 0.65F. In both cases the transferred nucleons were assumed to be bound by half the total separation energy. This procedure is adequate for our present purposes; however we are aware that other choices may be more realistic. This point is discussed for example by Jaffe and Gerace[12] and by L'Ecuyer *et al.*[13] The calculations were carried out using the computer code JULIE. The (complex) form factors were generated externally and fed in as data.

In Figs. 8.7-1 and 8.7-2 large differences in the magnitude of the cross sections predicted in the three calculations are evident for both transitions although the BZ and ZRI predictions are quite similar in shape. However the FRI calculations, which are intermediate in magnitude between the ZRI and BZ calculations at forward angles, fall considerably below the other curves at wider angles. In order to give an indication of how the three approximations might influence a test of wave functions for ^{58}Ni and ^{56}Ni using the (p,t) reaction we have listed in Table 8.7-2 the values predicted for the ratio of the cross section for the 2.64 MeV level to the cross section for the ground state using the calculations shown in Figs. 8.7-1 and 8.7-2. In the first column the ratios of total cross

Table 8.7-2. Cross section ratios predicted for the reaction ^{58}Ni(p,t)^{56}Ni at 50 MeV

Approximation	$\frac{\sigma_{total}(2.64\ MeV)}{\sigma_{total}(g.s.)}$	$\frac{d\sigma/d\Omega(2.64\ MeV, 12.5^\circ)}{d\sigma/d\Omega(g.s., 22.5^\circ)}$
ZRI	0.34	0.75
BZ	0.40	0.85
FRI	0.33	5.90

sections are listed. The FRI and ZRI predictions are almost identical while the BZ calculations predict a value some 20% higher. Consequently little error would result from failing to use the more accurate FRI treatment. However, in practise, the situation might be much more precarious if data were available only over a limited angular range. To illustrate this point with a very extreme example we list in Table 8.7-2 the predicted values for the ratio of the differential cross section for the 2.64 MeV level at the maximum near 12.5° to the ground state differential cross section at the maximum near 22.5°. There are spectacular differences between the predictions of the three approximations and it is evident that, for data covering a limited angular range, serious errors might arise from the omission or incorrect calculation of finite range effects.

In pickup reactions, finite range effects are expected to be largest in reactions in which the momentum change of the projectile is largest.[15] It is therefore no surprise that the reaction we have considered exhibits much larger finite range effects than have been calculated for medium energy (d,p) and (p,d) reactions. We recall that an exact finite range calculation carried out for the $^{40}Ca(d,\alpha)^{38}K$ two-nucleon pickup reaction,[15] with the assumption that the two nucleons were picked up from harmonic oscillator orbits, also differed substantially both in shape and magnitude from an otherwise identical zero range calculation. However, it is worth noting that the large differences between the finite range and zero range treatments observed for these calculations might be reduced if non-locality corrections were included[16] owing to the suppression of contributions to the cross-section from the nuclear interior.[15]

In order to investigate this point and as part of an investigation of the structure of the even nickel isotopes using the (p,t) reaction we have carried out calculations for the reaction $^{60}Ni(p,t)^{58}Ni$. The data were obtained using 50 MeV protons from the RHEL linear accelerator and a preliminary analysis has been presented[17] using the zero range interaction approximation of Glendenning.[7] In these calculations it was found that by increasing the imaginary part of the triton optical potential from 25 MeV, which best reproduces elastic scattering data, to 50 MeV much improved agreement with the experimental angular distributions could be obtained. In Ref. 17 this effect was ascribed to the omission of finite range corrections. In Fig. 8.7-3 we show calculations for transitions to the first 3 levels of ^{58}Ni. The optical potentials used are listed in Table 8.7-2 and include a triton imaginary well depth of 25 MeV. In the figure the calculations denoted by ZRI follow our zero-range interaction prescription[6] while FRNL denotes calculations in which we have included our first order finite range correction together with corrections for non-locality of 0.85F for nucleons and 0.2F for tritons. The two approximations lead to absolute cross sections which differ by nearly a factor of two. However, in the figure, where we have adjusted the two sets of curves to have the same magnitude at the maximum in the L = 2 distribution, it is clear that both the shapes and relative magnitudes are very similar in the two cases.

In carrying out the calculations for Fig. 8.7-3, spectroscopic amplitudes were used which were calculated from the shell model wave functions of Cohen *et al.*[18] using his matrix element set "C". In these wave functions the transferred neutrons originate from the $1f_{5/2}$, $2p_{3/2}$, and $2p_{1/2}$ orbits and the (p,t) predictions are very sensitive to the admixtures.[17] In Fig. 8.7-3 the same

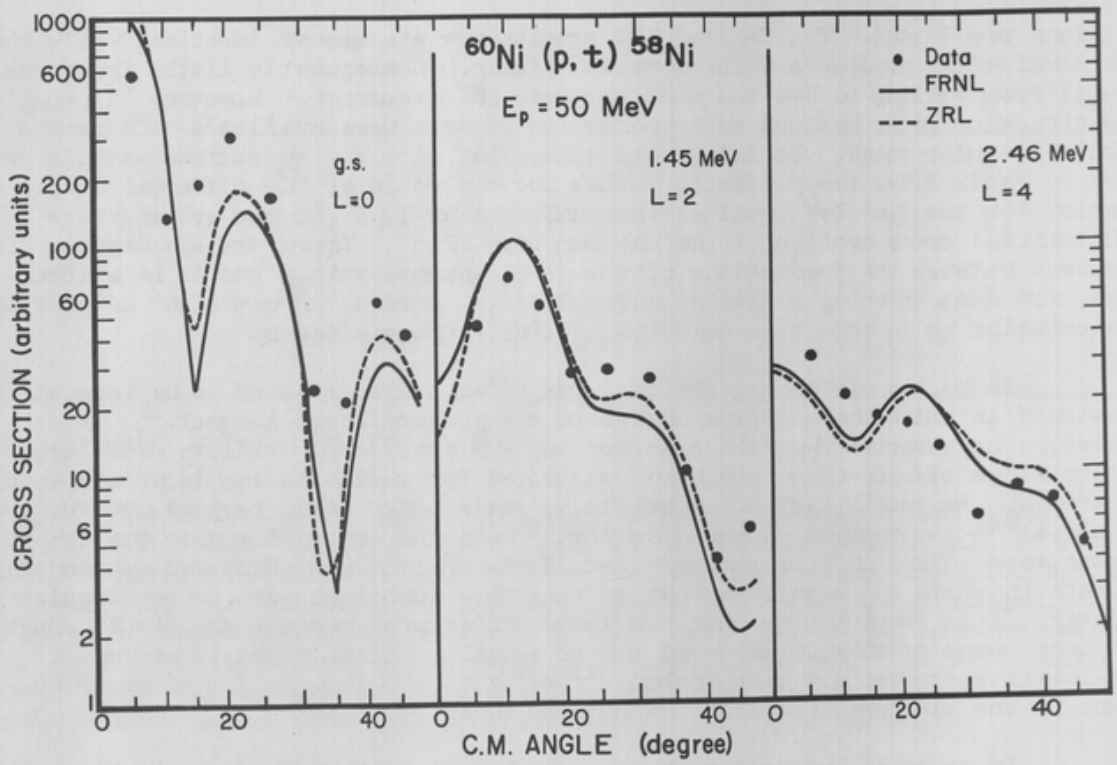

Fig. 8.7-3. Distorted wave calculations for the reaction ^{60}Ni(p,t)^{58}Ni at E_p = 50 MeV. The finite range non-local calculation is denoted by FRNL and the zero-range local calculation by ZRL.

normalization between theory and experiment was used for the three transitions shown and it is evident that Cohen's wave functions lead to reasonable predictions for the relative cross-sections. However the fits to the angular distributions are poor and, as yet, we have only succeeded in generating improved fits by increasing the triton imaginary potential. Thus our earlier conjecture that the effect of increasing the triton imaginary well is equivalent to including finite range corrections appears to be in error. Further calculations are planned. (N.S. Chant)

---

1. Nuclear Physics Laboratory Annual Report, University of Washington (1969), p. 63.
2. Gy. Bencze and J. Zimanyi, Nucl. Phys. *81*, 76 (1966).
3. Gy. Bencze and J. Zimanyi, Phys. Letters *9*, 126 (1964).
4. P.G.A. Buttle and L.J.B. Goldfarb, Proc. Phys. Soc. *83*, 701 (1964).
5. W.R. Smith, Nucl. Phys. *A94*, 550 (1967).
6. N.S. Chant and N.F. Mangelson, Nucl. Phys. *A140*, 81 (1970).
7. N.K. Glendenning, Phys. Rev. *137*, B102 (1965).
8. T.A. Brody and M. Moshinsky, Tables of Transformation Brackets (Monografias del Instituto de Fisica, Mexico 1960).

9. M. Baranger and K. Davies, Nucl. Phys. *79*, 403 (1966).
10. R.M. Drisko and F. Rybicki, Phys. Rev. Letters *16*, 275 (1966).
11. E.M. Henley and D.V.L. Yu, Phys. Rev. *133*, B1445 (1964).
12. R.L. Jaffe and W.J. Gerace, Nucl. Phys. *A125*, 1 (1969).
13. J. L'Ecuyer *et al.* To be published in Phys. Rev.
14. W.G. Davies *et al.*, Phys. Letters *27B*, 363 (1968).
15. R.M. Drisko and G.R. Satchler, Phys. Letters *9*, 342 (1964).
16. F.G. Perey, in *Direct Interactions and Nuclear Reaction Mechanisms*, ed. by E. Clementel and C. Villi (Gordon and Breach, New York, 1962), p. 125.
17. W.G. Davies *et al.*, *Proc. International Conf. on Properties of Nuclear States*, Montreal, 1969 (to be published).
18. S.G. Cohen *et al.*, Phys. Rev. *160*, 903 (1967).
19. Lingappa *et al.*, Williams Laboratory of Nuclear Physics Annual Report, University of Minnesota (1967), p. 21.
20. Hafele *et al.*, Phys. Rev. *155*, 1238 (1967).

8.8 The Prediction of Spectroscopic Quantities for One and Two-Nucleon Transfer Reactions for 1p-Shell Nuclei

The object of most studies of one-and two-nucleon transfer reactions is to test calculations of wave functions for the initial and final nuclear states involved. Generally such tests involve combining the results of DWBA calculations with spectroscopic quantities calculated from the nuclear wave functions. In the case of the 1p shell nuclei, wave functions obtained in intermediate coupling shell model calculations have been tabulated[1,2] so that calculation of spectroscopic quantities is relatively simple. In order to further simplify such calculations we have written two computer programs, one for single nucleon transfer and the other for two nucleon transfer. Both programs employ LS coupled basis functions for compatibility with the tabulations of Refs. 1 and 2.

In the case of one-nucleon transfer the quantity most convenient for comparison with theory is the spectroscopic factor[3] which is obtained experimentally by determining the ratio of the experimental cross section to some DWBA prediction. The theoretical calculation of this quantity is described in Ref. 3 for the case of wave functions written in an LS coupled basis and the resultant expression is evaluated in our one nuclear transfer program. Along with details of the nuclear wave functions, the input data must include the LS coupling one-particle coefficients of fractional parentage tabulated by Jahn and Van Wieringen[4] with the phase corrections given by Elliott *et al.*[5] As output the program lists configurations which are connected in the transition in question as well as the spectroscopic factor. We have used this program to calculate theoretical spectroscopic factors for an analysis of the reaction $^{13}C(p,d)^{12}C$ which has now been published.[7] In addition we have calculated spectroscopic factors for the reactions $^{7}Li(d,t)^{6}Li$ and $^{7}Li(d,^{3}He)^{6}Li$ discussed in Sec. 5.8 of this report.

For two nucleon transfer, spectroscopic amplitudes must be calculated theoretically and used in a DWBA calculation before a comparison between experiment and theory can be made.[6] The calculation of these amplitudes is similar to the calculation of single nucleon transfer spectroscopic factors and an expression appropriate to the case of LS coupled basis functions is described in Ref.6. This expression is evaluated in our two-nucleon transfer program. For this

program the two particle fractional parentage coefficients tabulated by Elliott *et al.*[5] must be supplied as input data in addition to the details of the nuclear wave functions. This program has been used to evaluate spectroscopic amplitudes for the reaction $^{14}N(p,^{3}He)^{12}C$ which was analyzed and published.[7] Finally we have evaluated spectroscopic amplitudes needed for the analysis of the $^{12}C(\alpha,d)^{14}N$ and $^{12}C(\alpha,pn)^{14}N$ reactions discussed in Sec. 8.2 of this report. (N.S. Chant)

1. A.N. Boyarkina, Bull. Acad. Sci. USSR Phys. Ser. *28*,255 (1964).
2. F.C. Barker, Nucl. Phys. *83*, 418 (1966).
3. M.H. Macfarlane and J.B. French, Rev. Mod. Phys. *32*, 567 (1960).
4. H.A. Jahn and H. Van Wieringen, *Proc. Royal Soc.* (London) , 515 (1952).
5. J.P. Elliott *et al.*, Phil. Trans. *A246*, 241 (1953).
6. J.C. Hardy and I.S. Tanner, Nuclear Physics Laboratory Report, Oxford.
7. D.K. Scott *et al.*, Nucl. Phys. *A141*, 497 (1970).

8.9 A Simple DWBA Program for Nucleon Transfer Reaction Calculations

Most of the two-nucleon transfer calculations described in Sec. 8.7 of this report were carried out using the Oak Ridge DWBA code JULIE run on the university of Washington IBM-7094-7040 direct coupled system. Complex form factors were calculated using subsidiary programs and fed as input data to JULIE. When the IBM computer was replaced by a CDC-6400 system the program JULIE became unavailable and a simple DWBA program TOON was written in order to carry out two-nucleon transfer calculations.

The program TOON utilizes distorted wave, bound state and Coulomb wave function subroutines due to the Oxford group.[1-3] In addition the Clebsch-Gordon coefficient subroutine due to Wills is used.[4] Spin-orbit distortions are not available for the distorted waves but non-locality corrections can be included. Currently the program is limited to angular momentum transfers of less than or equal to 6. Up to 50 partial waves may be used.

For two-nucleon transfer, in addition to the usual input parameters pertaining to the distorted waves, an externally calculated zero-range[5] form factor is supplied. The program then calculates the differential cross section with or without finite range corrections calculated as described in Ref. 5. The predictions for the $^{60}Ni(p,t)^{58}Ni$ reaction described in Sec. 8.7 if this report were calculated in this manner. However, the calculation of the zero-range form factor which utilizes the Moshinsky transformation is extremely time-consuming and hence costly. Since our treatment of the two-nucleon transfer reaction is restricted to relative s-state motion of the two transferred nucleons it is possible to utilize the direct integration method described by Bayman and Kallio[6] instead of the Moshinsky transformation. This method is expected to be much faster than our present method. A subroutine to carry out the direct integration has been written. It is proposed to combine this with the program TOON thus speeding up the calculation and eliminating the need for additional programs to prepare the zero-range form factor.

In addition to the currently available and projected two nucleon transfer facilities, options are available in TOON to carry out single nucleon transfer calculations including (if desired) a spin-orbit term and non-locality corrections for the transferred nucleon. In addition to a zero range option, Gaussian finite range corrections have been programmed[7] in order to carry out calculations for the ^{7}Li(d,t) and ^{7}Li(d,^{3}He) data described in Sec. 5.8 of this report.

Finally an option is available for any general complex form factor to be supplied to the program as data thus considerably extending the usefulness of the program. (N.S. Chant)

---

1. W.D. Hay and S.M. Perez, Nuclear Physics Theoretical Group Report No. 42, Oxford.
2. S.M. Perez, Nuclear Physics Theoretical Group Report No. 38, Oxford.
3. B. Buck *et al.*, Nuclear Physics Computing Group Report No. 12, Ref. 26/60, Oxford.
4. J.G. Wills, Oak Ridge National Laboratory Report ORNL-TM-1949.
5. N.S. Chant and N.F. Mangelson, Nucl. Phys. *A140*, 81 (1970).
6. B.F. Bayman and A. Kallio, Phys. Rev. *156*, 112 (1967).
7. R.H. Bassel, Phys. Rev. *149*, 791 (1966).

9.1 Gamma Transitions from High Spin States in the Beta-Vibrational Band of ^{154}Gd

The gamma transition rates between the beta band and ground band levels in rotational nuclei are very sensitive to the band mixing caused by the interactions between these bands. Furthermore, the branching ratios of the transition nuclei are quite different from what one would expect from a simple perturbation treatment with a macroscopic model.[1-12]

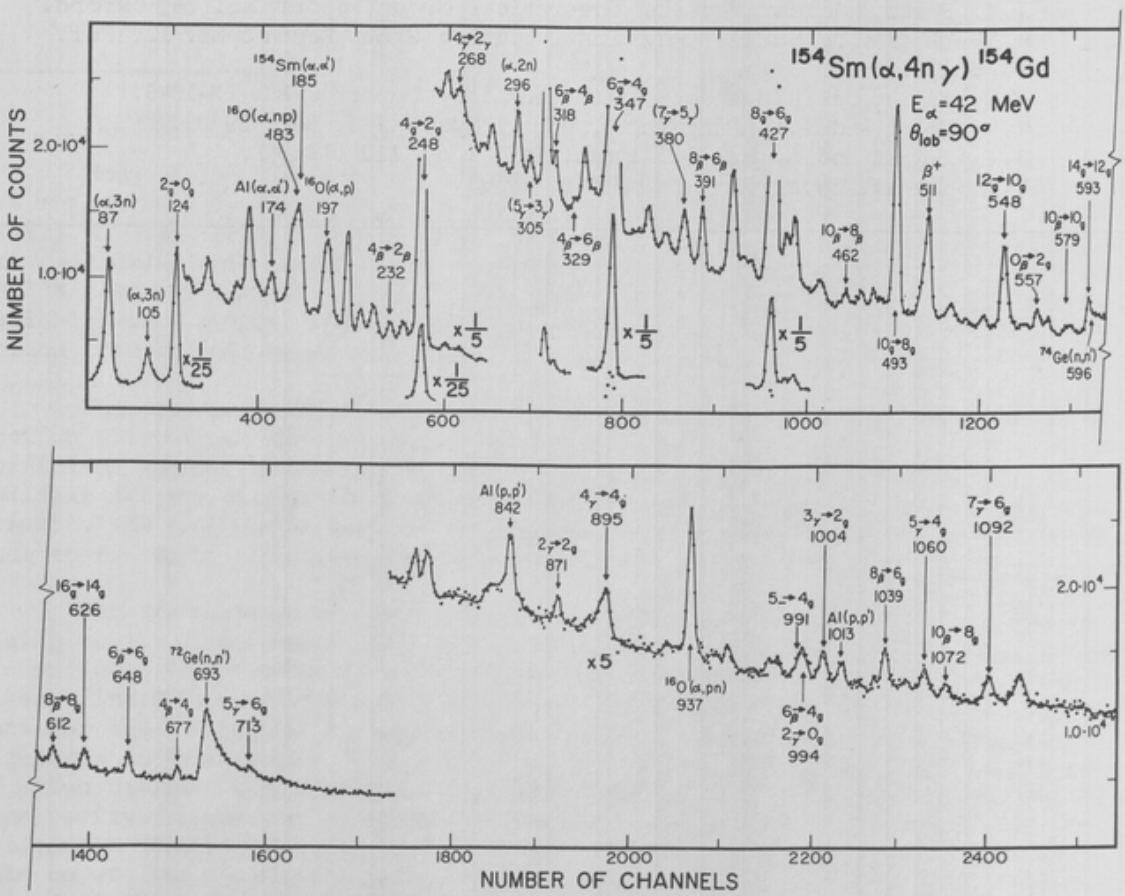

Fig. 9.1-1 The observed gamma ray spectrum for the ^{154}Sm(α,4nγ)^{154}Gd reaction at θ_{lab} = 90°. In order to reduce the number of points in the 4000 channel spectrum by a factor of 2, sums of counts in the two adjacent channels are plotted. The energies are in keV and the error is about ±1 keV.

In the present work we studied the gamma transitions from the excited states with spins up to 10^+ in the β-band[13,14] of ^{154}Gd. These states were populated through the ^{154}Sm(α,4nγ)^{154}Gd reaction with 42 MeV α particles provided by the 60" cyclotron. Beam intensities of about 20 nA were used to bombard an oxide of enriched ^{154}Sm (≥ 95%) on a 100 μg/cm^2 nylon film. A second self-supporting metallic foil target was used to obtain a cleaner spectrum for measuring angular distributions. Gamma rays were detected at θ_{lab} = 45°-125° to the beam by an 8cc Ge(Li) crystal. The best resolution obtained for 500 keV gamma rays was about 3.1 keV FWHM. The photon spectra were recorded with the help of an SDS 930 computer which was operated on line in a 4096 channel pulse-height analysis mode. The full energy peak efficiencies of the Ge(Li) detector were obtained by use of a number of standard radioactive sources. A Si(Li) detector was used as a monitor counter to detect elastically scattered alpha particles at θ_{lab} = 60°. Further details are given in Ref. 15. The observed gamma ray spectrum at 90 deg. taken with the first target is shown in Fig. 9.1-1. The level and transition scheme is illustrated in Fig. 9.1-2. The identification of the gamma rays of present interest is based mainly on the conversion electron data of the ^{152}Sm(α,2n) reaction[13,14] supplemented by the systematics of the observed gamma ray energies, intensities and branching ratios. The branching ratios of the inter- and intraband gamma transitions were obtained from the gamma ray yields at θ_0 = 125°, where $P_2(\cos\theta_0) \approx 0$ and are shown in Table 9.1-1. The contributions from the $A_4P_4(\cos\theta_0)$ term to the total cross-sections are estimated to be small (about 2% for I → I - 2 transitions and ≈ 5% for I → I E_2 transitions) and were therefore neglected.

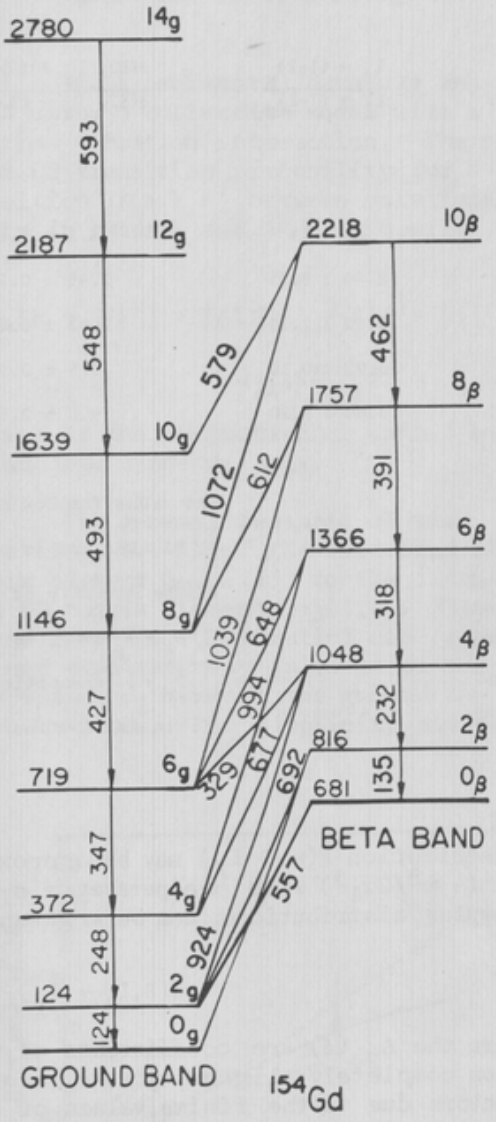

Fig. 9.1-2. Level and transition scheme of the beta-vibrational band and the ground band in ^{154}Gd. The transition energies are in units of keV.

The mixing ratios δ = ⟨E2⟩/⟨M1⟩ for the interband transitions ($I_\beta \rightarrow I_g$) are obtained from the angular distributions since the spins I_β are fairly well aligned in the plane perpendicular to the beam axis z.[14,16-18] The substate

Table 9.1-1. Branching ratios of transitions from levels in the β-vibrational band

I_β	$\frac{I_\beta \to (I-2)_g}{I_\beta \to (I-2)_\beta}$	$\frac{B(E2, I_\beta \to (I-2)_g)}{B(E2, I_\beta \to (I-2)_\beta)} \cdot 10^3$	$\frac{I_\beta \to I_g}{I_\beta \to (I-2)_\beta}$	$\frac{B(E2, I_\beta \to I_g)}{B(E2, I_\beta \to (I-2)_\beta)} \cdot 10^2$
2	65 ± 14	8.1 ± 1.6	235 ± 45	6.7 ± 1.5
4	2.40 ± 0.25	2.45 ± 0.25	5.85 ± 0.58	2.9 ± 0.3
6	0.72 ± 0.10†	2.43 ± 0.30	1.30 ± 0.06	$3.3^{+0.5}_{-0.7}$
8	0.73 ± 0.10	5.5 ± 0.7	0.64 ± 0.04	$3.45^{+1.2}_{-2.5}$
10	0.66 ± 0.20	9.8 ± 2.5	0.27 ± 0.08	8.8 ± 2.5*

The values for low spins $I_\beta = 2$ and 4 are from ref. (10).

* M1 admixture is not corrected.

† The intensity of the $2_\gamma \to 0_g$ transition, which is unresolved from the $6_\beta \to 4_g$ line, is estimated from the observed intensity of the $2_\gamma \to 2_g$ transition and the known branching ratio of the 2_γ state[10]. Then its contribution to the $6_\beta \to 4_g$ peak was subtracted.

distribution $P(m \equiv I_z)$ may be approximated by a Gaussian distribution as $P(m) \propto \exp(-m^2/2\sigma_I^2)$ with one parameter σ_I for the degree of alignment.[14,18] Then the angular distributions can be written as[19]

$$W(\theta, I_\beta \to I_g) = \sum_\nu a_{2\nu}(\sigma_I) A_{2\nu}(\delta) P_{2\nu}(\cos\theta). \qquad (1)$$

Here the $A_{2\nu}(\delta)$ are coefficients of the Legendre polynomial $P_{2\nu}$ for transitions from completely aligned spins I_β (i.e., $\sigma_I = 0$), and the $a_{2\nu}(\sigma_I)$ are attenuation factors due to the finite values of σ_I. The values σ_I and therefore $a_{2\nu}(\sigma_I)$ are obtained from a fit to the angular distributions of the stretched E2 transitions from the states I_β of present interest (Fig. 9.1-3). The beta-band and ground-band transitions show almost the same angular distributions, indicating that the spin alignment parameters σ_I have the same values for both bands. The attenuation factors for the states $I_\beta = 6$ and 8 are $a_2 = 0.68 \pm 0.07$, $a_4 = 0.3 \pm 0.05$ and $a_2 = 0.75 \pm 0.07$, $a_4 = 0.4 \pm 0.1$, respectively, in agreement with observed and calculated values for $(\alpha, xn\gamma)$ reactions on rare earth nuclei.[14,18] Using these attenuation coefficients, the values of the E2 to M1 mixing ratios δ are estimated roughly to be

$\delta = 3.5^{+2.5}_{-2.0}$ for the $6_\beta \to 6_g$ transition and $\delta = 1.0^{+0.7}_{-0.6}$ for the $8_\beta \to 8_g$ transition.

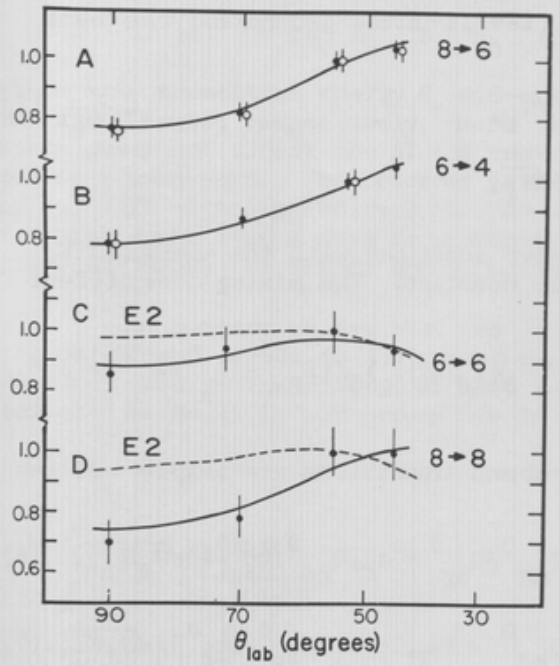

Fig. 9.1-3. Angular distributions of gamma rays for the transitions: $8_g \rightarrow 6_g$ (filled circles) and $8_\beta \rightarrow 6_\beta$ (open circles) (A); $6_g \rightarrow 4_g$ (filled circles) and $6_\beta \rightarrow 4_\beta$ (open circles)(B); $6_\beta \rightarrow 6_g$ (C); and $8_\beta \rightarrow 8_g$ (D). The solid lines here are those computed using the values of δ that give best fit. The dotted lines for the $6_\beta \rightarrow 6_g$ and $8_\beta \rightarrow 8_g$ are drawn for pure E2 transitions (i.e., for $\delta = \infty$) in order to give an idea of the effect of finite M1 mixing in those transitions.

Thus, there seem definitely to be M1 components in the interband transitions, but their amount remains relatively uncertain (Fig. 9.1-4).

We note that many weak gamma lines are expected to be present and consequently it is not completely ruled out that the strong peaks of present concern may contain contributions from weak unrelated lines. However we feel that the general trends of the intensity ratios as given could not be significantly changed due to such background effects.

The experimental data was analyzed using a collective model with a rotation-vibration interaction. The reduced E2 transition probability for a transition $IK \rightarrow I'K'$ between rotational levels in bands λ and λ' can be written[1,2]

$$B(E2, IK \rightarrow I'K') = |\langle IK2K' - K | I'K' \rangle|^2 \cdot |Q_{\lambda\lambda'}(I,I')|^2, \quad (2)$$

where K is the projection of spin I on the nuclear symmetry axis.

The general features of the ratio (Fig. 9.1-5) of the interband E2 matrix element $Q_{\beta g}(I,I')$ to the intraband E2 matrix element $Q_{\beta\beta}(I,I-2)$(obtained from the B(E2) ratio) can be explained qualitatively in terms of the interaction H_I between the ground and the beta bands. For simplicity one may

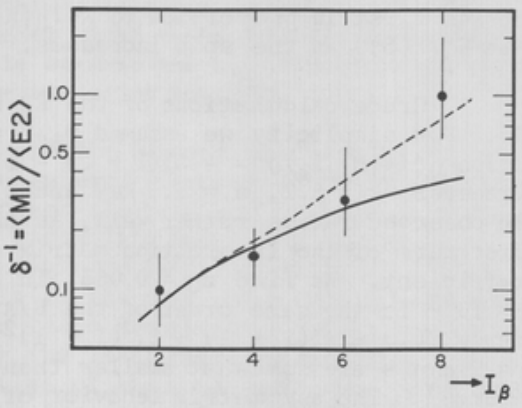

Fig. 9.1-4. M1 to E2 mixing ratios δ^{-1} for the transitions $I_\beta \rightarrow I_g$. The solid line is calculated using Eq. (8) with $\partial g_R/\partial\beta = 0.16$. The values for the $I_\beta = 2^+$ and 4^+ states are from Ref. (8). The dotted line is merely to guide the eye.

assume the following wave functions for the levels in the ground and the beta bands:

$$|I_g\rangle = (|I_g\rangle_0 + \alpha_I|I_\beta\rangle_0)/\sqrt{N_I}, \tag{3}$$

$$|I_\beta\rangle = (|I_\beta\rangle_0 - \alpha_I|I_g\rangle_0)/\sqrt{N_I}, \tag{4}$$

where $|I_g\rangle_0$ and $|I_\beta\rangle_0$ are the unperturbed wave functions with the energies E_g^0 and E_β^0, and $N_I \equiv 1 + \alpha_I^2$ is a normalization constant. The mixing coefficient α_I is easily obtained as

$$\alpha_I = [2\,{}_0\langle I_\beta|H_I|I_g\rangle_0/(E_\beta^0 - E_g^0)]^{-1} + [(2\,{}_0\langle I_\beta|H_I|I_g\rangle_0/(E_\beta^0 - E_g^0))^{-2} + 1]^{\frac{1}{2}}. \tag{5}$$

The matrix elements for the inter- and intraband transitions are simply written as

$$Q_{\beta g}(I,I') = Q_{\beta g}^0(I,I')[1 - \alpha_I\alpha_{I'} - \alpha_I Q_{gg}^0/Q_{\beta g}^0 + \alpha_{I'}Q_{\beta\beta}^0/Q_{\beta g}^0]/\sqrt{N_I N_{I'}}, \tag{6}$$

$$Q_{\beta\beta}(I,I') = Q_{\beta\beta}^0(I,I')[1 + \alpha_I\alpha_{I'}Q_{gg}^0/Q_{\beta\beta}^0 - (\alpha_{I'} + \alpha_I)Q_{\beta g}^0/Q_{\beta\beta}^0]/\sqrt{N_I N_{I'}}. \tag{7}$$

Here $Q_{\lambda\lambda'}^0(I,I')$ are the unperturbed E2 matrix elements between $|I'_\lambda\rangle_0$ and $|I_\lambda\rangle_0$. The $Q_{\beta g}(I,I')$ for $I' = I$ are affected very little since the two terms with $\alpha_{I'}$ and α_I almost cancel each other. The effect on the values of $Q_{\beta\beta}(I,I')$ is relatively small because of the small coefficient $Q_{\beta b}^0/Q_{\beta\beta}^0$. The spin dependence of the $Q_{\beta g}(I,I')$ may be due to the spin dependence of the coefficients α_I, which increases first in proportion to ${}_0\langle I_\beta|H_I|I_g\rangle_0 \propto I(I+1)$ and gradually saturates (see Eq. (5)) as the spin increases.

Crude calculations of the E2 matrix elements were made by using Eqs.(5)-(7). For simplicity we assumed $Q_{\beta\beta}^0 = Q_{gg}^0 = kQ_{\beta g}^0$ and the form of the interaction ${}_0\langle I_\beta|H_I|I_g\rangle_0 = -aI(I+1) - bI^2(I+1)^2$. The calculated values with parameters $k = 5.2$, $a = 8.5$ keV and $b = -34$ eV reproduce the general trends of the observed ratios rather well, as shown in Fig. 9.1-5. The parameter a of the first term of the interaction matrix element gives the value of the so-called z_0 coefficient. We find $z_0 = 0.065$, in agreement with expection.[6] The ratio $b/a \approx 4 \times 10^{-3}$ is the same order of the B/A in the general expansion of the rotational energy $E(I) \approx AI(I+1) + BI^2(I+1)^2$. The observed values of $Q_{\beta g}(I,I+2)$ for $I = 2$ and 4 are somewhat smaller than the calculated values, as in the case of ^{152}Sm.[20] The asymmetric behavior of the $\Delta I = 2$ and $\Delta I = -2$ transition matrix elements with respect to the center values for $\Delta I = 0$ may arise from unequal effects on the ground- and the beta-band levels from higher-lying levels.

The M1 transition between states in the β and ground bands with the same spin is forbidden if the beta-vibration is a pure quadrupole excitation with a constant rotational g factor, g_R. The M1 to E2 mixing ratio δ^{-1} is therefore expressed by a perturbation of the macroscopic model as[1,2]

$$|\delta|^{-1} = 245\, E_\gamma^{-1} Z^{-1} R_0^{-2} (I(I+1))^{\frac{1}{2}} |\langle I\ 0\ 20 | I\ 0\rangle|^{-1} |\partial g_R/\partial\beta|, \qquad (8)$$

where the transition energy E_γ and undeformed nuclear radius R_0 are in units of MeV and Fermis, respectively.[1] Here the band mixing between the beta and ground bands does not affect the $\Delta I = 0$ transitions very much as discussed in the preceding paragraphs. The observed values for δ^{-1} for the low spin states are fit by Eq. (8) with $|\partial g_R/\partial\beta| \approx 0.16$. As shown in Fig. 9.1-4 the M1 matrix elements for high spin states seem to be larger than expected for first-order perturbation, although the errors are quite large.

In summary we see that the interband E2 transition-matrix elements from the beta-band levels to the ground-band levels in the ^{154}Gd show characteristic features due to the effects of band mixing. A perturbation description of a collective model is not proper for the beta band-ground band transitions in the ^{154}Gd region, however.[8-12] Here the ratio of the rotational energy ($E(2_g)$) to the beta-vibrational energy ($E(0_\beta)$) is quite large. Therefore the mixing coefficient α_I, to which the interband E2 matrix element is sensitive, becomes large since it is roughly proportional to the quantity $(E(2_g)/E(0_\beta))\cdot(Q^0_{\beta g}/Q^0_{gg})$. The general trend of the spin dependence of the E2 matrix elements is explained mainly by taking into account all higher order terms[21] in the mixing coefficient α_I as given in Eq. (5) and up to the second order terms $bI^2(I+1)^2$ in the interaction matrix element. These higher order terms play an important role because the $Q_{\beta g}$ depend strongly on the variation $\partial\alpha_I/\partial I$.

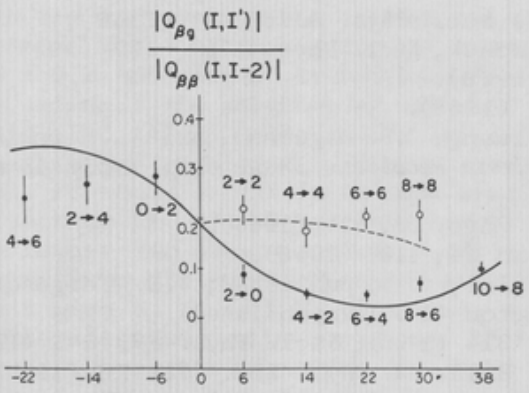

Fig. 9.1-5. The ratios of the interband E2 matrix elements $|Q_{\beta g}(I,I')|$ to the intraband ones $|Q_{\beta\beta}(I,I-2)|$. The values (filled circles) for the transitions with $\Delta I = I - I' = \pm 2$ are plotted versus $I(I+1) - I'(I'+1)$, while the values (open circles) for the transitions with $\Delta I = 0$ are plotted versus $4I - 2$. The solid and dotted lines are respectively calculated values for the transitions with $\Delta I = \pm 2$ and $\Delta I = 0$. A simple perturbation theory[1-11] with constant z_0 gives a straight line for the $\Delta I = \pm 2$ transitions and a constant value for the $\Delta I = 0$ transitions.

The present analysis gives only the general features of the transitions between the beta and ground bands since it takes into account only the beta band-ground band interaction, although this is the most important interaction for these transitions. When considering the level energies and other properties of the beta band, one needs to take into account additional interactions which are important for such properties. Consequently for a more detailed comparison of the variety of experimental values, elaborate calculations including the effects of the gamma-band levels,[4] pairing and other important levels, including higher order terms in the interaction matrix, would

be necessary. Further work on the Sm-Gd isotopes which includes some of these effects is now in progress.[22] (H. Ejiri, S.M. Ferguson, and R. Heffner)

1. A. Bohr and B.R. Mottelson, Lectures on Nuclear Structure and Energy Spectra (1962)(to be published).
2. B.R. Mottelson, in *Proc. of the International Conference on Nuclear Structure* (1967), ed. by J. Sanada (Physical Society of Japan), p. 87.
3. P.G. Hansen, O.B. Nielson, and R.K. Sheline, Nucl. Phys. *12*,389 (1959).
4. P.O. Lipas, Nucl. Phys. *39*, 468 (1962).
5. I.M. Pavlichenkov, Nucl. Phys. *55*, 225 (1964).
6. E.R. Marchalek, Phys. Rev. *158*, 993 (1967).
7. J.P. Davidson and M.G. Davidson, Phys. Rev. *138*, B316 (1965).
8. L.L. Riedinger, N.R. Johnson and J.H. Hamilton, Phys. Rev. Letters *19*, 1243 (1967), and Phys. Rev. *179*, 1214 (1969); J.H. Hamilton, in Proc. of the International Conference on Radioactivity, Nashville, Tennessee, (1969)(to be published); L.C. Whitlock, Ph.D. Thesis, Vanderbilt University (1969); J.H. Hamilton, A.V. Ramayya and L.C. Whitlock, Phys. Rev. Letters *22*, 65 (1968).
9. L.K. Ng, K.C. Mann and T.G. Walton, Nucl. Phys. *A116*, 433 (1968); L. Varnell, J.D. Bowman and J. Trischuk, Nucl. Phys. *A127*, 270 (1969).
10. R.A. Meyer, Phys. Rev. *170*, 1089 (1968).
11. W.G. Sperry, private communication (1968).
12. L.L. Riedinger, E. Eichler, J. Fuglsang, G.B. Hagemann, and B. Herskind, in *International Conference on Nuclear Reactions Induced by Heavy Ions*, (Heidelberg,1969).
13. O. Lönsjö and G.B. Hagemann, Nucl. Phys. *88*, 624 (1966).
14. H. Ejiri *et al.*, J. Phys. Soc. Japan *24*, 1189 (1968).
15. S.M. Ferguson, I. Halpern and H. Ejiri, to be published; S.M. Ferguson, Ph.D. Thesis, University of Washington (1969)(unpublished).
16. H. Ejiri *et al.*, Phys. Letters *18*, 314 (1965); Nucl. Phys. *89*, 641 (1966).
17. C.F. Williamson and B.J. Shepherd, Bull. Am. Phys. Soc. *10*, 428 (1965); C.F. Williamson, S.M. Ferguson, B.J. Shepherd and I. Halpern, Phys. Rev. *174*, 1544 (1968).
18. J.O. Newton *et al.*, Nucl. Phys. *A95*, 357 (1967).
19. L.C. Biedenharn and M.E. Rose, Rev. Mod. Phys. *25*, 729 (1953); T. Yamazaki, Nucl. Data *A3*, 1 (1967).
20. I.A. Fraser *et al.*, Phys. Rev. Letters *23*, 1047 (1969).
21. The importance of this has been pointed out by B. Elbek in Proceedings of the International Conference on Properties of Nuclear States, Montreal, (1969)(to be published) p. 63.
22. B. Elbek and G.B. Hagemann, private communication (1969).

9.2 Isomerism and the K-Quantum Number Purity in ^{174}Hf

We report here an investigation of a positive parity isomer in ^{174}Hf. The cyclotron provided a bunched 42 MeV α beam with 2ns width every 87 nsec. The gamma ray spectra following ^{174}Yb(α,4nγ)^{174}Hf and ^{173}Yb(α,3nγ)^{174}Hf reactions were measured between beam bursts with an 8cc Ge(Li) detector. In addition to the ground state rotational transitions, $6^+ \rightarrow 4^+$, $4^+ \rightarrow 2^+$, and $2^+ \rightarrow 0^+$, two strong gamma rays with E_γ = 1.251 MeV and 0.940 MeV were observed in the delayed

spectrum. Since the life time is estimated to be much longer than the beam interval (87 ns) of the cyclotron, we used for the life time measurement the $^{175}Lu(p,2n\gamma)^{174}Hf$ reaction with pulsed protons from the tandem accelerator. The beam flapper was adjusted to give one 0.5 μsec beam pulse every 10 μsec in view of the expected half life. A time-to-amplitude converter (TAC) was started by the beam flapper signal and stopped by a fast time pick-off signal from the detector. The SDS 930 computer was used to sort the gamma ray spectra into four time bins according to the TAC signal. The spectrum observed in the second time bin is shown in Fig. 9.2-1. From the successive decrease of the isomeric transitions in each time bin spectrum we obtained a half life of 2.1 ± 0.2 μsec, as shown in Fig. 9.2-2.

The two isomeric transitions are considered to be those from the 1.549 MeV isomer with $(J^{\pi}K) = (6^{+}6)$ to the ground band levels with $(J^{\pi}K) = (6^{+}0)$ and $(4^{+}0)$ in ^{174}Hf as given in Fig. 9.2-3. These assignments are based on the right energies and intensities of the delayed gamma rays, and the systematic behavior of the life times, spins and excitation energies of the isomers in the A = 174 region.[3,4] The observed $(\alpha,4n)$ cross sections for this isomer are also consistent with the systematics and theoretical predictions for a $J^{\pi}K = 6^{+}6$ level.[1] Furthermore the B(E2) ratio for the isomeric transitions is $B(E2,66\rightarrow60)/B(E2,66\rightarrow40) = 4.2 \pm 0.2$ assuming E2 transitions from the isomer to the ground band level as in the cases of the neighboring nuclei.[3] This ratio agrees well with the simple ratio of Clebsch-Gordon coefficients $\langle 6\ 2\ 2\ -\ 2|60\rangle^2/\langle 6\ 2\ 2\ -\ 2|40\rangle^2 = 3.7$ for the assumed transition. Finally, the possibility of $(J^{\pi}K) = (5^{-}5)$ is unlikely since it would result in an anomalously large hindrance factor 3.82×10^{10} with respect to the single particle estimate for a 1.251 MeV E1 transition with $\Delta K=5$. The lowest two quasi-particle state with $(J^{\pi}K) = (5^{+}5)$ is calculated to lie higher than the observed energy and the 2 μs life-time for that state would again give an unusual E2 hindrance factor for a $\Delta K = 5$ transition. The lack of further isomeric gamma rays above 80 keV almost excludes the possibility of another 2 sec isomer which decays to the 6^{+} isomer. The observed properties

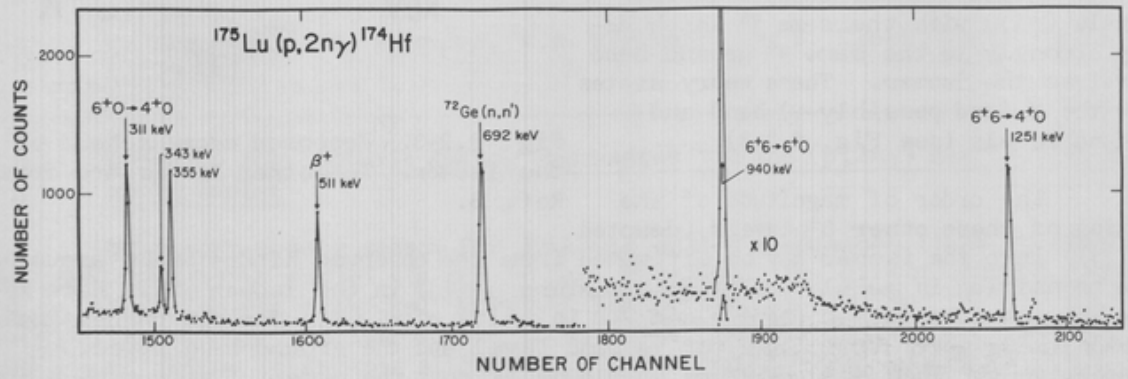

Fig. 9.2-1. Delayed gamma ray spectrum in the 2nd time bin.

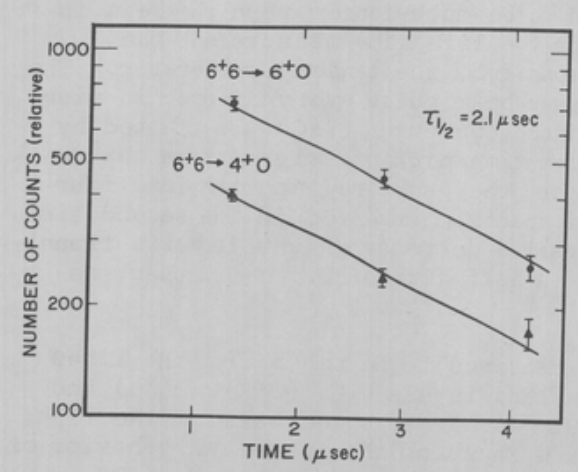

Fig. 9.2-2. Decay curves of the isomeric transitions.

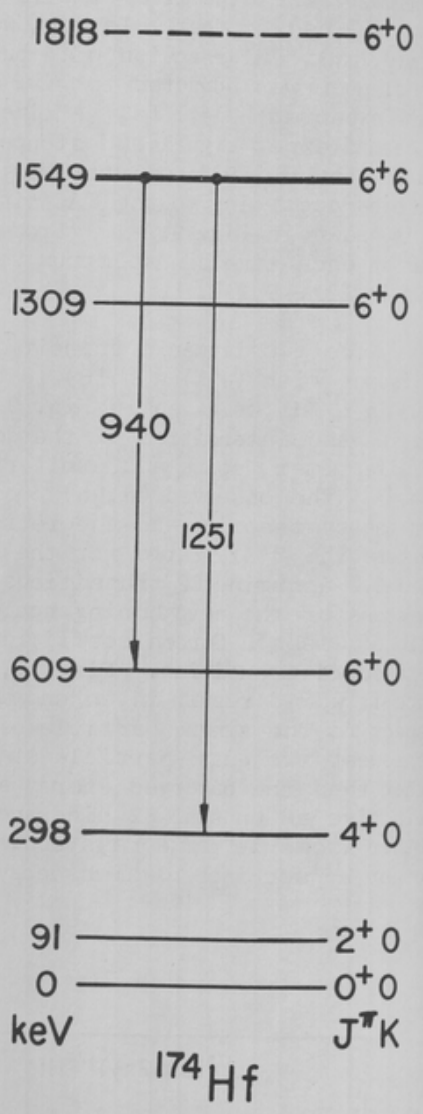

Fig. 9.2-3. Proposed decay scheme of the isomer. The other levels are from Ref. 3.

are summarized in Table 9.2-1. $(J^{\pi}K) = (6^{+}6)$ isomers[3] have also been found in two neighboring nuclei, ^{174}Yb and ^{176}Hf, as shown in the table.

The isomeric E2 transition $6^{+}6 \rightarrow 4^{+}0$ is hindered by a factor 1.36×10^{6} with respect to the single particle estimate $B(E2)_{sp}$. The degree of K hindrance for this transition is $\Delta K - 2 = 4$ and the hindrance factor per one degree is $F_W = 34$ (see Table 9.2-1). This large hindrance factor indicates the purity of the K quantum number for this rather highly excited isomer despite nearby levels ($|j\rangle$) with the same j^{π} which decay strongly to the same 4^{+} ground band level as the isomer. These neary states are the β (and possibly γ) band and ground levels (see Fig. 9.2-3).

The order of magnitude of the mixing of these other 6^{+} levels (denoted by $|j\rangle$) into the isomer may be estimated from the observed hindrance by assuming the transition is mainly due to an admixture $\alpha_{ij}|j\rangle$ in the isomer $|i\rangle$. Here we use the enhancement factors ≈ 5 and 200 in units of $B_{sp}(E2)$ for the transitions to the $(4^{+}0)$ level from the β (or γ) band level and the ground band level, respectively. Then the admixture should be at most the order of $\alpha^2_{i\beta \text{ or } \gamma} \approx 1.5 \times 10^{-7}$ and $\alpha^2_{ig} \approx 3 \times 10^{-9}$, respectively. By using the expression for the interaction matrix $\langle H_{ij} \rangle \simeq (\varepsilon_i - \varepsilon_j)\alpha_{ij}$, where ε_i and ε_j are the respective unper-

Table 9.2-1. Properties of (6^+6) isomers in ^{174}Hf region. Those for ^{174}Yb and ^{176}Hf are from Ref. 3.

Nucleus	Z	N	E (MeV)	$\tau_{\frac{1}{2}}$ (μsec)	$\left(\frac{B(E2\ 6^+6 - 4^+0)_{exp}}{B(E2)_{sp}}\right)^{-1}$	F_W	$\frac{B(E2\ 6^+6 - 6^+0)}{B(E2\ 6^+6 - 4^+0)}$
^{174}Yb	70	104	1.520	820	$7.0 \cdot 10^9$	290	77
^{174}Hf	72	102	1.549	2.1	$1.36 \cdot 10^6$	34	4.2
^{176}Hf	72	104	1.335	13	$4.8 \cdot 10^6$	47	10.3

turbed energies of the isomer and the mixed state, we get $|\langle H_{i\beta}\rangle| \leqslant 90$ eV and $|\langle H_{ig}\rangle| \leqslant 50$ eV. Assuming the γ-band 6^+ lies in an excitation energy region 1.0 - 2.0 MeV, one may also estimate $|\langle H_{i\gamma}\rangle|$ to be $\leqslant 200$ eV. These interactions are very small in comparison with, for instance, the β vibration-ground state rotation interaction $|\langle H_{\beta g}\rangle|$ and the pairing interaction $|\langle H_{pair}\rangle|$, which are of the order of 0.1 - 0.2 MeV. Such small interactions, probably due to the poor overlap between high K and low K states, might make the K quantum number reasonably good[1] above the energy gap even though there are many other levels with the same J^π. (H. Ejiri, S.M. Ferguson, R. Heffner, and H. Wieman)

1. S. Ferguson, I. Halpern, and H. Ejiri, to be published; H. Ejiri, I. Halpern, Bull. Am. Phys. Soc. *13*, 700 (1968); Nuclear Physics Laboratory Annual Report, University of Washington (1968).
2. N.L. Lark and H. Morinaga, Nucl. Phys. *63*, 466 (1963); T. Yamazaki and G.T. Ewan, Phys. Letters *24B*, 278 (1967); *ibid.*, Phys. Rev. Letters *20*, 1376 (1968).
3. J. Borggreen *et al.*, Nucl. Phys. *A96*, 561 (1967).
4. C.G. Gallagher and V.G. Soloviev, Mat. Fys. Skr. Dan. Vid. Selsk. *2*, no. 2 (1962).
5. R. Graetzer, G.B. Hagemann, K.A. Hagemann, and B. Elbek, Nucl. Phys. *76*, 1 (1966).

9.3 A Search for Isobaric Analog Resonances via the (p,2nγ) Reaction in Rare-Earth Nuclei

We report here a search for isobaric analog resonances (IAR) in highly deformed rare-earch nuclei via the (p,2nγ) reaction. The direct neutron decay of an IAR is isospin forbidden; however, the Coulomb force mixes the IAR with neighboring compound nuclear states of the same J^π. The neutron decay of the background states is isospin allowed and is enhanced through mixing with the analog state.[1]

There are several enticing reasons for attempting to populate IAR via the

$(p,2n\gamma)$ reaction. Closely spaced IAR in odd-odd deformed nuclei might possibly be investigated more easily through this reaction than, for example, through elastic or inelastic proton scattering. The $(p,2n\gamma)$ reaction in these nuclei populates a variety of spin states in the ground state rotational band of the residual nucleus. Thus different analog spin states might preferentially populate certain final spin states allowing even somewhat overlapping resonances to be studied independently.

Furthermore, a knowledge of the IAR neutron decay widths for different spin states in the same energy region might provide information concerning the spin dependence of the compound level densities. The nucleus ^{175}Lu is well suited for such a study since the parent analog states in ^{176}Lu are reasonably well spaced and exhibit widely different spins. [The target spin is $7/2^+$ and the lowest three IAR have spins 7^-, 8^-, and 1^-, respectively.]

The expected excitation energy of the ground state analog was calculated using the measured Coulomb energy shift for [^{181}Ta - ^{181}Hf] of 17.24 ± .05 MeV.[2] This Coulomb energy was corrected for mass and charge[3] to be applicable for the [^{175}Lu - ^{176}Hf] case. An excitation function was taken in 20 keV steps over the incident proton energy region of 10.86 MeV to 11.38 MeV. This energy region was chosen to span the lowest three IAR in ^{176}Hf. (The widths of the IAR in this mass region are expected to be about 100 keV.) The protons were provided by the tandem Van de Graaff. The gamma rays were detected at $\theta_{lab} = 90°$ with a 30 cc Ge(Li) detector. A Si(Li) counter at $\theta_{lab} = 135°$ was used to measure elastically and inelastically scattered protons. Standard high resolution electronics consisting of pole-zero cancellation and base-line restoration was used for the gamma spectra. The system resolution was 3.2 keV FWHM for 350 keV gamma rays. The SDS 930 computer collected data from both counters in an on-line mode. A pulser, triggered by pulses derived from the scattered protons, was fed into the gamma spectrum and was used to monitor the system dead time.

The excitation functions for the $8^+ \rightarrow 6^+$ and $6^+ \rightarrow 4^+$ ground state rotational band transitions showed no positive evidence of the IAR in the energy region investigated. We achieved a relative experimental error of about 5%. Hence we can set an upper limit for the manifestation of the IAR in ^{176}Hf via the $(p,2n\gamma)$ reaction of about this magnitude.

We note, however, that we could not make positive identification of any of the IAR from the elastic proton data either, although several small anomalies were observed. This lack of evidence in the elastic channel probably arises from the unfortunate design of the scattering chamber, however, and not from a miscalculation of the excitation energy of the IAR. (The calculated excitation energies are expected to be accurate to within 100 keV.) The proton detector could be placed only at $\theta_{lab} = 45°$, 90°, or 135°. The ground state and third excited state analogs involve $\ell = 3$ proton transitions which yield small elastic resonance effects at these angles. The second excited state analog involves an $\ell = 5$ transition and is expected to be smaller yet because of the inhibitive angular momentum barrier.

In conclusion, we find that the IAR yields from the $(p,2n\gamma)$ reaction in the mass 175 region are too small to give useful experimental information.
(H. Ejiri, S.M. Ferguson, I. Halpern, and R. Heffner)

1. D. Robson, J.D. Fox, P. Richard, and C.F. Moore, Physics Letters *18*, 86 (1965).
2. D.L. Allen, H.C. Britt, and F.A. Rickey, Jr., Physics Letters *27B*, 11 (1968).
3. D.D. Long, P. Richard, C.F. Moore, and J.D. Fox, Phys. Rev. *149*, 906 (1966); J.D. Anderson, C. Wong, and J.W. McClure, Phys. Rev. *138*, B615 (1964).

9.4 Competition between Neutron and Gamma Ray Emission in Nuclear De-excitation

The studies of (d,d'n) and (d,d'γ) reactions in ^{61}Ni to explore competition between neutron and gamma ray emission from excited nuclei, reported last year,[1] have been continued. An excitation function of ^{61}Ni(d,d')^{61}Ni, leading to the excitation energies of interest (near and above the neutron threshold), shows that the cross section is a maximum at about 19-MeV incident energy; subsequent experiments therefore have been carried out near 19 MeV.

Some modifications have been made in the deuteron and neutron detector systems: (1) the solid angle for the deuteron detector (a Δ-E-anti system) has been increased by using larger area counters (300 mm^2) placed 5.06 cm from the target; and (2) the phosphor used in the neutron scintillation counter has been changed from plastic to the liquid scintillator NE 213, to allow neutron-gamma ray pulse shape discrimination. The electronic system for studying coincidence events now processes the following analog signals: (1) particle energy signals from the deuteron telescope; (2) pulse height signals from the scintillator detector; (3) particle identification signals (PID) from the deuteron telescope system; (4) pulse shape discrimination signals (PSD) for distinguishing neutrons from gamma rays; and (5) time of flight (TOF) signals, using the deuteron signals for starts and the neutron counter signals for stops. These five signals are fed into the SDS 930 computer system. Each event is written in full on magnetic tape, and live two-dimensional storage and display of events is available for any selected pair of signals (e.g., deuteron energy and TOF, or neutron pulse height and PSD).

The trues-to-accidentals ratio has been improved through several modifications. The target thickness was doubled, beam collimation slits were eliminated, a 1 cm lead shield was placed in front of the scintillator to reduce low energy gamma rays from the target, and heavy lead shields were placed between the scintillator and the beam tube Faraday cup system. The improvement was found to be more than a factor of four.

Figure 9.4-1 shows results of tests of the overall system in terms of a two-dimensional display of deuteron energy and TOF. In making this plot windows were set in PID and PSD to accept only deuterons and neutrons with the exception that some gamma rays were purposely let through to facilitate the time calibration. The horizontal straight line locus is from (d,d'γ). The bands correspond to events leading to the ground state and to excited states of ^{60}Ni. The arrows on the plot indicate the neutron emission thresholds for the various ^{60}Ni final

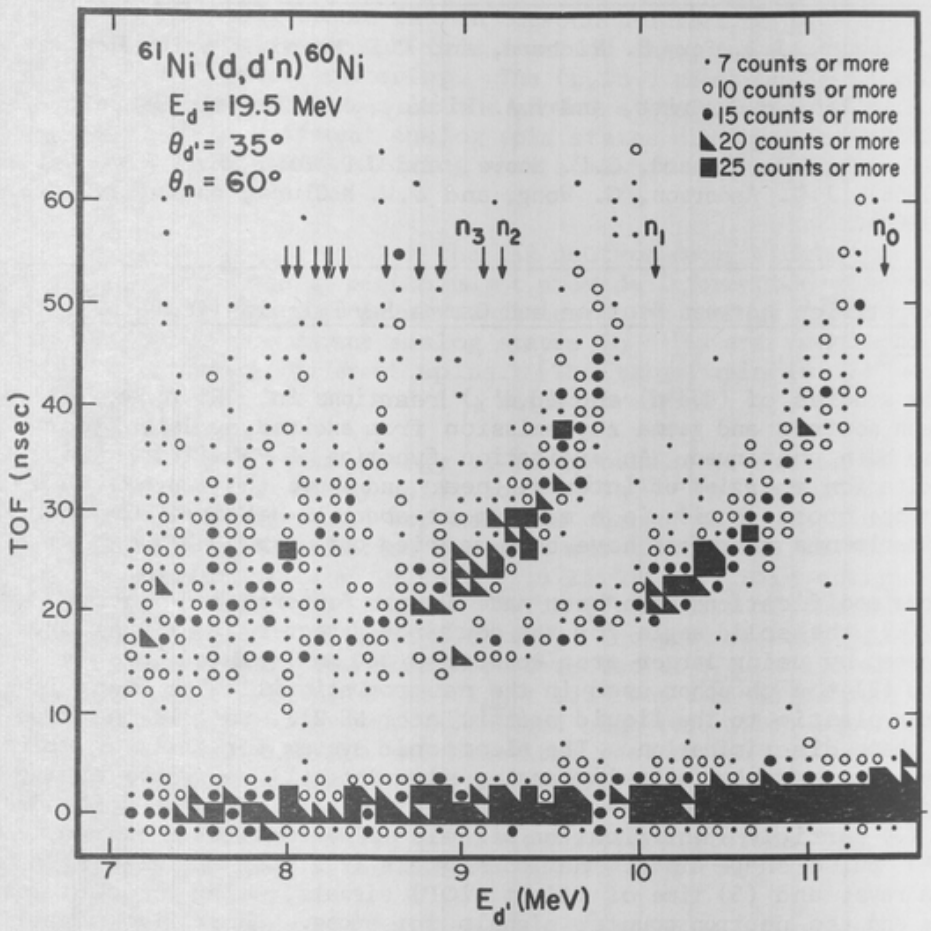

Fig. 9.4-1. Two-dimensional plot of particle energy versus TOF

states. The average background in such a run is about two to three counts.

It is believed that the system will now permit a quantitative determination of neutron yields as a function of the excitation energy of the intermediate nucleus, and runs to measure these yields are in progress.
(D. Bodansky, J. Calarco, J. Cameron, D. Chamberlin, and C. Ling)

---

1. Nuclear Physics Laboratory Annual Report, University of Washington (1969) p. 97.

10. NUCLEAR FISSION

10.1 Spontaneous Fission Isomerism in Uranium Isotopes

Spontaneous fission isomerism is now known to exist in a large number of americium and plutonium isotopes, but only one example of isomerism in the uranium isotopes has been established,[1] and less conclusive evidence for isomerism in one neptunium isotope has been reported.[1] The purpose of this investigation was to search for, identify, and characterize spontaneous fission isomers in uranium and neptunium isotopes which could be produced by 13 to 21 MeV deuteron bombardment of uranium isotopes.

200-500 $\mu g/cm^2$ targets of ^{234}U, ^{235}U, ^{236}U, and ^{238}U were bombarded with 13-21 MeV deuterons from the 60-in. cyclotron and by 18 MeV deuterons from the two-stage tandem Van de Graaff accelerator. The energy of the cyclotron deuteron beam was varied by use of degrader foils. Detection of delayed fission and half-life determinations were made by a direct electronic measurement of the elapsed time between arrival of a burst of particles at the target and the time of fission decay. The experimental details have been discussed previously.[2,3]

Initial experiments were performed with time intervals which were dictated by the oscillator of the cyclotron which produces beam packets of approximately 2 nsec duration at 87 nsec intervals. The delayed fission that was observed with ^{235}U, ^{236}U, and ^{238}U targets was so long-lived that half-life determinations were not possible. Excitation functions were taken with the 87 nsec intervals, but half-life determinations were made by use of an electrically-driven beam chopper which deflects two out of each three beam bursts and thus increases the time between bursts to approximately 262 nsec. This time interval was satisfactory for 110 nsec ^{236m}U, but marginal for 200 nsec ^{238m}U. A longer time interval between beam bursts was desirable in order to make a more precise determination of the half-life and to check for longer-lived contributions from other isomers. Therefore, the tandem Van de Graaff accelerator was used by chopping and bunching the deuteron beam from the ion source into packets of 50 nsec width at 760 nsec intervals.

Excitation functions for the delayed fission resulting from ^{236}U and ^{238}U bombardments at the cyclotron were taken in approximately 2 MeV steps, and are illustrated in Fig. 10.1-1. Half-life determinations were made for ^{236}U and ^{238}U at 21 MeV using the cyclotron, and at 18 MeV using the Van de Graaff. The two determinations were consistent within their uncertainties, yielding final values of (105 ± 20) nsec for the ^{236}U target, and (195 ± 30) nsec for the ^{238}U target. The decay curves are shown in Fig. 10.1-2. No delayed fissions were observed for the ^{234}U target at 21 MeV. The results are summarized in Table 10.1-1.

The half-life of (105 ± 20) nsec is in agreement with the (130 ± 30) nsec half-life of ^{236m}U reported by Lark *et al.* This suggests that we have observed the decay of ^{236m}U which was produced by a (d,d') or (d,pn) reaction, with the latter mechanism believed to predominate. The assignment of the 195 nsec activity to ^{238m}U is based primarily on the similarity of the two excitation functions in Fig. 10.1-1.

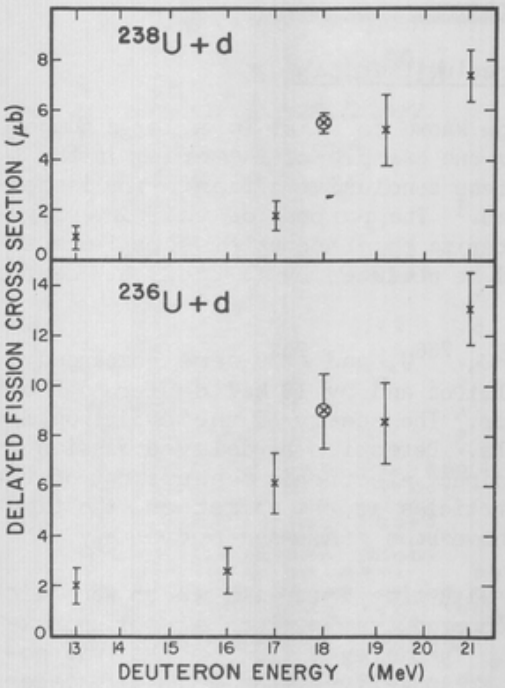

Fig. 10.1-1. Excitation functions for production of delayed fission for deuteron bombardment of ^{236}U and ^{238}U. The points at 18 MeV were determined in a different experiment using the Van de Graaff rather than the cyclotron.

Estimates of the isomer ratios have also been made and are given in Table 10.1-1. The isomer ratios for producing ^{236m}U and ^{238m}U are much smaller than observed for plutonium isomers. This fact, together with the surprising absence of detectable isomerism in other uranium isotopes or in neptunium isotopes, suggests that gamma decay of the shape-isomeric states in this mass region may be a predominant mode of decay. (M.K. Mehta, C.R. Rudy, P.A. Russo, R. Vandenbosch, and K.L. Wolf)

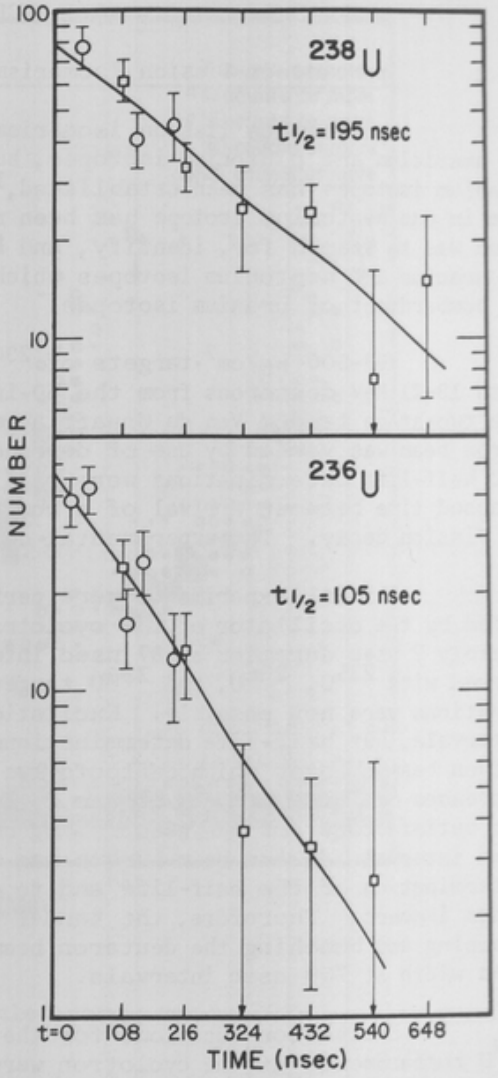

Fig. 10.1-2. Decay curves for ^{236m}U and ^{238m}U. The squares correspond to time bins of width equal to the distance between points, and were taken at 18 MeV using the tandem. The circles were obtained for deuteron energies between 19 and 21 MeV using the cyclotron, and have been normalized to the tandem data.

TABLE 10.1-1 SUMMARY OF RESULTS

Isomer	Reaction	Half-life (nsec)	Delayed Fission Cross Section at 21 MeV	Isomer Ratio
^{238}U	$^{238}U(d,pn)$	195 ± 30	7 μb	5×10^{-5}
^{236}U	$^{236}U(d,pn)$	105 ± 20	13 μb	9×10^{-5}
^{234}U (not observed)	$^{234}U + d$	if $t_{\frac{1}{2}} \geq 30$ nsec, $\sigma \leq 2$ μb		
	$^{232}Th + \alpha$	if $t_{\frac{1}{2}} \geq 20$ nsec, $\sigma \leq 0.1$ μb		
		if $t_{\frac{1}{2}} \geq 2$ nsec, $\sigma \leq 0.9$ μb		

1. N. Lark, G. Sletten, J. Pedersen and S. Bjørnholm, Nucl. Phys. *139*, 481 (1969).

2. R. Vandenbosch and K.L. Wolf, in *Physics and Chemistry of Fission*, (International Atomic Energy Agency, Vienna, 1969).

3. K.L. Wolf, Ph.D. Thesis, University of Washington, 1969 (unpublished).

10.2 Multi-Component Decay of the Fission Isomer ^{237m}Pu

A spontaneous fission isomer ^{237m}Pu with a half-life of approximately 110 nsec has been produced both in this laboratory[1] by the $^{235}U(\alpha,2n)$ reaction, and by Lark *et al.*[2] through the $^{237}Np(d,2n)$ reaction. There is also evidence for the possible existence of a shorter lived isomer when ^{237}Pu is produced by the $^{236}U(\alpha,3n)$ reaction, and more recently, a much longer-lived component has been reported.[3] The most likely explanation for more than one spontaneous fission isomer in an odd-A nuclide is that of spin isomerism associated with the occupation of different low-lying Nilsson states at the deformation corresponding to the second minimum in the potential energy surface.

The present study is directed toward further characterization of these isomers with particular emphasis on identification of the higher spin isomer. The short lived isomer was previously observed with the 88 nsec time interval between beam bursts from the 60 inch cyclotron. Attempts have been made to repeat these measurements with the cyclotron beam flapper to obtain 264 nsec intervals between beam bursts. This has not been successful due to malfunctioning of the beam flapper or failure of the cyclotron oscillator.

The existence of a much longer-lived isomer has also been confirmed, and preliminary estimates made of the ratio of production of the 110 nsec to the longer-lived isomer. Flapped and bunched negative helium ions accelerated by the two stage Van de Graaff were used to produce ^{237}Pu by the ^{235}U(α,2n) reaction. The experimental set-up and the electronic timing system have been described previously.[1] Bombardment of ^{235}U with 25kHz bunched alpha beam of 24.3 to 27.0 MeV gave the delayed fission excitation function shown in Fig. 10.2-1. The peak near 27 MeV identifies the ^{235}U(α,2n) reaction. A bunch width of 40 to 50 nsec was sufficient to measure the isomer half-life of 108 ± 9 nsec. The decay curve for this measurement appears in Fig. 10.2-2. The straight line is the least square fit to the data.

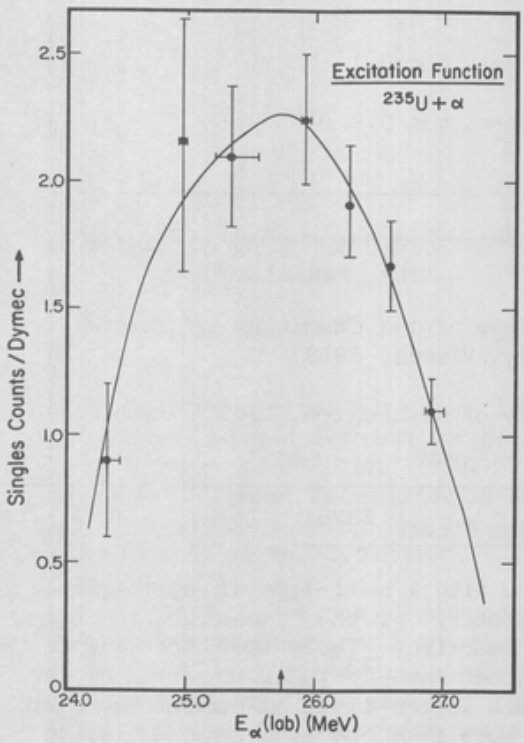

Fig. 10.2-1. Excitation function for 24 to 27 MeV alphas on ^{235}U.

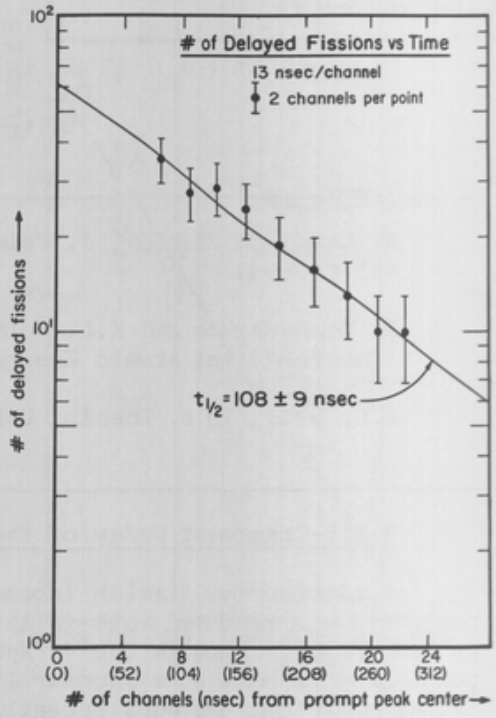

Fig. 10.2-2. Decay curve of the fission isomer ^{237m}Pu in the time interval between 40 and 300 nsec from the edge of the beam burst.

The most recent experiment was successful in observing both the 110 nsec and the long-lived component in ^{237m}Pu. 24 MeV alphas flapped at 0.25 MHz with a beam burst width of approximately one microsecond produced the decay curve given in Fig. 10.2-3. A least square fit to the data points beyond 250 nsec from the edge of the beam burst produced a half-life of 1360 ± 430 nsec. The shorter-lived component was identified by subtracting the extrapolated least square fit from the data points at short in-

times after the beam burst. Straight lines through these points gave an upper and lower limit of 135 and 70 nsec for the half-life of the shorter component. The previous measurement of 108 ± 9 nsec was assumed to be correct, and a line corresponding to this half-life was drawn through these points. Both straight lines were extrapolated to the edge of the beam burst, and the intercepts in this channel were used to compute the ratio of production rates of the longer- and shorter-lived components, R_L/R_S: R_L/R_S = 1 to 3.

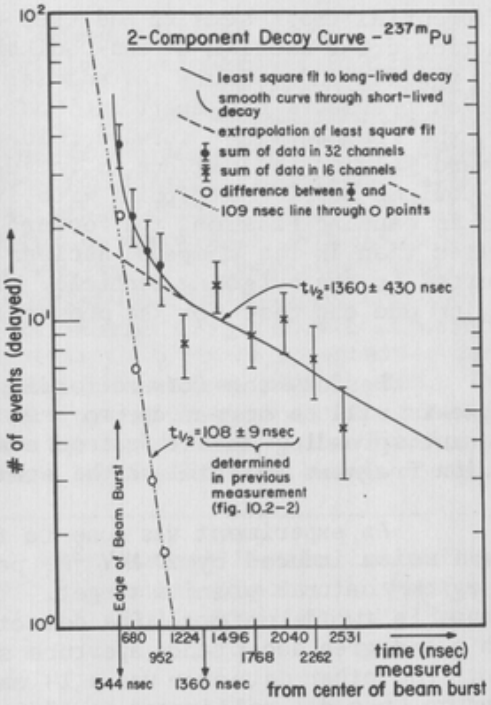

Fig. 10.2-3. Two-component decay curve of the fission isomer ^{237m}Pu in the time interval between 0.1 and 2.5 nsec from edge of beam burst.

Assuming that higher energy incident alphas will favor the population of higher angular momentum states, it should be possible to distinguish between a higher and lower spin for the two components by comparison of the ratio, R_L/R_S for 27 MeV alphas with that at 24 MeV. Any effect due to difference in thresholds can be eliminated by observing the production ratio for the $^{237}Np(d,2n)$ reaction at the appropriate bombarding energy to match the excitation energy of the compound nucleus produced in the $(\alpha,2n)$ reaction. The higher-spin isomer should be more favored in the $(\alpha,2n)$ reaction than in the $(d,2n)$ reaction due to the smaller angular momentum brought in by the lower energy deuterons. (M.K. Mehta, P.A. Russo, J.R. Tesmer, R. Vandenbosch, and K.L. Wolf)

1. R. Vandenbosch and K.L. Wolf, in *Physics and Chemistry of Fission*, (International Atomic Energy Agency, Vienna, 1969)
2. N.L. Lark, G. Sletlen, J. Pedersen and S. Bjornholm, Nucl. Phys. *A139*, 481 (1969).
3. S.M. Polikanov and G. Sletlen, private communication.

10.3 Search for Direct Fission Using the $(^3He,\alpha)$ Reaction

The experiment we describe here was an attempt to use the $(^3He,\alpha)$ reaction to pick up neutrons from the nuclear surface. If a ^3He particle impinges on a heavy target at energies below the Coulomb barrier the cross section for formation of a compound nucleus is inhibited. Under these circumstances the high positive Q value (~15 MeV) may make it favorable for the ^3He to pick up a neutron from the tail of the nuclear neutron distribution, though the differential cross section for such an event will be quite small. One way to circumvent this low

differential cross section and test a direct pick-up component of the ^{3}He induced reaction cross section at sub-Coulomb barrier energies is to use the ^{3}He to induce fission and measure the angular correlation between the fission fragments. Fission fragments fly apart anti-parallel in the center of mass; in the laboratory the fragments are forward folded. If a compound nucleus was formed, the forward folding is just due to incident particle momentum. If, however, it is sub-Coulomb barrier stripping with its usual backward peaked angular distribution that is causing fission, the forward folding of the fragments will in general be greater than in the compound-nuclear case due to the extra component of momentum imparted by the outgoing particle. Thus, by measuring this amount of forward folding one can test for the presence of a direct component in ^{3}He induced fission.

Besides the forward folding, the angular correlation between fission fragments will be spread due to pre- and post-fission particle evaporation. The dominant spreading due to neutron evaporation can be estimated using average fission fragment momenta and the statistical model for neutron evaporation.

An experiment was done to test for excess forward folding of fragments from fission induced by 20 MeV ^{3}He particles from the tandem Van de Graaff on a 100 $\mu g/cm^2$ natural uranium target. The fission fragments were detected in coincidence in two detectors. One detector was a standard fission fragment detector with a 1 degree acceptance aperture set at -70° with respect to the beam direction. The other detector was a 14 mm by 50 mm active area position sensitive detector (p.s.d.) collimated to 13.6 mm by 49 mm (12° acceptance in the reaction plane). The detector had a calibrated 0.7 mm position sensitivity and was set at 103° with respect to the beam to reduce the number of elastically scattered ^{3}He's detected. This detector was used because a preliminary investigation showed the count rate to be prohibitively low using two conventional fission fragment detectors. The energy and position-times-energy signals from the p.s.d. in coincidence with energy signals from the fission fragment detector were fed into an SDS 930 computer where the position and energies were each stored in 512 channels. This experiment revealed that the position sensitivity was non-uniform over the active surface of the p.s.d. Subsequent testing shows that the energy signal varies with position toward the ends of the active area of the detector. These two nonlinearities made it doubtful that our p.s.d. could be used for the accurate measurement of position and energy of fission fragments. Meanwhile, recent work by Alford[1] showed that the reaction ^{208}Pb(^{3}He,α) can be used to pick up neutrons from all the single particle states in the top shell of ^{208}Pb. This work motivated us to abandon the measurement of the fission fragment angular correlations as a way of detecting this surface pickup and pursue the measurement of the α particles emitted in a ^{3}He induced reaction. This work is reported elsewhere (Sec. 8.6). (R. Aley, D.R. Brown, and I. Halpern)

---

1. W.P. Alford and D. Burke, to be published.

10.4 Determination of First Chance Mass Yield Curve

This report completes the work mentioned in last year's report.[1] Solid state counters were used to measure kinetic energies of complementary fission

fragments and from these energies the fragment masses could be found. It is known that in the element region near radium triple-peaked mass-yield distributions are found. These represent a superposition of contributions from several nuclear species at different excitation energies. The triple-peakes mass distributions have sometimes been interpreted in terms of two separate fission modes: a single symmetric peak, characteristic of symmetric fission, associated with higher excitation energies, and a double-peaked distribution, characteristic of assymetric fission, associated with lower excitation energies. By a proper choice of proton and deuteron bombarding energies, and by a proper weighing of their respective mass yield curves, the mass distribution of a single species, ^{228}Ac, can be determined for a single excitation energy. Fig. 10.4-1 illustrates the mass yield curve so obtained for excitation energies near 27 MeV. The single symmetric peak is in agreement with the hypothesis of two fission modes. (A.W. Fairhall and D. Perry)

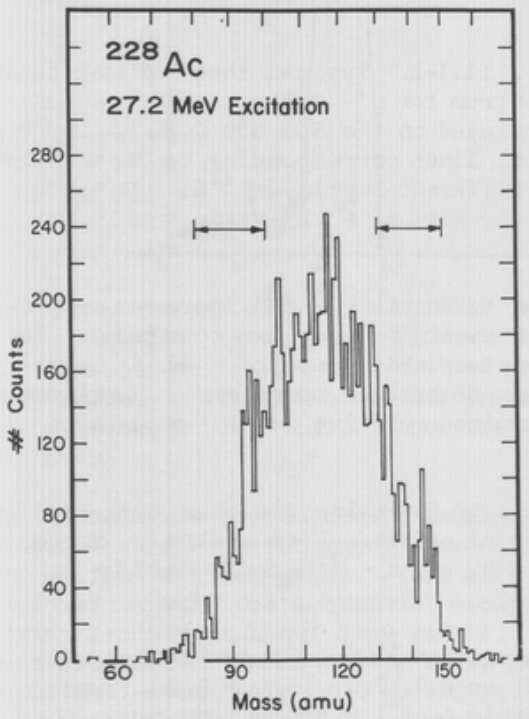

Fig. 10.4-1. First chance fission mass yield curve for ^{228}Ac at 27.2 MeV excitation energy. The arrows indicate the asymmetric fission positions.

---

1. Nuclear Physics Laboratory Annual Report, University of Washington (1969), p.106.

11. OTHER NUCLEAR PROCESSES

11.1 Particle Decay of Excited Nuclei Formed by Alpha Bombardment of ^{12}C

The study of single particle levels in nuclei above the particle emission threshold, using single counter techniques, becomes increasingly difficult as one goes to higher excitations. In these circumstances advantage may be taken of sequential reactions of the type

$$A + a \rightarrow b + B^* \rightarrow d + c + C.$$

In these reactions one can further make use of the selection rules for the formation and the decay of the nucleus B^* to determine the properties of the excited state.

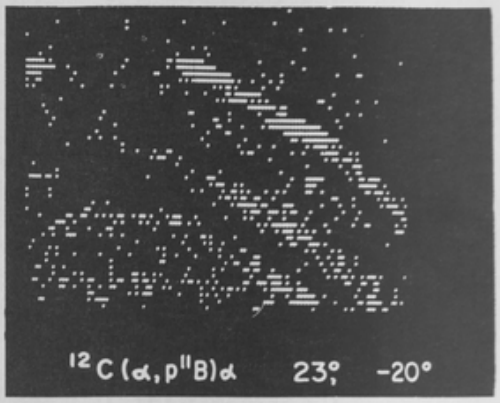

Fig. 11.1-1. Typical three-dimensional spectrum for p - ^{11}B coincidences as displayed on the SDS 930 C.R.T. The diagonal lines corresponding to transitions to different levels in ^{11}B. Detector angles were $\theta_p = 23°$, $\theta_{^{11}B} = 20°$.

In a study of the bombardment of ^{12}C by 42 MeV alpha particles discussed elsewhere in this report (Sec. 8.1) data were taken using a multiparameter program which stored on magnetic tape coincident events between two counters. The type of one of the coincident particles was determined by use of a ΔE-E telescope while the mass of the other particle was determined using the relationship mass $\propto Et^2$, the time-of-flight (t) being determined relative to the cyclotron oscillator.

The use of the time-of-flight criteria to determine the mass resulted in data which were essentially free from accidental events. From analysis of the data coincident events between p - ^{11}B, d - ^{10}B, and t - ^{12}C could easily be seen.

A three-dimensional display for the reaction $^{12}C(\alpha,^{11}Bp)\alpha$ is shown in Fig. 11.1-1. Events leading to states of ^{11}B at 0.0, 2.1, (4.4 + 5.0), and 7.3 MeV excitation can be seen as separate kinematic loci. A projection onto the E_p axis, of the locus corresponding to ground state, is shown in Fig. 11.1-2. The peaks in this two-dimensional spectrum are due to sequential processes. These sequential decays can be due to one of the reactions

$$^{12}C + \alpha \rightarrow {}^{15}N^* + p \rightarrow \alpha + {}^{11}B + p,$$

$$^{12}C + \alpha \rightarrow {}^{12}C^* + \alpha \rightarrow p + {}^{11}B + \alpha,$$

$$\text{or } {}^{12}C + \alpha \rightarrow {}^{11}B + {}^{5}Li^* \rightarrow {}^{11}B + p + \alpha.$$

In order to determine which of these reactions was responsible for the strong peaks seen in Fig. 11.1-2 we have taken data for a number of cases in which the proton detector was fixed and the heavy particle detector was moved. It was

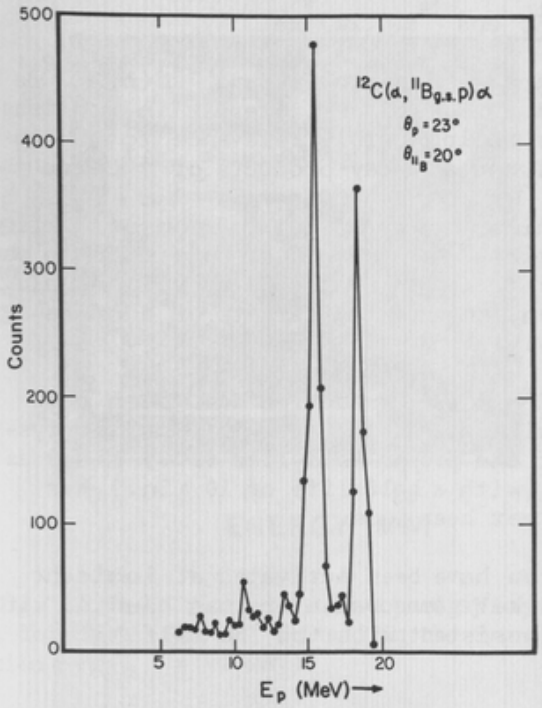

Fig. 11.1-2. Projection of the ground state locus of Fig. 11.1-1 onto the proton axis.

found that the proton energy remained constant while the energy of the ^{11}B varied for a given group. This allowed us to attribute the sequential decays to states in ^{15}N at about 13.6 and 15.7 MeV excitation. As these levels decay by alpha emission to the ^{11}B ground state they must have a large $T = \frac{1}{2}$ component.

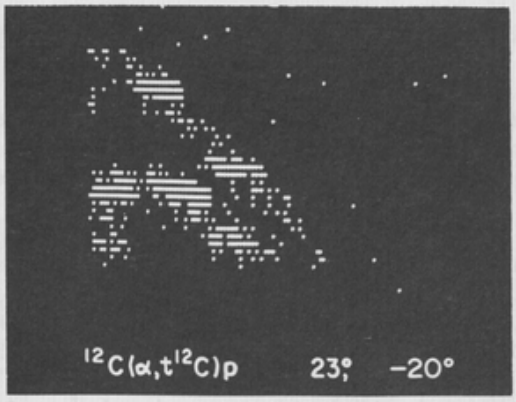

Fig. 11.1-3. Coincidence spectrum for the $^{12}C(\alpha,t^{12}C)p$ reaction at $\theta_p = 23°$, $\theta_{^{12}C} = 20°$.

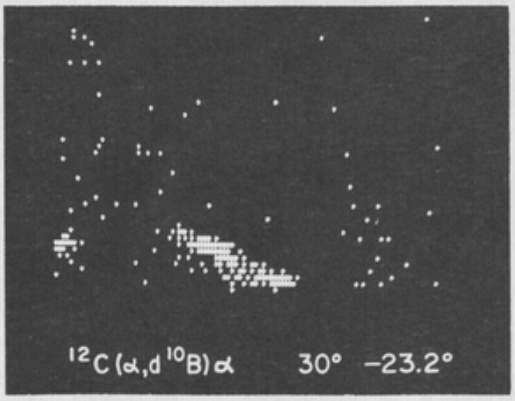

Fig. 11.1-4. Coincidence spectrum for the $^{12}C(\alpha,^{10}Bd)$ reaction at $\theta_d = 30°$, $\theta_{^{10}B} = 23.2°$.

A three-dimensional display for t - ^{12}C coincidences is shown in Fig. 11.1-3. Loci corresponding to ^{12}C being left in its ground states and 4.44 MeV level are easily discerned. In Fig.11.3-4 is shown a display of d - ^{10}B coincidences. Further analysis of these data are in progress to determine which compound nuclei are contributing sequential decays and to extract all information possible about these high lying excited states. (W.J. Braithwaite, J.M. Cameron, J.G. Cramer, and C.R. Rudy)

11.2 Excitation Functions for $^{14}N(p,\alpha)^{11}C$ and $^{14}N(p,2\alpha)^{7}Be$

A study has been under way to measure the $^{14}N(p,\alpha)^{11}C$ and $^{14}N(p,2\alpha)^{7}Be$ excitation functions via activation methods.[1] The primary interest in the measurement of these reaction cross sections is their possible relevance to nucleosynthesis of ^{11}B and ^{7}Li, which can be produced as decay products of ^{11}C and ^{7}Be.

A problem encountered in the preliminary study of both of these reactions was radiation from contaminants in the original targets (AlN evaporated onto pure Al catcher foil backings.) The problem was traced to Fe and Ni as well as aluminum oxide formed during target preparation. The use of targets of adenine ($C_5N_5H_5$) evaporated onto Al backings has solved these problems.

Preliminary investigations of the $^{14}N(p,\alpha)^{11}C$ reaction have been made using the adenine targets and detecting annihilation radiation in two NaI crystals operated in coincidence. Radiation of the proper half life (20.5 min.) as well as that from the reaction $^{14}N(p,d)^{13}N$ (with a half life of 10 min.) has been observed, but no final data runs have yet been made.

Targets for the $^{14}N(p,2\alpha)^{7}Be$ reaction have been activated at incident proton energies from 13 to 23 MeV. The 478 keV gamma radiation was counted with a NaI crystal. The observed half life is consistent with the ^{7}Be half life of 53.6 days.

Because of possible deterioration of the target, the proton elastic scattering peak from nitrogen was monitored during bombardment in order to determine the product of beam flux and the average nitrogen thickness. This determination requires knowledge of the elastic scattering cross section of protons on nitrogen at the various bombarding energies. Measurements of this cross section have been made using a gas target, although results so far have been obtained at only a few energies. There is still therefore some uncertainty (estimated to be about 20-30%) in the results for the $^{14}N(p,2\alpha)^{7}Be$ reaction. The present data indicates a rather rapid rise in the cross section as the incident proton energy is increased from threshold (11.5 MeV) to 19 MeV. At 21 MeV, the cross section is about 50 mb. (D. Bodansky, J. Cameron, and W. Jacobs)

---

1. Nuclear Physics Laboratory Annual Report, University of Washington (1969), p. 31.

11.3 Breakup of $^{16}O^*$, $^{20}Ne^*$, $^{32}S^*$ into Two Heavy Fragments

Symmetric fission of light nuclei at high excitation energy into two fragments such as seen in the reaction $^{28}Si(^{4}He,^{16}O)^{16}O$ has been shown to be a largely statistical process while single and few nucleon transfer reactions to low lying states in the residual nucleus are believed to be largely a direct reaction process. By simultaneously measuring angular distributions of various multi-nucleon transfer reactions one might be able to see how the transition from predominantly direct to predominantly statistical reactions is made as a function of number of nucleons transferred and as a function of the mass of the target nucleus.

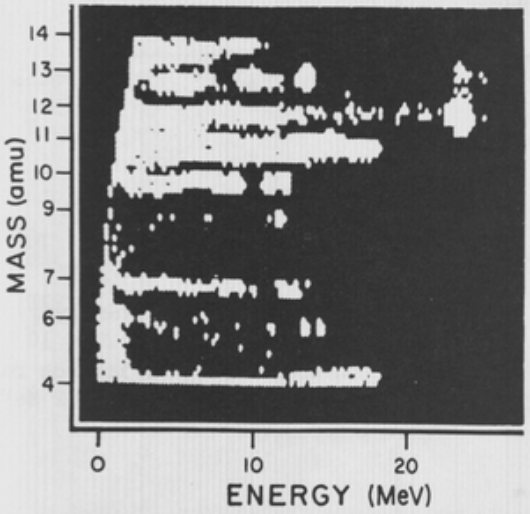

Fig. 11.3-1. A computer scope display of the isobars $4 \leq A \leq 12$ formed in the reaction $\alpha + \varepsilon (E_\alpha = 42$ MeV).

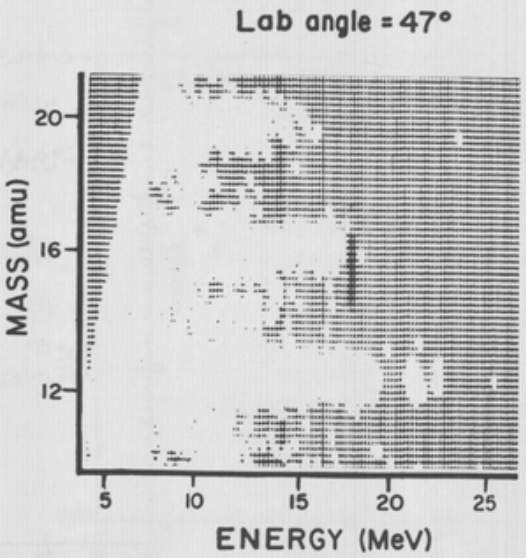

Fig. 11.3-2. A computer scope display of the isobars $10 \leq A \leq 20$ formed in the reaction α + Si(E_α = 42 MeV). The two spots above 20 MeV of the mass 12 isobar are due to carbon ions coming from the reactions $^{28}Si(\alpha,^{12}C)^{20}Ne_{g.s.}$ and $^{28}Si(\alpha,^{12}C)^{20}Ne(1.63$ MeV).

The mass distribution of heavy ions $Z \geq 3$, $A \geq 6$ resulting from 42 MeV alpha bombardment of carbon, oxygen and silicon has been measured. The mass of the product nucleus m was measured by use of the relationship $m \propto ET^2$ calculated on-line by an SDS 930 computer (for more details see Ref. 2), where E is the energy of the heavy reaction product and T is the flight time to the detector measured relative to the cyclotron RF signal. The heavy particles were detected by 100 μm thick thermoelectrically cooled surface barrier detectors located 25-29 in. from the target. Figure 11.3-1 shows a mass versus energy plot for $6 \geq A \geq 15$ resulting from 42 MeV bombardment of a thin carbon target with alpha particles. Figure 11.3-2 shows a similar plot for $10 \geq A \geq 20$ resulting from alpha bombardment of a thin silicon target. By observing both heavy reaction products (e.g., ^6Li and ^{10}B from $^{12}C(\alpha,^6Li)^{10}B$) to particular final states one measures simultaneously two center of mass angles for each reaction at one lab angle. This allows the measurement of angular distributions over a wider range than has in general been possible with ΔE-E particle identifier systems. Energy spectra of particular isobars are shown in Figs. 11.3-3,4, and 5. Cross sections for observed reactions are listed in Table 11.3-1. The cross sections were obtained by integrating over the listed angular range given in Table 11.3-1. Angular distributions obtained for some of the reactions are shown in Figs. 11.3-6 through 11.3-9. The $(\alpha,^6Li)$ reactions seem to be nearly symmetrical about 90° c.m., suggesting a predominantly compound nuclear mechanism.

Statistical Model calculations patterned after those done by Vogt *et al.*[3] have been performed in order to estimate the compound nuclear contributions to

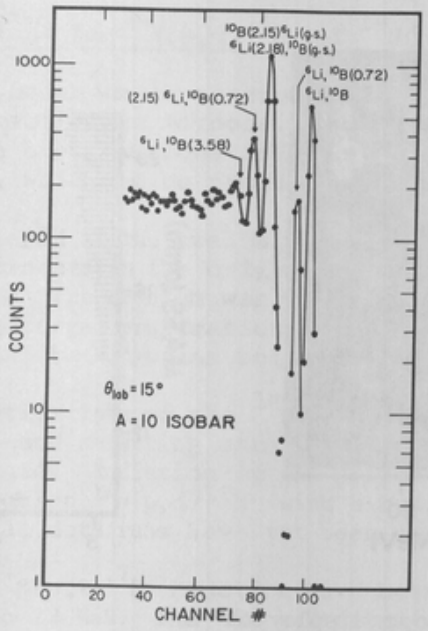

Fig. 11.3-3. Energy spectrum of the A = 10 isobars formed in the reaction α + C(E_α = 42 MeV).

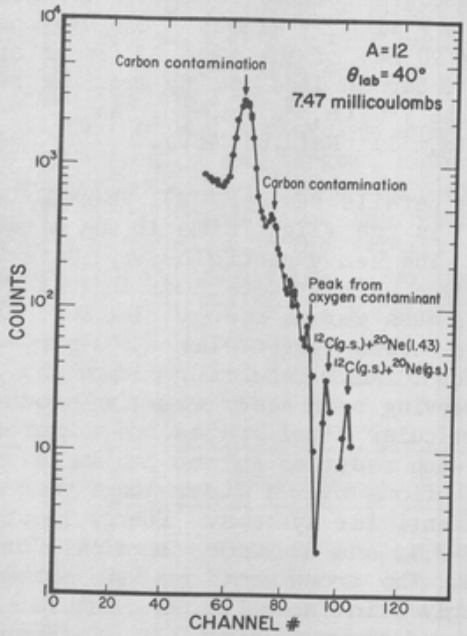

Fig. 11.3-4. Energy spectrum of the A = 12 isobars formed in the reaction α + Si(E_α = 42 MeV).

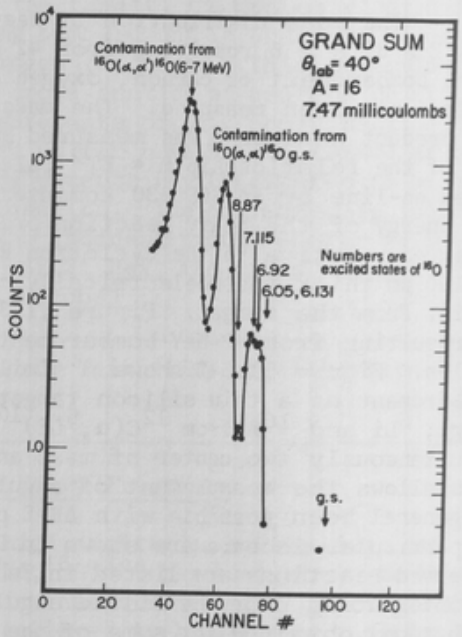

Fig. 11.3-5. Energy spectrum of the A = 16 isobars formed in the reaction α + Si(E_α = 42 MeV).

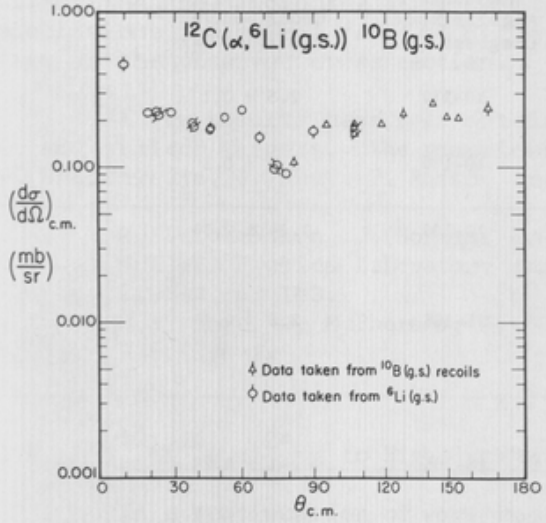

Fig. 11.3-6. Differential cross section of the reaction $^{12}C(^{4}He,^{6}Li)^{10}B_{g.s.}$

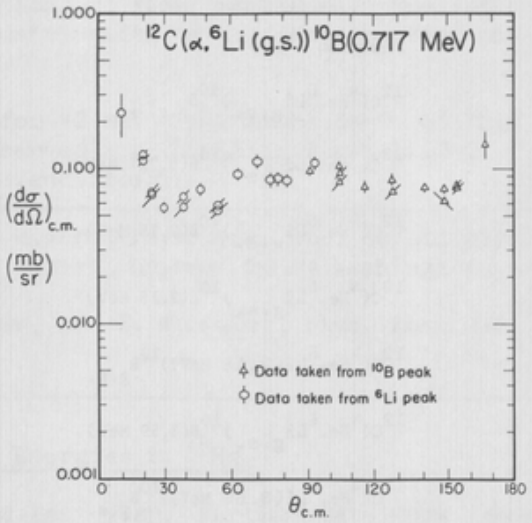

Fig. 11.3-7. Differential cross section of the reaction $^{12}C(^{4}He,^{6}Li)^{10}B$ (0.72) (E = 42 MeV).

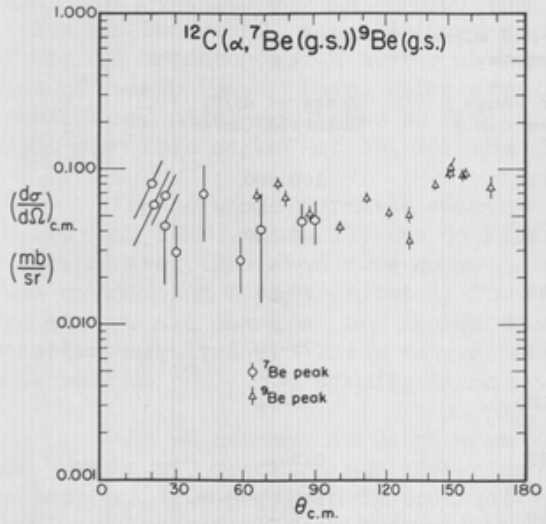

Fig. 11.3-8. Differential cross section of the reaction $^{12}C(^{4}He,^{7}Be)^{9}Be_{g.s.}$

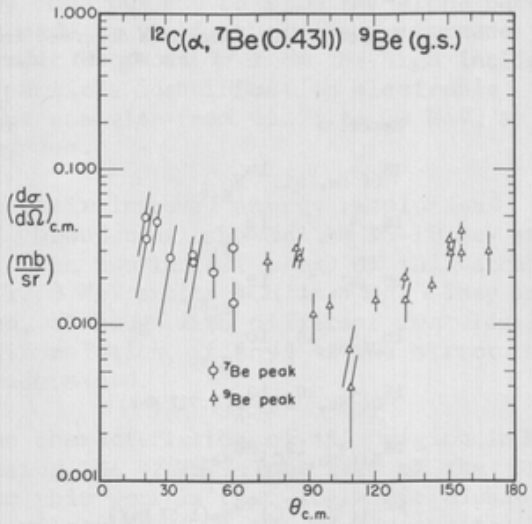

Fig. 11.3-9. Differential cross section of the reaction $^{12}C(^{4}He,^{7}Be(0.43))^{9}Be_{g.s.}$

Table 11.3-1. Reactions observed from 42 MeV alpha bombardment of a thin carbon target.

Reaction	Measured Angular Range (degrees c.m.)	Cross Section (millibarns)
$^{12}C(^{4}He, ^{6}Li_{g.s.})^{10}B_{g.s.}$	10-170	2.5 ± 0.1
$^{12}C(^{4}He, ^{6}Li_{g.s.})^{10}B(0.717\ MeV)$	10-170	1.1 ± 0.1
$^{12}C(^{4}He, ^{6}Li_{g.s.})^{10}B(2.15\ MeV)$	10-100	0.24 ± 0.06
$^{12}C(^{4}He, ^{6}Li_{g.s.})^{10}B(2.15\ MeV)$ $^{12}C(^{4}He, ^{6}Li(2.18\ MeV))^{10}B_{g.s.}$	95-166	2.3 ± 0.1
$^{12}C(^{4}He, ^{6}Li_{g.s.})^{10}B(3.59\ MeV)$ $^{12}C(^{4}He, ^{6}Li(3.56\ MeV))^{10}B_{g.s.}$	15-165	0.41 ± 0.23
$^{12}C(^{4}He, ^{6}Li(2.18\ MeV))^{10}B(0.717\ MeV)$	100-165	0.81 ± 0.07
$^{12}C(^{4}He, ^{7}Be_{g.s.})^{9}Be_{g.s.}$	20-170	0.74 ± 0.20
$^{12}C(^{4}He, ^{7}Be(0.431\ MeV))^{9}Be_{g.s.}$	20-170	0.32 ± 0.14

Table 11.3-2. Reactions observed from 42 MeV alpha bombardment of thin WO_3 and silicon targets.

Reaction	Angular Range (degrees c.m.)	Range of $d\sigma/d\Omega$ Observed (ub/sr)
$^{16}O(^{4}He, ^{6}Li)^{14}N_{g.s.}$	18-155	100-200
$^{16}O(^{4}He, ^{7}Be)^{13}C_{g.s.}$	20-110	30-100
$^{16}O(^{4}He, ^{7}Li)^{13}N_{g.s.}$	20-90	20-50
$^{16}O(^{4}He, ^{10}B)^{10}B_{g.s.}$	70-110	25-60
$^{16}O(^{4}He, ^{10}B)^{10}B(0.717\ MeV)$	80-100	15-30
$^{28}Si(^{4}He, ^{12}C)^{20}Ne_{g.s.}$	44-85	0.2-1
$^{28}Si(^{4}He, ^{12}C)^{20}Ne(1.63\ MeV)$	44-86	2-10
$^{28}Si(^{4}He, ^{16}O)^{16}O_{g.s.}$	46-90	0.1-0.2
$^{28}Si(^{4}He, ^{16}O)^{16}O(6\text{-}7\ MeV)$	60-93	3-4

to the above reactions. The calculations consider the decay of $^{16}O^*$ at an excitation energy of 38.7 MeV into all 2-body exit channels ($p, d, t, ^3He, ^4He, ^5He, ^5Li, ^6Li, ^7Li, ^7Be, ^8Be$) including internal excitations of these particles. Preliminary calculations indicate a compound nuclear contribution to the cross section as large as the observed cross section.

A few results have been obtained for 42 MeV alpha bombardment of thin WO_3 and silicon targets. The reactions observed are listed in Table 11.3-2. (W. Braithwaite, C. Rudy, P. Russo, and R. Vandenbosch)

1. R. Vandenbosch, J. Norman, and C. Bishop, Phys. Rev. *158*, 887 (1967).
2. Nuclear Physics Laboratory Annual Report, University of Washington (1969), p. 143.
3. E.W. Vogt, D. McPherson, J. Kuehner, and E. Almquist, Phys. Rev. *136*, B99 (1964).

11.4 $^{12}C(^{16}O,\alpha)^{24}Mg$ to High Excitation Energies in ^{24}Mg

In a continuation of work reported last year,[1] further data were taken on the $^{12}C(^{16}O,\alpha)^{24}Mg$ reaction at forward angles and incident ^{16}O energies from 30 to 50 MeV. The spectra in all cases showed considerable structure in the 15-18 MeV excitation energy region of ^{24}Mg. However, on the basis of the poor energy resolution obtained ($\approx$ 300 keV FWHM), resulting from straggling, the decision was made to discontinue use of the degrading foils which were being used to stop the heavy ions (elastic ^{16}O and recoil ^{12}C).

The present system consists of a ΔE-E telescope with the ΔE detector chosen to be thick enough to stop the heavy ions but not to stop the alpha particles of interest. A preliminary run was made to verify that the performance of the ΔE detector would suffer no significant degradation from the high incident flux of heavy ions. Then, using standard particle identification electronic techniques, data were taken at five incident energies from 41.75 to 50 MeV, at alpha particle angles of 10, 20, and 30 degrees.

These alpha-particle spectra with their improved energy resolution ($\approx$ 120 keV FWHM, primarily due to kinematic broadening) showed the 15-18 MeV excitation structure even more dramatically. The two largest peaks of this structure correspond to approximately 15.5 and 17.0 MeV excitation in ^{24}Mg. They are present at all energies and angles observed, although with different features and relative magnitudes. Their nature and their relation, if any, to the structure observed in $^{12}C + ^{12}C$ studies is not yet understood.

In an attempt to learn more of the characteristics of this region in Mg, the $^{24}Mg(\alpha,\alpha')$ reaction was investigated using the 42-MeV alpha beam of the cyclotron. The preliminary conclusion from this work is that inelastic alpha-particle scattering does not produce the same structure in the highly excited ^{24}Mg nucleus as does the $^{12}C(^{16}O,\alpha)^{24}Mg$ reaction.

The future study of the spectral structure in the $^{12}C(^{16}O,\alpha)^{24}Mg$ reaction will be facilitated by several experimental improvements: (a) to increase

the reliability of the alpha-particle energy calibration during the runs, a mechanical device has been built which lowers a pair of ^{212}Bi-^{212}Po alpha-sources between the two detectors of the telescope, thus providing two low energy calibration points for each spectrum. It is hoped that this will allow determination of the intermediate energies to better than ±50 keV. (b) The greater ^{16}O flux available from the recently installed direct extraction ion source of the tandem accelerator should speed data accumulation. (c) A further increase in the rate of data accumulation may also be achieved through use of up to 4 E-ΔE telescope systems simultaneously, together with an appropriate on-line computer analysis program. (D. Bodansky, D. Chamberlin, C. Ling, and D. Oberg)

---

1. Nuclear Physics Laboratory Annual Report, University of Washington (1969), p. 116.

11.5 Mass Determinations of Two Neutron-Deficient Isotopes by (p,2n) Threshold Measurements

The p,2n threshold measurements reported last uear have been completed, and the masses of two neutron-deficient isotopes have been determined.

The reactions involved in the measurements were

$$^{89}Y(p,2n)^{88}Zr\ (85\ d)$$

and

$$^{141}Pr(p,2n)^{140}Nd\ (3.3d).$$

Stacked foils of the appropriate targets (2 to 4 foils per stack) spaced with aluminum degraders were bombarded by proton beams from the 2-stage Van de Graaff accelerator. Previously described anslysis[1] of the gamma spectra of the bombarded foils led to the identification of the product nucleus and evaluation of the (p,2n) cross section at each energy. A 3 in. by 3 in. NaI(Tℓ) scintillator was used to analyze the activated ^{141}Pr foils. For the ^{89}Y foils, analysis after bombardment was carried out with an 8 cm^3 planar Ge(Li) detector in order to satisfy higher resolution requirements.

Thresholds were determined by two fitting methods. The first method involved extrapolation of a linear plot of the square root of the normalized target activity as a function of energy. Linear least square fits were used to determine the intercept on the energy axis which is the experimental threshold.

The second method fit the excitation functions to curves constructed by the Jackson neutron evaporation model.[2] This method has been described previously.[1]

The experimental thresholds resulting from these fits and the mass excesses of the product nuclei computed from these thresholds are compiled in Table 11.5-1.

The ^{89}Y results in Table 11.5-1 are in reasonable agreement with a recently determined Q value of the $^{89}Y(p,2n)$ reaction computed from experimental

Table 11.5-1. Experimental Thresholds and Mass Defects

Target Nucleus	Threshold (MeV, Center of Mass) / Mass Excess (MeV)	
	Linear Extrapolation	Jackson Model
^{140}Nd	10.65 ± 0.04	10.65 ± 0.04
	-84.26 ± 0.06	-84.26 ± 0.06
^{88}Zr	12.87 ± 0.03	12.96 ± 0.03
	-83.66 ± 0.04	-83.57 ± 0.04
	† 12.95 ± 0.003	
	-83.58 ± 0.01	

† Corresponds to linear least square fit eliminating the high energy data points which show a deviation from linearity.

results:[4]

$$Q(^{89}Y(p,2n)) = 12.906 \pm 0.015 \text{ MeV}.^{3}$$

^{140}Nd decays by electron capture to ^{140}Pr. The electron capture Q value is calculated using the experimental threshold in Table 11.5-1:

$$Q_{E.C.} = 0.50 \pm 0.09 \text{ MeV}.$$

Using this number, the value of $\log(f_{E.C.}t)$ is obtained by the method of Mozkowski.[5] The result is:

$$\log(f_{E.C.}t) = 5.6.$$

This value indicates the allowed (normal) beta decay mode ($\Delta I = 0$ or 1, no parity change) which is consistent with the spin and parity assignments of ^{140}Nd(0^+) and ^{140}Pr(1^+).

The experimental mass excesses can be compared to values predicted by several semi-empirical mass equations 6.,7.,8.,9). The calculated masses are shown in Table 11.5-2. The experimental values of Table 11.5-2 show good agreement with the semi-empirical calculations in some cases. The deviations are generally of the magnitude expected on the basis of the systematic deviation between other experimental and calculated masses.

Table 11.5-2. Predicted Mass Excesses

Mass Table	Mass Excess (MeV)	
	^{88}Zr	^{140}Nd
Garvey, *et al.* 6.)	-83.93	-84.27
Cameron and Elkin 7.)	-83.636	-84.026
Meyers and Swiatecki 8.)	-83.120	-84.288
Seeger and Perisho 9.)	-83.350	-83.882

(P.A. Russo and R. Vandenbosch)

1. P. Russo and R. Vandenbosch, Nuclear Physics Laboratory Annual Report, University of Washington (1969), p. 118.
2. J.D. Jackson, Can. J. Phys. *34*, 767 (1956).
3. J.B. Ball, private communication.
4. J.B. Ball, R.L. Auble, R.M. Drisko, and P.G. Roos, Phys. Rev. *177*, 1699 (1969).
5. S.A. Mozkowski, Phys. Rev. *82*, 35 (1951).
6. G.T. Garvey, W.J. Gerace, R.L. Jaffe, I. Talmi, and I. Kelson, Rev. Mod. Phys. *41*, 51 (1969).
7. A.G.W. Cameron and R.M. Elkin, "Role of the Symmetry Energy in Atomic Mass Formulas", Goddard Institute for Space Studies, N.Y. (1957), unpublished.
8. W.D. Myers and W.J. Swiatecki, UCRL-11980 (1965), unpublished.
9. P.A. Seeger and R.C. Perisho, LA-3751 (1967), unpublished.

11.6 Search for Double Analog States in Intermediate Mass Nuclei Using the (^{3}He,n2p) Reaction

Although excitations of many T = 2 analog states in T = 0 self conjugate nuclei below ^{40}Ca are well known, excitations of analog states with $T = T_{gs} + 2$ i.e., $T_{>>}$ or double analog states, have only been reported once in the higher mass region.[1] That report asserts that a T-forbidden (p,n) reaction was used to excite $T_{>>}$ states in ^{59}Ni and ^{90}Nb. The evidence for these excitations comes primarily from the observation of a peak in the neutron time-of-flight spectrum near the energy calculated for a $T_{>>}$ state. However, this observation has never been confirmed, and the strength of the peaks observed cast some doubt that they are the product of an isospin-violating reaction.

The present work is an attempt to observe the excitation of $T_{>>}$ states in the intermediate mass nuclei using the isospin allowed (^{3}He,n) reaction. Since the analog states thereby formed are unbound to both proton and diproton emission, such excitations may, in principle, be studied by observing the decay protons rather than the neutrons, in a manner similar to that used in studying

(d,np) reactions.[2]

We selected as a target ^{124}Sn since it has two holes in the $h_{11/2}$ subshell as one of its principal configurations. A two nucleon transfer reaction forming the $T_{>>}$ analog state could place the two protons in $1h_{11/2}$, $2d_{3/2}$, or $3s_{1/2}$ orbits, as shown in Fig. 11.6-1. We have done a crude calculation of the competition between proton and diproton decay from such an analog state. The transmission coefficients were calculated for both types of process, considering the diproton to have the same optical model potential as a "deuteron" with z = 2. Since the diproton decay can have $\ell = 0$ while the single proton decay must have the ℓ-value characteristic of the shell, such calculations show a favoring of diproton decay. Table 11.6-1 gives the ratios of calculated transmission coefficients. As can be seen, the diproton decay is favored in these calculations by a factor of 15 or more. While these crude calculations cannot be taken too seriously, they provide some indication that diproton decay should compete strongly with single proton decay.

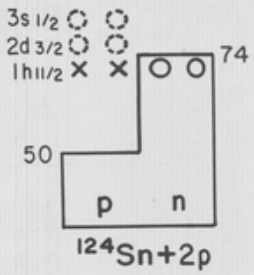

Fig. 11.6-1. Shell Diagram of ^{124}Sn+2p.

Table 11.6-1. Ratios of Proton to Diproton Transmission Coefficients

$n\ell j$	T_p/T_{2p}
$3s_{1/2}$	5.8×10^{-2}
$2d_{3/2}$	1.2×10^{-2}
$1h_{11/2}$	1.3×10^{-4}

The excitation energy of the $T_{>>}$ state was computed from the Coulomb displacement energy given by Long, Richard, Moore, and Fox.[3] The Q-value for ^{124}Sn $(^3$He,n$)^{126}$Te ($T_{>>}$) was calculated to be Q = - 21.099 MeV. A single proton decay from the $T_{>>}$ state in ^{126}Te to the lowest $T_>$ state in the next nucleus over, ^{125}Sb, will have an energy E_{p1} = 5.627 MeV. The $T_>$ state in ^{125}Sb is also unbound to proton emission and will decay back to the ^{124}Sn ground state with energy E_{p2} = 7.784 MeV. The transition energy for diproton decay is the sum of E_{p1} and E_{p2}, so E_{2p} = 13.411 MeV.

In the case of the successive single proton decays, the angular momenta of the transition from $T_{>>}$ to $T_>$ to T_0 for shell $n\ell j$ is $0^+(\frac{1}{2}\ell)j\ (\frac{1}{2}\ell)0^+$. Using the notation of Sharp *et al.*,[4] the angular correlation function $W_{p\text{-}p}(\theta)$ between the two protons is just

$$W_{p\text{-}p}(\theta) = \sum_k Z^2(\ell j \ell j; \tfrac{1}{2} k).$$

Table 11.6-2 gives $W_{p\text{-}p}(\theta)$ for appropriate j-value, where θ is the angle between the two protons and j is the spin of the $T_>$ intermediate state. It should be noted that $W_{p\text{-}p}(\theta)$ depends only on j and not on ℓ or π.

Unfortunately, the tables used[4] do not include j = 11/2 but numerical

Table 11.6-2. p-p Angular Correlation Functions

j	$W_{p-p}(\theta)$
$\frac{1}{2}$	1
$\frac{3}{2}$	$1 + P_2(\cos\theta)$
$\frac{5}{2}$	$1 + \frac{8}{7} P_2 + \frac{6}{7} P_4$
$\frac{7}{2}$	$1 + \frac{25}{31} P_2 + \frac{81}{77} P_4 + \frac{25}{33} P_6$
$\frac{9}{2}$	$1 + \frac{40}{33} P_2 + \frac{162}{143} P_4 + \frac{32}{33} P_6 + \frac{98}{143} P_8$

evaluation of W_{p-p} for lower j-values shows the trend clearly: $W_{p-p}(\theta)$ has peaks around $\theta = 0°$ and $180°$ and is small elsewhere. Therefore one should try to observe p-p coincidences from the sequential decays with $180°$ or near $0°$ geometry.

The angular dependence of the diproton decay should also have an enhancement near $0°$, the actual maximum angle determined by the ratio of decay momentum to breakup momentum. The actual angles selected for the experiment were $\pm 170°$, i.e., an angle of $\theta = 20°$ between the two counters. This geometry was a reasonable compromise which should permit the observation of both diproton and sequential proton decay from the $T_{>>}$ state of interest.

Two counter telescopes using 100 silicon surface barrier ΔE detectors and 2mm Si(Li) E detectors were placed 8" from a 94.7% isotopically enriched self-supporting ^{124}Sn target with an area density of about 1.6 mg/cm^2. A beam of about 100 ma of $^3He^{++}$ bombarded the target at several energies ranging from 24.75 MeV to 26.50 MeV.

Data was accumulated in the SDS 930 computer with a two-telescope two parameter program which performed $(E + \Delta)^{1.73} - E^{1.73}$ particle identification on both telescopes and stored the coincident events identified as proton-proton coincidences in a 64 × 64 channel array. All coincident events were blocked and stored on magnetic tape for further analysis.

Figure 11.6-2 shows a sample two parameter spectrum. Diagonal lines from the $^{124}Sn(^3He,2p)^{125}Sn$ reaction are clearly visible. These events can be distinguished from $^{124}Sn(^3He,n2p)$ because the latter remain unchanged in energy as the bombarding energy is varied. Figure 11.6-3 shows the same spectrum after summing all channels on a given diagonal $E_1 + E_2 = \text{const}$. The small arrows indicate the expected positions of ^{125}Sn states observed in $^{124}Sn(d,p)$, and these are found to be in good agreement with the observed states. The large arrow

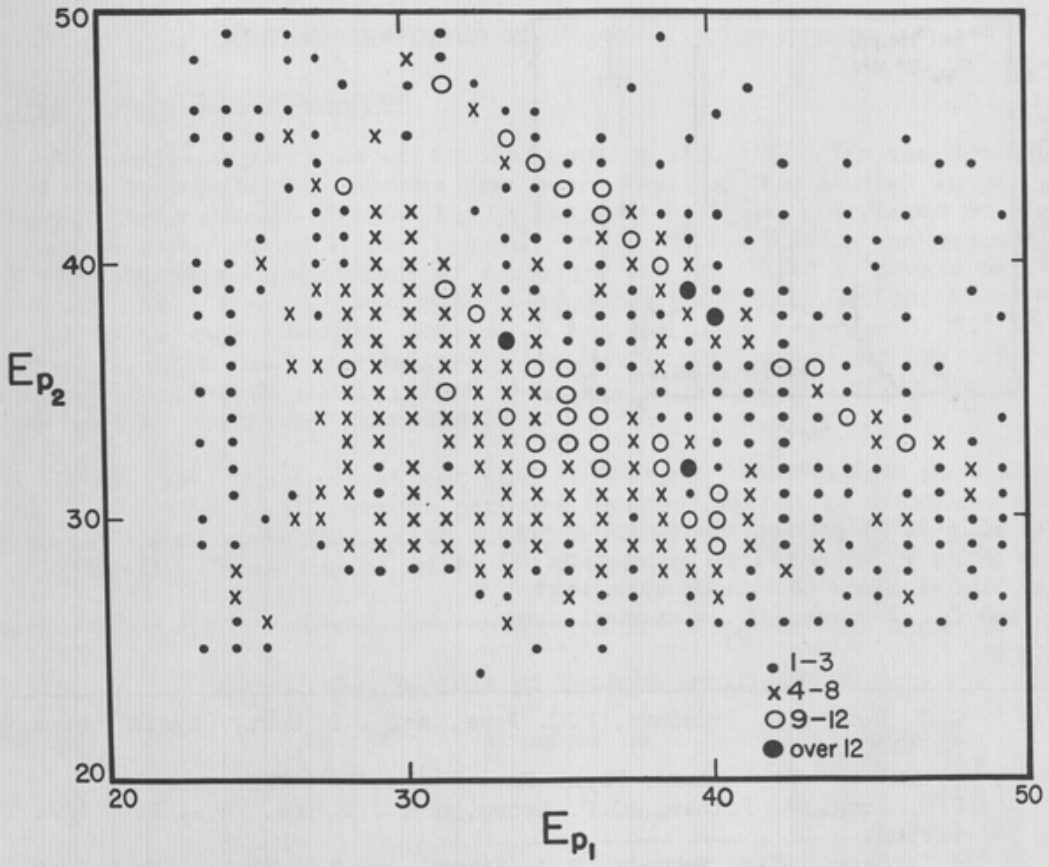

Fig. 11.6-2. Two parameter energy spectrum of proton-proton coincidences from ^{124}Sn + ^{3}He at E_{He} = 24 MeV. $\theta_{p1} = \theta_{p2} = 170°$.

indicates the expected position of the $T_{>>}$ state. No evidence is found for the excitation of that state in the present reaction. Moreover, no evidence is found for the excitation of the quasi-analog $T_{>}$ state expected about 8 MeV below the $T_{>>}$ state. This state is best described as the analog of the anti-analog of the $T_{>}$ state in the next nucleus over. This state is predicted to be excited about (2T + 1) more strongly than the $T_{>>}$ but may be highly fragmented.

Re-analysis of the data tapes in search of d-p coincidences from the reaction $^{124}Sn(^{3}He,d\bar{p})$ for the excitation and decay of the $T_{>}$ state in ^{125}Sb also showed no evidence of this excitation.

Further work is planned, using the technique described above with other targets and also observing the neutrons directly from (^{3}He,n) using a bunched beam. (M.P. Baker, W.J. Braithwaite, J.M. Cameron, N.S. Chant, J.G. Cramer, R. Hinrichs, and N. Mangelson)

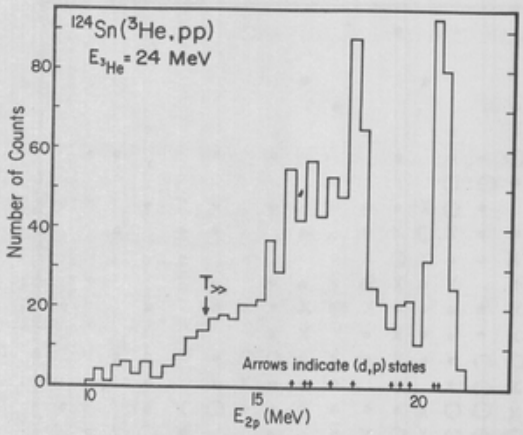

Fig. 11.6-3. Diproton energy spectrum from ^{124}Sn + ^{3}He obtained by summing Fig. 11.6-2 along diagonals such that C_{p1} and C_{p2} = const.(C_{pi} = channel number).

1. C.J. Batty, E. Friedman, P.C. Rowe, and J.B. Hunt, Physics Letters *19*, 33 (1965).
2. N. Cue and P. Richard, Phys. Rev. *173*, 1108 (1968).
3. D.D. Long, P. Richard, C.F. Moore, and J.D. Fox, Phys. Rev. *149*, 906 (1966).
4. W.T. Sharp, J.M. Kennedy, B.J. Sears, and M.G. Hoyle, "Tables of Coefficients for Angular Distribution Analysis", CRT-556, Chalk River, Ontario AECL. No. 97 (Revised 1954).

12. RESEARCH PERFORMED BY USER OR VISITOR GROUPS

12.1 *In vivo* Neutron Activation

The preliminary studies of *in vivo* neutron activation for the determination of total body calcium in humans have been completed and studies in patients have begun. The precision of counting in patients has been calculated to have a coefficient of variation of 1.2%. The uniformity of irradiation was measured by placing MnO_2 capsules in the bones of a cadaver and was found to have a standard deviation of 5.6%. Extensive dosimetry measurements and calculations have been carried out and reveal a neutron dose of .2 Rad and gamma ray does of 0.1 Rad. Three cadavers which had been repeatedly irradiated were ashed and the total calcium content measured chemically, thus enabling the estimation of bone mass in grams of calcium from patient irradiations.

In the first phase of patient studies 53 human irradiations have been performed (see Table 12.1). Several patients have had serial examinations and preliminary results in patients with advanced renal osteodystrophy suggest an average negative calcium balance of 6% (60 grams) per year.

Table 12.1. Results of Patient Irradiations

Disease	No. of Patients	Grams of Ca		Grams Ca /m^2 Body Surface Area	
		Mean	Range	Mean	Range
1. Normals	2	1190	1020-1360	646	580-712
2. Renal Osteodystrophy	22	1077	701-1440	607	473-782
3. Osteoporosis	4	739	631-867	436	387-538
4. Multiple Myeloma	6	896	578-1182	488	330-612
5. Hyperparathyroidism	1	962		476	
6. Hypoparathyroidism	1	1001		626	
7. Cushing's Syndrome	1	871		573	
8. Hand-Schüller Christian Disease	1	830		380	

Continued studies in humans will involve in addition to repeated longitudinal studies of the above patients: simulated weightlessness experiments in conjunction with NASA (the first two subjects were examined in February 1970 and will be reexamined after 16 weeks of bed rest); patients before and after renal transplantation; and a cooperative study between the University of Washington and the University of Oklahoma to investigate the efficacy of intravenous calcium therapy in osteoporosis using neutron activation analysis to monitor changes in

bone mass. (J.D. Denny*, G. Hinn*, R. Murano*, W.B. Nelp*, K.G. Pailthorp*, H.E. Palmer*, T. Rudd*, and J. Williams*)

---

* Department of Nuclear Medicine, University of Washington.

12.2 A Study of the Gamma Decay of the Compound Nucleus, ^{68}Ge

Experiments have been performed to study the gamma emission originating from the decay of the compound nucleus ^{68}Ge, both from the point of view of nuclear spectroscopy and reaction studies.

The 42 MeV alpha-particle beam from the University of Washington cyclotron was used to bombard target foils of isotopically pure ^{64}Zn and ^{65}Cu. A 30 cc Ge(Li) detector with a resolution initially of 3.3 keV at 1.3 MeV was employed to measure the gamma radiation.

Gamma spectra were measured at angles ranging from 45° to 125° with respect to the incident beam direction and covering gamma energies up to 8 MeV. Figure 12.2-1 shows a typical gamma spectra measured at 90° and covering the low gamma-energy region.

In a different set of experiments at a different installation an isotopically pure target of ^{52}Cr was bombarded with a variable energy ^{16}O beam. The ranges of energies varied from 30 to 56 MeV including the point of energy correspondence between the two different beams to form the compound nucleus ^{68}Ge at the same excitation energy.

The identification of these gamma rays is not straighforward as little is known in this region. From radioactivity studies performed simultaneously it has been suggested that the main product is the (p,n) product, ^{66}Ga; however, little correspondence is noted between the observed gammas and known levels in ^{66}Ga. It is hoped that the cross bombardment technique of the different targets as well as the excitation function performed with the ^{16}O bombardment will aid the identification process.

At present the main aim of the study is to elucidate the effects of angular momentum on the emission of gamma rays from the compound nucleus as well as perform nuclear spectroscopy studies on the levels of the neutron deficient isotopes of Ge and Ga. (B.D. Pate*, J.M. D'Auria*, and S. Barkan**)

---

* Department of Chemistry, Simon Fraser University, Burnaby, B.C.
** Department of Physics, University of Turkey, Istanbul.

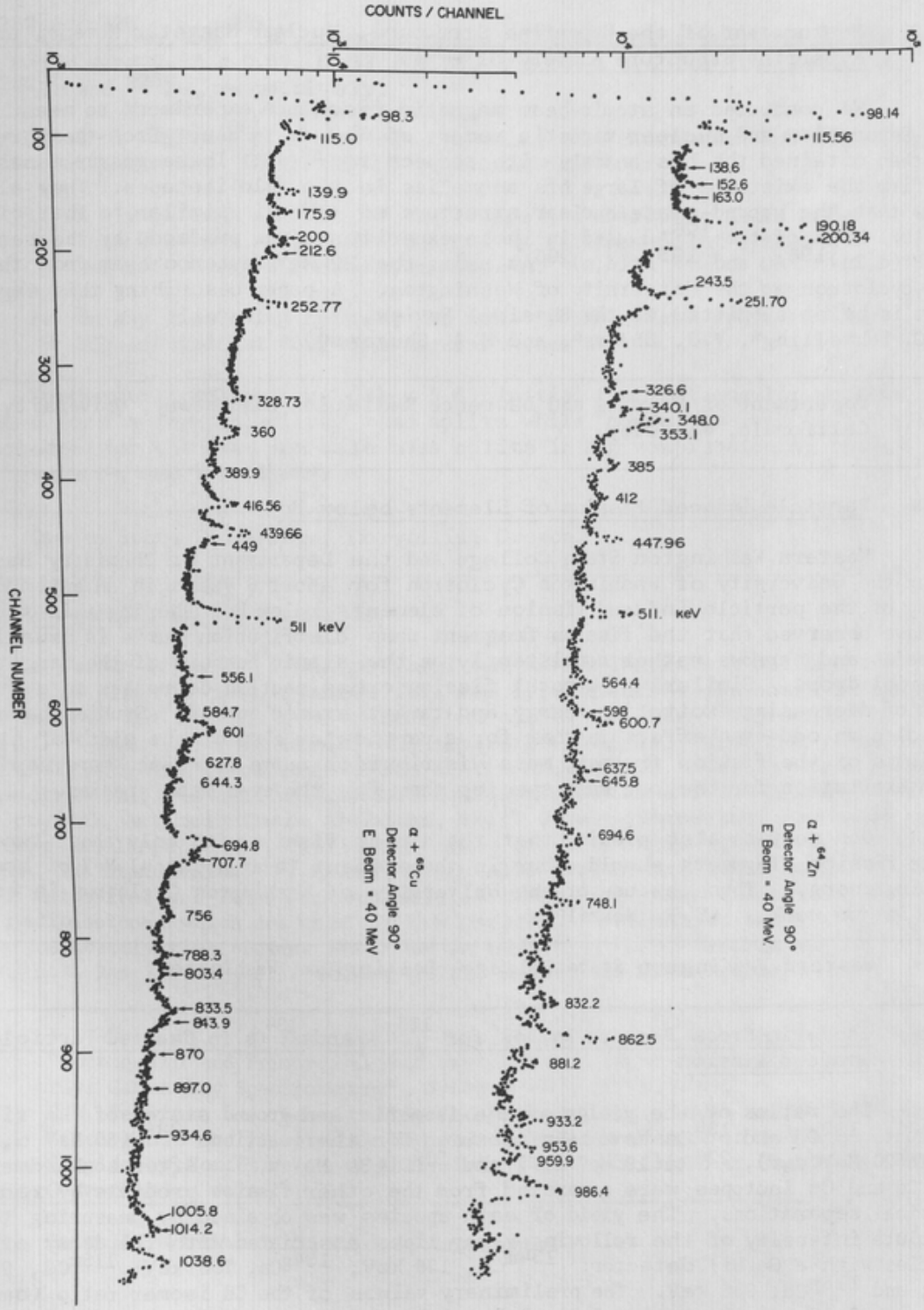

Fig. 12.2-1. A typical gamma ray spectrum.

12.3 Measurement of the Hyperfine Structure, Nuclear Magnetic Moment, and Hyperfine Structure Anomaly of ^{196}Au

We conducted an atomic-beam magnetic-resonance experiment to measure the hfs separation and nuclear magnetic moment of 6.2-day ^{196}Au. From these results we then obtained the hfs anomaly with respect to ^{197}Au. These measurements reconfirm the existence of large hfs anomalies in the gold isotopes. They also show that the ground-state nuclear structure of ^{196}Au is similar to that of ^{198}Au. Much of the ^{196}Au used in these experiments was produced by the reactions ^{196}Pt(d,2n)^{196}Au and ^{195}Pt(d,n)^{196}Au using the 22 MeV deuteron beam from the 60-in. cyclotron at the University of Washington. A paper describing this experiment is being submitted to the Physical Review.
(S.G. Schmelling*, V.J. Ehlers*, and H.A. Shugart*)

---

* Department of Physics and Lawrence Radiation Laboratory, University of California, Berkeley.

12.4 Particle Induced Fission of Elements below Po

Western Washington State College and the Department of Chemistry has been using the University of Washington Cyclotron for about 6 years in an extended study of the particle induced fission of elements below Po. During this study we have observed that the fission fragment mass distribution curve is usually gaussian and narrows rather consistently as the atomic numbers of the target material drops. Similarly the total fission cross section decreases as a function of decreasing excitation energy and target atomic number. Studies have also revealed an odd-even effect in that for a particular element the width of half maximums of the fission fragment mass distribution curve decreases more rapidly with excitation for the odd mass species than for the even mass species.

Our results also predict that the direct fission with only about two or three fission fragments should occur in the element Ta at about 41 MeV of bombarding energy. Thus the use of the University of Washington Cyclotron is essential in our work. (E.F. Neuzil*)

---

* Western Washington State College, Bellingham, Washington.

12.5 Isomeric Cross Section Ratios for ^{115}Cd and ^{134}Cs in Charged Particle Induced Fission

The ratios of the yields of the isomeric and ground states of the fission products ^{115}Cd and ^{134}Cs have been measured for the reactions ^{238}U(35 MeV α,f) ^{232}Th(20 MeV d,f), ^{226}Ra(19 MeV d,f) and ^{209}Bi(34 MeV α,f). After bombardment, the Cd and Cs isotopes were separated from the other fission products by radiochemical separations. The yield of each species was obtained by measuring the absolute intensity of the following γ-ray lines associated with the decay of each species with a Ge(Li) detector: ^{134m}Cs, 128 keV; ^{134g}Cs, 796 keV; ^{115m}Cd, 935 keV; and ^{115g}Cd, 335 keV. The preliminary values of the Cd isomer ratio ($\sigma m/\sigma m + \sigma g$) were 0.09 ± 0.01, 0.11 ± 0.02, 0.9 ± 0.5, and 0.9 ± 0.4 for the fission of

^{238}U, ^{232}Th, ^{226}Ra and ^{209}Bi, respectively. The preliminary values of the Cs isomer ratio were 0.51 ± 0.05, 0.57 ± 0.05, and 0.2 ± 0.1 for the fission of ^{238}U, ^{232}Th and ^{226}Ra, respectively.

Detailed analysis of these results using the Vandenbosch-Huizenga formalism is now in progress. The preliminary conclusions are:

1. A significant portion of the trends and absolute values shown in the isomer ratio data are due to scission point dynamics and not charge distribution effects.

2. In any fissioning system, the most probable mass split has the highest initial fragment angular momentum.

Furthermore, rather low ($\langle J \rangle \leq 5\hbar$) initial fragment angular momenta are indicated for the low probability mass splits while "normal" values ($\langle J \rangle \sim 8\text{-}10\hbar$) are indicated for the most probable mass splits in a given fissioning system. (W.D. Loveland*, and Y.S. Shum*)

---

* Oregon State University, Corvallis, Oregon.

12.6 Production of ^{48}V Standards

A source of pure ^{48}V was prepared for use in instrument calibration. A 0.010" thick piece of pure titanium foil was irradiated for two hours in the internal beam of the University of Washington cyclotron. The ^{48}V produced by the $^{48}Ti(p,n)^{48}V$ reaction was subsequently separated chemically from the titanium target foil and, after standardization of the solution on a Ge(Li) diode gamma-ray spectrometer, was used in standard counting geometries for calibration of large crystal, anticoincidence shielded, NaI(T) multidimensional gamma-ray spectrometers and large volume, anti-coincidence shielded Ge(Li) gamma-ray spectrometers. The standardized ^{48}V solution was also used in the fabrication of mock-ups of meteorites and lunar surface samples containing known quantities of various radioisotopes which are used in our program of evaluation and interpretation of the radioactivities present in lunar samples.[1,2] (R.L. Brodzinski*, R.W. Perkins*, L.A. Rancitelli*, J.A. Cooper*, J.H. Kaye*, and N.A. Wogman*)

---

1. R.W. Perkins, L.A. Rancitelli, J.A. Cooper, J.H. Kaye, and N.A. Wogman, "Cosmogenic and Primordial Radionuclides in Lunar Samples by Nondestructive Gamma-Ray Spectrometry", *Science 167*, 577 (1970).
2. R.W. Perkins, L.A. Rancitelli, J.A. Cooper, J.H. Kaye, and N.A. Wogman, "Cosmogenic and Primordial Radionuclide Measurements in Apollo 11 Lunar Samples by Nondestructive Analysis", to be published in Geochimica et Cosmochimica Acta.

---

* Battelle Northwest, Richland, Washington

12.7 Alpha-Particle Irradiation of Reactor Materials

Alpha-particle irradiations of fast-reactor cladding and structural materials are being carried out under a program at Atomics International sponsored by the AEC-DRDT called "Accelerator-Induced Irradiation Effects", Task 10B, Contract AT(04-3)-701, (now called "Irradiation Damage in Cladding and Core Structural Material", Task 2, Contract AT(04-3)-824) using the University of Washington's cyclotron. The cyclotron provides a fast and convenient method of introducing large concentrations of helium into various cladding candidates.

The program is divided into two sections; the first is the investigation of the variables, flux, fluence, temperature, and helium concentration, on the formation of voids in stainless steel. The cyclotron is used to implant helium in the alloys in a uniform manner at a low temperature. This is followed by accelerator proton irradiation to produce voids in the material. Electron microscopy is then used to ascertain the effects of the above mentioned variables on the size and distribution of the produced voids.

The second part is the study of high-temperature helium embrittlement in fast-breeder reactor cladding alloys. Helium is deposited uniformly in small sheet tensile samples prior to mechanical testing. Light and electron microscopy are used to study the effects of various thermo-mechanical treatments on the motion, agglomeration, and trapping of helium atoms and to determine the effect of helium on the mechanism of failure in the alloy.

The cyclotron is also used to irradiate samples in support of other AEC programs, including (1) the "Mixed Carbide Fuels" program, Task 11, Contract AT(04-3)-701. The motion of helium bubbles in a steep temperature gradient is being studied to gain further understanding of the mechanisms of fuel swelling. (2) "Radiation Damage in Crystalline Solids", Task 17, Contract AT(04-3)-701, which is investigating the formation of accelerator-induced voids in pure materials. (D. Kramer*, D.W. Keefer*, K.R. Garr*, G. Ervin, Jr.*, H.H. Neely*, A. Pard* and C.G. Rhodes*)

---

* Atomics International, Canoga Park, California.

12.8 Alpha-Particle Irradiations of Nickel and Stainless Steel

Alpha-particle irradiations of high-purity nickel and AISI type 316 stainlesl steel were conducted during the year under USAEC Contract AT(45-1)-1830. These irradiations were done for the purpose of injecting helium into thin-foil electron microscope specimens; irradiation conditions were chosen to produce a helium concentration of 0.3×10^{-6} percent by weight. The specimens are now being irradiated in EBR-II, a fast breeder reactor, and will be examined to determine whether the injected helium atoms affect the formation of voids (three-dimensional aggregates of lattice vacancies) in the two materials. This question is of primary concern in the US AEC Liquid Metal Fast Breeder Reactor (LMFBR) program, since the formation of voids results in unacceptable volumetric expansion of reactor structural components. The possibility of nucleation of voids at or stabilization of void nuclei by helium atoms produced by fast (n,α)

reactions must be established, and this will be done in the present experiment by irradiating materials previously doped with helium. (J.J. Laidler*)

---

* Battelle Northwest, Richland, Washington

12.9 Production of Voids in Stainless Steels by Cyclotron Bombardment

Initial experiments were performed by G. E. personnel at the University of Washington Nuclear Physics Laboratory. The purpose of these experiments was to develop experimental techniques for the production of voids in stainless steels by cyclotron bombardment. In these initial experiments, specimens of annealed and cold-worked Type 316 stainless steel were bombarded with high energy alpha particles at 500°C for times up to 10^4 seconds. (J.S. Armijo*)

---

* General Electric Company, Sunnyvale, California

---

13. APPENDIX

13.1 Nuclear Physics Laboratory Personnel

Faculty

Peter Axel, Visiting Professor[1]
John S. Blair, Professor
David Bodansky, Professor
John G. Cramer, Associate Professor
Albert Demeyer, Visiting Assistant Professor[2]
William W. Eidson, Visiting Professor[3]
Arthur W. Fairhall, Professor
George W. Farwell, Professor
James B. Gerhart, Professor
I. Halpern, Professor
Madhukar K. Mehta, Visiting Professor
Fred H. Schmidt, Professor
Henry C. Thomas, Visiting Professor[6]
Thomas A. Tombrello, Visiting Professor[7]
Robert Vandenbosch, Professor

Research Staff

John R. Calarco, Research Associate
John M. Cameron, Research Associate
Nicholas S. Chant, Research Associate
Hiroyasu Ejiri, Senior Research Associate[8]
Thomas D. Hayward, Research Associate[9]
Nolan F. Mangelson, Reserach Associate[10]
Gero Michel, Research Associate[11]
Ekkehard Preikschat, Research Associate
Derek W. Storm, Research Associate
William G. Weitkamp, Senior Research Associate, Technical Director, Nuclear Physics Laboratory

Laboratory Supervisory Personnel

Harold Fauska, Research Electronics Supervisor; Assistant Technical Director, Nuclear Physics Laboratory
John W. Orth, Accelerator Engineer; Assistant Technical Director, Nuclear Physics Laboratory

Predoctoral Research Associates

Chemistry

Charles J. Bishop[12]
Dennis G. Perry[13]
Clifford Rudy
Robert W. Shaw, Jr.
Kevin L. Wolf[14]

Physics

Michael P. Baker
Wilfred J. Braithwaite
Douglas R. Brown
David Chamberlin
Gary M. Chenevert[15]
Juri Eenmaa
Stephen M. Ferguson[16]
Robert H. Heffner
Roger A. Hinrichs[17]
William A. Jacobs
David L. Johnson
Thomas K. Lewellen
Ching C. Ling
Dennis L. Oberg
Donald M. Patterson
William Q. Sumner
Joseph R. Tesmer
William R. Wharton

Research Assistants

Chemistry

Ronald Aley[18]
Phyllis A. Russo

Physics

William J. Courtney[20]
Roscoe E. Marrs
K. Gopinathan Nair
Howard H. Wieman

Full-Time Technical Staff

Accelerator Operators

Barbara K. Lewellen

Accelerator Technicians

Carl E. Linder
Georgia J. Rohrbaugh
George E. Saling

Chemists

Joanne M. Heagney
Shirley Kellenbarger

Design and Drafting

Peggy Douglass, Graphics Aide
David W. Gough, Designer
Lewis E. Page, Draftsman

Electronics Technicians

Laverne H. Dunning
Kyum-Ha Lee
Norman G. Ward

Engineering and Physics

Noel R. Cheney, Computer Systems Engineer
Judith E. George, Engineering Aide
Rod E. Stowell, Field Engineer
Gary W. Roth, Physicist

Developmental Machinists

Harvey E. Bennett[19]
Norman E. Gilbertson
Charles E. Hart, Foreman
Gustav E. Johnson
Edwin P. McArthur
Byron A. Scott
Anthony Virant, Leadman
Allen L. Willman

Administrative Staff

N. Lynn Avedovech
Jennifer S. Osterman[20]
Susan E. Lambert[20]
Helene G. Turner, Administrative Secretary

Part-Time Technical Staff

Student Helpers

Jack R. Davis
Robert A. Falk
Emanuel L. Finch[20]
David O. Hall
William R. Mallgren
James F. Peterson[20]
Peter S. Rabinovitch
Eric Schnellman
Fred Weiss

---

1. Permanent address: University of Illinois, Urbana, Ill.
2. Permanent address: Institut de Physique Nucléaire, Faculté des Sciences, Lyon, France.
3. Permanent address: University of Missouri at St. Louis, Mo.
4. On leave; at Niels Bohr Institute, Copenhagen, Denmark.
5. On leave from Bhabha Atomic Research Centre, Bombay, India.
6. Permanent address: Texas Technological College, Lubbock, Texas.
7. Permanent address: California Institute of Technology, Pasadena, Calif.

8. Permanent address: Institute for Nuclear Study, University of Tokyo, Tokyo, Japan
9. Now at Duke University, Durham, North Carolina
10. Now at Brigham Young University, Provo, Utah
11. Now at Swiss Federal Institute for Nuclear Research, Würenlingen, Switzerland
12. Now at The Boeing Company, Kent, Washington
13. Now at Brookhaven National Laboratory, Upton, N.Y.
14. Now at Argonne National Laboratory, Argonne, Ill.
15. Now at University of Kentucky, Lexington, Ky.
16. Now at Kansas State University, Manhattan, Kansas
17. Now at Michigan State University, East Lansing, Mich.
18. Now Computer Consultant in Department of Physics, University of Washington
19. Retired July 31, 1969
20. Terminated

13.2 Advanced Degrees Granted, Academic Year 1969-1970

C.J. Bishop: Ph.D. "Competition between Neutron Emission and Fission at Moderate Excitation Energies in the Uranium Region".

G.M. Chenevert: Ph.D. " Highly Inelastic Scattering of Medium Energy ^{3}He and ^{4}He Particles by Heavy Nuclei".

S.M. Ferguson: Ph.D. "Transitions Feeding the Ground State Rotational Band Following (α,xn) Reactions Which Lead to Distorted Even-Even Nuclei".

R.A. Hinrichs: Ph.D. "Single Nucleon Transfer Reactions: The Extraction of Reliable Spectroscopic Factors and Charge Exchange Effects".

D.G. Perry: Ph.D. "Nuclear Fission of Actinium Nuclei and the Two-Mode Hypothesis".

D.W. Storm: Ph.D. "Measurements of Proton-Proton Bremsstrahlung at 20 MeV".

K.L. Wolf: Ph.D. "Spontaneous Fission Isomers".

13.3 List of Publications

"Fission Chips", I. Halpern and E.M. Henley, Comments on Nuclear and Particle Physics *3*, 52 (1969).

"Suppression of Vertical 'Jitter' of the Beam from an Inclined Field Tube 3-Stage FN-type Tandem Van de Graaff Accelerator", N.J. Caling, H. Fauska, and F.H. Schmidt, IEEE Trans. Nucl. Sci.*NS-16*, 96 (1969).

"A Beam Chopper for Use with a 60-in. Fixed Frequency Cyclotron", H. Fauska, R.E. Karns, and D.M. Drake, Nucl. Instr. and Meth. *72*, 233 (1969).

"Isobaric Analogue Resonant (p,γ) Reactions on ^{92}Mo", H. Ejiri, S.M. Ferguson, I. Halpern, and R. Heffner, in *Nuclear Isospin*, ed. by J.O. Anderson, S.D. Bloom, J. Cerny and W. True (Academic Press, New York, 1969), p. 65.

"The ^{140}Ce(p,γ)^{141}Pr Reaction through Isobaric Analogue Resonances in ^{141}Pr", H. Ejiri, P. Richard, S. Ferguson, R. Heffner, and D. Perry, Nucl. Phys. *A128*, 388 (1969).

"Beta Decay of ^{10}C", D.R. Brown, S.M. Ferguson, and D.H. Wilkinson, Nucl. Phys. *A135*, 159 (1969).

"An improved method of calculating finite range corrections in two nucleon transfer reactions", N.S. Chant and N.F. Mangelson, Nucl. Phys. *A140*, 81 (1970).

"The reactions ^{14}N(p,^{3}He)^{12}C, ^{14}N(d,α)^{12}C, ^{13}C(p,d)^{12}C and the 4^{+} level of ^{12}C", D.K. Scott, P.M. Portner, J.M. Nelson, A.C. Shotter, A.J. Mitchell, N.S. Chant, D.G. Montague and K. Ramavataram, Nucl. Phys. *A141*, 497 (1970).

"Spin Flip in the Inelastic Scattering of Protons", W.A. Kolasinski, J. Eenmaa, F.H. Schmidt, H. Sherif, and J.R. Tesmer, Phys. Rev. *180*, 1006 (1969).

"Low Lying Levels of ^{208}Pb with $g_{9/2}$, $i_{11/2}$, or $j_{15/2}$ Neutron Particle Configurations", Patrick Richard, P. von Brentano, H. Wieman, W. Wharton, W.G. Weitkamp, W.W. McDonald, and D. Spalding, Phys. Rev. *183*, 1007 (1969).

"Energy and Angular Dependence of Differential Cross Sections for the ^{16}O(^{16}O,α)^{28}Si Reaction", R.W. Shaw, Jr., J.C. Norman, R. Vandenbosch, and C.J. Bishop, Phys. Rev. *184*, 1040 (1969).

"Structure of ^{15}N and the ^{14}N(d,p)^{15}N Reaction", G.W. Phillips and W.W. Jacobs, Phys. Rev. *184*, 1052 (1969).

"Experimental Test of Statistical Approximations when $\Gamma/D > 1$", R.W. Shaw, Jr., A.A. Katsanos, and R. Vandenbosch, Phys. Rev. *184*, 1089 (1969).

"Analog Resonances of ^{206}Tℓ and ^{204}Tℓ", W.R. Wharton, W.J. Courtney, and Patrick Richard, Phys. Rev. *188*, 1934 (1969).

"Elastic Scattering of Alpha Particles by Intermediate-Mass Nuclei", B. Fernandez and J.S. Blair, Phys. Rev. *C1*, 523 (1970).

"Inelastic Scattering of 42-MeV Alpha Particles by ^{25}Mg", J.S. Blair and I.M. Naqib, Phys. Rev. *C1*, 569 (1970).

"Persistence of Odd-Even Effect on Nuclear Level Densities at High Excitation Energy", A.A. Katsanos, R.W. Shaw, Jr., R. Vandenbosch, and D. Chamberlin, Phys. Rev. *C1*, 594 (1970).

"Spontaneous Fission Isomers with Very Short Half-lives", R. Vandenbosch and K.L. Wolf, in *Physics and Chemistry of Fission*, (International Atomic Energy Agency, Vienna, 1969), p. 439.

"Gamma Ray Transitions from Isobaric Analogue States to Low-Lying States in ^{93}Ti", H. Ejiri, S.M. Ferguson, I. Halpern, and R. Heffner, Phys. Letters *29B*, 111 (1969).

"Proton-Channel Analog Resonances and Weak Coupling in the ^{206}Tℓ(d,p)^{206}Tℓ Reaction", W.R. Wharton, R.A. Hinrichs, G.W. Phillips, and J.G. Cramer, Phys. Letters *30B*, 33 (1969).

Manuscripts in Press or Submitted for Publication:

"Excitation Energy Dependence of Neutron Yields and Fragment Kinetic Energy Release in the Proton-induced Fission of ^{233}U and ^{238}U", C.J. Bishop, R. Vandenbosch, R. Aley, R.W. Shaw, Jr., and I. Halpern, (to be published in Nucl. Phys.).

"A Study of some (p,t) and (p,^{3}He) reactions induced by 49.5 MeV polarized protons", J.M. Nelson, N.S. Chant, and P.S. Fisher (submitted to Nucl. Phys.).

"Gamma Transitions from High Spin States in the β-Vibrational Band of ^{154}Gd", S.M. Ferguson, R. Heffner, and H. Ejiri (submitted to Nucl. Phys.).

"Spontaneous Fission Isomerism in Uranium Isotopes", K.L. Wolf, R. Vandenbosch, P.A. Russo, M.K. Mehta, and C.R. Rudy (to be published in Phys. Rev.).

"Substate Populations and Nuclear Polarization Produced by Inelastic Alpha-Particle Scattering on Carbon-12", T.D. Hayward and F.H. Schmidt (to be published in Phys. Rev.).

"The $^{20}Ne(p,t)^{18}Ne$ reaction as a test of the ^{18}Ne wave function", J. L'Ecuyer, R.D. Gill, K. Ramavataram, N.S. Chant, and D.G. Montague (submitted to Phys. Rev.).

"A comparison of polarization analyzing powers of two nucleon transfer reactions leading to mirror final states", J.M. Nelson, N.S. Chant, and P.S. Fisher (submitted to Phys. Letters).

"Spectra of High Energy Photons Emitted from the Compound System ^{64}Zn in Various Nuclear Reactions", D. Drake, S.L. Whetstone, and I. Halpern (submitted to Phys. Rev. Letters).

"An improved method of calculating finite range effects in two-nucleon transfer reactions", N.S. Chant and N.F. Mangelson, to be published in Proceedings of the Symposium on Nuclear Reaction Mechanisms and Polarization Phenomena, University of Laval, Quebec (1969).

"A comparison of polarization analyzing powers of two nucleon transfer reactions leading to mirror final states", J.M. Nelson, N.S. Chant, and P.S. Fisher, to be published in Proceedings of the Symposium on Nuclear Reaction Mechanisms and Polarization Phenomena, University of Laval, Quebec (1969).

"Nuclear Polarization of $^{12}C^{*}(4.44)$ Nuclei Excited by Inelastic Alpha Scattering", F.H. Schmidt and T.D. Hayward, to be published in Proceedings of Symposium on Nuclear Reaction Mechanisms and Polarization Phenomena, University of Laval, Quebec (1969).

"Levels in the A = 5 nuclei excited in single and double nucleon pickup reactions", M.P. Baker, J.M. Cameron, N.S. Chant, N.F. Mangelson and D.W. Storm, to be published in Proceedings of the International Conference on Properties of Nuclear States, Montreal (1969). Paper 8.12.

"The structure of the even nickel isotopes from the (p,t) reaction", W.G. Davies, W. McLatchie, J.E. Kitching, D.G. Montague, K. Ramavataram, and N.S. Chant, to be published in Proceedings of the International Conference on Properties of Nuclear States, Montreal (1969). Paper 8.58.

"Study of the Energy Dependence of the p-p Quasi-Free Scattering in the Reaction D(p,2p)n", W.J. Braithwaite, J.M. Cameron, D.W. Storm, D.J. Margaziotis, G. Paic, P. Tomas, J.R. Richardson, and J.W. Verba, to be published in Proceedings of the International Conference on the Three Body Problem, Birmingham (1969).

"Isomer in ^{174}Hf", by H. Ejiri, S.M. Ferguson, R. Heffner, and H. Wieman, to be published in Proceedings of International Conference on Radioactivity in Nuclear Spectroscopy, Nashville, Tenn. (1969).

Papers given at Meetings and Conferences other than those listed above

"Spontaneous Fission Isomers with Short Half-Lives", Kevin L. Wolf, Gordon Research Conference on Nuclear Chemistry, June 1969 (invited paper).

"Nuclear Reactions with Identical Heavy Ions", R. Shaw and R. Vandenbosch, American Chemical Society Meeting at New York, Sept. 1969 (invited paper).

"The Energy Dependence of the Reaction $^{2}H(p,d)p$ between 7 and 14.5 MeV", W.J. Braithwaite, J.M. Cameron, D.W. Storm, and T.A. Tombrello, Bull. Am. Phys. Soc. *14*, 1211 (1969).

"Study of the Energy Dependence of the p-p Quasi free Scattering in the Reaction D(p,2p)n", D.J. Margaziotis, G. Paic, J.G. Rogers, J.W. Verba, J.C. Young, W.J. Braithwaite, J.M. Cameron, and D.W. Storm, Bull. Am. Phys. Soc. *14*, 1212 (1969).

"Gamma Decay of the 4.71 MeV $d_{5/2}$ Analog Resonance in the $^{90}Zr(p,\gamma)$ Reaction", S.M. Shafroth, J.M. Joyce, T. Hain, H. Ejiri, and J.G.F. Legge, Bull. Am. Phys. Soc. *14*, 1215 (1969).

"Isospin Coupling in ^{94}Zr + p and $^{98,100}Mo$ + p Reactions", G.W. Phillips, R.A. Hinrichs, J.G. Cramer, H. Wieman, and K.G. Nair, Bull. Am. Phys. Soc., *14*, 1216 (1969).

"Substate Cross Sections in the Inelastic Scattering of Protons from $^{58}Ni(1.45\ MeV,2^{+})$ and $^{12}C(4.44\ MeV,2^{+})$", J.R. Tesmer, J. Eenmaa, T. Lewellen, D.M. Patterson, and F.H. Schmidt, Bull. Am. Phys. Soc. *14*, 1220 (1969).

"A Test of the Isospin Quantum Numbers of the $^{12}C(\alpha,d^{*})^{14}N$ Reaction", W.J. Braithwaite, J.M. Cameron, J.G. Cramer, and C.R. Rudy, Bull. Am. Phys. Soc. *14*, 1220 (1969).

"Dependence of Γ_n/Γ_f on Excitation Energy in the Uranium Region", C.J. Bishop, R. Vandenbosch, I. Halpern, R. Shaw, and R. Aley, Bull. Am. Phys. Soc., *14*, 852 (1969).

"Proton-Proton Bremsstrahlung Measurement at 20 MeV", Derek W. Storm and R. Heffner, Bull. Am. Phys. Soc. *15*, 475 (1970).

"Quasifree Scattering in the Reaction D(p,pn)p", W.J. Braithwaite, J.R. Calarco, J.M. Cameron, and D.W. Storm, Bull. Am. Phys. Soc. *15*,477 (1970).

"Spectra of High Energy Photons from Proton Bombardment of ^{64}Zn", D.M. Drake, S.L. Whetstone, and I. Halpern, Bull. Am. Phys. Soc. *15*,481 (1970).

"Evidence for Singlet Deuteron Enhancement from a Comparison of the Reactions $^{6}Li(d,pn)^{6}Li^{*}$ at 2.18 and 3.56 MeV", W.J. Braithwaite, J.M. Cameron, J.G. Cramer, and C.R. Rudy, Bull. Am. Phys. Soc. *15*, 519 (1970).

"Excited States in A = 6 Nuclei", M.P. Baker, J.R. Calarco, J.M. Cameron, N.S. Chant, and N.F. Mangelson, Bull. Am. Phys. Soc. *15*, 519 (1970).

"Particle Hole States in ^{208}Pb with the Configuration $(d_{5/2}, j^{-1})$", J.G. Kulleck, P. Richard, D. Burch, C. Fred Moore, W.R. Wharton, and P. von Brentano, Bull. Am. Phys. Soc. *15*, 546 (1970).

"The $^{12}C(^{4}He, ^{6}Li)^{10}B$ and $^{12}C(^{4}He, ^{7}Be)^{9}Be$ Reactions", C.R. Rudy, W.J. Braithwaite, P. Russo, and Robert Vandenbosch, Bull. Am. Phys. Soc. *15*, 629 (1970).

A photograph of 84.6% of the Laboratory personnel.

McArthur
Gilbertson Johnson Willman Hart
Johnson Heagney Fauska Gerhart Orth Linder Virant Cameron
Gough Russo Marrs Nair Rudy Shaw Weiss Rabinovitch Weitkamp
Hall Tesmer Roth Brown Bodansky Vandenbosch Stowell Preikschat Heffner Storm Lee Scott Lewellen
Jacobs Page Chamberlin Patterson Wharton Sumner Wieman Kellenbarger Baker Rohrbaugh Schmidt Turner Cramer Dunning Ward Ling Blair Eenmaa
Lewellen Douglass